BUCKLING AND STABILITY PROBLEMS FOR THIN SHELL STRUCTURES USING HIGH PERFORMANCE FINITE ELEMENTS

by
BJØRN HAUGEN

Siv.Ing., Norwegian Institute of Technology, 1988
M.S., University of Colorado, 1991

A dissertation submitted to the
Faculty of the Graduate School of the
University of Colorado in partial fulfillment
of the requirements for the degree of
Doctor of Philosophy
Aerospace Engineering Sciences
1994

This dissertation for the Doctor of Philosophy degree by

Bjørn Haugen

has been approved for the

Department of

Aerospace Engineering Sciences

by

C. A. Felippa

K. C. Park

Date _____

Haugen, Bjørn (Ph.D., Aerospace Engineering Sciences, 1994)
Buckling and Stability Problems for Thin Shell Structures
Using High Performance Finite Elements
Dissertation directed by Professor Carlos A. Felippa

A hierarchical co-rotational theory for analysis of geometrically nonlinear shell structures has been developed that addresses attributes identified as desirable: self-equilibrium, consistency, invariance, symmetrizability and element-independence. The unified formulation recovers different existing co-rotational formulations by making certain simplifying kinematic and static assumptions. This unification offers additional flexibility to finite element developers in that tradeoffs between simplicity, robustness and generality can be more clearly understood.

The nonlinear response of the co-rotational finite element models is obtained by incremental/iterative continuation methods. The equilibrium-path-following algorithm combines a standard arc length predictor phase with two alternative versions of a true-Newton corrector phase: the normal-plane corrector of Riks-Wempner and the orthogonal trajectory accession corrector proposed by Fried. The algorithm is treated with scaling techniques that aim to make the solution algorithm performance insensitive to discretization changes. Numerical experiments indicate that the orthogonal trajectory corrector in general outperforms the normal plane corrector in terms of robustness and allowance of larger stepsizes when tracing smooth response paths.

A modification of the predictor-corrector continuation algorithm to detect and handle traversal of bifurcation points has been developed. The modified algorithm relies on linearized buckling analysis carried out at two "bracketing" configurations in the neighborhood of the bifurcation point. The estimated buckling mode is used to initiate branch switching into the outgoing (secondary) path. The normal plane corrector constraint is modified to avoid the "switch-back" to the incoming (primary) path. This modification has proven to be robust in handling symmetric bifurcation points in the test problems reported here.

A new four-noded quadrilateral shell element has been developed based on the Assumed Natural-coordinate Deviatoric Strains formulation. This element is derived with reference to a flat geometry defined by the medians of the generally-warped quadrilateral. Projector matrices are used to fulfill self-equilibrium conditions in the warped geometry. The numerical results indicate that then new quadrilateral element delivers modeling accuracy similar to that of existing Free Formulation elements, but without the burden of numerical inversion to form the higher order stiffness.

ACKNOWLEDGEMENTS

I would like to to express my gratitude to my advisor Carlos Felippa, who has been a major reason why I have pursued a Ph.D. at University of Colorado. His interest, knowledge and forthcoming personality has been an inspiration and encouragement both professionally and personally.

Recognition is also due Professor Kjell Magne Mathisen for his long time advisory role and Professor K.C. Park for his interest in my work and the field of nonlinear shell analysis. In addition, I wish to thank the additional members of my advisory committee: Professor Charbel Farhat, Professor Lee Peterson and Professor Kaspar Willam.

The financial support for this work from the Norwegian Space Center and the Royal Norwegian Council for Scientific and Industrial Research in the form of a graduate fellowship, and partial support from the U.S. National Science Foundation under HPCC Grant ASC-9217394, are gratefully acknowledged.

Finally, the acknowledgements would be incomplete without the recognition of the many conversations with several friends like Scott Alexander, Scott Keating and Ken Alvin on topics ranging from the professionally very useful to the completely irrelevant, but fun, ones.

CONTENTS

Tables

Boxes

Chapter 1

Introduction.

Because of their high-strength and lightweight nature, aerospace structures often fail by elastic buckling. Furthermore, a structure or structural component may behave elastically while well into the post-buckling regime. Designers checking stability are often interested in questions of the following nature: can the structure, after overall buckling, maintain functionality in some sense? and, can the structure withstand localized buckling and post-buckling of a component? These questions are typical for aircraft-structures that are often critically designed by counting on load-carrying capability in the post-buckling range.

These considerations explain why reliable stability and post-buckling analysis tools are important components of the design of aerospace structures. One important analysis simplification is the assumption that material deformations stay small – usually in the elastic range – before and after buckling. This simplification has important benefits in constructing finite element models for stability analysis. It allows the use of linear finite element models to capture the deformational response whereas the large rigid-body motions characteristic of post-buckling are treated separately.

The co-rotational formulation of geometrically nonlinear analysis is based upon such explicit separation of rigid-body motions – translations and rotations – from deformational motions. This treatment "segregates the nonlinearity" into the former. The key benefit gained through this approach is "reuse": existing linear finite element models can be taken advantage of. Given the large investments made into the development of finite element libraries, including many years of fine tuning to efficient handle a spectrum of problems, reuse makes investment sense as long as users of programs based on the co-rotational formulation are aware of certain modeling limitations.

1.1 Survey of related work.

The present work focuses on the co-rotational finite element analysis of nonlinear shell structures. Thus it represents a fusion of three largely independent topics: the co-rotational formulation, the computation of the nonlinear response by continuation algorithms, and the construction of shell finite elements. A historical account of these topics is provided in the following sections.

1.1.1 Nonlinear co-rotated formulations.

The concept of a co-rotated formulation was first introduced by Wempner [64] in 1969 and by Belytschko and co-workers [10] in 1973. In 1976 Fraeijs de Veubeke [30] developed a co-rotated formulation for dynamic analysis of structures using a single co-rotated frame for the whole structure. De Veubeke's approach was geared towards analytical solutions rather than finite element formulations. The concept of a rotating frame attached to the elements was also used by Bergan and Horrigmoe [12,34] and Argyris [4]. In 1986 Rankin and Brogan introduced an element independent co-rotated formulation [52], which was later refined by Nour-Omid and Rankin [46,53]. Cardona [19] used the co-rotational consept for analysis of mechanisms in 1989. A co-rotational formulation for beam elements was developed by Crisfield [22] in 1990.

The starting point of the present research work has been the co-rotated formulation that started with Bergan and Horrigmoe [12,34] and has been further developed by Nygård [47], Levold [40], Mathisen [42] and Bjærum [17]. This formulation exploits the concept of a co-rotated orthonormal frame that is flexibly attached to the deformable element. The motion of the element frame also determines the motion of a rigid undeformed element, often called "ghost reference" or "shadow element". This formulation has proven satisfactory for many applications. For some problems, however, the formulation exhibits deficiencies, most notably with respect to consistency of the tangent stiffness with respect to the residual forces, and self-equilibrium of warped quadrilateral elements.

Several of these problems were also experienced by Rankin and Brogan [52] in their initial version of the element independent co-rotational formulation. Nour-Omid and Rankin [46,53] later addressed the questions of consistency and equilibrium. However, the current formulation of Nour-Omid and Rankin still places restrictions on how many degrees of freedom can participate in the rotation of the element frame while maintaining consistency of the tangent stiffness. These constraints lead to loss of mesh invariance; that is, the computed solution may depends on node numbering.

The present work tries to combine the best features of both co-rotational formulations. More specifically, the invariant nature of the Bergan et al. formulation, and the equilibrium and consistency of the Rankin et al. formulation.

1.1.2 Nonlinear solution algorithms.

There has been rapid progress over the last 20 years in algorithms for computing equilibrium solutions of geometrically nonlinear structural problems. Before the mid-1970s, such problems were usually treated with purely incremental methods under load control. Purely incremental methods have the important disadvantage that the accumulated drift error causes computed solutions to move away from the equilibrium path. Since those methods do not check residuals, the accumulated drift error can be practically assessed only by running the problem with smaller increments. In addition, load control makes automatic traversal of critical points difficult or impossible.

The drift-error disadvantage was eliminated with the introduction of incremental/iterative methods, in which a predictor step was followed by Newton-like corrective iterations to move back the solution onto the equilibrium path. The problem of traversing critical points, which is of crucial importance in nonlinear analysis, required modifications to the control strategy enforced during the corrector phase so as to allow both displacements and loads to change simultaneously. Early attempts to address the problem of critical point traversal in the 1960s resulted in the development of displacement control [2], and the introduction of artificial springs [56,67]. Refinement of the former evolved into the hyperplane displacement control method [59] in the early 1980s.

The arc length control method, which presently has become one of the most widely used incremental/iterative techniques, was independently proposed in the early 1970s by Riks [54] and Wempner [65]. This method, however, did not attract attention until popularized by Crisfield [20] in the early 1980s. Since then additional refinements of the arc length method and its variants have been published at an accelerated pace. Key contributions are by Bathe et al. [5,6], Batoz and Dhatt [8], Crisfield [21], Ramm [51] and Riks [55]. In addition, the orthogonal trajectory accession method of Fried [31] merits attention in that, unlike the conventional arc length methods, the corrector iterations are not controlled by an algebraic constraint.

1.1.3 Linear finite elements.

The Free Formulation (FF for short) was developed by Bergan and coworkers at Trondheim during the period 1972-1984. The development of the FF began with a landmark paper by Bergan and Hanssen [11]. This paper introduces the Individual Element Test (IET), which sets forth *a priori* conditions for an element to pass the Patch Test. A "final" form of the FF was described in a paper by Bergan and Nygård [14]. The FF stiffness matrix consists of two contributions called *basic* and *higher order* respectively. The *basic stiffness* is constructed in accordance with the IET, and thus ensures satisfaction of the Patch Test.

The *higher order stiffness* is constructed in order to obtain correct rank and to improve performance of the element. Bergan and Felippa [15] argued that the higher order stiffness can be scaled with a positive number without violating the IET. This Scaled FF was incorporated in the framework of variational calculus by Felippa and Militello [25,26,44] who showed that the Scaled FF was derivable from a parametrized hybrid variational principle.

The Assumed Natural Strain (ANS) formulation was developed in the early 1980 by several investigators [7,36,41,58]. The name was coined by Park and Stanley while developing a nine node shell element [49]. The basic ANS technique was adopted to the basic plus higher order decomposition by Militello and Felippa, who called this variant the Assumed Natural Deviatoric Strains (ANDES) formulation [45, 44]. This formulation allowed increased flexibility compared to the FF in that the higher order strains where no longer restricted to be consistent with higher order displacement modes.

Often the two formulations: FF and ANDES, give identical elements, as in the case of the "optimal" three node membrane element with drilling degrees of freedom based on the Extended FF and the ANDES formulations [1,27]. When coalescence occurs the ANDES formulation is usually more computationally efficient since it shortcuts the complicated transformation from generalized modes to visible degrees of freedom, a task that often has to be carried out numerically for the FF elements.

1.2 Dissertation outline.

Chapter 2 of the present work starts out with a description of the finite-displacement motion of a co-rotated medium. This description is discretized to a subdomain or finite element of the structural continuum, where the necessary expressions for an "element independent" tangent stiffness are developed. The present formulation is then compared to two similar formulations, namely those of Bergan et al. [17,42,47] and Rankin et al. [46,53] with respect to the key properties of equilibrium, consistency and invariance.

Chapter 3 discusses the global nonlinear equilibrium equations for geometrically nonlinear structures with emphasis on methodology to construct response tracing algorithms. A generalized arc-length type algorithm is then developed. The algorithm is shown to include such algorithms as load control, displacement control and state control as special cases. The section compares the normal-plane corrector of Riks and Wempner [54,55,65] and the orthogonal trajectory corrector developed by Fried [31] are compared. The detection of critical points such as limit points and bifurcation points is discussed, and a procedure for branch switching based on linearized buckling analysis is developed.

Chapters 4 and 5 describe three node and four node linear shell elements, respectively. These chapters also cover specific extensions necessary to include these shell elements in the co-rotated nonlinear formulation described in Chapter 2. The four node element is a new shell element based on the ANDES formulation, whereas the three node element is the ANDES shell element developed for linear analysis by Militello and Felippa [27,45]. The nonlinear extensions for the elements are compared to the formulations of Bergan et al. [47] and Rankin et al. [53].

Chapter 6, 7 and 8 present numerical results obtained with the present co-rotational formulation on a wide spectrum of shell and space-beam problems. Chapter 6 presents linear static problems and evaluates the three and four node plate, membrane and shell elements relative to existing elements. Chapter 7 presents linearized buckling problems. These problems assess the performance of the geometric stiffness of the elements without putting the finite displacement formulation to any severe tests, since these problems pertain to linearized prebuckling. Truly nonlinear problems are presented in Chapter 8. These problems embody finite displacements and rotations as well as traversal of critical points of limit and bifurcation types.

Finally, Chapter 9 summarizes the achievements of the present research work and suggests directions for further research.

Chapter 2

Co-rotational Formulation of Geometrically Nonlinear Problems.

2.1 Previous work.

As mentioned in the Introduction, the co-rotated formulation explicitly separates rigid-body and deformational components of the motion. This idea can be translated to a finite element framework by effecting the separation at the element level. Specific techniques for carrying out this separation have varied according to the taste and background of the investigators that developed these formulations. Two approaches: shadow element and projectors, are considered here.

The concept of a shadow configuration was first described by Fraeijs de Veubeke for a complete structure [30]. This paper clearly states: "We therefore try to define a set of Cartesian mean axis accompanying the body, or dynamic reference frame, with respect to which the relative displacements, velocities or accelerations of material points due to deformations are minimal in some global sense. If the body does not deform, any set of axes fixed into the body is of course a natural dynamic reference frame." The determination of such frames for a complete structure, however, is a difficult problem and not satisfactorily solved as yet if the deformations are large. The difficulties are circumvented by selecting a frame for each individual element, and assuming that the deformations with respect to this frame are small in some sense.

The concept of shadow configuration was taken to the element level by Bergan and Nygård [16,47]. In this work the shadow element was coined "ghost-reference". Such a concept is a useful visualization tool, and can help the understanding of the co-rotated formulation. The shadow element concept was used by Bergan and Nygård to separate out the rigid body motion of each element to extract its deformational motion, from which the internal force vector of the element is computed. However the derivatives of these co-rotated internal forces were not not used directly in forming the tangent stiffness, which leads to a loss of consistency.

The formulation of Rankin and Brogan [52] and the later refinements of Nour-Omid and Rankin [46] does not explicitly use the concept of a shadow element, but the way of extracting the deformational displacements is similar to that of Bergan and Nygård. These authors used the co-rotated formulation

directly to form the tangent stiffness, which thus provides a consistent stiffness with respect to the internal forces. The work relies heavily on the use of projection operators.

Other important contributions to the co-rotational formulation of geometrically nonlinear finite elements are those of Argyris [4] and Crisfield [22]. It should be mentioned that the term "co-rotational" as used by the structural mechanics community has evolved to be differentiated clearly from two related kinematic descriptions: Updated Lagrangian and convected-coordinat formulations. The latter are characterized by the moving configuration being referred to a generally curvilinear coordinate system, which requires the metric of individual elements to be updated as the motion progresses. In the co-rotational formulation such system remains Cartesian. This is the source of both computational advantages (reuse of existing elements) and disadvantages (choice of unnatural strain-displacement relations for some elements).

2.2 Organization of present chapter.

This Chapter starts with a description of motion for an element undergoing finite displacements and rotations but small deformations. The co-rotated description with shadow element is adopted to enhance visualization. This description is applied to finite elements with both translational and rotational nodal degrees of freedom. The finite element equations for the present formulation are derived, and following this, a set of requirements for judging the adequacy of a co-rotated formulation is established. These requirements are used to review and evaluate different "schools" of co-rotated formulations for geometrically nonlinear problems.

This organization has been chosen because introducing the present formulation first develops useful expressions and vocabulary. Several co-rotated formulations can then be discussed in a unified fashion, using the present notation, without the need to specialize such discussion with different terminology.

2.3 Description of motion for co-rotated formulation.

Consider an individual element as shown in Figure 2.1. Its initial configuration is denoted by C_0. This configuration is referred to a local coordinate system defined by the triad of unit orthogonal vectors $(\mathbf{i}_1^0, \mathbf{i}_2^0, \mathbf{i}_3^0)$, referred to a global system defined by $(\mathbf{I}_1, \mathbf{I}_2, \mathbf{I}_3)$. The transformation of a vector $\mathbf{x}$ referred to the global system to the same vector expressed in local system as $\tilde{\mathbf{x}}$ can be written

$$\tilde{\mathbf{x}} = \mathbf{T}_0 \mathbf{x} \quad \text{and} \quad \mathbf{x} = \mathbf{T}_0^T \tilde{\mathbf{x}} \qquad \text{where} \qquad \mathbf{T}_0 = \begin{bmatrix} \mathbf{i}_1^{0^T} \\ \mathbf{i}_2^{0^T} \\ \mathbf{i}_3^{0^T} \end{bmatrix} . \tag{2.3.1}$$

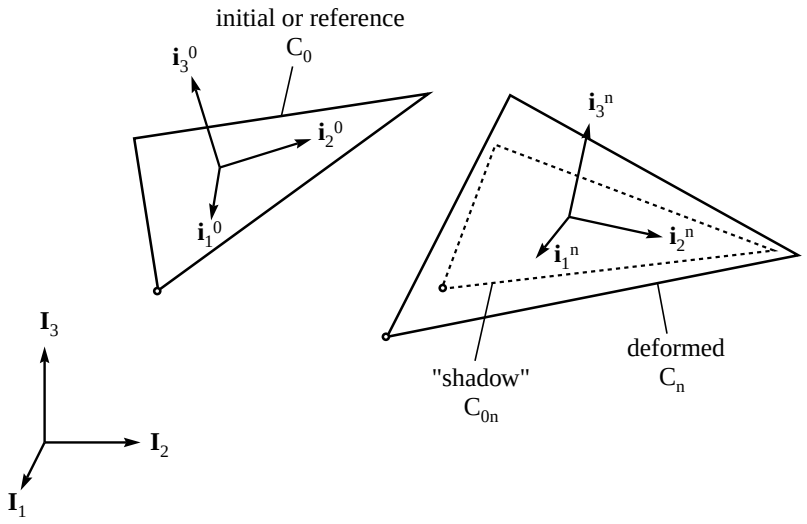

Figure 2.1. The reference, "shadow" and deformed configurations of an element.

The motion of the element under slowly applied loads carries it to a deformed configuration, denoted by C_n. Subscript n will be later identified with the nonlinear solution step in an incremental analysis, but for the present will be left generic. The rigid body motion undergone by the element brings the initial configuration C_0 to the shadow configuration C_{0n}. Both the deformed element C_n and the shadow element C_{0n} are referred to a common local coordinate system defined by the triad of orthonormal vectors $(\mathbf{i}_1^n, \mathbf{i}_2^n, \mathbf{i}_3^n)$. This local coordinate system triad is body-attached to the shadow element, and follows through its rigid body motions.

The position of the shadow element C_{0n} is obtained by a closest possible, or "best fit", of the initial element C_0 to the deformed element through a rigid body translation $\mathbf{u}_c$ and rigid body rotation $\mathbf{R}_{0n}$. If the centroids of C_n and C_{0n} coincide, the rigid body translation $\mathbf{u}_c$ is given as the translation of the centroid of the element. The use of the term "centroid" refers here to the arithmetic average of the nodal coordinates of an element. This "centroid" does not in general coincide with the mass center of an element.

The common coordinate system of the C_n and C_{0n} configurations is obtained from the rigid body rotation of the base vectors of the initial configuration :

$$\mathbf{i}_i^n = \mathbf{R}_{0n}\mathbf{i}_i^0 \qquad \Leftrightarrow \qquad \mathbf{T}_n^T = \mathbf{R}_{0n}\mathbf{T}_0^T. \tag{2.3.2}$$

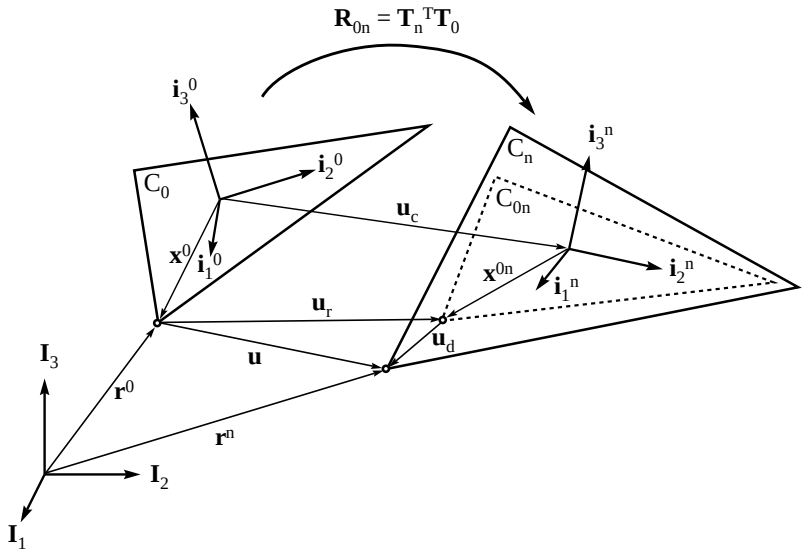

Figure 2.2. Nodal translations using a shadow element representation.

Because $\mathbf{T}_0$, $\mathbf{T}_n$ and $\mathbf{R}_{0n}$ are orthonormal matrices, $\mathbf{R}_{0n}$ can be extracted on postmultiplying (2.3.2) by $\mathbf{T}_0$:

$$\mathbf{R}_{0n} = \mathbf{T}_n^T \mathbf{T}_0 \qquad \text{and} \qquad \mathbf{R}_{0n}^T = \mathbf{T}_0^T \mathbf{T}_n. \tag{2.3.3}$$

2.3.1 Translation of an element node from C_0 to C_n.

Consider an element node that moves from the initial position $\mathbf{r}^0$ to its deformed position $\mathbf{r}^n$. The nodal displacement vector is given by

$$\mathbf{r}^n = \mathbf{r}^0 + \mathbf{u} \quad \Rightarrow \quad \mathbf{u} = \mathbf{r}^n - \mathbf{r}^0 \,. \tag{2.3.4}$$

This displacement can be split, in accordance with the co-rotational approach, into a rigid body and a deformational component:

$$\mathbf{u} = \mathbf{u}_r + \mathbf{u}_d \,. \tag{2.3.5}$$

The rigid body displacement $\mathbf{u}_r$ is given by the difference in position of the node in the initial C_0 and co-rotated C_{0n} configurations. Similarly the deformational displacement $\mathbf{u}_d$ is given by the difference between the co-rotated and deformed configurations C_{0n} and C_n :

$$\begin{aligned} \mathbf{u}_r &= \mathbf{r}^{0n} - \mathbf{r}^0, \\ \mathbf{u}_d &= \mathbf{r}^n - \mathbf{r}^{0n}, \end{aligned} \qquad \text{where} \qquad \begin{aligned} \mathbf{r}^0 &= \mathbf{r}_c^0 + \mathbf{x}^0, \\ \mathbf{r}^{0n} &= \mathbf{r}_c^0 + \mathbf{u}_c + \mathbf{R}_{0n}\mathbf{x}^0, \end{aligned} \tag{2.3.6}$$

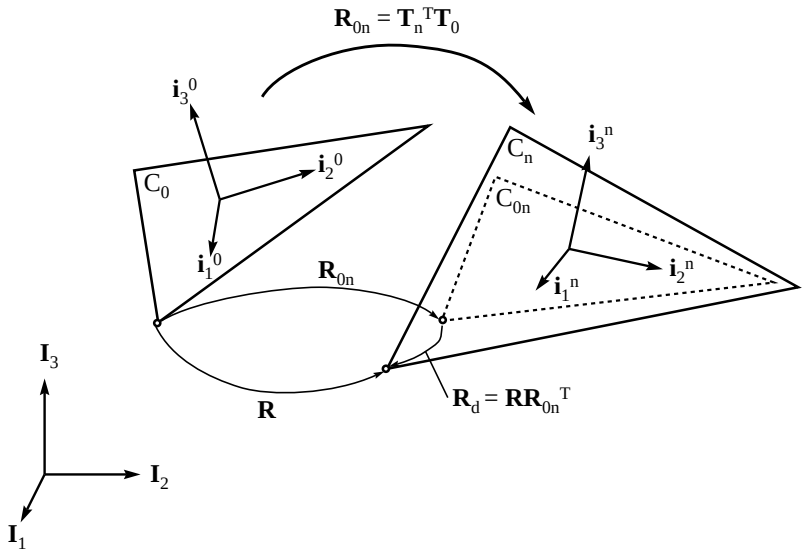

Figure 2.3. Nodal rotations using a shadow element representation.

and $\mathbf{x}^0$ contains the coordinates of the node in the initial configuration relative to the element centroid. Combining these equations gives

$$\mathbf{u}_r = \mathbf{u}_c + (\mathbf{R}_{0n} - \mathbf{I})\mathbf{x}^0. \tag{2.3.7}$$

The deformational translation can be extracted as

$$\begin{aligned} \mathbf{u}_d &= \mathbf{u} - \mathbf{u}_r = \mathbf{u} - (\mathbf{u}_c + (\mathbf{R}_{0n} - \mathbf{I})\mathbf{x}^0) \\ &= \mathbf{u} - \mathbf{u}_c - (\mathbf{R}_{0n} - \mathbf{I})\mathbf{x}^0. \end{aligned} \tag{2.3.8}$$

The deformational translation referred to the local coordinate system becomes

$$\begin{aligned} \tilde{\mathbf{u}}_d &= \mathbf{T}_n \mathbf{u}_d = \tilde{\mathbf{u}} - \tilde{\mathbf{u}}_c - \mathbf{T}_n(\mathbf{R}_{0n} - \mathbf{I})\mathbf{T}_n^T \tilde{\mathbf{x}}^0 \\ &= \tilde{\mathbf{u}} - \tilde{\mathbf{u}}_c - (\tilde{\mathbf{R}}_{0n} - \mathbf{I})\tilde{\mathbf{x}}^0, \end{aligned} \tag{2.3.9}$$

where quantities measured in the local (co-rotated) coordinate system are identified with superposed tildes. In equation (2.3.9), $\tilde{\mathbf{x}}^0$ denotes the nodal coordinate vector of the shadow element with respect to that system:

$$\tilde{\mathbf{x}}^0 = \mathbf{T}_0 \mathbf{x}^0 = \mathbf{T}_n \mathbf{x}^{0n}. \tag{2.3.10}$$

2.3.2 Rotation of an element node from C_0 to C_n.

The rotation of a node as it moves from its initial position in the C_0 configuration to its deformed position in the C_n configuration can be described by the rotation tensor $\mathbf{R}$. Proceeding as in the translational analysis, $\mathbf{R}$ is assumed to be decomposed into a rigid body rotation $\mathbf{R}_{0n}$ and a deformational rotation $\mathbf{R}_d$ as:

$$\mathbf{R} = \mathbf{R}_d \mathbf{R}_{0n} \mathbf{I} \,. \tag{2.3.11}$$

Note, however, that the opposite decomposition of the deformational rotation first followed by the rigid body rotation is not equivalent since $\mathbf{R}_d \mathbf{R}_{0n} \neq \mathbf{R}_{0n} \mathbf{R}_d$. The choice of rotation order in (2.3.11) is consistent with Bergan et al. and Rankin et al. From equation (2.3.3) and (2.3.11) the deformational rotation in the global system can be extracted as

$$\mathbf{R}_d = \mathbf{R}\mathbf{R}_{0n}^T = \mathbf{R}\mathbf{T}_0^T \mathbf{T}_n \,. \tag{2.3.12}$$

This deformational rotation can be expressed in the (co-rotated) local coordinate system of C_{0n} and C_n as

$$\tilde{\mathbf{R}}_d = \mathbf{T}_n \mathbf{R}_d \mathbf{T}_n^T = \mathbf{T}_n \mathbf{R} \mathbf{T}_0^T \,. \tag{2.3.13}$$

The deformational rotation measured by either (2.3.12) or (2.3.13) is assumed to be small but finite. Therefore, a procedure to extract a rotation pseudo-vector from a given rotation tensor is needed. This pseudo-vector can be subsequently identified with the deformational rotational degrees of freedom $\boldsymbol{\theta}_d$ carried out at each node.

2.3.3 Rodrigues representation of the rotation tensor.

The Rodrigues formula for expressing the rotation tensor from a rotation θ about an axis given by the unit vector $\mathbf{n}$ can be obtained from purely geometric considerations [4]. This representation is also consistent with an exponential mapping of rotations [4,46,57].

A rotation of a vector $\mathbf{r}_0$ through an angle θ about an axis oriented through the unit vector $\mathbf{n}^T = [\, n_1 \quad n_2 \quad n_3 \,]$ gives a new vector $\mathbf{r}$ that can be represented as

$$\mathbf{r} = \mathbf{R}\mathbf{r}_0 \qquad \text{where} \qquad \mathbf{R} = (\mathbf{I} + \mathbf{N}\sin\theta + \mathbf{N}^2(1 - \cos\theta)) \tag{2.3.14}$$

and

$$\mathbf{N} = \mathrm{Spin}(\mathbf{n}) = \begin{bmatrix} 0 & -n_3 & n_2 \\ n_3 & 0 & -n_1 \\ -n_2 & n_1 & 0 \end{bmatrix}, \tag{2.3.15}$$

$$\mathbf{N}^2 = \mathbf{n}\mathbf{n}^T - \mathbf{I} = \begin{bmatrix} n_1 n_1 - 1 & n_1 n_2 & n_1 n_3 \\ n_2 n_1 & n_2 n_2 - 1 & n_2 n_3 \\ n_3 n_1 & n_3 n_2 & n_3 n_3 - 1 \end{bmatrix} . \tag{2.3.16}$$

Substitution of (2.3.15) and (2.3.16) into (2.3.14) yields the explicit form in terms of the rotation axis and angle

$$\mathbf{R}(\mathbf{n},\theta) = \begin{bmatrix} 1 + (1-c)(n_1^2 - 1) & (1-c)n_1 n_2 - n_3 s & (1-c)n_1 n_3 + n_2 s \\ (1-c)n_2 n_1 + n_3 s & 1 + (1-c)(n_2^2 - 1) & (1-c)n_2 n_3 - n_1 s \\ (1-c)n_3 n_1 - n_2 s & (1-c)n_3 n_2 + n_1 s & 1 + (1-c)(n_3^2 - 1) \end{bmatrix} , \tag{2.3.17}$$

where $c = \cos\theta$ and $s = \sin\theta$. If $\mathbf{R}(\mathbf{n},\theta)$ is given, the rotation axis $\mathbf{n}$ and rotation angle θ can be extracted as

$$\begin{aligned} d_1 &= n_1 \sin\theta = \frac{1}{2}(R_{32} - R_{23}) , \\ d_2 &= n_2 \sin\theta = \frac{1}{2}(R_{13} - R_{31}) , \\ d_3 &= n_3 \sin\theta = \frac{1}{2}(R_{21} - R_{12}) . \end{aligned} \tag{2.3.18}$$

Since $(n_1^2 + n_2^2 + n_3^2) = 1$, we have

$$\sin\theta = \sqrt{d_1^2 + d_2^2 + d_3^2} \qquad \text{and} \qquad \begin{Bmatrix} n_1 \\ n_2 \\ n_3 \end{Bmatrix} = \frac{1}{\sin\theta} \begin{Bmatrix} d_1 \\ d_2 \\ d_3 \end{Bmatrix} . \tag{2.3.19}$$

The rotation vector $\boldsymbol{\theta}$ associated with the rotation tensor is then given as

$$\boldsymbol{\theta} = \theta\mathbf{n} = \frac{\theta}{\sin\theta} \begin{Bmatrix} d_1 \\ d_2 \\ d_3 \end{Bmatrix} . \tag{2.3.20}$$

Observe that as $\theta \to 0$, $\boldsymbol{\theta} \to \mathbf{d}$. Some care should be exercized if θ is very small because $\theta/\sin\theta$ approches $0/0$. In order to avoid numerical difficulities the fraction $\theta/\sin\theta$ should be set to 1 for small angles, e.g. $\theta < 1.0^{-8}$, or a truncated Taylor series for, say $\theta < 1.0^{-2}$, can be used.

The present expressions for obtaining the rotation tensor $\mathbf{R}$ as a function of the pseudo-vector $\boldsymbol{\theta}$ in equations (2.3.14) and (2.3.17) can be formally expressed the using exponential mapping of rotations as

$$\mathbf{R}(\boldsymbol{\theta}) = e^{\mathrm{Spin}(\boldsymbol{\theta})} . \tag{2.3.21}$$

The inverse relationship for obtaining the pseudo-vector $\boldsymbol{\theta}$ from the rotations tensor $\mathbf{R}$, as described by equation (2.3.18), (2.3.19) and (2.3.20), can be compactly expressed as

$$\boldsymbol{\theta} = \mathrm{Axial}(\mathrm{Spin}(\boldsymbol{\theta})) = \mathrm{Axial}(\ln(e^{\mathrm{Spin}(\boldsymbol{\theta})})) = \mathrm{Axial}(\ln(\mathbf{R})) . \tag{2.3.22}$$

2.3.4 The deformational displacement vector.

An element with N nodes has initial coordinates $\mathbf{x}_a^0$, where a is used as nodal index. The finite displacement state of the element is described by the nodal translational displacement $\mathbf{u}_a$ and the rotational orientation $\mathbf{R}_a$ of the nodes. The set $(\mathbf{u}_a, \mathbf{R}_a)$ for $a = 1, \ldots N$ collectively defines the visible nodal displacement vector $\hat{\mathbf{v}}$; where the qualifier "visible" means that those quantities are "seen" by nodes of adjacent elements. Note, however, that $\hat{\mathbf{v}}$ may not constitute a vector in the conventional sense because the components of the nodal finite-rotation tensors $\mathbf{R}_a$ do not transform as vectors. The interpretation of $\hat{\mathbf{v}}$ as an array of numbers that defines the position of the deformed element is more appropriate. The displacement vector notation used in the present work is summarized in Box 2.1.

The goal is to establish the deformational nodal displacement vector $\mathbf{v}_d$ for the element based on the finite displacement state of the nodes given by $\hat{\mathbf{v}}$. This vector $\mathbf{v}_d$ contains translational and rotational degrees of freedom for each node ordered as

$$\mathbf{v}_d = \left\{ \begin{array}{c} \mathbf{u}_{d1} \\ \boldsymbol{\theta}_{d1} \\ \vdots \\ \mathbf{u}_{dN} \\ \boldsymbol{\theta}_{dN} \end{array} \right\}. \tag{2.3.23}$$

The sequence of operations required to obtain $\mathbf{v}_d$, given $\mathbf{x}_a^0$, $\mathbf{u}_a$ and $\mathbf{R}_a$, is compiled in Box 2.2.

This procedure of forming the deformational displacement vector $\mathbf{v}_d$ should be seen in context with the updating procedure for the global displacement state $\hat{\mathbf{v}}$ described in Box 3.1, of Chapter 3.

Box 2.1. Displacement vector notation.

$\hat{\mathbf{v}}$: Represents the total displacement state at both element and global level. The nodal translations are represented as the vector $\mathbf{u}_a$, and the nodal rotations by the rotation tensor $\mathbf{R}_a$. The set $(\mathbf{u}_a, \mathbf{R}_a)$ for each node represents the "array" $\hat{\mathbf{v}}$ that defines the position of the structure or element. All quantities are referred to an inertial coordinate system.

$\mathbf{v}_d$: Deformational displacement vector for an element. The vector exists only at the element level. The translations and rotations are finite quantities, but in general much smaller than the global displacements in $\hat{\mathbf{v}}$. The translations are represented by the vector $\mathbf{u}_{da}$, and the rotations by the rotational pseudovector $\boldsymbol{\theta}_{da}$. For an element this is collected in the vector

$$\mathbf{v}_d^T = [\, \mathbf{u}_{d1}^T \quad \boldsymbol{\theta}_{d1}^T \quad \cdots \quad \mathbf{u}_{dN}^T \quad \boldsymbol{\theta}_{dN}^T \,]$$

measured in the co-rotated coordinate system of the element or the inertial system.

$\mathbf{v}$, $\delta\mathbf{v}$: The visible degrees of freedom for an incremental/iterative solution algorithm. The translations are incremental displacement vectors $\delta\mathbf{u}_a$ and the rotational increment is represented by the instantaneous rotation axis $\delta\boldsymbol{\omega}_a$. A displacement increment is represented by the vector:

$$\delta\mathbf{v}^T = [\, \delta\mathbf{u}_1^T \quad \delta\boldsymbol{\omega}_1^T \quad \cdots \quad \delta\mathbf{u}_N^T \quad \delta\boldsymbol{\omega}_N^T \,]$$

referred to an inertial coordinate system.

Box 2.2. Forming the deformational displacement vector.

Establish the initial local coordinate system $\mathbf{T}_0$ from the initial nodal coordinates $\mathbf{x}_a^0$ and form the nodal coordinates in the local system:

$$\tilde{\mathbf{x}}_a^0 = \mathbf{T}_0(\mathbf{x}_a^0 - \mathbf{x}_c^0), \quad \text{where} \quad \mathbf{x}_c^0 = \frac{1}{N}\sum_{a=1}^{N} \mathbf{x}_a^0. \tag{2.3.24}$$

Establish the deformed local coordinate system $\mathbf{T}_n$ from the deformed coordinates $\mathbf{x}_a^n = \mathbf{x}_a^0 + \mathbf{u}_a$ and form the nodal coordinates in the local system:

$$\tilde{\mathbf{x}}_a^n = \mathbf{T}_n(\mathbf{x}_a^n - \mathbf{x}_c^n), \quad \text{where} \quad \mathbf{x}_c^n = \frac{1}{N}\sum_{a=1}^{N} \mathbf{x}_a^n. \tag{2.3.25}$$

for each node $a = 1, \ldots N$ do

Compute the deformational translations

$\tilde{\mathbf{u}}_{da} = \tilde{\mathbf{x}}_a^n - \tilde{\mathbf{x}}_a^0$

Compute the deformational rotations

$\tilde{\boldsymbol{\theta}}_{da} = \text{Axial}(\ln(\tilde{\mathbf{R}}_d))$ where $\tilde{\mathbf{R}}_d = \mathbf{T}_n \mathbf{R}_a \mathbf{T}_0^T$ (2.3.26)

end do

Collect in the element deformational displacement vector

$$\tilde{\mathbf{v}}_d^T = \left[\tilde{\mathbf{u}}_{d1}^T \quad \tilde{\boldsymbol{\theta}}_{d1}^T \quad \cdots \quad \tilde{\mathbf{u}}_{dN}^T \quad \tilde{\boldsymbol{\theta}}_{dN}^T \right]. \tag{2.3.27}$$

2.4 Variation of the deformational displacements.

The variation of the element deformational displacement vector $\mathbf{v}_d$ with respect to the element visible degrees of freedom $\mathbf{v}$ can be expressed as the matrix relationship

$$\delta \mathbf{v}_d^R = \frac{\partial \mathbf{v}_d^R}{\partial \mathbf{v}} \delta \mathbf{v} \ , \tag{2.4.1}$$

where δ denotes an admissible variation in the sense of variational calculus. It is important to notice that the relationship sought is the variation of the corotated displacements $\mathbf{v}_d^R$ with respect to the inertial visible degrees of freedoms $\mathbf{v}$. Vector $\mathbf{v}_d$ and $\mathbf{v}$ are summarized in Box 2.1. Superscript $(\ ^R\ )$ is used to stress that a quantity is measured in a rotating frame. To establish the relationship in equation (2.4.1) one needs to obtain the variations of the co-rotated coordinate system of the shadow element represented by $\mathbf{T}_n$, and the rigid body rotation of the shadow element represented by the rotation matrix $\mathbf{R}_{0n}$. These matrices are related as shown in equation (2.3.3).

2.4.1 Variation of the transformation matrix $\mathbf{T}_n$.

The variation of $\mathbf{T}_n$ is entirely defined by its variation with respect to the instantaneous rotation axis $\tilde{\boldsymbol{\omega}}$, where $\tilde{\boldsymbol{\omega}}$ is measured in the local inertial coordinate system:

$$\begin{aligned}
\delta \mathbf{T}_n &= \frac{\partial \mathbf{T}_n}{\partial \tilde{\omega}_i} \delta \tilde{\omega}_i \\
&= \begin{bmatrix} \mathbf{0}^T \\ \mathbf{i}_3^{nT} \\ -\mathbf{i}_2^{nT} \end{bmatrix} \delta \tilde{\omega}_x + \begin{bmatrix} -\mathbf{i}_3^{nT} \\ \mathbf{0}^T \\ \mathbf{i}_1^{nT} \end{bmatrix} \delta \tilde{\omega}_y + \begin{bmatrix} \mathbf{i}_2^{nT} \\ -\mathbf{i}_1^{nT} \\ \mathbf{0}^T \end{bmatrix} \delta \tilde{\omega}_z \\
&= \begin{bmatrix} 0 & \delta\tilde{\omega}_z & -\delta\tilde{\omega}_y \\ -\delta\tilde{\omega}_z & 0 & \delta\tilde{\omega}_x \\ \delta\tilde{\omega}_y & -\delta\tilde{\omega}_x & 0 \end{bmatrix} \begin{bmatrix} \mathbf{i}_1^{nT} \\ \mathbf{i}_2^{nT} \\ \mathbf{i}_3^{nT} \end{bmatrix} = -\mathrm{Spin}(\delta\tilde{\boldsymbol{\omega}}) \mathbf{T}_n \ .
\end{aligned} \tag{2.4.2}$$

Because $\mathrm{Spin}(\tilde{\boldsymbol{\omega}}) = \mathbf{T}_n \mathrm{Spin}(\boldsymbol{\omega}) \mathbf{T}_n^T$ and $\mathbf{T}_n$ is orthogonal it follows that

$$\delta \mathbf{T}_n = -\mathrm{Spin}(\delta\tilde{\boldsymbol{\omega}}) \mathbf{T}_n = -\mathbf{T}_n \mathrm{Spin}(\delta\boldsymbol{\omega}) \ . \tag{2.4.3}$$

Furthermore, since $\mathrm{Spin}(\delta\boldsymbol{\omega})$ is anti-symmetric,

$$\delta \mathbf{T}_n^T = \mathbf{T}_n^T \mathrm{Spin}(\delta\tilde{\boldsymbol{\omega}}) = \mathrm{Spin}(\delta\boldsymbol{\omega}) \mathbf{T}_n^T \ . \tag{2.4.4}$$

2.4.2 Variation of the rotation matrix $\mathbf{R}_{0n}$.

Equation (2.4.3) can be used to find the variation of the rigid body rotation tensor $\mathbf{R}_{0n} = \mathbf{T}_n^T \mathbf{T}_0$:

$$\begin{aligned} \delta\mathbf{R}_{0n} &= \delta\mathbf{T}_n^T\mathbf{T}_0 + \mathbf{T}_n^T\delta\mathbf{T}_0 = \delta\mathbf{T}_n^T\mathbf{T}_0 = \mathrm{Spin}(\delta\boldsymbol{\omega})\mathbf{T}_n^T\mathbf{T}_0 \\ &= \mathrm{Spin}(\delta\boldsymbol{\omega})\mathbf{R}_{0n} \,. \end{aligned} \tag{2.4.5}$$

Referring this variation to the local coordinate system gives

$$\delta\tilde{\mathbf{R}}_{0n} = \mathbf{T}_n\delta\mathbf{R}_{0n}\mathbf{T}_n^T = \mathrm{Spin}(\delta\tilde{\boldsymbol{\omega}})\tilde{\mathbf{R}}_{0n} \,. \tag{2.4.6}$$

If the variation is taken about $\tilde{\boldsymbol{\theta}} = \mathbf{0}$ one has $\mathbf{R}_{0n} = \mathbf{I}$, and thus

$$\delta\tilde{\mathbf{R}}_{0n}\Big|_{\tilde{\theta}\to\mathbf{0}} = \mathrm{Spin}(\delta\tilde{\boldsymbol{\omega}}) \,. \tag{2.4.7}$$

2.4.3 Variation of inertial $\mathbf{u}_d$ with respect to inertial $\mathbf{v}$.

The centroid displacement $\mathbf{u}_c$ of a N node element can be defined as the average of the nodal displacements:

$$\mathbf{u}_c = \frac{1}{N}\sum_{a=1}^{N}\mathbf{u}_a \,. \tag{2.4.8}$$

Specializing equation (2.3.8) to node a gives the following expression for its deformational translation:

$$\mathbf{u}_{da} = \sum_{b=1}^{N}\mathbf{P}_{ab}\mathbf{u}_b - (\mathbf{R}_{0n} - \mathbf{I})\,\mathbf{x}_a^0 \quad \text{where} \quad \mathbf{P}_{ab} = (\delta_{ab} - \frac{1}{N})\,\mathbf{I}. \tag{2.4.9}$$

Its variation is

$$\delta\mathbf{u}_{da} = \sum_{b=1}^{N}\mathbf{P}_{ab}\delta\mathbf{u}_b - \delta\mathbf{R}_{0n}\mathbf{x}_a^0 \,, \tag{2.4.10}$$

since $\delta\mathbf{P}_{ab} = \mathbf{0}$, $\delta\mathbf{I} = \mathbf{0}$ and $\delta\mathbf{x}_a^0 = \mathbf{0}$. Substituting (2.4.5) for $\delta\mathbf{R}_{0n}$ gives

$$\begin{aligned} \delta\mathbf{R}_{0n}\mathbf{x}_a^0 &= \mathrm{Spin}(\delta\boldsymbol{\omega})\mathbf{R}_{0n}\mathbf{x}_a^0 = \mathrm{Spin}(\delta\boldsymbol{\omega})\mathbf{x}_a^{0n} = -\mathrm{Spin}(\mathbf{x}_a^{0n})\delta\boldsymbol{\omega} \\ &= -\mathrm{Spin}(\mathbf{x}_a^{0n})\mathbf{G}\,\delta\mathbf{v} \,, \end{aligned} \tag{2.4.11}$$

where matrix $\mathbf{G}$ connects the variation of the rigid body rotation to the variation of the visible node displacements:

$$\delta\boldsymbol{\omega} = \mathbf{G}\delta\mathbf{v} = \sum_{a=1}^{N}\mathbf{G}_a\,\delta\mathbf{v}_a \,. \tag{2.4.12}$$

$\mathbf{G}$ is an element dependent matrix that can be split in its nodal submatrices $\mathbf{G}_a$ as indicated above. The matrix $\mathbf{G}$ for three and four node shell elements is described in Sections 4.5 and 5.5 respectively.

Introducing (2.4.11) into (2.4.10) provides the variation of the nodal deformational displacements:

$$\delta\mathbf{u}_{da} = \sum_{b=1}^{N}([\,\mathbf{P}_{ab} \quad \mathbf{0}\,] + \mathrm{Spin}(\mathbf{x}_a^{0n})\mathbf{G}_b)\,\delta\mathbf{u}_b\ . \tag{2.4.13}$$

When transforming to local coordinate system one should keep in mind the relationship

$$\tilde{\mathbf{x}}_a^0 = \mathbf{T}_0\mathbf{x}_a^0 = \mathbf{T}_n\mathbf{x}_a^{0n}\ , \tag{2.4.14}$$

which simply states that the coordinates of the shadow element in local coordinate system are constant. Consequently, transformation of (2.4.13) to the local coordinate system gives

$$\delta\tilde{\mathbf{u}}_{da} = \sum_{b=1}^{N}([\,\tilde{\mathbf{P}}_{ab} \quad \mathbf{0}\,] + \mathrm{Spin}(\tilde{\mathbf{x}}_a^0)\tilde{\mathbf{G}}_b)\,\delta\tilde{\mathbf{v}}_b\ , \tag{2.4.15}$$

in which $\tilde{\mathbf{v}}_b$ contains both the translational and rotational inertial degrees of freedom of a node b as $\delta\tilde{\mathbf{v}}_b^T = [\,\delta\tilde{\mathbf{u}}_b^T \quad \delta\tilde{\boldsymbol{\omega}}_b^T\,]$.

2.4.4 Variation of co-rotated $\mathbf{u}_d$ with respect to inertial $\mathbf{v}$.

The variation of an arbitrary vector in an inertial frame can be expressed as

$$\delta\mathbf{x} = \delta\mathbf{x}^R + \delta\boldsymbol{\omega}\times\mathbf{x}\ , \tag{2.4.16}$$

where $\delta\mathbf{x}^R$ is the variation of the vector in the co-rotating frame and $\delta\boldsymbol{\omega}$ is the inertial rotation of that frame. This expression can be used to obtain the variation of the deformation vector $\mathbf{u}_d$ in the rotating frame $\delta\mathbf{u}_d^R$ in terms of its variation in the inertial frame $\delta\mathbf{u}_d$. Recall the relationship

$$\mathbf{x}_a^n = \mathbf{x}_a^{0n} + \mathbf{u}_{da}\ , \tag{2.4.17}$$

between the nodal coordinates of the shadow element $\mathbf{x}_a^{0n}$ and the coordinates of the deformed element $\mathbf{x}_a^n$. Taking the variation of $\mathbf{x}_a^n$ in the inertial frame gives

$$\begin{aligned}\delta\mathbf{x}_a^n &= \delta\mathbf{x}_a^{0n} + \delta\mathbf{u}_{da} = \delta\mathbf{u}_{da} + \mathrm{Spin}(\delta\boldsymbol{\omega})\mathbf{x}_a^{0n} = \delta\mathbf{u}_{da} - \mathrm{Spin}(\mathbf{x}_a^{0n})\delta\boldsymbol{\omega}\\ &= \sum_{b=1}^{N}\mathbf{P}_{ab}\delta\mathbf{u}_b,\end{aligned} \tag{2.4.18}$$

where (2.4.13) has been used in the last transformation. Taking the variation of $\mathbf{x}_a^n$ in the co-rotating frame gives

$$\delta\mathbf{x}_a^{Rn} = \delta\mathbf{x}_a^{R0n} + \delta\mathbf{u}_{d\,a}^R = \delta\mathbf{u}_{d\,a}^R \ , \tag{2.4.19}$$

because the coordinates of the shadow element $\mathbf{x}_a^{0n}$ are constant in the co-rotating frame. Substituting (2.4.18) and (2.4.19) into (2.4.16) and solving with respect to $\delta\mathbf{u}_{d\,a}^R$ gives

$$\begin{aligned}\delta\mathbf{u}_{d\,a}^R &= \sum_{b=1}^N \mathbf{P}_{ab}\delta\mathbf{u}_b - \delta\boldsymbol{\omega}\times\mathbf{x}_a^n = \sum_{b=1}^N \mathbf{P}_{ab}\delta\mathbf{u}_b - \mathrm{Spin}(\delta\boldsymbol{\omega})\mathbf{x}_a^n \\ &= \sum_{b=1}^N \mathbf{P}_{ab}\delta\mathbf{u}_b + \mathrm{Spin}(\mathbf{x}_a^n)\,\delta\boldsymbol{\omega} = \sum_{b=1}^N([\,\mathbf{P}_{ab}\quad\mathbf{0}\,] + \mathrm{Spin}(\mathbf{x}_a^n)\mathbf{G}_b)\,\delta\mathbf{v}_b \ .\end{aligned} \tag{2.4.20}$$

Transforming this expression to the local coordinate system:

$$\delta\tilde{\mathbf{u}}_{d\,a}^R = \sum_{b=1}^N([\,\tilde{\mathbf{P}}_{ab}\quad\mathbf{0}\,] + \mathrm{Spin}(\tilde{\mathbf{x}}_a^n)\tilde{\mathbf{G}}_b)\,\delta\tilde{\mathbf{v}}_b \ , \tag{2.4.21}$$

which gives the variation of the co-rotated $\tilde{\mathbf{u}}_d$ with respect to the inertial visible degrees of freedom $\tilde{\mathbf{v}}$.

Note that the only difference between the variations $\delta\tilde{\mathbf{u}}_{da}$ in the inertial coordinate system and the rotating coordinate system is that equation (2.4.15) contains the shadow element coordinates in $\mathrm{Spin}(\tilde{\mathbf{x}}_a^0)$, whereas equation (2.4.21) contains the deformed element coordinates in $\mathrm{Spin}(\tilde{\mathbf{x}}_a^n)$.

2.4.5 Variation of co-rotated $\boldsymbol{\theta}_d$ with respect to co-rotated $\boldsymbol{\omega}_d$.

Equation (2.3.26) gives the deformational pseudovector $\boldsymbol{\theta}_{da}$ at a node a in the compact form

$$\boldsymbol{\theta}_{da} = \mathrm{Axial}(\ln(\mathbf{R}_{da}). \tag{2.4.22}$$

The variation of $\boldsymbol{\theta}_{da}$ with respect to the inertial visible degrees of freedom requires its variation with respect to the instantaneous deformational rotation $\boldsymbol{\omega}_{da}$:

$$\delta\boldsymbol{\theta}_{da} = \frac{\partial\boldsymbol{\theta}_{da}}{\partial\boldsymbol{\omega}_{da}}\delta\boldsymbol{\omega}_{da} = \mathbf{H}_a\delta\boldsymbol{\omega}_{da} \ . \tag{2.4.23}$$

This relationship is given by Nour-Omid and Rankin [46] based on the inverse relationship of equation (2.4.23) as established by Simo [57] and Szwabowicz [62]. Equation (A.14) of Ref. [46] gives

$$\mathbf{H} = \frac{\partial \boldsymbol{\theta}}{\partial \boldsymbol{\omega}} = \mathbf{I} - \tfrac{1}{2}\mathrm{Spin}(\boldsymbol{\theta}) + \eta\,\mathrm{Spin}(\boldsymbol{\theta})^2 \ , \tag{2.4.24}$$

where

$$\eta = \frac{\sin(\frac{1}{2}\theta) - \frac{1}{2}\theta\cos(\frac{1}{2}\theta)}{\theta^2 \sin(\frac{1}{2}\theta)} \quad \text{and} \quad \theta = \sqrt{\boldsymbol{\theta}^T\boldsymbol{\theta}} = \|\boldsymbol{\theta}\| \ . \tag{2.4.25}$$

Observe that for $\theta \to 0,\ \eta \to 0/0$, which amplifies computational errors for small rotation angles. To circumvent this difficulty, η is computed from a truncated power series for small values of θ :

$$\eta \approx \tfrac{1}{12} + \tfrac{1}{720}\theta^2 + \tfrac{1}{30240}\theta^4 \quad \text{for} \quad \theta < 0.05\,\text{radians} \ . \tag{2.4.26}$$

This series establishes that $\eta\big|_{\theta\to 0} = \frac{1}{12}$.

2.4.6 Variation of co-rotated $\boldsymbol{\theta}_d$ with respect to inertial v.

The instantaneous deformational rotation $\boldsymbol{\omega}_{da}$ of a node a is the difference between the instantaneous nodal rotation and the rigid body rotation of the element:

$$\boldsymbol{\omega}_{da} = \boldsymbol{\omega}_a - \boldsymbol{\omega}_r \ . \tag{2.4.27}$$

Varying this vector gives

$$\begin{aligned} \delta\boldsymbol{\omega}_{da} &= \delta\boldsymbol{\omega}_a - \delta\boldsymbol{\omega}_r = \delta\boldsymbol{\omega}_a - \frac{\partial \boldsymbol{\omega}_r}{\partial v_i}\delta v_i \\ &= \delta\boldsymbol{\omega}_a - \mathbf{G}\ \delta\mathbf{v} \ . \end{aligned} \tag{2.4.28}$$

Hence

$$\delta\boldsymbol{\omega}_r = \frac{\partial \boldsymbol{\omega}_r}{\partial v_i}\delta v_i = \mathbf{G}\,\delta\mathbf{v} \tag{2.4.29}$$

which gives the variation of the instantaneous deformational rotation as

$$\delta\boldsymbol{\omega}_{da} = \sum_{b=1}^{N} (\delta_{ab}\,[\,\mathbf{0} \quad \mathbf{I}\,] - \mathbf{G}_b)\,\delta\mathbf{v}_b \ , \tag{2.4.30}$$

where $\delta\mathbf{v}_b$ contains both the translational and rotational degrees of freedom of a node b as $\delta\mathbf{v}_b^T = [\,\delta\mathbf{u}_b^T \quad \delta\boldsymbol{\omega}_b^T\,]$. Finally, combining equation (2.4.23) and (2.4.30) gives the varaition of the co-rotated deformational nodal rotation pseudo-vector $\boldsymbol{\theta}_{da}$ with respect to the visible degrees of freedom $\mathbf{v}$ as

$$\delta\boldsymbol{\theta}_{da} = \frac{\partial \boldsymbol{\theta}_{da}}{\partial \boldsymbol{\omega}_{da}} \sum_{b=1}^{N} \frac{\partial \boldsymbol{\omega}_{da}}{\partial \boldsymbol{\omega}_b}\,\delta\boldsymbol{\omega}_b = \mathbf{H}_a \sum_{b=1}^{N} (\delta_{ab}\,[\,\mathbf{0} \quad \mathbf{I}\,] - \mathbf{G}_b)\,\delta\mathbf{v}_b \ . \tag{2.4.31}$$

2.4.7 Variation of co-rotated $\mathbf{v}_d$ with respect to inertial v.

Collecting the translational and rotational variations in equations (2.4.21) and (2.4.31), the variation of the co-rotated deformational degrees of freedom $\mathbf{v}_d$ with respect to the visible inertial degrees of freedom $\mathbf{v}$ (both vectors defined in Box 2.1) can be compactly expressed as

$$\delta \mathbf{v}_d^R = \mathbf{H}\mathbf{P}\delta\mathbf{v} \ , \tag{2.4.32}$$

in which

$$\mathbf{H} = \begin{bmatrix} \mathbf{H}_{11} & \cdots & \mathbf{0} \\ \vdots & \ddots & \vdots \\ \mathbf{0} & \cdots & \mathbf{H}_{NN} \end{bmatrix} \quad \text{with} \quad \mathbf{H}_{aa} = \begin{bmatrix} \mathbf{I} & \mathbf{0} \\ \mathbf{0} & \mathbf{H}_a \end{bmatrix}, \tag{2.4.33}$$

where $\mathbf{H}_a$ is defined in Section 2.4.5, and $\mathbf{P}$ is a nonlinear projection operator (often called "projector" for brevity) expressible as

$$\mathbf{P} = (\mathbf{I} - \mathbf{P}_T - \mathbf{P}_R) \ . \tag{2.4.34}$$

In this expression $\mathbf{P}_T$ accounts for the centroid translation of the element:

$$\mathbf{P}_T = \begin{bmatrix} \mathbf{P}_{T11} & \cdots & \mathbf{P}_{T1N} \\ \vdots & \ddots & \vdots \\ \mathbf{P}_{TN1} & \cdots & \mathbf{P}_{TNN} \end{bmatrix} \quad \text{with} \quad \mathbf{P}_{Tab} = \begin{bmatrix} \frac{1}{N}\mathbf{I} & \mathbf{0} \\ \mathbf{0} & \mathbf{0} \end{bmatrix}, \tag{2.4.35}$$

whereas $\mathbf{P}_R$ accounts for the nodal displacement components from the rigid body rotation about the element centroid:

$$\mathbf{P}_R = \mathbf{S}\mathbf{G} = \begin{bmatrix} -\text{Spin}(\mathbf{x}_1^n) \\ \mathbf{I} \\ \vdots \\ -\text{Spin}(\mathbf{x}_N^n) \\ \mathbf{I} \end{bmatrix} \mathbf{G} \ . \tag{2.4.36}$$

Here $\mathbf{S}$ is a matrix defined by the bracketed expression. $\mathbf{G}$ is defined in general terms in equation (2.4.12) and for three and four node shell elements in Sections 4.5 and 5.5 respectively.

2.4.8 Properties of the projector matrix.

If the matrix $\mathbf{P}$ defined in equation (2.4.34) is to behave as a true projector it must verify that $\mathbf{P}^2 = \mathbf{P}$. The physical meaning of this property is that a second projection does not alter an already projected vector. Expansion of equation (2.4.34) gives

$$\begin{aligned}\mathbf{PP} &= (\mathbf{I}-\mathbf{P}_T-\mathbf{P}_R)(\mathbf{I}-\mathbf{P}_T-\mathbf{P}_R)\\ &= \mathbf{I}-2\mathbf{P}_T-2\mathbf{P}_R+\mathbf{P}_T\mathbf{P}_T+\mathbf{P}_T\mathbf{P}_R+\mathbf{P}_R\mathbf{P}_T+\mathbf{P}_R\mathbf{P}_R \qquad (2.4.37)\\ &= \mathbf{I}-\mathbf{P}_T-\mathbf{P}_R=\mathbf{P}\ .\end{aligned}$$

In order to prove this result the following identities must be verified:

$$\mathbf{P}_T\mathbf{P}_T=\mathbf{P}_T\ ,\quad \mathbf{P}_R\mathbf{P}_R=\mathbf{P}_R\ ,\quad \mathbf{P}_T\mathbf{P}_R=\mathbf{0}\ ,\quad \mathbf{P}_R\mathbf{P}_T=\mathbf{0}\ . \qquad (2.4.38)$$

Proof that $\mathbf{P}_T\mathbf{P}_T=\mathbf{P}_T$. By considering a generic ab submatrix of $\mathbf{P}_T\mathbf{P}_T$ it is verified that

$$(\mathbf{P}_T\mathbf{P}_T)_{ab}=\sum_{c=1}^{N}\mathbf{P}_{Tac}\mathbf{P}_{Tcb}=\sum_{c=1}^{N}\begin{bmatrix}\frac{1}{N^2}\mathbf{I} & \mathbf{0}\\ \mathbf{0} & \mathbf{0}\end{bmatrix}=\begin{bmatrix}\frac{1}{N}\mathbf{I} & \mathbf{0}\\ \mathbf{0} & \mathbf{0}\end{bmatrix}=\mathbf{P}_{Tab}\ , \qquad (2.4.39)$$

where a, b and c are node indecies.

Proof that $\mathbf{P}_R\mathbf{P}_R=\mathbf{P}_R$.

$$\mathbf{P}_R\mathbf{P}_R=\mathbf{SGSG}=\mathbf{SIG}=\mathbf{SG}=\mathbf{P}_R \qquad (2.4.40)$$

The identity

$$\mathbf{GS}=\mathbf{I}\ , \qquad (2.4.41)$$

used in (2.4.40) holds because the columns of $\mathbf{S}$ are simply displacement vectors associated with the rigid body rotations $\theta_x=1$, $\theta_y=1$ and $\theta_z=1$, respectively. Each of these displacement vectors give the appropriate rigid body rotation vector when multiplied with $\mathbf{G}$.

Proof that $\mathbf{P}_T\mathbf{P}_R=\mathbf{0}$.

$$\mathbf{P}_T\mathbf{P}_R=\mathbf{P}_T\mathbf{SG}=\begin{bmatrix}-\mathrm{Spin}(\bar{\mathbf{x}}^n)\\ \mathbf{0}\\ \vdots\\ -\mathrm{Spin}(\bar{\mathbf{x}}^n)\\ \mathbf{0}\end{bmatrix}\mathbf{G}=\mathbf{0}\ , \qquad (2.4.42)$$

since

$$\text{Spin}(\bar{\mathbf{x}}^n) = \mathbf{0} \qquad \text{when} \qquad \bar{\mathbf{x}}^n = \frac{1}{N}\sum_{a=0}^{N} \mathbf{x}_a^n = \mathbf{0}\ . \tag{2.4.43}$$

A zero nodal coordinate mean $\bar{\mathbf{x}}^n$ emerges as a necessary condition for $\mathbf{P}_T\mathbf{P}_R = \mathbf{0}$. Therefore, the element coordinates $\mathbf{x}_a^n$ must be referred to the element centroid.

Proof that $\mathbf{P}_R\mathbf{P}_T = \mathbf{0}$.

$$\mathbf{P}_R\mathbf{P}_T = \mathbf{S}\mathbf{G}\mathbf{P}_T = \mathbf{S}\,[\,\bar{\mathbf{G}}_t \quad \mathbf{0} \quad \cdots \quad \bar{\mathbf{G}}_t \quad \mathbf{0}\,] = \mathbf{0}\ , \tag{2.4.44}$$

since

$$\bar{\mathbf{G}}_t = \frac{1}{N}\sum_{a=0}^{N} \mathbf{G}_{ta} = \mathbf{0}\ . \tag{2.4.45}$$

$\mathbf{G}\mathbf{P}_T$ must be zero because each column of $\mathbf{P}_T$ represents a displacement vector associated with a rigid translation, which will not generate a rigid body rotation when premultiplied by $\mathbf{G}$.

2.5 Higher order variations.

The development of the internal force and tangent stiffness in Sections 2.7 and 2.8 requires the variation of the nonlinear projector $\mathbf{P}^T$ contracted with a force vector $\mathbf{f}$, where $\mathbf{f}$ is to be treated as constant with respect to variations. Similarly, one needs the variation of the pseudo-vector Jacobian $\mathbf{H}_a^T$ from equation (2.4.23) contracted with a moment vector $\mathbf{m}$, where $\mathbf{m}$ is not to be varied. These relations are established here to streamline the derivation of element expressions.

2.5.1 Variation of vector contracted $\mathbf{H}_a$.

The variation of $\mathbf{H}_a^T$ from equation (2.4.23) contracted with a constant vector $\mathbf{m}_a$ can be expressed as

$$\delta\mathbf{H}^T\mathbf{m} = \frac{\partial \mathbf{H}^T}{\partial \omega_i}\mathbf{m}\,\delta\omega_i = \mathbf{M}\,\delta\boldsymbol{\omega}\ , \tag{2.5.1}$$

where the nodal index a has been suppressed to reduce clutter. This relationship was established by Nour-Omid and Rankin [46] in the form

$$\mathbf{M} = (-\frac{1}{2}\text{Spin}(\mathbf{m}) + \eta\,((\mathbf{m}^T\boldsymbol{\theta})\mathbf{I} + \boldsymbol{\theta}\mathbf{m}^T - 2\mathbf{m}\boldsymbol{\theta}^T) + \nu\,\text{Spin}(\boldsymbol{\theta})^2\mathbf{m}\boldsymbol{\theta}^T)\mathbf{H} \tag{2.5.2}$$

where η is defined in equation (2.4.25) and

$$\nu = \frac{\theta(\theta + \sin\theta) - 8\sin^2(\frac{1}{2}\theta)}{4\theta^4\sin^2(\frac{1}{2}\theta)}\ . \tag{2.5.3}$$

As in the case of η, for $\theta \to 0,\ \nu \to 0/0$, wich amplifies computational errors for small angles. To maintain accuracy ν is computed from a truncated power series for small values of θ :

$$\nu \approx \tfrac{1}{360} + \tfrac{1}{7560}\theta^2 + \tfrac{1}{201600}\theta^4 \quad \text{for} \quad \theta < 0.05\,\text{radians}\,. \tag{2.5.4}$$

This series also establishes $\nu\big|_{\theta\to 0} = \frac{1}{360}$.

2.5.2 Variation of vector contracted P.

The variation of the nonlinear projector can be expressed as

$$\delta\mathbf{P} = \delta\mathbf{I} - \delta\mathbf{P}_T - \delta\mathbf{P}_R = -\delta\mathbf{P}_R = -\delta\mathbf{S}\,\mathbf{G} - \mathbf{S}\,\delta\mathbf{G}\,. \tag{2.5.5}$$

In the tangent stiffness expressions one needs the variations of $\mathbf{P}^T$ contracted with an element force vector $\mathbf{f}$. This force vector can be decomposed into a balanced (self equilibrium) force $\mathbf{f}_b$ and an unbalanced force $\mathbf{f}_u$:

$$\mathbf{f} = \mathbf{f}_b + \mathbf{f}_u \quad \text{where} \quad \mathbf{f}_b = \mathbf{P}^T\mathbf{f} \quad \text{and} \quad \mathbf{f}_u = (\mathbf{I} - \mathbf{P}^T)\mathbf{f}\,. \tag{2.5.6}$$

The variation of $\mathbf{P}^T$ contracted with the force vector can then be expressed as

$$\begin{aligned}\delta\mathbf{P}\mathbf{f} &= -(\mathbf{G}^T\delta\mathbf{S}^T + \delta\mathbf{G}^T\mathbf{S}^T)(\mathbf{f}_b + \mathbf{f}_u)\\ &= -\mathbf{G}^T\delta\mathbf{S}^T\mathbf{P}^T\mathbf{f} - (\mathbf{G}^T\delta\mathbf{S}^T + \delta\mathbf{G}^T\mathbf{S}^T)\mathbf{f}_u\\ &= -\mathbf{G}^T\delta\mathbf{S}^T\mathbf{P}^T\mathbf{f} + \delta\mathbf{P}^T\mathbf{f}_u\,.\end{aligned} \tag{2.5.7}$$

$\mathbf{S}^T\mathbf{f}_b = \mathbf{0}$ since $\mathbf{S}$ simply represents the three rigid body rotations vectors which does not generate any "work" when multiplied with an equilibrium force vector. The term $\delta\mathbf{P}^T\mathbf{f}_u$ will in general go towards zero when C_{0n} and C_n are close because in this case $\mathbf{f}_u$ goes towards zero.

If $\mathbf{G}$ is sufficiently simple one can show that the term $\delta\mathbf{P}^T\mathbf{f}_u$ is identically zero regardless of the closeness of C_{0n} and C_n. Assume that $\mathbf{G}$ can be expressed as

$$\mathbf{G} = \mathbf{X}\mathbf{A}, \quad \text{with the variation} \quad \delta\mathbf{G} = \delta\mathbf{X}\mathbf{A}\,, \tag{2.5.8}$$

where $\mathbf{X}$ is a coordinate dependent invertible matrix and $\mathbf{A}$ is a constant matrix. The identity in equation (2.4.41) gives the inverse and variation of $\mathbf{X}$ as

$$\mathbf{G}\mathbf{S} = \mathbf{X}\mathbf{A}\mathbf{S} = \mathbf{I} \quad \Rightarrow \quad \mathbf{X}^{-1} = \mathbf{A}\mathbf{S}\,, \tag{2.5.9}$$

and

$$\delta\mathbf{G}\mathbf{S} + \mathbf{G}\delta\mathbf{S} = \delta\mathbf{X}\mathbf{A}\mathbf{S} + \mathbf{G}\delta\mathbf{S} = \mathbf{0} \quad \Rightarrow \quad \delta\mathbf{X} = -\mathbf{G}\delta\mathbf{S}\mathbf{X}\,. \tag{2.5.10}$$

Using (2.5.9) and (2.5.10) give the variation

$$\begin{aligned}\delta\mathbf{P}^T\mathbf{f}_u &= -(\mathbf{G}^T\delta\mathbf{S}^T + \mathbf{A}^T\delta\mathbf{X}^T\mathbf{S}^T)\mathbf{f}_u \\ &= -(\mathbf{G}^T\delta\mathbf{S}^T - \mathbf{A}^T\mathbf{X}^T\delta\mathbf{S}^T\mathbf{G}^T\mathbf{S}^T)\mathbf{f}_u \\ &= -(\mathbf{G}^T\delta\mathbf{S}^T - \mathbf{G}^T\delta\mathbf{S}^T\mathbf{P}_R^T)\mathbf{f}_u = -\mathbf{G}^T\delta\mathbf{S}^T(\mathbf{I}-\mathbf{P}_R^T)\mathbf{f}_u \\ &= -\mathbf{G}^T\delta\mathbf{S}^T(\mathbf{I}-\mathbf{P}_R^T)(\mathbf{I}-\mathbf{P}^T)\mathbf{f} = \mathbf{0}\ ,\end{aligned} \tag{2.5.11}$$

because $(\mathbf{I}-\mathbf{P}_R^T)(\mathbf{I}-\mathbf{P}^T)\mathbf{f} = \mathbf{P}_T^T\mathbf{f} = \mathbf{0}$ if the initial force vector $\mathbf{f}$ is in translational equilibrium. Translational equilibrium at the element level is satisfied unless the linear stiffness matrix does not represent rigid body translations correctly, which is unlikely.

2.6 Governing equations for geometric nonlinear analysis.

The global equilibrium equations of geometric nonlinear discretized by the finite element method can be compactly stated as the force residual $\mathbf{r}$ vanishing along an equilibrium trajectory:

$$\mathbf{r}(\hat{\mathbf{v}}, \lambda) = \mathbf{f}(\hat{\mathbf{v}}) - \mathbf{p}(\lambda) = \mathbf{0} \quad \text{where} \quad \hat{\mathbf{v}} = \hat{\mathbf{v}}(\lambda) \; . \tag{2.6.1}$$

Here vector (or rather array) $\hat{\mathbf{v}}$ collects the global node displacements of the structure, as discussed in Section 2.3.4, $\mathbf{f}$ is the vector of internal forces induced by the displacements $\hat{\mathbf{v}}$, and $\mathbf{p}$ is the vector of applied external loads written as a function of a single loading parameter λ. The total displacements of the structure, collected in $\hat{\mathbf{v}}$, contains both the translations and the rotational orientation of each node. The rotational orientation can be given in various representations, examples being the rotation tensor according to the Rodrigues representation, Euler angles, or Euler parameters. The symbol ($\hat{}$) is used to distinguish the total displacement state from an incremental displacement vector $\delta\mathbf{v}$ in which the rotations are the instantaneous rotation axis $\delta\boldsymbol{\omega}$, and a deformational displacement vector $\mathbf{v}_d$ where the rotations are rotational pseudovectors $\boldsymbol{\theta}_d$ (see Box 2.1).

Since the force residual is identical zero the first derivative of the equilibrium equations with respect to the load parameter λ must vanish:

$$\frac{d\mathbf{r}}{d\lambda} = \frac{\partial \mathbf{f}}{\partial \mathbf{v}} \frac{d\mathbf{v}}{d\lambda} - \frac{d\mathbf{p}}{d\lambda} = \mathbf{K}\frac{d\mathbf{v}}{d\lambda} - \frac{d\mathbf{p}}{d\lambda} = \mathbf{K}\mathbf{w} - \mathbf{q} = \mathbf{0} \; , \tag{2.6.2}$$

where $\mathbf{K}$ is the tangent stiffness matrix, $\mathbf{w}$ is the incremental velocity vector and $\mathbf{q}$ is the incremental load vector. Incremental/iterative solution algorithms that use equation (2.6.1) and (2.6.2) on the global level are described in Chapter 3. The essential ingredients required in such solution algorithms are the internal force vector $\mathbf{f}$ and the tangent stiffness $\mathbf{K}$. The computation of these quantities at the element level is dealt with in the following sections.

2.7 Internal force.

This section covers the computation of element internal forces. The exposition addresses the most comprehensive form of such computation used in the present work. This formulation is identified later as Consistent Symmetrizable Self-Equilibrated (CSSE) formulation since the internal force formulation lead to a self-equilibrium element internal force vector, which then generates a symmetrizable tangent stiffness matrix through its consistent variation. Symmetrizable means that although the tangent stiffness is not symmetric, the asymptotic convergence rate of equilibrium iterations is not impaired when the symmetrized stiffness is used. From this comprehensive form, simpler consistent formulations can be obtained through specific simplifying assumptions.

The strain displacement relationship in local coordinate system of the C_{0n} and C_n configurations is

$$\tilde{\boldsymbol{\epsilon}} = \tilde{\mathbf{B}}\tilde{\mathbf{v}}_d \ , \tag{2.7.1}$$

where $\tilde{\mathbf{v}}_d$ is the deformational displacement vector from C_{0n} to C_n. Furthermore, the constitutive relationship in the local coordinate system is

$$\tilde{\boldsymbol{\sigma}} = \tilde{\mathbf{C}}\tilde{\boldsymbol{\epsilon}} \ . \tag{2.7.2}$$

The element internal force vector in the global coordinate system can be computed as

$$\mathbf{f}(\hat{\mathbf{v}}) = \mathbf{T}^T\tilde{\mathbf{P}}^T\tilde{\mathbf{H}}^T \int_V \tilde{\mathbf{B}}^T\tilde{\mathbf{C}}\tilde{\mathbf{B}}\, dV\, \tilde{\mathbf{v}}_d = \mathbf{T}^T\tilde{\mathbf{P}}^T\tilde{\mathbf{H}}^T\tilde{\mathbf{K}}_e\tilde{\mathbf{v}}_d \ , \tag{2.7.3}$$

where $\tilde{\mathbf{K}}_e$ can be recognized as the familiar linear theory element stiffness matrix. In Sections 2.3 and 2.4 one has established the expressions

$$\tilde{\mathbf{v}}_d = \tilde{\mathbf{v}}_d(\hat{\mathbf{v}}) \ , \quad \tilde{\mathbf{P}} = \tilde{\mathbf{P}}(\hat{\mathbf{v}}) \ , \quad \tilde{\mathbf{H}} = \tilde{\mathbf{H}}(\hat{\mathbf{v}}) \ , \tag{2.7.4}$$

all being functions of the global displacement state $\hat{\mathbf{v}}$. For an element with N nodes and six degrees of freedoms per node, that is, three translational degrees of freedom and three rotational degrees of freedom, the transformation matrix $\mathbf{T}$ in equation (2.7.3) consists of $\mathbf{T}_n$ from equation (2.7.5) repeated $2N$ times along the diagonal:

$$\mathbf{T} = \begin{bmatrix} \mathbf{T}_n & & \mathbf{0} \\ & \ddots & \\ \mathbf{0} & & \mathbf{T}_n \end{bmatrix} . \tag{2.7.5}$$

Note that $\mathbf{T}$ is a function of the global displacement state; $\mathbf{T} = \mathbf{T}(\hat{\mathbf{v}})$. Furthermore, if the strain displacement matrix $\tilde{\mathbf{B}}$ in equations (2.7.1) and (2.7.3) is expressed with respect to the shadow element C_{0n} one has

$$\tilde{\mathbf{B}} = \text{constant}, \tag{2.7.6}$$

but $\tilde{\mathbf{B}} = \tilde{\mathbf{B}}(\hat{\mathbf{v}})$ if the strain displacement relationship is expressed with respect to the deformed element geometry C_n. The constitutive matrix $\tilde{\mathbf{C}}$ is constant if the material is linearly elastic. The condition that $\tilde{\mathbf{B}}$ be constant, and thus expressed with respect to the shadow element, is the key condition for an element independent formulation.

This approach to the computation of the internal force for an element, with $\tilde{\mathbf{B}}$ expressed with respect to C_{0n}, is similar to the procedure of Nour-Omid and Rankin [46]. If both $\mathbf{P}$ and $\mathbf{H}$ are set to the identity matrix so that $\mathbf{f} = \mathbf{T}^T\tilde{\mathbf{K}}_e\tilde{\mathbf{v}}_d$, the internal force expressions used by Bergan et al. [17,42,47] are recovered.

2.8 Consistent tangent stiffness.

The tangent stiffness $\mathbf{K}$ is said to be consistent with the internal forces if it relates the variation of $\mathbf{f}$ with respect to variations in $\mathbf{v}$:

$$\delta\mathbf{f} = \frac{\partial \mathbf{f}}{\partial v_i}\delta v_i = \frac{\partial \mathbf{f}}{\partial \mathbf{v}}\,\delta\mathbf{v} = \mathbf{K}\,\delta\mathbf{v}\,. \tag{2.8.1}$$

Denoting by $\tilde{\mathbf{f}}_e = \tilde{\mathbf{K}}_e\mathbf{v}_d$, the variation of equation (2.7.3) with respect to $\mathbf{v}$ gives

$$\begin{aligned}\delta\mathbf{f} &= \delta\mathbf{T}^T\tilde{\mathbf{P}}^T\tilde{\mathbf{H}}^T\tilde{\mathbf{f}}_e + \mathbf{T}^T\delta\tilde{\mathbf{P}}^T\tilde{\mathbf{H}}^T\tilde{\mathbf{f}}_e + \mathbf{T}^T\tilde{\mathbf{P}}^T\delta\tilde{\mathbf{H}}^T\tilde{\mathbf{f}}_e + \mathbf{T}^T\tilde{\mathbf{P}}^T\tilde{\mathbf{H}}^T\delta\tilde{\mathbf{f}}_e \\ &= (\mathbf{K}_{GR} + \mathbf{K}_{GP} + \mathbf{K}_{GM} + \mathbf{K}_M)\,\delta\mathbf{v} = \mathbf{K}\,\delta\mathbf{v}\,.\end{aligned} \tag{2.8.2}$$

The contributions of the various terms of (2.8.2) to $\mathbf{K}$ are examined in the following subsections, where the following names will be further explained: $\mathbf{K}_M$ is called the material stiffness, $\mathbf{K}_{GM}$ is the moment-correction geometric stiffness, $\mathbf{K}_{GP}$ is the equilibrium-projection geometric stiffness, and $\mathbf{K}_{GR}$ is the rotational geometric stiffness.

2.8.1 Material stiffness.

The last term on the right hand side of equation (2.8.2) generates the so-called material stiffness $\mathbf{K}_M$:

$$\begin{aligned}\mathbf{T}\tilde{\mathbf{P}}^T\tilde{\mathbf{H}}^T\delta\tilde{\mathbf{f}}_e &= \mathbf{T}^T\tilde{\mathbf{P}}^T\tilde{\mathbf{H}}^T\delta\tilde{\mathbf{K}}_e\tilde{\mathbf{v}}_d + \mathbf{T}^T\tilde{\mathbf{P}}^T\tilde{\mathbf{H}}^T\tilde{\mathbf{K}}_e\,\delta\tilde{\mathbf{v}}_d \\ &= \mathbf{T}^T\tilde{\mathbf{P}}^T\tilde{\mathbf{H}}^T\tilde{\mathbf{K}}_e\tilde{\mathbf{H}}\tilde{\mathbf{P}}\,\delta\tilde{\mathbf{v}} = \mathbf{T}^T\tilde{\mathbf{P}}^T\tilde{\mathbf{H}}^T\tilde{\mathbf{K}}_e\tilde{\mathbf{H}}\tilde{\mathbf{P}}\mathbf{T}\,\delta\mathbf{v} = \mathbf{K}_M\,\delta\mathbf{v}\end{aligned} \tag{2.8.3}$$

in which

$$\mathbf{K}_M = \mathbf{T}^T\tilde{\mathbf{P}}^T\tilde{\mathbf{H}}^T\tilde{\mathbf{K}}_e\tilde{\mathbf{H}}\tilde{\mathbf{P}}\mathbf{T} \tag{2.8.4}$$

provided $\delta\tilde{\mathbf{K}}_e = \mathbf{0}$. This assumption is only satisfied when $\tilde{\mathbf{B}}$ is expressed with respect to the shadow configuration C_{0n} because if so

$$\delta\tilde{\mathbf{B}} = \frac{\partial\tilde{\mathbf{B}}}{\partial\tilde{v}_i}\,\delta\tilde{v}_i = \mathbf{0}\ . \tag{2.8.5}$$

The linear element stiffness matrix $\tilde{\mathbf{K}}_e$ thus stays constant when it is expressed in the moving co-rotated coordinate system with respect to the shadow element geometry, and the material is modeled as linearly elastic (hence $\tilde{\mathbf{C}}$ is constant). The validity and effect of expressing $\tilde{\mathbf{B}}$ with respect to the C_{0n} configuration is discussed in Section 2.11.

The deformational displacements $\tilde{\mathbf{v}}_d$ are expressed in co-rotated coordinate system and the relationship

$$\delta\tilde{\mathbf{v}}_d = \tilde{\mathbf{H}}\tilde{\mathbf{P}}\delta\tilde{\mathbf{v}} \tag{2.8.6}$$

established in Section 2.4.7 must express the variation the co-rotated $\tilde{\mathbf{v}}_d$ with respect to the inertial visible degrees of freedom $\tilde{\mathbf{v}}$.

2.8.2 Rotational geometric stiffness.

The rotational geometric stiffness appears as the gradient of the force vector with respect to the rigid rotation of the element. This interpretation is physically intuitive because a rigid rotation of a stressed element necessarily reorients the stress vectors by that amount. Consequently the internal element forces must rigidly rotate to preserve equilibrium. The rotational geometric stiffness is obtained from the first term on the right hand side of equation (2.8.2) .

$$
\begin{aligned}
\delta\mathbf{T}^T\tilde{\mathbf{P}}\tilde{\mathbf{H}}^T\tilde{\mathbf{f}}_e = \delta\mathbf{T}^T\tilde{\mathbf{f}} &= \begin{bmatrix} \delta\mathbf{T}_n^T\tilde{\mathbf{n}}_1 \\ \delta\mathbf{T}_n^T\tilde{\mathbf{m}}_1 \\ \vdots \\ \delta\mathbf{T}_n^T\tilde{\mathbf{n}}_N \\ \delta\mathbf{T}_n^T\tilde{\mathbf{m}}_N \end{bmatrix} = \begin{bmatrix} \mathbf{T}_n^T\mathrm{Spin}(\delta\tilde{\boldsymbol{\omega}}_r)\tilde{\mathbf{n}}_1 \\ \mathbf{T}_n^T\mathrm{Spin}(\delta\tilde{\boldsymbol{\omega}}_r)\tilde{\mathbf{m}}_1 \\ \vdots \\ \mathbf{T}_n^T\mathrm{Spin}(\delta\tilde{\boldsymbol{\omega}}_r)\tilde{\mathbf{n}}_N \\ \mathbf{T}_n^T\mathrm{Spin}(\delta\tilde{\boldsymbol{\omega}}_r)\tilde{\mathbf{m}}_N \end{bmatrix} \\
&= -\mathbf{T}^T\begin{bmatrix} \mathrm{Spin}(\tilde{\mathbf{n}}_1)\delta\tilde{\boldsymbol{\omega}}_r \\ \mathrm{Spin}(\tilde{\mathbf{m}}_1)\delta\tilde{\boldsymbol{\omega}}_r \\ \vdots \\ \mathrm{Spin}(\tilde{\mathbf{n}}_N)\delta\tilde{\boldsymbol{\omega}}_r \\ \mathrm{Spin}(\tilde{\mathbf{m}}_N)\delta\tilde{\boldsymbol{\omega}}_r \end{bmatrix} = -\mathbf{T}^T\begin{bmatrix} \mathrm{Spin}(\tilde{\mathbf{n}}_1) \\ \mathrm{Spin}(\tilde{\mathbf{m}}_1) \\ \vdots \\ \mathrm{Spin}(\tilde{\mathbf{n}}_N) \\ \mathrm{Spin}(\tilde{\mathbf{m}}_N) \end{bmatrix}\delta\tilde{\boldsymbol{\omega}}_r \\
&= -\mathbf{T}^T\tilde{\mathbf{F}}_{nm}\delta\tilde{\boldsymbol{\omega}}_r = -\mathbf{T}^T\tilde{\mathbf{F}}_{nm}\tilde{\mathbf{G}}\mathbf{T}\delta\mathbf{v} \ .
\end{aligned}
\tag{2.8.7}
$$

In these derivations the following relations have been used

$$
\delta\mathbf{T}_n^T = \mathbf{T}_n^T\mathrm{Spin}(\delta\tilde{\boldsymbol{\omega}}_r) \quad \text{and} \quad \mathrm{Spin}(\delta\tilde{\boldsymbol{\omega}}_r)\tilde{\mathbf{n}}_a = -\mathrm{Spin}(\mathbf{n}_a)\delta\tilde{\boldsymbol{\omega}}_r \ . \tag{2.8.8}
$$

The rotational geometric stiffness is thus given by

$$
\mathbf{K}_{GR} = -\mathbf{T}^T\tilde{\mathbf{F}}_{nm}\tilde{\mathbf{G}}\mathbf{T} \ , \tag{2.8.9}
$$

$$
\text{where} \quad \tilde{\mathbf{F}}_{nm} = \begin{bmatrix} \mathrm{Spin}(\tilde{\mathbf{n}}_1) \\ \mathrm{Spin}(\tilde{\mathbf{m}}_1) \\ \vdots \\ \mathrm{Spin}(\tilde{\mathbf{n}}_N) \\ \mathrm{Spin}(\tilde{\mathbf{m}}_N) \end{bmatrix} \quad \text{from} \quad \tilde{\mathbf{f}} = \begin{bmatrix} \tilde{\mathbf{n}}_1 \\ \tilde{\mathbf{m}}_1 \\ \vdots \\ \mathbf{n}_N \\ \tilde{\mathbf{m}}_N \end{bmatrix} = \tilde{\mathbf{P}}^T\tilde{\mathbf{H}}^T\tilde{\mathbf{f}}_e \ , \tag{2.8.10}
$$

and $\tilde{\mathbf{P}}$ is defined in equation (2.4.34).

2.8.3 Moment correction geometric stiffness.

The third term in the right hand side of equation (2.8.2) contributes a stiffness term that arises from the variation the rotation pseudo-vector Jacobian $\mathbf{H}$ contracted with the nodal moment vector $\mathbf{m}$. From equation (2.4.33) and using equation (2.5.1) this term can be written as

$$\begin{aligned}
\mathbf{T}^T\tilde{\mathbf{P}}^T\delta\tilde{\mathbf{H}}^T\tilde{\mathbf{f}}_e &= \mathbf{T}^T\tilde{\mathbf{P}}^T\begin{bmatrix}\mathbf{0}\\ \delta\tilde{\mathbf{H}}_1^T\tilde{\mathbf{m}}_1\\ \vdots\\ \mathbf{0}\\ \delta\tilde{\mathbf{H}}_N^T\tilde{\mathbf{m}}_N\end{bmatrix} = \mathbf{T}^T\tilde{\mathbf{P}}^T\begin{bmatrix}\mathbf{0}\\ \tilde{\mathbf{M}}_1\delta\tilde{\boldsymbol{\omega}}_{d1}\\ \vdots\\ \mathbf{0}\\ \tilde{\mathbf{M}}_N\delta\tilde{\boldsymbol{\omega}}_{dN}\end{bmatrix} \\
&= \mathbf{T}^T\tilde{\mathbf{P}}^T\begin{bmatrix}\mathbf{0} & & & & \\ & \tilde{\mathbf{M}}_1 & & & \\ & & \ddots & & \\ & & & \mathbf{0} & \\ & & & & \tilde{\mathbf{M}}_N\end{bmatrix}\delta\tilde{\mathbf{v}}_d \\
&= \mathbf{T}^T\tilde{\mathbf{P}}^T\tilde{\mathbf{M}}\tilde{\mathbf{P}}\mathbf{T}\delta\mathbf{v}\ .
\end{aligned} \tag{2.8.11}$$

The moment correction geometric stiffness is thus given by

$$\mathbf{K}_{GM} = \mathbf{T}^T\tilde{\mathbf{P}}^T\tilde{\mathbf{M}}\tilde{\mathbf{P}}\mathbf{T}\ , \tag{2.8.12}$$

where

$$\tilde{\mathbf{M}} = \begin{bmatrix}\mathbf{0} & & & & \\ & \tilde{\mathbf{M}}_1 & & & \\ & & \ddots & & \\ & & & \mathbf{0} & \\ & & & & \tilde{\mathbf{M}}_N\end{bmatrix}, \tag{2.8.13}$$

and $\tilde{\mathbf{M}}_a$ is defined in equation (2.5.1).

2.8.4 Equilibrium projection geometric stiffness.

The equilibrium projection geometric stiffness arises from the variation of the projector $\tilde{\mathbf{P}}$ with respect to the deformed element geometry. The equilibrium-projection geometric stiffness expresses the change in the projection of the internal force vector $\tilde{\mathbf{f}}_e$ as the the element geometry changes. (This can be thought of as: In the vector space of element force vectors the subspace of self-equilibrium force vectors changes as the element geometry changes. The projected force vector thus has a gradient with respect to the changing self-equilibrium subspace, even though the element force $\tilde{\mathbf{f}}_e$ does not change).

By decomposing the force vector $\tilde{\mathbf{H}}^T\tilde{\mathbf{f}}_e$ into balanced $\tilde{\mathbf{f}}_b$ and unbalanced $\tilde{\mathbf{f}}_u$ forces according to equation (2.5.6), the second term in the right hand side of equation (2.8.2) can be transformed as

$$\begin{aligned}\mathbf{T}^T\delta\tilde{\mathbf{P}}^T\tilde{\mathbf{H}}^T\tilde{\mathbf{f}}_e &= -\mathbf{T}^T\tilde{\mathbf{G}}^T\delta\tilde{\mathbf{S}}^T\tilde{\mathbf{P}}^T\tilde{\mathbf{H}}^T\tilde{\mathbf{f}}_e + \mathbf{T}^T\delta\tilde{\mathbf{P}}^T(\mathbf{I}-\mathbf{P}^T)\tilde{\mathbf{H}}^T\tilde{\mathbf{f}}_e \\ &= -\mathbf{T}^T\tilde{\mathbf{G}}^T\delta\tilde{\mathbf{S}}^T\tilde{\mathbf{f}}_b + \mathbf{T}^T\delta\tilde{\mathbf{P}}^T\tilde{\mathbf{f}}_u\ .\end{aligned} \tag{2.8.14}$$

According to the arguments in Section 2.5.2 the term $\mathbf{T}^T\delta\tilde{\mathbf{P}}^T\tilde{\mathbf{f}}_u$ can be neglected because this will be small when C_{0n} and C_n are close. Moreover, that term is identically zero if $\tilde{\mathbf{G}}$ is sufficiently simple to be expressed as $\tilde{\mathbf{G}} = \tilde{\mathbf{X}}\mathbf{A}$, where $\mathbf{A}$ is a constant matrix and $\tilde{\mathbf{X}}$ is an invertible 3×3 matrix.

This gives the variation as

$$\begin{aligned}\mathbf{T}^T\delta\tilde{\mathbf{P}}^T\tilde{\mathbf{H}}^T\tilde{\mathbf{f}}_e &= -\mathbf{T}^T\tilde{\mathbf{G}}^T\sum_{i=1}^{N}\begin{bmatrix}\mathrm{Spin}(\delta\tilde{\mathbf{x}}_i^n) & \mathbf{0}\end{bmatrix}\begin{bmatrix}\tilde{\mathbf{n}}_i\\ \tilde{\mathbf{m}}_i\end{bmatrix} \\ &= -\mathbf{T}^T\tilde{\mathbf{G}}^T\sum_{i=1}^{N}\begin{bmatrix}-\mathrm{Spin}(\tilde{\mathbf{n}}_i) & \mathbf{0}\end{bmatrix}\begin{bmatrix}\delta\tilde{\mathbf{x}}_i^n\\ \delta\tilde{\boldsymbol{\theta}}_i\end{bmatrix} \\ &= -\mathbf{T}^T\tilde{\mathbf{G}}^T\sum_{i=1}^{N}\begin{bmatrix}-\mathrm{Spin}(\tilde{\mathbf{n}}_i) & \mathbf{0}\end{bmatrix}\begin{bmatrix}\delta\tilde{\mathbf{u}}_{di}\\ \delta\tilde{\boldsymbol{\theta}}_{di}\end{bmatrix} \\ &= -\mathbf{T}^T\tilde{\mathbf{G}}^T\tilde{\mathbf{F}}_n^T\tilde{\mathbf{P}}\mathbf{T}\delta\mathbf{v}\ .\end{aligned} \tag{2.8.15}$$

The equilibrium projection geometric stiffness is then given by

$$\mathbf{K}_{GP} = -\mathbf{T}^T\tilde{\mathbf{G}}^T\tilde{\mathbf{F}}_n^T\tilde{\mathbf{P}}\mathbf{T}\ , \tag{2.8.16}$$

$$\text{where}\quad \tilde{\mathbf{F}}_n = \begin{bmatrix}\mathrm{Spin}(\tilde{\mathbf{n}}_1)\\ \mathbf{0}\\ \vdots\\ \mathrm{Spin}(\tilde{\mathbf{n}}_N)\\ \mathbf{0}\end{bmatrix}\quad \text{from}\quad \tilde{\mathbf{f}}_b = \begin{bmatrix}\tilde{\mathbf{n}}_1\\ \tilde{\mathbf{m}}_1\\ \vdots\\ \mathbf{n}_N\\ \tilde{\mathbf{m}}_N\end{bmatrix} = \tilde{\mathbf{P}}^T\tilde{\mathbf{H}}^T\tilde{\mathbf{f}}_e\ , \tag{2.8.17}$$

and in which $\tilde{\mathbf{P}}$ is defined in equation (2.4.34) .

2.8.5 Additional terms in geometric stiffness.

The term dropped in the transition from equation (2.8.14) to (2.8.15) can be computed as

$$\begin{aligned} \mathbf{T}^T \delta\tilde{\mathbf{P}}^T \tilde{\mathbf{f}}_u &= -(\tilde{\mathbf{G}}^T \delta\tilde{\mathbf{S}}^T + \delta\tilde{\mathbf{G}}^T \tilde{\mathbf{S}}^T)\tilde{\mathbf{f}}_u \\ &= (\mathbf{K}_{A1} + \mathbf{K}_{A2})\delta\mathbf{v} \ . \end{aligned} \tag{2.8.18}$$

By following the derivations in equation (2.8.15) the first term of (2.8.18) is obtained as

$$\mathbf{K}_{A1} = -\mathbf{T}^T \tilde{\mathbf{G}}^T \tilde{\mathbf{F}}_{nu}^{\ T} \tilde{\mathbf{P}} \mathbf{T}, \tag{2.8.19}$$

where $\tilde{\mathbf{F}}_{nu}$ is based on the unbalanced forces $\tilde{\mathbf{f}}_u = (\mathbf{I} - \tilde{\mathbf{P}}^T)\tilde{\mathbf{f}}_e$. Define the unbalanced resultant moment acting on the element as

$$\tilde{\mathbf{m}}_u = \tilde{\mathbf{S}}^T \tilde{\mathbf{f}}_u \ , \tag{2.8.20}$$

through which the second term in (2.8.18) can be written as

$$\begin{aligned} \mathbf{K}_{A2}\delta\mathbf{v} = -\mathbf{T}^T \delta\tilde{\mathbf{G}} \tilde{\mathbf{m}}_u &= -\mathbf{T}^T \frac{\partial \tilde{\mathbf{G}}}{\partial \mathbf{v}} \tilde{\mathbf{m}}_u \, \delta\tilde{\mathbf{v}} \\ &= -\mathbf{T}^T \frac{\partial \tilde{\mathbf{G}}}{\partial \tilde{\mathbf{v}}} \tilde{\mathbf{m}}_u \mathbf{T} \, \delta\mathbf{v} \ . \end{aligned} \tag{2.8.21}$$

These terms have not been implemented in the present work based on the argument in Section 2.5.2 that they are usually small. However, in the case of quadrilateral shell elements subjected to significant warping those terms may be necessary to maintain quadratic convergence of a true Newton nonlinear solution algorithm.

2.8.6 Summary of consistent tangent stiffness.

Combining equations (2.8.2) , (2.8.4) , (2.8.12) , (2.8.9) and (2.8.19) the following expressions for the consistent tangent stiffness results:

$$\begin{aligned} \mathbf{K} &= \mathbf{T}^T (\tilde{\mathbf{K}}_M + \tilde{\mathbf{K}}_{GM} + \tilde{\mathbf{K}}_{GR} + \tilde{\mathbf{K}}_{GP}) \mathbf{T} \\ &= \mathbf{T}^T (\tilde{\mathbf{P}}^T \tilde{\mathbf{H}}^T \tilde{\mathbf{K}}_e \tilde{\mathbf{H}} \tilde{\mathbf{P}} + \tilde{\mathbf{P}}^T \tilde{\mathbf{M}} \tilde{\mathbf{P}} - \tilde{\mathbf{F}}_{nm} \tilde{\mathbf{G}} - \tilde{\mathbf{G}}^T \tilde{\mathbf{F}}_n^T \tilde{\mathbf{P}}) \mathbf{T} \ , \end{aligned} \tag{2.8.22}$$

where

$$\tilde{\mathbf{P}} = \mathbf{I} - \tilde{\mathbf{P}}_T - \tilde{\mathbf{P}}_R \ ,$$

and

$$\tilde{\mathbf{F}}_{mn} = \begin{bmatrix} \mathrm{Spin}(\tilde{\mathbf{n}}_1) \\ \mathrm{Spin}(\mathbf{m}_1) \\ \vdots \\ \mathrm{Spin}(\tilde{\mathbf{n}}_N) \\ \mathrm{Spin}(\mathbf{m}_N) \end{bmatrix}, \; \tilde{\mathbf{F}}_n = \begin{bmatrix} \mathrm{Spin}(\tilde{\mathbf{n}}_1) \\ \mathbf{0} \\ \vdots \\ \mathrm{Spin}(\tilde{\mathbf{n}}_N) \\ \mathbf{0} \end{bmatrix} \text{ from } \tilde{\mathbf{f}} = \begin{bmatrix} \tilde{\mathbf{n}}_1 \\ \tilde{\mathbf{m}}_1 \\ \vdots \\ \mathbf{n}_N \\ \tilde{\mathbf{m}}_N \end{bmatrix} = \tilde{\mathbf{P}}^T \tilde{\mathbf{H}}^T \tilde{\mathbf{f}}_e \; . \tag{2.8.23}$$

2.8.7 Properties of the stiffness matrix.

The tangent stiffness matrix in (2.8.22) has some properties that may be exploited to verify the computer implementation. By post and premultiplying with $\mathbf{S}$ from equation (2.4.36) one obtains the following identities.

Postmultiplying with $\mathbf{S}$.

$$\begin{aligned} \mathbf{KS} &= \mathbf{P}^T\mathbf{H}^T\mathbf{K}_e\mathbf{HPS} + \mathbf{P}^T\mathbf{MPS} - \mathbf{F}_{nm}\mathbf{GS} - \mathbf{G}^T\mathbf{F}_n^T\mathbf{PS} \\ &= -\mathbf{F}_{nm} \; . \end{aligned} \tag{2.8.24}$$

In the equation above one has used $\mathbf{GS} = \mathbf{I}$ from equation (2.4.41) , and the relationship

$$\begin{aligned} \mathbf{PS} &= \mathbf{IS} - \mathbf{P}_T\mathbf{S} - \mathbf{SGS} \\ &= \mathbf{S} - \mathbf{0} - \mathbf{S} = \mathbf{0} \; . \end{aligned} \tag{2.8.25}$$

Premultiplying with $\mathbf{S}^T$.

$$\begin{aligned} \mathbf{S}^T\mathbf{K} &= \mathbf{S}^T\mathbf{P}^T\mathbf{H}^T\mathbf{K}_e\mathbf{HP} + \mathbf{S}^T\mathbf{P}^T\mathbf{MP} - \mathbf{S}^T\mathbf{F}_{nm}\mathbf{G} - \mathbf{S}^T\mathbf{G}^T\mathbf{F}_n^T\mathbf{P} \\ &= -\mathbf{S}^T\mathbf{F}_{nm}\mathbf{G} - \mathbf{F}_n^T\mathbf{P} = -\mathbf{S}^T\mathbf{F}_{nm} - \mathbf{F}_n^T + \mathbf{F}_n^T\mathbf{P}_T + \mathbf{F}_n^T\mathbf{SG} \\ &= -\mathbf{F}_n^T + (\mathbf{F}_n^T\mathbf{S} - \mathbf{S}^T\mathbf{F}_{nm})\mathbf{G} \\ &= -\mathbf{F}_n^T \; , \end{aligned} \tag{2.8.26}$$

since

$$\begin{aligned} (\mathbf{F}_n^T\mathbf{S} - \mathbf{S}^T\mathbf{F}_{nm}) &= \sum_{a=1}^{n} (\mathrm{Spin}(\mathbf{n}_a)\mathrm{Spin}(\mathbf{x}_a) - \mathrm{Spin}(\mathbf{x}_a)\mathrm{Spin}(\mathbf{n}_a) - \mathrm{Spin}(\mathbf{m}_a)) \\ &= \sum_{a=1}^{n} \mathrm{Spin}(\mathbf{n}_a \times \mathbf{x}_a - \mathbf{m}_a) = \mathbf{0}. \end{aligned}$$

Equation (2.8.24) and (2.8.26) can be summarized as

$$\begin{aligned} \mathbf{K}\mathbf{S} &= -\mathbf{F}_{nm} \ , \\ \mathbf{S}^T\mathbf{K} &= -\mathbf{F}_n^T \ , \end{aligned} \qquad \text{or} \qquad \begin{aligned} \mathbf{K}_M\mathbf{S} &= \mathbf{0} \\ \mathbf{K}_{GR}\mathbf{S} &= -\mathbf{F}_{nm} \\ \mathbf{K}_{GP}\mathbf{S} &= \mathbf{0} \\ \mathbf{S}^T\mathbf{K}_M &= \mathbf{0} \\ \mathbf{S}^T(\mathbf{K}_{GR}+\mathbf{K}_{GP}) &= -\mathbf{F}_n^T \ . \end{aligned} \tag{2.8.27}$$

Matrix $\mathbf{S}$ is easy to form based on the nodal coordinates of an element. From the output of the internal force computations one can easily form $\mathbf{F}_{nm}$ and $\mathbf{F}_n$. The matrix products in (2.8.27) with $\mathbf{K}$ as the output of the stiffness routine can be checked against $\mathbf{F}_{nm}$ and $\mathbf{F}_n$ as output of the internal force routine. This procedure tests the programming of the projector matrix $\mathbf{P}$ because it checks the null-space of $\mathbf{P}$. It also indicates whether the projector matrix is used correctly in the stiffness formulation. However, the expressions in (2.8.27) do not entail a complete verification of consistency between the internal force and the tangent stiffness because $\mathbf{H}$ is left unchecked. Full verification of consistency can be numerically done through finite difference techniques.

2.9 Three consistent co-rotated formulations.

The previous formulation of the internal force and tangent stiffness can produce three co-rotated consistent formulations that satisfy self-equilibrium and symmetry to varying degree. Sections 2.7 and 2.8 present the most comprehensive one, called the Consistent Symmetrizable Self-Equilibrated (CSSE) co-rotated formulation. The following subsections describe the three versions in the order of increasing complexity.

2.9.1 Consistent co-rotated formulation (C).

The internal force is computed as in the co-rotated formulation of Bergan et al. [47,42,17]. This is obtained from equation (2.7.3) by setting $\mathbf{H}=\mathbf{I}$ and $\mathbf{P}=\mathbf{I}$. The expression for the tangent stiffness in (2.8.2) simplifies with $\delta\mathbf{P}=\mathbf{0}$ and $\delta\mathbf{H}=\mathbf{0}$, while retaining $\delta\tilde{\mathbf{v}}_d = \tilde{\mathbf{P}}^T\tilde{\mathbf{H}}^T\,\delta\tilde{\mathbf{v}}$:

$$\begin{aligned} \mathbf{f} &= \mathbf{T}^T\tilde{\mathbf{K}}_e\tilde{\mathbf{v}}_d \ , \\ \mathbf{K} &= \mathbf{T}^T(\tilde{\mathbf{K}}_e\tilde{\mathbf{H}}\tilde{\mathbf{P}} - \tilde{\mathbf{F}}_{mn}\tilde{\mathbf{G}})\mathbf{T} \ , \end{aligned} \tag{2.9.1}$$

where $\tilde{\mathbf{F}}_{nm}$ is computed according to equation (2.8.23) using $\tilde{\mathbf{f}} = \tilde{\mathbf{K}}_e\tilde{\mathbf{v}}_d$. The internal force is in equilibrium with respect to the shadow element configuration C_{0n}. The material stiffness approaches symmetry as the element mesh is refined if the membrane strains are "small". With mesh refinement the deformational rotation pseudo-vectors $\tilde{\boldsymbol{\theta}}_{ad}$ gets smaller and approach vector properties that

make $\mathbf{H}$ approach the identity matrix. With small membrane strains $\tilde{\mathbf{K}}_e$ is indifferent with respect to postmultipliplication with $\tilde{\mathbf{P}}$ because the C_{0n} and C_n configurations will be close: $\tilde{\mathbf{K}}_e\mathbf{P} \rightarrow \tilde{\mathbf{K}}_e$. The consistent geometric stiffness is always unsymmetric, even at equilibrium. Because of this fact one can not expect quadratic convergence for this formulation unless a non-symmetric solver is used.

This formulation is not satisfactory for quadrilateral shell elements since the C_{0n} and C_n reference can be far apart. Only in the limit of a highly refined element mesh will the C_{0n} and C_n references in general be close, and a satisfactory equilibrium ensured.

2.9.2 Consistent Self-Equilibrated co-rotated formulation (CSE).

The internal force is equilibrated through pre-multiplication by the projector matrix $\mathbf{P}^T$. On the other hand, matrix $\mathbf{H}$ is set to the identity matrix in the force expression and consequently the stiffness is simplified with $\delta\mathbf{H} = \mathbf{0}$:

$$\begin{aligned} \mathbf{f} &= \mathbf{T}^T\tilde{\mathbf{P}}^T\tilde{\mathbf{K}}_e\tilde{\mathbf{v}}_d \ , \\ \mathbf{K} &= \mathbf{T}^T(\tilde{\mathbf{P}}^T\tilde{\mathbf{K}}_e\tilde{\mathbf{H}}\tilde{\mathbf{P}} - \tilde{\mathbf{F}}_{mn}\tilde{\mathbf{G}} - \tilde{\mathbf{G}}^T\tilde{\mathbf{F}}_n^T\tilde{\mathbf{P}})\mathbf{T} \ , \end{aligned} \tag{2.9.2}$$

where $\tilde{\mathbf{F}}_{nm}$ and $\tilde{\mathbf{F}}_n$ are computed according to equation (2.8.23) using $\tilde{\mathbf{f}} = \tilde{\mathbf{P}}^T\tilde{\mathbf{K}}_e\tilde{\mathbf{v}}_d$.

Due to the symmetric precence of $\tilde{\mathbf{P}}$, the material stiffness of this formulation approaches symmetry as the mesh is refined regardless of the strain magnitude. The geometric stiffness at the element level is non-symmetric, but the assembled global geometric stiffness will become symmetric as global equilibrium is approached, provided that there are no applied nodal moments and the displacement boundary conditions are conserving. A symmetrized tangent stiffness maintains quadratic convergence for refined element meshes with this formulation. (Convergence rates are discussed in Section 3.5.)

2.9.3 Consistent Symmetrizable Self-Equilibrated co-rotated formulation (CSSE).

The internal force is coerced into self-equilibrium by pre-multiplying with $\mathbf{P}^T$ and the material stiffness part of the tangent stiffness is rendered symmetric by premultiplying the internal force with $\mathbf{H}^T$:

$$\begin{aligned} \mathbf{f} &= \mathbf{T}^T\tilde{\mathbf{P}}^T\tilde{\mathbf{H}}^T\tilde{\mathbf{K}}_e\tilde{\mathbf{v}}_d \ , \\ \mathbf{K} &= \mathbf{T}^T(\tilde{\mathbf{P}}^T\tilde{\mathbf{H}}^T\tilde{\mathbf{K}}_e\tilde{\mathbf{H}}\tilde{\mathbf{P}} + \tilde{\mathbf{P}}^T\tilde{\mathbf{M}}\tilde{\mathbf{P}} - \tilde{\mathbf{F}}_{mn}\tilde{\mathbf{G}} - \tilde{\mathbf{G}}^T\tilde{\mathbf{F}}_n^T\tilde{\mathbf{P}})\mathbf{T} \ , \end{aligned} \tag{2.9.3}$$

where $\tilde{\mathbf{F}}_{nm}$ and $\tilde{\mathbf{F}}_n$ are computed according to equation (2.8.23) using $\tilde{\mathbf{f}} = \tilde{\mathbf{P}}^T\tilde{\mathbf{H}}^T\tilde{\mathbf{K}}_e\tilde{\mathbf{v}}_d$. The assembled global geometric stiffness for this formulation is symmetric as in the CSE case, and since the material stiffness is always symmetric one can expect quadratic convergence with a symmetrized tangent stiffness without the refined mesh limit of the CSE formulation. However, the restriction of no applied nodal moments and conserving boundary conditions still applies for the assembled global geometric stiffness to become symmetric at equilibrium. This is further discussed in Section 3.5.2.

2.10 Remarks on the co-rotated formulations.

This section discusses and critiques different nonlinear formulations based on the co-rotated formulation. The most common way of deriving the finite element equations in conservative problems is based on the stationary value of a discrete functional. If such a functional exists we have a variational principle. The second variation of the functional provides the incremental equation with a symmetric tangent stiffness matrix.

In a consistent co-rotated formulation the tangent stiffness is not generally symmetric. Consequently, the finite element discretization cannot be derived from a functional. This is largely due to the fact that the formulation contains rotational degrees of freedom referred to a moving reference system, which are non-integrable. The finite rigid body motions are only obtained on an element average form, not in a continuous sense. This makes the strain measure used closely linked to the discretization of a problem since the extraction of the rigid body motions needs an element mesh in order to be defined. A (possible) variational principle for this formulation is inextricably linked to the presence of a finite element mesh. In the absence of a functional, the starting point for the co-rotational formulation is the force equilibrium equations, which in a functional-based formulation appear at the first variation level.

2.10.1 Requirement for the nonlinear formulations.

It is convenient to set forward a set of requirements for geometrically nonlinear analysis with respect to which different co-rotated formulations can be evaluated. The requirements are listed below in order of increasing importance:

1. *Equilibrium.*
2. *Consistency.*
3. *Invariance.*
4. *Symmetrizability.*
5. *Element independence.*

Equilibrium: The continuum solution of a static structural problem requires that every particle be in equilibrium. On the other hand, in the finite element solution of the problem one requires that each discrete finite element be in equilibrium, while at the same time the global nodes are in equilibrium. From an equilibrium point of view the only difference between linear and geometrically nonlinear analysis is the choice of equilibrium configuration. The linear finite element method requires that the elements be in equilibrium with respect to their initial configuration C_0. The geometrically nonlinear formulation requires that elements be in equilibrium with respect to the deformed configuration C_n. By the equilibrium requirement is thus meant to what extent the finite element internal force vector $\mathbf{f}$ is in self-equilibrium with respect to the deformed element geometry C_n. As discussed in Chapter 3, this is a fundamental requirement for tracing the correct equilibrium path that satisfies the vanishing of the force residual

$$\mathbf{f}(\hat{\mathbf{v}}) - \mathbf{p}(\lambda) = \mathbf{0} \ . \tag{2.10.1}$$

Consistency: a formulation is called consistent if the tangent stiffness is the gradient of the internal forces with respect to the degrees of freedom:

$$\mathbf{K} \equiv \frac{\partial \mathbf{f}}{\partial \mathbf{v}} \ . \tag{2.10.2}$$

This requirement determines the convergence rate of an incremental/iterative solution algorithm. An inconsistent tangent stiffness may give poor convergence, but does not alter the equilibrium path since this is entirely prescribed by the equilibrium requirement. A poor tangent stiffness may cause the solution algorithm to fail completely, but most often if a solution path is found, however slowly, the solution path is the correct one. However, lack of consistency may affect the location of bifurcation (buckling) points and the branch switching

mechanism for post-buckling analysis. In other words, an inconsistent tangent stiffness matrix may locate (see) a bifurcation where equilibrium is not satisfied from the residual equation. Subsequent branch-switching will then be difficult because the corrector iterations need to "jump" to the secondary path as "seen" by the residual equation.

Invariance: this term is used to describe whether different element orientations give different results. For example, does a local element-node reordering give an altered equilibrium path or change the convergence characteristics for the analysis for an otherwise identical mesh?

The main contributor to a lack of invariance is the way the deformational displacement vector $\mathbf{v}_d$ is extracted from the total displacements, which also affects the variation of the deformational displacements with respect to the visible degrees of freedom $\mathbf{v}$;

$$\mathbf{v}_d = \mathbf{v}_d(\hat{\mathbf{v}}) \quad \text{and} \quad \delta\mathbf{v}_d = \frac{\partial \mathbf{v}_d}{\partial \mathbf{v}}\delta\mathbf{v} = \mathbf{HP}\delta\mathbf{v} \ . \tag{2.10.3}$$

In the expression for the variation of the deformational displacement vector the matrix $\mathbf{G}$, which links the variation of the rigid body rotation to that of the visible degrees of freedom, gives the best indication of a lack of invariance.

Symmetrizability: this term means that a symmetrized tangent stiffness can be used without loss of convergence rate even when the consistent tangent away from equilibrium is not symmetric. In the examples studied here this requirement was met when the material stiffness of the formulation was rendered symmetric. This is further described in Section 3.5.2.

Element independence: this term means that the formulation is unique for all elements with the same node and degrees of freedom configuration. For example: does the internal force and consistent stiffness expressions incorporate all three node shell elements with six degrees of freedoms per node?

The co-rotated formulation of Bergan et al and Rankin et al. are now reviewed with respect to these criteria.

2.10.2 The co-rotated formulation of Bergan et al.

The internal force is computed as in the C formulation in Section 2.9.1:

$$\mathbf{f} = \mathbf{T}^T \tilde{\mathbf{f}}_e = \mathbf{T}^T \tilde{\mathbf{K}}_e \tilde{\mathbf{v}}_d \ , \tag{2.10.4}$$

where $\tilde{\mathbf{K}}_e$ is computed relative to the C_{0n} reference. The internal force vector is thus in equilibrium with respect to the shadow element geometry C_{0n}, but not with respect to the deformed element geometry C_n. This approximation appears to be acceptable if the strains remain small and simplex elements such as two-node beams and three-node shell elements are used, because if so the C_{0n} and C_n configurations are guaranteed to remain close. As a refinement the work of Levold [40], who developed a co-rotated three node shell element utilizing Green-Lagrange strains that satisfied equilibrium with respect to the true deformed state C_n, should be cited.

The procedure for extracting the deformational displacement vector $\tilde{\mathbf{v}}_d$ from the total displacements satisfies the invariance criterion.

A consistent tangent stiffness for this formulation can be computed as described in Section 2.9.1, but the tangent stiffness used in Refs. [17,42,47] is usually computed as

$$\mathbf{K} = \mathbf{T}^T (\tilde{\mathbf{K}}_e + \tilde{\mathbf{K}}_G) \mathbf{T} \ , \tag{2.10.5}$$

where the geometric stiffness $\tilde{\mathbf{K}}_G$ is based on application of the principle of virtual work to membrane stresses and simplified or actual bending shape functions. This tangent stiffness is not necessarily consistent with the internal force expression of equation (2.10.4).

Bjærum [17] optimized the geometric stiffness $\tilde{\mathbf{K}}_G$ for linearized buckling analysis by using the displacement shape functions of the linear element as basis for forming the geometric stiffness. This gives very good results for linearized buckling analysis because high interpolation order of the buckling mode over the element is obtained. Sections 4.5 and 5.5 indicate that the geometric interpolation shape functions control the the rigid rotation of the element, and determine its geometric stiffness. Tuning the geometric stiffness generally results in loss of consistency.

2.10.3 The co-rotated formulation of Rankin et al.

The internal force is computed as

$$\mathbf{f} = \mathbf{T}^T \tilde{\mathbf{P}} \bar{\tilde{\mathbf{f}}}_e \ , \tag{2.10.6}$$

where $\bar{\tilde{\mathbf{f}}}_e = \tilde{\mathbf{H}}^T \tilde{\mathbf{K}}_e \tilde{\mathbf{v}}_d$ and $\tilde{\mathbf{K}}_e$ is computed relative to the C_0 reference. The deformational displacements $\mathbf{v}_d$ are extracted in a similar fashion to Bergan et al., although without using the concept of a shadow element. The tangent stiffness is computed as

$$\begin{aligned} \mathbf{K} &= \mathbf{T}^T (\bar{\tilde{\mathbf{K}}}_M + \tilde{\mathbf{K}}_{GR} + \tilde{\mathbf{K}}_{GP}) \mathbf{T} \\ &= \mathbf{T}^T (\tilde{\mathbf{P}}^T \tilde{\mathbf{K}}_e \tilde{\mathbf{P}} - \tilde{\mathbf{F}}_{nm} \tilde{\mathbf{G}} - \tilde{\mathbf{G}}^T \tilde{\mathbf{F}}_n^T \tilde{\mathbf{P}}) \mathbf{T} \ , \end{aligned} \tag{2.10.7}$$

where

$$\bar{\tilde{\mathbf{K}}}_M = \tilde{\mathbf{P}}^T \tilde{\mathbf{K}}_e \tilde{\mathbf{P}} + \tilde{\mathbf{P}}^T \tilde{\mathbf{M}} \tilde{\mathbf{P}} \tag{2.10.8}$$

and

$$\tilde{\mathbf{P}} = \mathbf{I} - \tilde{\mathbf{P}}_R \ , \tag{2.10.9}$$

$$\tilde{\mathbf{F}}_{nm} = \begin{bmatrix} \mathrm{Spin}(\tilde{\mathbf{n}}_1) \\ \mathrm{Spin}(\mathbf{m}_1) \\ \vdots \\ \mathrm{Spin}(\tilde{\mathbf{n}}_N) \\ \mathrm{Spin}(\mathbf{m}_N) \end{bmatrix} , \ \tilde{\mathbf{F}}_n = \begin{bmatrix} \mathrm{Spin}(\tilde{\mathbf{n}}_1) \\ \mathbf{0} \\ \vdots \\ \mathrm{Spin}(\tilde{\mathbf{n}}_N) \\ \mathbf{0} \end{bmatrix} \ \text{from} \ \tilde{\mathbf{f}} = \begin{bmatrix} \tilde{\mathbf{n}}_1 \\ \tilde{\mathbf{m}}_1 \\ \vdots \\ \mathbf{n}_N \\ \tilde{\mathbf{m}}_N \end{bmatrix} = \tilde{\mathbf{P}}^T \bar{\tilde{\mathbf{f}}}_e \ . \tag{2.10.10}$$

A difference between Rankin's formulation and the present one is that Rankin's projector lacks the $\mathbf{P}_T$ term and thus does not filter the rigid body translations, as can be seen by comparing equations (2.4.34) and (2.10.9). The present formulation is thus more rigorous with respect to the variation of the deformational displacement vector as $\delta\tilde{\mathbf{v}}_d = \tilde{\mathbf{H}}\tilde{\mathbf{P}}\mathbf{T}\delta\mathbf{v}$. However this difference does not affect the computations unless a linear element that is not in translational balance is used. In Rankins's formulation, the terms concerning the variation of the rotational pseudovector gradients are classified as material stiffness terms. These are called geometric stiffness terms in the current formulation since they vanish for a zero internal force or stress state.

More importantly, the expressions for filtering the deformational displacements $\tilde{\mathbf{v}}_d$ from the total displacements in Rankin's formulation is not element orientation invariant. This is further discussed in the element sections where the $\mathbf{G}$ matrices for different formulations are developed.

2.10.4 Summary of co-rotated formulations.

A summary of the co-rotated formulations considered in this work is given in Table 2.1. The table contains the formulations of Bergan et al. [17,47,42] and Nour-Omid and Rankin [46,53] as well as the formulations developed in the present work and summarized in Section 2.9.

Table 2.1. Summary of co-rotated formulations.

Formulation	S.Equil.	Consist.	Invar.	Symm.	Elem.ind.
Bergan et al.			√		
Rankin et al.	√	√		√	√
C		√	√		√
CSE	√	√	√		√
CSSE	√	√	√	√	√

The column labels in Table 2.1 denote the following. "S.Equil." indicates whether the element is in self equilibrium with respect to the deformed element configuration C_n. "Consist." means that the tangent stiffness is the $\mathbf{v}$-gradient of the element internal force. "Invar." is checked if the formulations is insensitive to choice of node numbering. "Symm." is checked if the formulations maintain quadratic convergence of a true Newton solution algorithm with a symmetrized tangent stiffness matrix. "Elem.ind." indicates whether the tangent stiffness expressions are element independent in the sense that it is common for all elements with the same node and degree-of-freedom configuration.

2.11 Evaluation of the formulation with respect to element types.

The current formulation is element independent since it does not contain any gradient of any intrinsically element dependent quantities such as the strain displacement relationship. This treatment is sufficient for elements where the restriction to small strains automatically implies that the shadow element and the deformed element configurations are close. In particular this holds for low order simplex elements such as two-node beam and three-node shell elements.

The main practical reason for limiting element independence to low-order elements is the softening effect of the nonlinear projector $\mathbf{P}$. The use of $\mathbf{P}$ to restore the correct rigid body motions, and hence equilibrium with respect

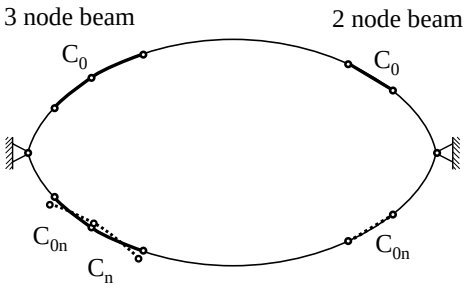

Figure 2.4. Positioning of shadow element for 2 and 3 node beam elements for snap-thru of an arch.

to the deformed element geometry, effectively reduces the eigenvalues of the material stiffness relative to the shadow element material stiffness $\mathbf{K}_e$. This softening effect becomes significant if the C_{0n} and C_n geometries are far apart.

Such softening effect can be noticeable for four-node initially-warped shell elements. Assume that the element is initially warped with "positive" warping. The element material stiffness of this initial positive warping is then $\mathbf{K}_+ = \mathbf{P}_+^T \mathbf{K}_e \mathbf{P}_+ = \mathbf{K}_e$. Give the element displacements that switch this warping to the opposite of the initial one; that is, a "negative" warping. The new element material stiffness then becomes $\mathbf{K}_- = \mathbf{P}_-^T \mathbf{K}_e \mathbf{P}_- \neq \mathbf{K}_e$ One will intuitively want the two element configurations to have the same "stiffness" in the sense of the dominant nonzero eigenvalues of the tangent stiffness matrix. But it can be shown that the eigenvalues of the projected material stiffness matrix $\mathbf{K}_-$ can be significantly lower than those of the initial stiffness matrix $\mathbf{K}_+$. If the element stiffness $\mathbf{K}_e$ is referred to the flat element projection, one will restore symmetry of $\mathbf{K}_+$ and $\mathbf{K}_-$ with respect to dominant nonzero eigenvalues, but not remove the softening effect.

This argument also carries over to higher order elements that are curved in the initial reference configuration. This is illustrated in the arch snap-through problem in Figure 2.4, which is modeled by two and tree node beam elements. The three-node beam element undergoes a significant softening effect from the projector $\mathbf{P}$ because the shadow element C_{0n} can not be closely fit to the deformed element C_n, even in the absence of large strains. The two-node beam element does not suffer from this limitation.

Chapter 3

Nonlinear Solution Algorithms.

Before the mid-1970s, geometrically nonlinear structural problems were usually treated with purely incremental methods under load control. These methods have the disadvantage of causing computed solutions to drift away from the equilibrium path. This drift error is step-size dependent and often accumulates during the analysis, thus requiring a very fine step-size for accurate analysis. This accumulated drift error can only be practically assessed by re-running the problem with different step-sizes. Furthermore, traversal of critical points is difficult or even impossible if one enforces load control, as discussed below.

These shortcomings motivated the development of incremental/ iterative methods where the increment was followed by equilibrium-correcting iterations that brings the solution back to the equilibrium path. Introduction of a corrector has the advantage that the drift error is eliminated and thus, as long as the iterative phase converges, the computed equilibrium path is independent of the increment step-size.

Geometrically non-linear structures usually reach a maximum load level. At that state the structure is unable to withstand further load increases until a significant change in geometry occurs. Such states are called *critical points*, and are generally characterized by a singular tangent stiffness matrix. Critical points may be classified into *limit* and *bifurcation* points. If the tangent stiffness is singular, but the equilibrium path is still smooth with a tangent component along the gradient of the incremental load, the critical point is a *limit point*. If the stable path after the limit point has an abrupt change in tangent direction, and that direction does not have a component along the incremental load, the critical point is called a *bifurcation point*.

A load control strategy may be able to detect a limit point but cannot generally traverse it. Traversal is often desirable to assess whether the structure has residual load carrying capabilities after what might be a localized instability. A number of methods of traversing the equilibrium path beyond limit points have been described in the literature. One can mention the method of artificial springs [56, 67], methods based on controlling the load increment with the "current stiffness parameter" and suppressing iterations around limit points [13] and the displacement control techniques first introduced by Argyris [2].

During the past 20 years important improvements have been made by allowing loads and displacements to be simultaneously varied in each incremental step. The most practically important instances of these strategies are the hyper

plane displacement control developed by Simons, Bergan and Nygård [59] and the arc-length methods originally proposed by Riks [54] and Wempner [65] and later refined by Bathe et al. [5,6], Batoz and Dhatt [8], Crisfield [20], Ramm [51] and Riks [55]. Unfortunately, none of these algorithms are best for all problems. However, the arc-length type algorithms are generally considered as the most versatile algorithms in terms of the range of problems they can solve. An arc-length type algorithm has been adopted for the present work. Two corrector strategies have been compared: the normal plane corrector of Riks and Wempner, and the orthogonal-trajectory corrector proposed by Fried [31].

3.1 Governing equations for response tracing.

The global equilibrium equations of geometric nonlinear problems can be stated as the force residual $\mathbf{r}$ being zero:

$$\mathbf{r}(\hat{\mathbf{v}}, \lambda) = \mathbf{f}(\hat{\mathbf{v}}) - \mathbf{p}(\lambda) = \mathbf{0} \quad \text{where} \quad \hat{\mathbf{v}} = \hat{\mathbf{v}}(\lambda) \; . \tag{3.1.1}$$

where $\mathbf{f}$ are the deformation-resisting internal forces, $\hat{\mathbf{v}}$ is the displacement state of the structure and $\mathbf{p}$ is the external load on the structure written as a function of a single loading parameter λ.

Since the force residual is identical zero the first derivative of equation (3.1.1) with respect to the load parameter λ must also vanish when evaluated at the equilibrium path:

$$\frac{d\mathbf{r}}{d\lambda} = \frac{\partial \mathbf{f}}{\partial \mathbf{v}} \frac{d\mathbf{v}}{d\lambda} + \frac{d\mathbf{p}}{d\lambda} = \mathbf{K} \frac{d\mathbf{v}}{d\lambda} + \frac{d\mathbf{p}}{d\lambda} = \mathbf{K}\mathbf{w} - \mathbf{q} = \mathbf{0} \; . \tag{3.1.2}$$

Here $\mathbf{K} = \partial \mathbf{f} / \partial \mathbf{v}$ is the tangent stiffness matrix introduced in Chapter 2, $\mathbf{q} = d\mathbf{p}/d\lambda$ is the incremental load vector, and $\mathbf{w} = d\mathbf{v}/d\lambda$ is the incremental velocity vector. Equation (3.1.2) is the differential equation of the equilibrium path. To trace this path numerically by an incremental method, (3.1.2) is integrated with a finite step-size:

$$\Delta \mathbf{r} = \mathbf{K}\Delta \mathbf{v} - \mathbf{q}\Delta\lambda = \Delta\lambda(\mathbf{K}\mathbf{w} - \mathbf{q}) = \mathbf{0} \; . \tag{3.1.3}$$

A unit tangent vector along the equilibrium path can be defined as

$$\bar{\mathbf{t}} = \frac{1}{f} \begin{Bmatrix} \mathbf{w} \\ 1 \end{Bmatrix} \quad \text{where} \quad f = \sqrt{1 + \mathbf{w}^T \mathbf{w}} \; . \tag{3.1.4}$$

This is illustrated in Figure 3.1. The superposed bar $(\bar{\ })$ is used to indicate a vector in the load-displacement space $(\mathbf{v}, \lambda)$.

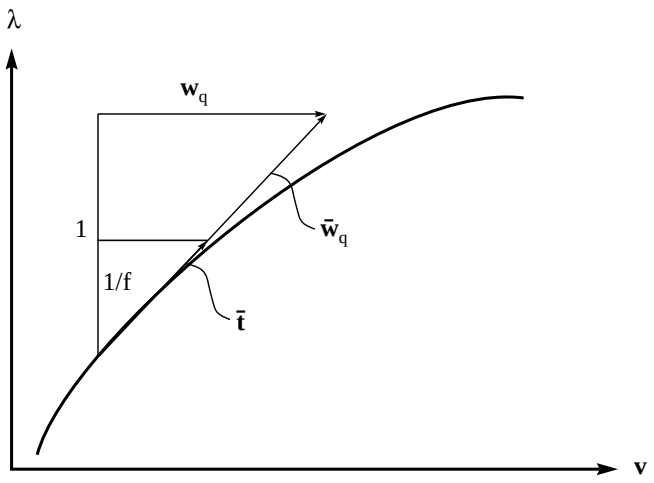

Figure 3.1. Tangent vector along an equilibrium path.

3.2 Arc-length type response tracing algorithms.

The following section develops a generalized arc-length algorithm. The algorithm is sought to be discretization independent in the sense that a mesh refinement or load scaling will not change the incremental step-sizes. The generalized arc-length algorithm includes load control and displacement control as special cases.

3.2.1 Updating the global displacement state.

The global finite displacement state for a finite element model of a structure is defined by the translational displacements and rotational orientations of all the nodes. For a node a one thus needs to update the translational displacements vector $\mathbf{v}_a$ and the rotational orientation represented by the rotation tensor $\mathbf{R}_a$. The rotation tensor $\mathbf{R}_a$ can be defined by Euler angles, Euler parameters, Rodrigues parameters or the Cayley representation. If one is not particularly concerned about memory usage for a finite element code, the tensor representation works well. It requires storage of a matrix of nine elements instead of, for instance, four Euler parameters, three pseudo-vector components, or three Euler angles. The work of Nygård [47], Mathisen [42] and Bjærum [17] has typically utilized the tensor representation of the rotational orientation, and this is the form chosen here.

The global displacement state can be thought of as a "vector" or array $\hat{\mathbf{v}}$ consisting of the nodal displacement vectors $\mathbf{v}_a$ and rotation tensors $\mathbf{R}_a$ for all the nodes of the finite element model (see Box 2.1). From the response tracing algorithms one computes a global incremental displacement vector $\Delta\mathbf{v}$ that contains incremental translations vectors $\Delta\mathbf{v}_a$ and incremental rotations

vectors $\Delta\boldsymbol{\omega}_a$ for each node a. The update of the global displacement state can be written as

$$\hat{\mathbf{v}} := \hat{\mathbf{v}} \oplus \Delta\mathbf{v} \; . \tag{3.2.1}$$

The symbol := takes the meaning of a programmers equal sign; one computes the right hand side and assigns the value to the left hand side. The symbol $\oplus$ has the meaning of a plus sign for the translational degrees of freedom where the incremental translation is added to the total displacements. For the rotational degrees of freedom $\oplus$ means that the nodal rotation vector is "added" to the rotation tensor as

$$\mathbf{R}_a := \mathbf{R}(\Delta\boldsymbol{\omega}_a)\mathbf{R}_a \; . \tag{3.2.2}$$

This updating procedure symbolized by equation (3.2.1) is described in further detail in Box 3.1.

Box 3.1. Updating the global displacement state.

The expression $\hat{\mathbf{v}} := \hat{\mathbf{v}} \oplus \Delta\mathbf{v}$ (3.2.3)
is computed as:

foreach node a do
Extract $\Delta\mathbf{v}_a$ and $\Delta\boldsymbol{\omega}_a$ from $\Delta\mathbf{v}$
Form $\mathbf{R}(\Delta\boldsymbol{\omega}_a)$ from equation (2.3.17)
Update $\mathbf{v}_a := \mathbf{v}_a + \Delta\mathbf{v}_a$
Update $\mathbf{R}_a := \mathbf{R}(\Delta\boldsymbol{\omega}_a)\mathbf{R}_a$
enddo

3.2.2 Conventional arc length algorithm.

The equilibrium path is a curve in the $N+1$ dimensional space spanned by the loading parameter λ and the N degrees of freedom vector $\mathbf{v}$. An incremental displacement vector $\Delta\mathbf{v}$ with matching load increment $\Delta\lambda$ can be written as the augmented displacement vector $\Delta\bar{\mathbf{v}}$:

$$\Delta\bar{\mathbf{v}} = \left\{ \begin{array}{c} \Delta\mathbf{v} \\ \Delta\lambda \end{array} \right\}, \tag{3.2.4}$$

where prefix Δ is used for the incremental step (or predictor step) of the arc length algorithm. For the equilibrium iterations the increment in the augmented space is written

$$\delta\bar{\mathbf{v}} = \left\{ \begin{array}{c} \delta\mathbf{v} \\ \delta\lambda \end{array} \right\}, \tag{3.2.5}$$

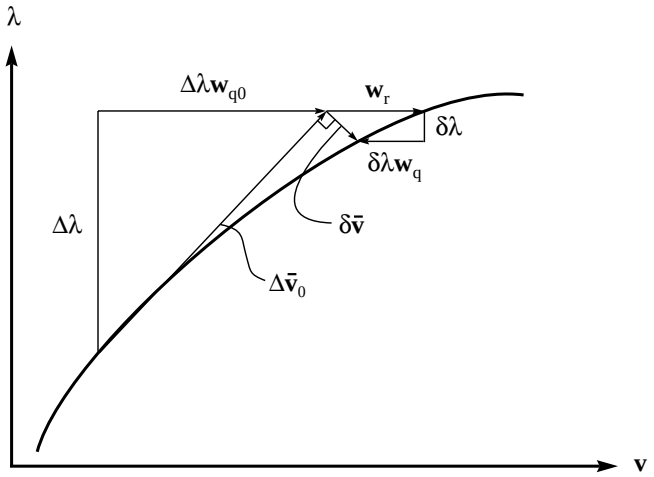

Figure 3.2. Predictor and corrector step for the normal plane method.

where prefix δ denotes corrector changes. The resulting arc length algorithm is illustrated in Box 3.2. The following sections describe the predictor step and corrector iterations in further detail.

Predictor step.
Advancing from a converged solution $(\lambda, \hat{\mathbf{v}})$ gives the incremental load solution $\mathbf{w}_{q0}$ from solving $\mathbf{K}(\hat{\mathbf{v}})\mathbf{w}_{q0} = \mathbf{q}(\lambda)$. The incremental displacement step is set to

$$\Delta\bar{\mathbf{v}} = \Delta\lambda\bar{\mathbf{w}}_{q0} = \Delta\lambda \left\{ \begin{array}{c} \mathbf{w}_{q0} \\ 1 \end{array} \right\}. \tag{3.2.6}$$

By requiring the step in the load-displacement space to have a prescribed length Δs the vector length definition

$$\Delta s = \sqrt{\Delta\bar{\mathbf{v}}^T \Delta\bar{\mathbf{v}}} \tag{3.2.7}$$

gives

$$\Delta\lambda = \pm \frac{\Delta s}{\sqrt{1 + \mathbf{w}_{q0}^T \mathbf{w}_{q0}}} \,. \tag{3.2.8}$$

The sign for $\Delta\lambda$ can be determined by assuming that the equilibrium path is smooth, and that in an "advancing" solution process the present predictor step must form a positive vector product with the previous predictor step.

Normal plane iterations.
The normal plane method was developed by Riks [54,55] and Wempner [65] and is often referred to as the Riks-Wempner method. Here the name "normal plane iterations" is adopted due to its more descriptive character.

The corrector steps should reach back to the equilibrium path as quickly as possible. Because the predictor step direction $\bar{\mathbf{w}}_{q0}$ is a good approximation of the tangent direction of the equilibrium path, in the absence of further information one may assume that the shortest distance to the equilibrium path lies in a direction orthogonal to the predictor step, as depicted in Figure 3.2. Because the normal plane to the predictor step is a hyperplane, subsequent corrector iteration are forced to lie on that surface. This is the rationale behind the normal plane iteration method. The iteration displacement vector can be written as

$$\delta\bar{\mathbf{v}} = \left\{ \begin{array}{c} \delta\mathbf{v} \\ \delta\lambda \end{array} \right\}. \tag{3.2.9}$$

Note that the symbol δ is here used to denote a corrector iteration increment, whereas Δ is used for a predictor step increment, see (3.2.8) .

To force $\delta\bar{\mathbf{v}}$ onto the normal plane, it is decomposed into two contributions, one due to the residual solution $\mathbf{w}$ and the ohter due to the incremental load solution $\mathbf{w}_q$ from $\mathbf{K}(\hat{\mathbf{v}})\mathbf{w}_r = \mathbf{r}(\hat{\mathbf{v}}, \lambda)$ and $\mathbf{K}(\hat{\mathbf{v}})\mathbf{w}_q = \mathbf{q}(\lambda)$ respectively. The combined solution is

$$\delta\bar{\mathbf{v}} = \bar{\mathbf{w}}_r + \delta\lambda\bar{\mathbf{w}}_q = \left\{ \begin{array}{c} \mathbf{w}_r \\ 0 \end{array} \right\} + \delta\lambda \left\{ \begin{array}{c} \mathbf{w}_q \\ 1 \end{array} \right\}. \tag{3.2.10}$$

Scaling the load increment $\delta\lambda$ so that $\delta\bar{\mathbf{v}}$ stays in the normal-plane gives

$$\delta\lambda = -\frac{\mathbf{w}_{q0}^T\mathbf{w}_r}{(1 + \mathbf{w}_{q0}^T\mathbf{w}_q)} , \tag{3.2.11}$$

which satisfies the constraint $\bar{\mathbf{w}}_{q0}^T\delta\bar{\mathbf{v}} = 0$.

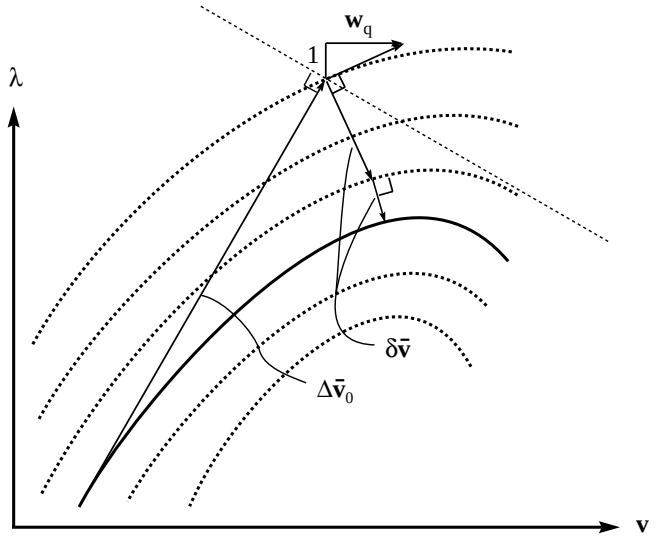

Figure 3.3. Corrector iterations for the orthogonal trajectory method. Dotted line illustrates that normal plane iterations may miss a sharp turn of the equilibrium path.

Orthogonal trajectory iterations.
The orthogonal trajectory iteration method was developed by Fried [31] as a way of inducing convergence to an equilibrium state from an arbitrary starting configuration. In the present work the method is use in the correction phase of an incremental/iterative solution process.

One requires the combined iterations increment of equation (3.2.10) to be orthogonal to the incremental flow at a current (non-equilibrium) configuration, as illustrated in Figure 3.3. This orthogonality condition gives the scaling of the load increment as

$$\delta\lambda = -\frac{\mathbf{w}_q^T \mathbf{w}_r}{(1 + \mathbf{w}_q^T \mathbf{w}_q)} \ , \tag{3.2.12}$$

from $\bar{\mathbf{w}}_q^T \delta\bar{\mathbf{v}} = 0$. Note the similarities between equation (3.2.11) and (3.2.12). Figure 3.3 also depicts the hyperplane of the normal plane iterations, which in the illustrated case "miss" the equilibrium path. The present numerical experiments have shown that the orthogonal trajectory iteration method is more robust then the normal plane iteration method. More specifically, in most of the nonlinear problems presented in Chapter 8 it allowed predictor stepsizes of up to 5 times those permitted by the normal plane corrector.

Box 3.2. Arc-length type algorithm.

Predictor step with arc length Δs:

Solve $\mathbf{K}(\hat{\mathbf{v}})\mathbf{w}_{q0} = \mathbf{q}$ with respect to $\mathbf{w}_{q0}$

Set $f = \sqrt{1 + \mathbf{w}_{q0}^T \mathbf{w}_{q0}}$ (3.2.13)

If $\mathbf{w}_{q0}^T \mathbf{v}_0 > 1 \quad \Delta\lambda = \dfrac{\Delta s}{f}$

else $\Delta\lambda = -\dfrac{\Delta s}{f}$

Set $\mathbf{v}_0 = \Delta\lambda \mathbf{w}_{q0}$

Update $\lambda := \lambda + \Delta\lambda$ and $\hat{\mathbf{v}} := \hat{\mathbf{v}} \oplus \Delta\lambda \mathbf{w}_q$

Corrector iterations:

Do $k = 1, \ldots$

Solve $\mathbf{K}(\hat{\mathbf{v}})\mathbf{w}_q = \mathbf{q}$ for $\mathbf{w}_q$
and $\mathbf{K}(\hat{\mathbf{v}})\mathbf{w}_r = -\mathbf{r}(\hat{\mathbf{v}}, \lambda)$ for $\mathbf{w}_r$

Solve $\delta\lambda$ from (3.2.11), (3.2.12) or (3.2.22)

Update $\lambda := \lambda + \delta\lambda$ and $\hat{\mathbf{v}} := \hat{\mathbf{v}} \oplus (\mathbf{w}_r + \delta\lambda \mathbf{w}_q)$

until $\|\mathbf{r}(\hat{\mathbf{v}}, \lambda)\| < \varepsilon$

where ε is a pre-selected convergence criterion.

3.2.3 Discretization independent arc-length definition.

The main parameters controlling a path following algorithm are the step size Δs and the convergence criterion ϵ. Although it is impossible to make the optimal values of these parameters problem independent, one should strive to make them as insensitive to the actual discretization as possible. In particular:

- A mesh refinement should not influence the actual displacement size that matches a prescribed arc-length Δs. Nor should a mesh refinement make a convergence criterion ϵ more strict or relaxed with respect to the actual corrector iterations.
- A scaling of the actual applied loads (in order to get the target λ at a desired value) should not change the actual step-size of the path following algorithm.

To make the arc-length algorithm as discretization independent as possible one needs to change the definition of the arc-length and the convergence criterion of the traditional arc-length method.

Traditionally, the arc-length Δs is defined in the load-parameter and displacement vector space $(\lambda, \mathbf{v})$ as

$$\Delta s = \sqrt{\Delta\lambda^2 + \mathbf{v}^T\mathbf{v}} = \Delta\lambda\sqrt{1 + \mathbf{w}^T\mathbf{w}}\,. \tag{3.2.14}$$

The key difficulty with this definition is the mismatch of physical quantities: $\Delta\lambda$ and $\mathbf{v}$ have different physical dimensions, thus (3.2.14) adds apples and oranges. Equation (3.2.14) gives the increment in the load-parameter $\Delta\lambda$, the displacement increment $\Delta\mathbf{v}$ and the force increment $\Delta\mathbf{p}$ as

$$\Delta\lambda = \frac{\Delta s}{\sqrt{1 + \mathbf{w}^T\mathbf{w}}}\,, \quad \Delta\mathbf{v} = \Delta\lambda\mathbf{w} \quad \text{and} \quad \Delta\mathbf{p} = \Delta\lambda\mathbf{q}\,. \tag{3.2.15}$$

Unfortunately this arc-length definition gives a load increment $\Delta\mathbf{p} = \Delta\lambda\mathbf{q}$ that is dependent on the definition of $\mathbf{q}$, since the incremental loading parameter $\Delta\lambda$ is independent of the incremental load $\mathbf{q}$. A scaling of the incremental load as $\mathbf{q}_b = b\mathbf{q}_0$ will give proportional increment in the step size of the predictor step since the actual load increment has been scaled, even though the loading parameter increment and prescribed arc length are unchanged. This is not desirable. One wants a path-following algorithm where the step-size and optimal algorithm parameters depend only on the physical characteristics of the problem, rather than modeling of the problem.

A better choice for the load increment is $\Delta\bar{\lambda} = \Delta\lambda\, l_q$, where l_q is the norm of the incremental load $\mathbf{q}$. This definition of the loading parameter gives an actual load increment $\Delta\mathbf{p}$ that is independent of the scaling of the incremental load $\mathbf{q}$. Furthermore, if $\mathbf{q}$ changes in response to a change in the number of elements, as happens in mesh refinement or mesh adaptation, l_q still reflects the resultant force.

The norm of the incremental displacements as given by $\sqrt{\mathbf{w}^T\mathbf{w}}$ does not give a good measure of the physical incremental displacements of a structure. This quantity typically grows as the mesh is refined even if the structural displacement remain the same. The norm of the incremental displacements should thus be scaled with $\frac{1}{n}$ where n denotes the number of nodes in the element mesh.

This suggests the following discretization "independent" arc-length definition

$$\Delta s = \sqrt{\Delta\bar{\lambda}^2 + \frac{1}{n}\mathbf{v}^T\mathbf{v}} = \Delta\lambda\sqrt{l_q^2 + \frac{1}{n}\mathbf{w}^T\mathbf{w}}\,, \tag{3.2.16}$$

which gives for the corresponding load increment $\Delta\lambda$:

$$\Delta\lambda = \frac{\Delta s}{\sqrt{l_q^2 + \frac{1}{n}\mathbf{w}^T\mathbf{w}}} \quad \text{and} \quad \Delta\mathbf{p} = \Delta\lambda\mathbf{q}\,. \tag{3.2.17}$$

3.2.4 Convergence criterion for corrector iterations.

The convergence criterion for the corrector phase is of importance for several reasons. If the convergence threshold is too strict computational time is wasted. If the threshold is overly lenient the solution process may not give sufficient accuracy, or even induce divergence because of large equilibrium drifts. The convergence of the corrector iterations is usually monitored through the Euclidean norm of the residual $\mathbf{r}$, in which case the acceptance test is

$$\sqrt{\mathbf{r}^T\mathbf{r}} = \sqrt{\sum_{i=1}^{n} r_i^2} < \epsilon_r \ , \tag{3.2.18}$$

or the Euclidean norm of the displacement correction:

$$\sqrt{\delta\mathbf{v}^T\delta\mathbf{v}} = \sqrt{\sum_{i=1}^{n} \delta r_i^2} < n\epsilon_v \ . \tag{3.2.19}$$

Note that the convergence criterion for the incremental displacements is multiplied by the number of nodes n in order to make it approximately mesh independent.

Another popular convergence check relies on the "residual energy" test used by Stanley [61] and Mathisen [42]

$$\delta\mathbf{v}^T\mathbf{r} = \sum_{i=1}^{n} \delta v_i r_i < \epsilon_e \ . \tag{3.2.20}$$

This convergence criterion has the advantage that it adopts consistent unit of energy for both rotational and translational degrees of freedom. It also represents a balancing act between the residual norm and the displacement norm. For instance in the vicinity of critical points the residual can be almost zero whereas the incremental displacements are still fairly large because of the near-singularity of the tangent stiffness.

3.2.5 Generalized normal-plane algorithm.

Scaling the loading parameter λ with a user defined factor f_λ and the displacements in an entry by entry fashion with the vector $\mathbf{f}_v$ gives a generalized arc-length definition which includes the load control, displacement control and state control strategies as special cases.

The modeling independent generalized arc-length algorithm is obtained from Box 3.2 by substituting the predictor step in equation (3.2.13) with

$$f = \sqrt{f_\lambda l_q^2 + \frac{1}{n}\mathbf{w}_{fq0}^T \mathbf{w}_{fq0}}\ , \tag{3.2.21}$$

where $\mathbf{w}_{fq0} = \mathbf{f}_v * \mathbf{w}_{q0}$ is defined in equation (3.2.23) below. The corrector iteration is given by

$$\delta\lambda = -\frac{\frac{1}{n}\mathbf{w}_{fq0}^T \mathbf{w}_{fr}}{(f_\lambda l_q^2 + \frac{1}{n}\mathbf{w}_{fq0}^T \mathbf{w}_{fq})}\ . \tag{3.2.22}$$

The symbol $*$ denotes an entry by entry multiplication of two vectors:

$$\mathbf{w}_{fq} = \mathbf{f}_v * \mathbf{w}_q = \left\{ \begin{array}{c} f_1 w_{q1} \\ \vdots \\ f_i w_{qi} \\ \vdots \\ f_n w_{qn} \end{array} \right\}. \tag{3.2.23}$$

Through particular choices for the load scaling f_λ and displacement scaling $\mathbf{f}_v$ several special control strategies can be recovered.

Load control: Setting $f_\lambda = 1/l_q^2$ and $\mathbf{f}_v = \mathbf{0}$ gives the load control algorithm:

$$\Delta\lambda = \Delta s \quad \text{and} \quad \delta\lambda = 0\ . \tag{3.2.24}$$

Displacement control: By setting $f_\lambda = 0$, $f_i = \sqrt{n}$ at degree of freedom i and $f_j = 0$ for all degrees of freedom $j \neq i$, one obtains the displacement control through the i-th degree of freedom:

$$\Delta\lambda = \frac{\Delta s}{w_{q_i}} \quad \text{and} \quad \delta\lambda = \frac{w_{q0_i} w_{ri}}{w_{q0_i} w_{q_i}}\ . \tag{3.2.25}$$

State control: Setting $f_\lambda = 0$ and $\mathbf{f} = \sqrt{n}\mathbf{I}$ gives state control where the the Euclidian norm of the incremental displacements is constrained to be Δs:

$$\Delta\lambda = \frac{\Delta s}{\sqrt{\mathbf{w}_{q0}^T \mathbf{w}_{q0}}} \quad \text{and} \quad \delta\lambda = \frac{\mathbf{w}_{q0}^T \mathbf{w}_r}{\mathbf{w}_{q0} \mathbf{w}_q}\ . \tag{3.2.26}$$

3.3 Linearized buckling analysis.

The generalized eigenvalue problem arising from a linearized buckling analysis can be expressed as

$$(\mathbf{K}_0 + \lambda_\phi \mathbf{K}_G)\boldsymbol{\phi} = \mathbf{0} \ , \tag{3.3.1}$$

where $\mathbf{K}_0$ is the initial stiffness of the structure and $\mathbf{K}_G$ is the rate of change of the stiffness with respect to the loading parameter λ as

$$\mathbf{K}_G = \frac{d\mathbf{K}}{d\lambda}\Big|_{\hat{\mathbf{v}}=\hat{\mathbf{0}}} \ . \tag{3.3.2}$$

The critical load of the structure is then given by the eigenvalue λ_ϕ closest to zero with the associated buckling mode given by the eigenvector $\boldsymbol{\phi}$.

3.3.1 Linearizing about the initial state.

The linearized buckling analysis predicts the critical buckling load with respect to the initial geometry of the structure. The tangent stiffness for a structure is in general given as a function of the present displacement state $\hat{\mathbf{v}}$ as $\mathbf{K}(\hat{\mathbf{v}})$ rather than as a function of the load level directly. This has to be considered when computing the stiffnesses $\mathbf{K}_0$ and $\mathbf{K}_G$ in equation (3.3.1) . One uses $\mathbf{K}_0$ as the initial stiffness for the structure:

$$\mathbf{K}_0 = \mathbf{K}(\hat{\mathbf{0}}) \ . \tag{3.3.3}$$

The gradient of the tangent stiffness should be computed according to the initial geometry of the structure with the element internal force computed according to linear theory. This is difficult with a nonlinear analysis code. Instead the rate of change of the stiffness is based on the secant formula applied between $(\lambda = 0, \hat{\mathbf{v}} = \hat{\mathbf{0}})$ and a small load increment and its associated converged solution $(\lambda_\Delta, \hat{\mathbf{v}}_\Delta)$ as

$$\mathbf{K}_G = \frac{1}{\lambda_\Delta}(\mathbf{K}(\hat{\mathbf{v}}_\Delta) - \mathbf{K}(\hat{\mathbf{0}})) \ . \tag{3.3.4}$$

This secant stiffness will usually deviate slightly from the true tangent stiffness at $\lambda = 0$. In order to minimize this effect one will usually ensure that λ_Δ is small compared to the computed critical load λ_{cr} by doing an *a posteriori* check of the ratio between λ_Δ and λ_{cr}: for instance $\lambda_\Delta < 0.01\,\lambda_{cr}$.

3.3.2 Generalized linearization.

As an extension of the foregoing technique, equation (3.3.1) can be solved using two points on the equilibrium path to define the initial and secant stiffness. If the two points are given by the load level λ and converged solutions $\hat{\mathbf{v}}$ as $(\lambda_1, \hat{\mathbf{v}}_1)$ and $(\lambda_2, \hat{\mathbf{v}}_2)$ this linearization gives

$$\begin{aligned} \mathbf{K}_0 &= \mathbf{K}(\hat{\mathbf{v}}_1) \ , \\ \mathbf{K}_G &= \frac{1}{(\lambda_2 - \lambda_1)} (\mathbf{K}(\hat{\mathbf{v}}_2) - \mathbf{K}(\hat{\mathbf{v}}_1)) \ . \end{aligned} \tag{3.3.5}$$

The critical load is then

$$\lambda_{cr} = \lambda_1 + \lambda_\phi \ , \tag{3.3.6}$$

with the associated buckling mode given by the eigenvector $\boldsymbol{\phi}$.

3.3.3 Solving the eigenvalue problem.

One is usually only interested in either the lowest, or a few of the lowest eigenvalues and associated eigenvectors when solving the eigenvalue problem in equation (3.3.1). Computing all the eigenvalues and eigenvectors would be computationally costly and not add knowledge because the higher eigenvalues and eigenvectors have no physical meaning in terms of the actual structure. Most eigenvalue solvers return the highest, or a set of the highest, eigenvalues and eigenvectors rather than the full set of eigenvalues and eigenvectors. In order to utilize these methods one has to rewrite the problem as

$$(\mathbf{K}_G + \xi \mathbf{K}_0)\boldsymbol{\phi} = \mathbf{0} \quad \text{where} \quad \xi = \frac{1}{\lambda_\phi} \ . \tag{3.3.7}$$

Solving this will return the highest ξ which corresponds to the lowest λ_ϕ. If this technique is used, care must be taken since $\mathbf{K}_0$ is in general positive definite whereas $\mathbf{K}_G$ is not.

Box 3.3. Inverse power-iterations for the buckling eigenproblem.

Pick random $\boldsymbol{\phi}^1$

Do $k = 1, \ldots$

Multiply $\quad \mathbf{y} = \mathbf{K}_G \boldsymbol{\phi}^k$

Solve $\quad \bar{\mathbf{K}}_0 \boldsymbol{\phi}^{k+1} = \mathbf{y} \quad$ with respect to $\boldsymbol{\phi}^{k+1}$

Scale $\quad \boldsymbol{\phi}^{k+1} = \dfrac{1}{\xi} \boldsymbol{\phi}^{k+1} \quad$ where $\quad |\xi| = \|\boldsymbol{\phi}^{k+1}\|_\infty$

until $\quad |\phi_i^{k+1} - \phi_i^k| < \varepsilon \quad$ for every $i = 1, \ldots, n$

where ε is a pre-selected convergence criterion.

Solving the eigenvalue problem using inverse power-iterations.
If $\boldsymbol{\phi}$ is an eigenvector of the above problem, $\boldsymbol{\phi}$ will also be an eigenvector of the shifted eigenvalue problem

$$(\bar{\mathbf{K}}_0 + \bar{\lambda} \mathbf{K}_G) \boldsymbol{\phi} = \mathbf{0} \,, \tag{3.3.8}$$

where

$$\bar{\lambda} = (\lambda - \mu) \qquad \text{and} \qquad \bar{\mathbf{K}}_0 = (\mathbf{K}_0 + \mu \mathbf{K}_G) \,. \tag{3.3.9}$$

The inverse power-iteration algorithm applied to this shifted eigenvalue problem is summarized in Box 3.3.

The best approximation eigenvalue of the original eigenvalue problem in equation (3.3.1) can then be retrieved as the Rayleigh quotient:

$$\lambda = -\frac{\boldsymbol{\phi}^T \mathbf{K}_0 \boldsymbol{\phi}}{\boldsymbol{\phi}^T \mathbf{K}_G \boldsymbol{\phi}} \qquad \text{where} \qquad \boldsymbol{\phi} = \boldsymbol{\phi}^{k+1} \,, \tag{3.3.10}$$

By using the initial shift $\mu = 0$ the algorithm can be made to converge to the lowest eigenvalue and associated eigenvector. A shift can also be performed after a certain number of iterations in order to speed up convergence of the algorithm. If one has a good initial guess of the location of a particular eigenvalue, the algorithm can be targeted to find the eigenvalue and eigenvector closest to this guess by performing the shift $\mu = \lambda_{guess}$ initially.

3.4 Handling of critical points.

Successfully dealing with a bifurcation point when traversing an equilibrium path can be split into two sub-problems: *detecting* the bifurcation point and *switching* to the secondary path.

3.4.1 Detecting a bifurcation point.

Using the factorization $\mathbf{K} = \mathbf{L}\mathbf{D}\mathbf{L}^T$ when solving for the displacement increments when traversing the equilibrium path gives a simple way to check for critical points. It is known that the number of negative elements in the diagonal matrix $\mathbf{D}$ is equal to number of negative eigenvalues of $\mathbf{K}$. By monitoring the number of negative diagonal elements one can detect that a critical point has been passed if the number of negative diagonal-elements has changed since the last converged solution. If the previous converged solution is $(\lambda_1, \hat{\mathbf{v}}_1)$ and the current converged solution is $(\lambda_2, \hat{\mathbf{v}}_2)$, there will exist a point $(\lambda_\phi, \hat{\mathbf{v}}_\phi)$ on the equilibrium path where where the tangent stiffness has a null-eigenvector $\boldsymbol{\phi}$ as

$$\mathbf{K}(\hat{\mathbf{v}}_\phi)\boldsymbol{\phi} = \mathbf{0} \quad \text{and} \quad \boldsymbol{\phi}^T\mathbf{K}(\hat{\mathbf{v}}_\phi) = \mathbf{0}^T \,. \tag{3.4.1}$$

Finding the exact position of the critical point $(\lambda_\phi, \mathbf{v}_\phi)$ is often difficult, because the tangent stiffness becomes ill conditioned as the critical point is approached. An approximation of the eigenvalue λ_ϕ and the buckling mode $\boldsymbol{\phi}$ can be obtained by solving the secant-linearized eigenvalue problem between $(\lambda_1, \hat{\mathbf{v}}_1)$ and $(\lambda_2, \hat{\mathbf{v}}_2)$, as described in Section 3.3.2:

$$(\mathbf{K}_0 + \Delta\lambda\mathbf{K}_G)\boldsymbol{\phi} = \mathbf{0} \,,$$

where

$$\mathbf{K}_0 = \mathbf{K}(\hat{\mathbf{v}}_1), \quad \mathbf{K}_G = \frac{1}{(\lambda_2 - \lambda_1)}(\mathbf{K}(\hat{\mathbf{v}}_2) - \mathbf{K}(\hat{\mathbf{v}}_1)) \,, \tag{3.4.2}$$

with respect to the eigenvector $\boldsymbol{\phi}$ and $\Delta\lambda$. The critical load is given by

$$\lambda_\phi = \lambda_1 + \Delta\lambda \,. \tag{3.4.3}$$

Following detection one must determine whether the critical point is a *limit point* or a *bifurcation point*. By pre-multiplying equation (3.1.2) with $\boldsymbol{\phi}^T$ and using equation (3.4.1) one gets

$$\boldsymbol{\phi}^T\mathbf{q}\,\Delta\lambda = 0 \,. \tag{3.4.4}$$

This relation can be satisfied in two ways. If $\boldsymbol{\phi}^T\mathbf{q} \neq 0$ we must have $\Delta\lambda = 0$, which signals a limit point. On the other hand, if $\boldsymbol{\phi}^T\mathbf{q} = 0$ $\Delta\lambda$ can be arbitrary and we have a bifurcation point.

$$\begin{aligned} \boldsymbol{\phi}^T\mathbf{q} = 0 \;:&\quad \textit{Bifurcation point} \\ \boldsymbol{\phi}^T\mathbf{q} \neq 0 \;:&\quad \textit{Limit point} \end{aligned} \tag{3.4.5}$$

Numerically, $\boldsymbol{\phi}^T\mathbf{q}$ is not likely to be exactly zero. In order to better judge the numerical value of the product it is recommended to use the normalized vectors $\boldsymbol{\phi}$ and $\mathbf{q}$ for the vector-product, and compare to a small value

$$\frac{\boldsymbol{\phi}^T\mathbf{q}}{\|\boldsymbol{\phi}\|\|\mathbf{q}\|} < \epsilon \,, \tag{3.4.6}$$

where ϵ is in the order of 10^{-3}. The left side of equation (3.4.6) can be recognized as the cosine of the angle between the vectors $\boldsymbol{\phi}$ and $\mathbf{q}$. In general ϵ should be a solver input since a large step-size will usually give less accurate prediction of the eigenvector and thus higher value for $\cos(\boldsymbol{\phi}, \mathbf{q})$.

If one has determined the critical point to be a limit point, no branch switching is necessary. The arc-length algorithm will continue along the primary path automatically. In the case of the critical point being a bifurcation point additional operations are needed to effect the so-called "branch-switching", in which one arrives at the bifurcation point along one branch and exits along another branch.

It should be noted that checking whether the critical point is a bifurcation point by computing the eigenvector $\boldsymbol{\phi}$ and checking orthogonality with respect to the incremental load $\mathbf{q}$ is time consuming. When the critical point is a limit point neither the eigenvalue λ_ϕ or the eigenvector $\boldsymbol{\phi}$ is needed in order to continue to traverse along the equilibrium path. Bjærum [17] lists several conditions where the critical point can be flagged as a limit point without computing λ_ϕ or $\boldsymbol{\phi}$. These conditions are based on sign changes in the current stiffness parameter [13] and the last load increment. These methods are time saving, but not fully robust. An example where this strategy fails is when a bifurcation point and a limit point are close together and both lie within the bracket of the two last solutions.

3.4.2 A simple branch switching procedure.

Suppose that a bifurcation point has been detected between two converged solutions $(\lambda_1, \hat{\mathbf{v}}_1)$ and $(\lambda_2, \hat{\mathbf{v}}_2)$, with estimated eigenvalue λ_ϕ and eigenvector $\boldsymbol{\phi}$. A branch switching to the secondary path can then be performed by doing a predictor-step from $(\lambda_1, \hat{\mathbf{v}}_1)$ to an estimated point on the secondary path $(\lambda_\phi, \hat{\mathbf{v}}_1 \oplus \Delta\mathbf{v})$ by setting

$$\Delta\mathbf{v} = \frac{(\lambda_\phi - \lambda_1)}{(\lambda_2 - \lambda_1)}\mathbf{v}_s + f\frac{\|\mathbf{v}_s\|}{\|\boldsymbol{\phi}\|}\boldsymbol{\phi} \,. \tag{3.4.7}$$

The factor f is used to scale the step onto the secondary path. $f = 1$ gives a step along the secondary path equal to the length of the secant vector $\mathbf{v}_s$.

Care has to be taken so that the corrector iterations do not converge back to the primary path. This "switchback" can be avoided by using the normal plane iterations and ensuring that the augmented normal plane vector $\bar{\mathbf{v}}_n$ is perpendicular to the augmented secant vector $\bar{\mathbf{v}}_s$. When using the normal vector as a linear combination of the eigenvector and the secant vector

$$\bar{\mathbf{v}}_n = \bar{\boldsymbol{\phi}} + \beta \bar{\mathbf{v}}_s = \left\{ \begin{array}{c} \boldsymbol{\phi} \\ 0 \end{array} \right\} + \beta \left\{ \begin{array}{c} \mathbf{v}_s \\ \Delta\lambda_s \end{array} \right\} = \left\{ \begin{array}{c} \mathbf{v}_n \\ \Delta\lambda_n \end{array} \right\}, \tag{3.4.8}$$

the orthogonality condition $\bar{\mathbf{v}}_s^T \bar{\mathbf{v}}_n = 0$ gives

$$\beta = -\frac{\mathbf{v}_s^T \boldsymbol{\phi}}{\Delta\lambda_s^2 + \mathbf{v}_s^T \mathbf{v}_s} \ . \tag{3.4.9}$$

Setting the corrector increment equal to a linear combination of the residual solution $\bar{\mathbf{v}}_r$ and the the incremental load solution $\bar{\mathbf{v}}_q$ as

$$\delta\bar{\mathbf{v}} = \bar{\mathbf{w}}_r + \bar{\mathbf{v}}_q = \left\{ \begin{array}{c} \mathbf{w}_r \\ 0 \end{array} \right\} + \delta\lambda \left\{ \begin{array}{c} \mathbf{w}_q \\ 1 \end{array} \right\}, \tag{3.4.10}$$

the normal plane orthogonality condition $\bar{\mathbf{v}}_n^T \delta\bar{\mathbf{v}} = 0$ gives

$$\delta\lambda = -\frac{\mathbf{v}_n^T \mathbf{w}_r}{\Delta\lambda_n + \mathbf{v}_n^T \mathbf{w}_q} \ . \tag{3.4.11}$$

Note that equation (3.4.11) allows $\Delta\lambda_n$ to be zero (which is often the case) whereas equation (3.2.11) can not handle this unless $\mathbf{w}_{q0}$ is an infinity vector.

This procedure is attractive due to its simplicity, and appears to be sufficient for symmetric bifurcation. For more complex bifurcation points a branch switching algorithm that utilizes the higher order derivatives of the equilibrium path is probably necessary. With non-symmetric bifurcation one also needs a criterion for picking the branch direction with the lowest energy. This is can be done by doing a trial step in each direction and comparing the energy of each direction, but is not rigorously possible unless an energy functional exists. This procedure has not been implemented in the present investigation.

3.5 Convergence of response tracing algorithms.

The convergence rate of the corrector phase of a true-Newton nonlinear solution algorithm can indicate whether the tangent stiffness matrix is consistent. This rate can also quantify what is lost when a symmetrized tangent stiffness is used rather than a consistent nonsymmetric stiffness. True Newton correctors are known to have ultimate quadratic convergence if consistency with the residual is enforced.

3.5.1 Convergence rate.

Suppose that quantity v gets computed as a sequence of approximants v_n. The error of the approximant as a function of the iteration count n is then $\epsilon_n = v_n - v$. The series of solutions v_n is said to converge to v at rate p if

$$\epsilon_n = C\,\epsilon_{n-1}^p \quad \text{as} \quad \epsilon_n \to 0\,, \tag{3.5.1}$$

where C is a bounded constant. If $p = 1$ and $C \in \langle 0, 1\rangle$ one is has linear convergence. ($p = 1$ and $C > 1$ gives divergence since the error is increasing). Linear convergence adds significant digits at a constant rate with respect to n. If $p > 1$ the convergence is said to be superlinear. This adds number of significant digits at an increasing rate as the iterations progress. Quadratic convergence is given by $p = 2$ and the number of significant digits will asymptotically double at each iteration. Due to their asymptotic nature these convergence rates are measured and obtained as one gets near the solution.

Two value convergence rate indicators.
Assuming one has the error ϵ at step n and $n-1$ the convergence rate can be evaluated by computing

$$C_n = \frac{\epsilon_n}{\epsilon_{n-1}} \quad \text{from} \quad \epsilon_n = C_n\,\epsilon_{n-1}\,. \tag{3.5.2}$$

Linear convergence can be diagnosed as C_n remains approximately constant as the exact solution is approached (eventually round off will mask this effect). If C_n decreases one has superlinear convergence.

Similarly, if one computes

$$C_n = \frac{\epsilon_n}{\epsilon_{n-1}^2} \quad \text{from} \quad \epsilon_n = C\,\epsilon_{n-1}^2\,. \tag{3.5.3}$$

and finds that c_n is increasing with n one has sub-quadratic convergence.

A three value convergence rate estimator.

The concept behind Richardson's extrapolation [18] can be used to obtain an estimate of the convergence rate based on three consecutive error values ϵ_n, ϵ_{n-1} and ϵ_{n-2}. Assume that the convergence rate is given by the two equations

$$\epsilon_n = C\,\epsilon_{n-1}^p \quad \text{and} \quad \epsilon_{n-1} = C\,\epsilon_{n-2}^p\ . \tag{3.5.4}$$

By taking the natural log of each side of the equations and subtracting the second equation from the first one obtains

$$p = \frac{\ln\epsilon_n - \ln\epsilon_{n-1}}{\ln\epsilon_{n-1} - \ln\epsilon_{n-2}} = \frac{\ln(\frac{\epsilon_n}{\epsilon_{n-1}})}{\ln(\frac{\epsilon_{n-1}}{\epsilon_{n-2}})}\ . \tag{3.5.5}$$

This estimator can be used from iteration $n = 3$ and on to give an estimate of the convergence rate of an algorithm.

The Euclidian norm of the force residual $\mathbf{r}$ is used to assess the convergence rate of the present formulations and algorithms:

$$e_r = \|\mathbf{r}\| = \sqrt{\mathbf{r}^T\mathbf{r}}\ . \tag{3.5.6}$$

The "exact" value of this norm is zero when the solution process has converged. This gives the norm of the residual as an error measure directly. The convergence rate p has been determined from equation (3.5.5) , and based on the asymptotic value of p one classifies:

$$\begin{aligned} &\textit{Linear convergence} &&: \quad p \in [1.0, 1.1\rangle \\ &\textit{Superlinear convergence} &&: \quad p \in [1.1, 1.8] \\ &\textit{Quadratic convergence} &&: \quad p > 1.8 \end{aligned} \tag{3.5.7}$$

3.5.2 Expected convergence rates.

Quadratic convergence of a true Newton corrector can be expected the global tangent stiffness matrix is consistent. Furthermore, the use of a symmetrized tangent stiffness will still give quadratic convergence if the nonsymmetric stiffness is vanishing at the same rate as the residual, as stated in the following theorem proven by Nour-Omid and Rankin [46]:

Theorem. *Ignoring the antisymmetric part of the tangent matrix when solving the linearized system in a Newton-Raphson type algorithm results in a quadratic rate of convergence if*

$$\|\mathbf{K}_i^A\| \leq \alpha \|\mathbf{r}(\hat{\mathbf{v}}_i)\| \,, \tag{3.5.8}$$

where α is a constant.

Here i is the iteration count, $\mathbf{K}^A$ is the anti-symmetric part of the tangent stiffness matrix and $\mathbf{r}$ is the force residual.

For this theorem to apply, the displacement boundary conditions must be such that they are derivable from a functional, that is, the boundary conditions must be conservative. This applies to the applied load as well, since nonconservative forces gives nonsymmetric load-displacement tangent stiffness matrix [42].

Chapter 4

Triangular Shell Elements.

An important advantage of the co-rotational formulation is the "reuse" of existing linear finite elements for large-rotation small-strain analysis. Chapters 4 and 5 develop high-performance shell elements that can efficiently provide the internal forces $\mathbf{f}_e$ and linear stiffness $\mathbf{K}_e$ used in the co-rotational nonlinear analysis presented in Chapters 2 and 3. The term "high performance" collectively identifies elements that can provide engineering accuracy with fairly coarse discretization.

Chapter 4 develops a triangular shell element whereas Chapter 5 develops a 4-node quadrilateral shell element. Both elements include drilling degrees of freedom as part of their membrane components.

In the exposition below, the special identifiers used in the previous chapters to distinguish linear and nonlinear components are dropped for clarity since the most of the development deals with the formulation of linear elements. Thus $\mathbf{K}_e$, for example, is written simply as $\mathbf{K}$.

4.1 Element stiffness by the ANDES formulation.

Let $\mathbf{K}$ denote the linear element stiffness matrix, $\mathbf{v}$ the visible element degrees of freedoms and $\mathbf{f}$ the corresponding element forces. The element stiffness equations for the elements developed below can be written as

$$\mathbf{K}\mathbf{v} = (\mathbf{K}_b + \mathbf{K}_h)\mathbf{v} = \mathbf{f} \ . \tag{4.1.1}$$

Here $\mathbf{K}_b$ and $\mathbf{K}_h$ are called *basic* and *higher-order* stiffness matrices respectively. This decomposition of the element stiffness equations also applies to the quadrilateral shell element constructed in the next chapter.

$\mathbf{K}_b$ is formulation independent in that it is entirely defined by an assumed constant stress together with an assumed boundary displacement field. This approach to forming the basic stiffness was first developed by Bergan and Hanssen [11] and later integrated in the the more developed form of the Free Formulation (FF) by Bergan and Nygård [14,47].

$\mathbf{K}_h$ can be formed using several different formulations, most notably the FF, the Extended Free Formulation (EFF) [1] and the Assumed Natural Deviatoric Strains (ANDES) formulation. The latter grew out of work done by Felippa to incorporate FF into a variational framework [25,26], combined with further developments by Militello and Felippa [44,45].

4.1.1 Basic stiffness construction.

The procedure for constructing the basic stiffness can be found in several sources. Militello has a very enlightening description in his Ph.D thesis [45]. This step by step outline of the basic stiffness construction is also described in Reference [1], and is outlined below here for easy reference.

B1. Assume a constant stress state, $\bar{\boldsymbol{\sigma}}$ inside the element. This gives the associated boundary tractions $\bar{\boldsymbol{\sigma}}_n$:

$$\bar{\boldsymbol{\sigma}}_n = \bar{\boldsymbol{\sigma}} \cdot \mathbf{n} = \mathbf{T}_n \bar{\boldsymbol{\sigma}} \ , \tag{4.1.2}$$

where $\mathbf{n}$ is the outward unit normal vector on the element boundary and $\mathbf{T}_n$ is a transformation matrix that substitutes the tensor-product $\bar{\sigma_{ni}} = \bar{\sigma}_{ij} n_j$ with an equivalent matrix-multiply.

B2. Connect a boundary displacement field, $\mathbf{d}$, to the visible degrees of freedom, $\mathbf{v}$ as

$$\mathbf{d} = \mathbf{N}_d \mathbf{v} \ . \tag{4.1.3}$$

Matrix $\mathbf{N}_d$ contains boundary displacement functions that must satisfy inter-element continuity, and exactly include rigid body and constant strains motion. Note, however, that the internal displacement field need not be defined here at this point; and in fact in the ANDES formulation such field is not explicitly constructed.

B3. Construct the force-lumping matrix, $\mathbf{L}$, that consistently "lumps" the boundary tractions $\bar{\boldsymbol{\sigma}}_n$ to element node forces that are conjugate to the visible degrees of freedom $\mathbf{v}$ in the virtual work sense:

$$\int_S \delta \mathbf{d}^T \bar{\boldsymbol{\sigma}}_n dS = \int_S \delta \mathbf{v}^T \mathbf{N}_d^T \mathbf{T}_n \bar{\boldsymbol{\sigma}} dS = \delta \mathbf{v}^T \int_S \mathbf{N}_{dn}^T dS \, \bar{\boldsymbol{\sigma}} = \delta \mathbf{v}^T \mathbf{L} \bar{\boldsymbol{\sigma}} = \delta \mathbf{v}^T \bar{\mathbf{f}}. \tag{4.1.4}$$

This equation provides the lumping matrix $\mathbf{L}$ as

$$\mathbf{L} = \int_S \mathbf{N}_d^T \mathbf{T}_n dS = \int_S \mathbf{N}_{dn}^T dS \ . \tag{4.1.5}$$

B4. The basic stiffness is constructed as

$$\mathbf{K}_b = \frac{1}{V} \mathbf{L} \mathbf{C} \mathbf{L}^T \ , \tag{4.1.6}$$

where $\mathbf{C}$ is the stress-strain constitutive matrix, and V is the volume of a three-dimensional element. (V is replaced by area and length measures for two-dimensional and one-dimensional elements, respectively.)

4.1.2 Higher order stiffness by the ANDES formulation.

Militello gives a thorough description of the ANDES formulation in his Ph.D thesis [45] . This includes a point by point description of the construction of the higher order stiffness. This is also described by Felippa and Militello in [27] . The essence of this development outlined below is the use of assumed strain distribution, rather than displacement modes, to characterize the higher-order behavior of the element.

H1. Select locations in the element where "natural straingage" locations are to be chosen. For many ANDES elements these gages are placed on *reference lines* but this is not a general rule. By appropriate interpolation, express the element natural strains $\boldsymbol{\epsilon}$ in terms of the "straingage readings" at those locations:

$$\boldsymbol{\epsilon} = \mathbf{A}_\epsilon \mathbf{g} \,, \tag{4.1.7}$$

where $\boldsymbol{\epsilon}$ is a strain field in natural coordinates that must include all constant strain states. (For structural elements the term "strain" is to be interpreted in a generalized sense, for example curvatures for beams or plate bending elements.)

H2. Relate the Cartesian strains $\mathbf{e}$ to the natural strains:

$$\mathbf{e} = \mathbf{T}\boldsymbol{\epsilon} = \mathbf{T}\mathbf{A}_\epsilon \mathbf{g} = \mathbf{A}\mathbf{g} \tag{4.1.8}$$

at each point in the element. (If $\mathbf{e} \equiv \boldsymbol{\epsilon}$, or if it is possible to work throughout in natural coordinates, this step is skipped. This is often the case if $\mathbf{T}$ is constant over the element as for the triangular shell elements developed here.)

H3. Relate the natural straingage readings $\mathbf{g}$ to the visible degrees of freedom

$$\mathbf{g} = \mathbf{Q}\mathbf{v} \,, \tag{4.1.9}$$

where $\mathbf{Q}$ is a straingage-to-node displacement transformation matrix. Techniques for doing this vary from element to element and it is difficult to state rules that apply to every situation. Often this step is amenable to breakdown into subproblems; for example

$$\mathbf{g} = \mathbf{Q}_1\mathbf{v}_1 + \mathbf{Q}_2\mathbf{v}_2 + \ldots \tag{4.1.10}$$

where $\mathbf{v}_1$, $\mathbf{v}_2$, ... are conveniently selected subsets of $\mathbf{v}$. Some of these components may be derivable from displacements while others are not.

H4. Split the Cartesian strain field into mean (volume-averaged) and deviatoric strains:

$$\mathbf{e} = \bar{\mathbf{e}} + \mathbf{e}_d = (\bar{\mathbf{A}} + \mathbf{A}_d)\mathbf{g} \,, \tag{4.1.11}$$

where $\bar{\mathbf{A}} = \frac{1}{V}\int_V \mathbf{T}\mathbf{A}_\epsilon dV$, and $\mathbf{e}_d = \mathbf{A}_d\mathbf{g}$ has mean zero value over V. For elements with simple element geometry this decomposition can often be done in advance, and $\mathbf{e}_d$ constructed directly. Furthermore, this step may also be carried out on the natural strains if $\mathbf{T}$ is constant.

H5. The higher order stiffness matrix is given by

$$\mathbf{K}_h = \beta \mathbf{Q}^T \mathbf{K}_d \mathbf{Q} \,, \quad \text{with} \quad \mathbf{K}_d = \int_V \mathbf{A}_d^T \mathbf{C} \mathbf{A}_d \, dV \,, \tag{4.1.12}$$

where $\beta > 0$ is a scaling coefficient. It is often convenient to combine the product of $\mathbf{A}$ and $\mathbf{Q}$ into a single strain-displacement matrix called (as usual) $\mathbf{B}$, which splits into $\bar{\mathbf{B}}$ and $\mathbf{B}_d$:

$$\mathbf{e} = \mathbf{A}\mathbf{Q} = (\bar{\mathbf{A}} + \mathbf{A}_d)\mathbf{Q}\mathbf{v} = (\bar{\mathbf{B}} + \mathbf{B}_d)\mathbf{v} = \mathbf{B}\mathbf{v} \,, \tag{4.1.13}$$

in which case

$$\mathbf{K}_h = \beta \int_V \mathbf{B}_d^T \mathbf{C} \mathbf{B}_d \, dV \,. \tag{4.1.14}$$

We next apply these rules to the construction of a three-node triangular shell element. Because the element is flat, the membrane and bending can be developed separately. Both developments, however, share the geometric information presented in the following subsection.

4.2 Geometric definitions for a triangular element.

The geometry of a three-node triangular element is graphically defined in Figure 4.1.

By defining l_i to be length of side edge opposite to node i and h_i as height from node i to side i according to Figure 4.1 one obtains

$$l_i = \sqrt{x_{jk}^2 + y_{jk}^2} \qquad \text{and} \qquad h_i = \frac{2A}{l_i} \,, \tag{4.2.1}$$

where A is the triangle area, which may be calculated as

$$2A = x_{21}y_{31} - x_{31}y_{21} = x_{31}y_{12} - x_{12}y_{32} = x_{13}y_{23} - x_{23}y_{13} \,. \tag{4.2.2}$$

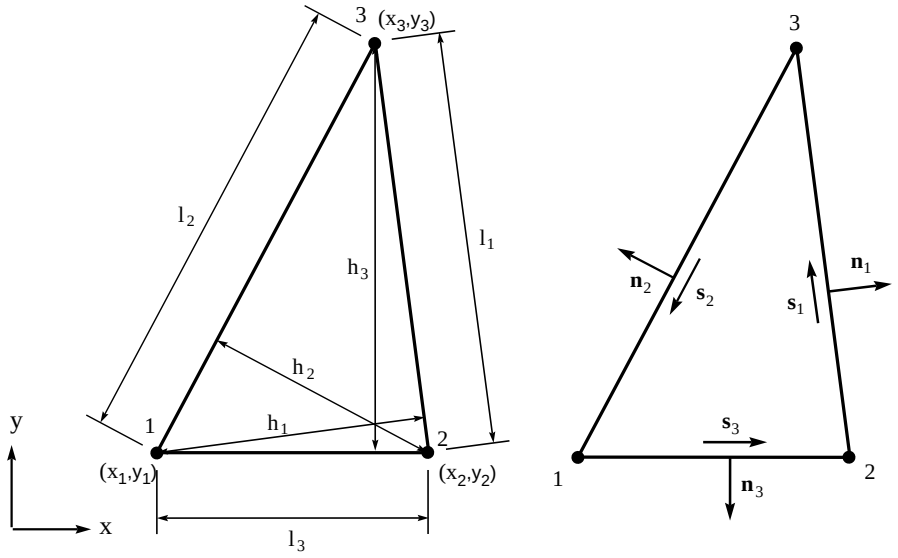

Figure 4.1. Geometric dimensions and unit vector definitions for a triangular element.

The unit vector $\mathbf{s}_i$ along side i and the outward normal vector $\mathbf{n}_i$ at side i can then be defined as

$$\mathbf{s}_i = \left\{ \begin{array}{c} s_{ix} \\ s_{iy} \\ 0 \end{array} \right\} = \frac{1}{l_i} \left\{ \begin{array}{c} x_{kj} \\ y_{kj} \\ 0 \end{array} \right\} \qquad \text{and} \qquad \mathbf{n}_i = \left\{ \begin{array}{c} n_{ix} \\ n_{iy} \\ 0 \end{array} \right\} = \left\{ \begin{array}{c} -s_{iy} \\ s_{ix} \\ 0 \end{array} \right\} . \tag{4.2.3}$$

4.3 The triangular membrane element.

The construction of an ANDES triangular membrane element is described by Felippa and Militello in [27]. The present description is adapted to the notation used for the four-node quadrilateral element in Chapter 5.

The nodal degrees of freedom $\mathbf{v}_i$ for the membrane element consists of the in-plane translations u, v and the "drilling" degree of freedom θ_z :

$$\mathbf{v}_i = \left\{ \begin{array}{c} u_i \\ v_i \\ \theta_{zi} \end{array} \right\} . \tag{4.3.1}$$

4.3.1 Basic stiffness.

The lumping of the constant membrane stresses to a node j is only a function of the neighboring side edges ij and jk. The total lumping matrix can thus be divided into the contributions to the separate nodes as

$$\mathbf{L} = \begin{bmatrix} \mathbf{L}_1 \\ \mathbf{L}_2 \\ \mathbf{L}_3 \end{bmatrix} , \tag{4.3.2}$$

where

$$\mathbf{L}_j = \frac{1}{2} \begin{bmatrix} y_{ki} & 0 & -x_{ki} \\ 0 & -x_{ki} & y_{ki} \\ \frac{\alpha}{6}(y_{ij}^2 - y_{kj}^2) & \frac{\alpha}{6}(x_{ij}^2 - x_{kj}^2) & \frac{\alpha}{3}(x_{kj}y_{kj} - x_{ij}y_{ij}) \end{bmatrix} , \tag{4.3.3}$$

and the nodal indices (i, j, k) take cyclic permutations of $(1, 2, 3)$. The basic stiffness is then computed as

$$\mathbf{K}_b = \frac{t}{A}\mathbf{L}\mathbf{C}\mathbf{L}^T , \tag{4.3.4}$$

where t is the element thickness and A the element area.

4.3.2 Higher order stiffness.

Felippa and Millitello [27] extracted the higher order behavior of the element by defining the higher order degrees of freedom $\tilde{\theta}_i$ as the nodal drilling degrees of freedom minus the rigid body and constant strain rotation θ_0 of the CST element

$$\tilde{\theta}_i = \theta_i - \theta_0 , \tag{4.3.5}$$

where

$$\theta_0 = \frac{1}{4A} [\, -x_{32} \quad -y_{32} \quad 0 \quad -x_{13} \quad -y_{13} \quad 0 \quad -x_{21} \quad -y_{21} \quad 0 \,] \, \mathbf{v} . \tag{4.3.6}$$

By further splitting the hierarchical rotations into mean $\bar{\theta} = (\tilde{\theta}_1 + \tilde{\theta}_2 + \tilde{\theta}_3)/3$ and deviatoric components $\theta'_i = \tilde{\theta}_i - \bar{\theta}$ one gets

$$\begin{Bmatrix} \theta'_1 \\ \theta'_2 \\ \theta'_3 \\ \bar{\theta} \end{Bmatrix} = \begin{bmatrix} 0 & 0 & \frac{2}{3} & 0 & 0 & -\frac{1}{3} & 0 & 0 & -\frac{1}{3} \\ 0 & 0 & -\frac{1}{3} & 0 & 0 & \frac{2}{3} & 0 & 0 & -\frac{1}{3} \\ 0 & 0 & -\frac{1}{3} & 0 & 0 & -\frac{1}{3} & 0 & 0 & \frac{2}{3} \\ \frac{x_{32}}{4A} & \frac{y_{32}}{4A} & \frac{1}{3} & \frac{x_{13}}{4A} & \frac{y_{13}}{4A} & \frac{1}{3} & \frac{x_{21}}{4A} & \frac{y_{21}}{4A} & \frac{1}{3} \end{bmatrix} \begin{Bmatrix} v_{x1} \\ v_{y1} \\ \theta_1 \\ v_{x2} \\ v_{y2} \\ \theta_2 \\ v_{x3} \\ v_{y3} \\ \theta_3 \end{Bmatrix} , \tag{4.3.7}$$

which in matrix form reads

$$\boldsymbol{\theta}_h = \mathbf{H}_{\theta v}\mathbf{v} \; . \tag{4.3.8}$$

The pure-bending field.
The pure bending field is connected to the deviatoric hierarchical rotations θ_i' as

$$\boldsymbol{\epsilon}_{b1} = \left\{ \begin{array}{c} \epsilon_{b21|1} \\ \epsilon_{b32|1} \\ \epsilon_{b13|1} \end{array} \right\} = \left[\begin{array}{ccc} \rho_1\chi_{21|1} & -\rho_2\chi_{21|1} & \rho_4\chi_{21|1} \\ \rho_5\chi_{32|1} & \rho_3\chi_{32|1} & -\rho_3\chi_{32|1} \\ -\rho_1\chi_{13|1} & \rho_4\chi_{13|1} & \rho_2\chi_{13|1} \end{array} \right] \left\{ \begin{array}{c} \theta_1' \\ \theta_2' \\ \theta_3' \end{array} \right\} = \mathbf{Q}_{b1}\boldsymbol{\theta}'$$

$$\boldsymbol{\epsilon}_{b2} = \left\{ \begin{array}{c} \epsilon_{b21|2} \\ \epsilon_{b32|2} \\ \epsilon_{b13|2} \end{array} \right\} = \left[\begin{array}{ccc} \rho_2\chi_{21|2} & -\rho_1\chi_{21|2} & \rho_4\chi_{21|2} \\ \rho_4\chi_{32|2} & \rho_1\chi_{32|2} & -\rho_2\chi_{32|2} \\ -\rho_3\chi_{13|2} & \rho_5\chi_{13|2} & \rho_3\chi_{13|2} \end{array} \right] \left\{ \begin{array}{c} \theta_1' \\ \theta_2' \\ \theta_3' \end{array} \right\} = \mathbf{Q}_{b2}\boldsymbol{\theta}'$$

$$\boldsymbol{\epsilon}_{b1} = \left\{ \begin{array}{c} \epsilon_{b21|3} \\ \epsilon_{b32|3} \\ \epsilon_{b13|3} \end{array} \right\} = \left[\begin{array}{ccc} \rho_3\chi_{21|3} & -\rho_3\chi_{21|3} & \rho_5\chi_{21|3} \\ \rho_4\chi_{32|3} & \rho_2\chi_{32|3} & -\rho_1\chi_{32|3} \\ -\rho_2\chi_{13|3} & \rho_4\chi_{13|3} & \rho_1\chi_{13|3} \end{array} \right] \left\{ \begin{array}{c} \theta_1' \\ \theta_2' \\ \theta_3' \end{array} \right\} = \mathbf{Q}_{b3}\boldsymbol{\theta}' \tag{4.3.9}$$

where

$$\chi_{ij|k} = \frac{4A}{3l_{ij}^2} \quad \text{and} \quad \chi_{ij|i} = \chi_{ij|j} = -\frac{2A}{3l_{ij}^2} \tag{4.3.10}$$

and the ρ_i are numerical coefficients to be chosen. Coefficients ρ_i that optimize in-plane bending behavior of rectangular mesh units are found to be [28]

$$\rho_2 = 1 \; , \quad \rho_3 = \frac{1}{2} \quad \text{and} \quad \rho_1 = \rho_4 = \rho_5 = 0 \; . \tag{4.3.11}$$

Having defined the matrices $\mathbf{Q}_{bi}$ in (4.3.9), the bending strains over the element can now be interpolated linearly between the nodes:

$$\epsilon_b = (\zeta_1\mathbf{Q}_{b1} + \zeta_2\mathbf{Q}_{b2} + \zeta_2\mathbf{Q}_{b2})\boldsymbol{\theta}' = \mathbf{B}_b\boldsymbol{\theta}' \; . \tag{4.3.12}$$

The torsional field.
The torsional field is connected to the mean deviatoric rotation $\bar{\theta}$ and is given in [27] as

$$\epsilon_t = \left\{ \begin{array}{c} \epsilon_{t21} \\ \epsilon_{t32} \\ \epsilon_{t13} \end{array} \right\} = 3 \left\{ \begin{array}{c} \chi_{21|1}\zeta_{21} \\ \chi_{32|2}\zeta_{21} \\ \chi_{13|3}\zeta_{21} \end{array} \right\} \bar{\theta} = \mathbf{B}_t\bar{\boldsymbol{\theta}} \; .$$

The total strain field.

The total natural coordinate strain field is the combination of the pure-bending and torsional strain fields expressed with respect to the visible degrees of freedom

$$\begin{aligned}\boldsymbol{\epsilon} &= \boldsymbol{\epsilon}_b + \boldsymbol{\epsilon}_t \\ &= \mathbf{B}_b\boldsymbol{\theta}' + \mathbf{B}_t\bar{\theta} \\ &= [\,\mathbf{B}_b \quad \mathbf{B}_t\,]\,\boldsymbol{\theta}_h \\ &= [\,\mathbf{B}_b \quad \mathbf{B}_t\,]\,\mathbf{H}_{\theta v}\mathbf{v} \\ &= \mathbf{B}\mathbf{v}\ .\end{aligned} \tag{4.3.13}$$

The stiffness matrix.

The higher order stiffness matrix is computed as

$$\mathbf{K}_h = \int_A \mathbf{B}^T\mathbf{C}_\epsilon\mathbf{B}\,dA \quad \text{where} \quad \mathbf{C}_\epsilon = \mathbf{T}^T\mathbf{C}\mathbf{T}\ , \tag{4.3.14}$$

and

$$\mathbf{T}^{-1} = \begin{bmatrix} {s_{12}}_x^2 & {s_{12}}_y^2 & s_{12x}s_{12y} \\ {s_{23}}_x^2 & {s_{23}}_y^2 & s_{23x}s_{23y} \\ {s_{31}}_x^2 & {s_{31}}_y^2 & s_{31x}s_{31y} \end{bmatrix}. \tag{4.3.15}$$

Matrix $\mathbf{T}$ transforms the natural coordinate strains to Cartesian strains, while $\mathbf{T}^{-1}$ does the opposite.

4.4 The triangular bending elements.

The bending component of the triangular shell element is based on the linear three node plate bending element AQR developed by Militello [45]. A higher order stiffness is also developed by sanitizing the BCIZ element [9]. Two basic stiffnesses exist, one based on linear interpolation of normal rotations along a side edge and one based on quadratic variation of the normal rotation. The triangular ANDES bending elements can thus be formed by combining several basic and higher order stiffnesses.

The nodal bending degrees of freedom $\mathbf{v}_i$ consists of the out of plane translation w and the in-plane rotations θ_x and θ_y

$$\mathbf{v}_i = \left\{ \begin{array}{c} w_i \\ \theta_{x\,i} \\ \theta_{x\,i} \end{array} \right\}. \tag{4.4.1}$$

4.4.1 Basic stiffnesses.

$\mathbf{K}_b$ is one of the basic stiffness matrices described by Militello in [45] as

$$\mathbf{K}_b = \frac{1}{A}\mathbf{L}_l\mathbf{C}\mathbf{L}_l^T \quad \text{or} \quad \mathbf{K}_b = \frac{1}{A}\mathbf{L}_q\mathbf{C}\mathbf{L}_q^T \,,$$

where

$$\mathbf{L}_l = \begin{bmatrix} \mathbf{L}_{l1} \\ \mathbf{L}_{l2} \\ \mathbf{L}_{l3} \end{bmatrix} \quad \text{and} \quad \mathbf{L}_q = \begin{bmatrix} \mathbf{L}_{q1} \\ \mathbf{L}_{q2} \\ \mathbf{L}_{q3} \end{bmatrix} .$$

$\mathbf{L}_{q_i}$ and $\mathbf{L}_{q_i}$ are described in equation (5.3.4) and (5.3.5) respectively. The nodal indices (i, j, k) in the equations above takes the cyclic permutations of $(1, 2, 3)$ as in the case of the membrane lumping.

4.4.2 BCIZ higher order stiffness.

The BCIZ element developed by Bazeley et al. [9] is an historically important nonconforming element. However, the element is known not to pass the Patch Test. In fact the puzzling behavior of the element motivated the original development of that test. The use of the BCIZ element as an higher order stiffness for a triangular Free Formulation plate bending element was developed by Felippa, Haugen and Militello [29]. The transverse displacement field of the BCIZ element was given explicitly by Felippa [24] as

$$w = \begin{Bmatrix} \zeta_1^2(3-2\zeta_1) + 2\zeta_1\zeta_2\zeta_3 \\ -\zeta_1^2(y_{12}\zeta_2 + y_{13}\zeta_3) - \frac{1}{2}(y_{12}+y_{13})\zeta_1\zeta_2\zeta_3 \\ \zeta_1^2(x_{12}\zeta_2 + x_{13}\zeta_3) + \frac{1}{2}(x_{12}+x_{13})\zeta_1\zeta_2\zeta_3 \\ \zeta_2^2(3-2\zeta_2) + 2\zeta_1\zeta_2\zeta_3 \\ -\zeta_2^2(y_{23}\zeta_3 + y_{21}\zeta_1) - \frac{1}{2}(y_{23}+y_{21})\zeta_1\zeta_2\zeta_3 \\ \zeta_2^2(x_{23}\zeta_3 + x_{21}\zeta_1) + \frac{1}{2}(x_{23}+x_{21})\zeta_1\zeta_2\zeta_3 \\ \zeta_3^2(3-2\zeta_3) + 2\zeta_1\zeta_2\zeta_3 \\ -\zeta_3^2(y_{31}\zeta_1 + y_{32}\zeta_2) - \frac{1}{2}(y_{31}+y_{32})\zeta_1\zeta_2\zeta_3 \\ \zeta_3^2(x_{31}\zeta_1 + x_{32}\zeta_2) + \frac{1}{2}(x_{31}+x_{32})\zeta_1\zeta_2\zeta_3 \end{Bmatrix}^T \mathbf{v}$$

The strain displacement matrix $\mathbf{B}_\chi$ giving the natural curvatures from the visible degrees of freedom is obtained by double differentiation of the displacement field with respect to the triangular coordinates and appropriate relations detailed in the Appendix of [29]:

$$\boldsymbol{\chi} = \begin{Bmatrix} \chi_{12} \\ \chi_{23} \\ \chi_{31} \end{Bmatrix} = \mathbf{B}_\chi\mathbf{v} = (\mathbf{B}_{\chi 0} + \mathbf{B}_{\chi 1}\zeta_1 + \mathbf{B}_{\chi 2}\zeta_2 + \mathbf{B}_{\chi 3}\zeta_3)\mathbf{v} \,,$$

where

$$\mathbf{B}_{\chi 0}^T = \begin{bmatrix} 6 & 0 & 6 \\ 0 & 0 & 0 \\ 0 & 0 & 0 \\ 6 & 6 & 0 \\ 0 & 0 & 0 \\ 0 & 0 & 0 \\ 0 & 6 & 6 \\ 0 & 0 & 0 \\ 0 & 0 & 0 \end{bmatrix}, \quad \mathbf{B}_{\chi 1}^T = \begin{bmatrix} -12 & -4 & -12 \\ 4y_{12} & y_{12}+y_{13} & 4y_{13} \\ -4x_{12} & -x_{12}-x_{13} & -4x_{13} \\ 0 & -4 & 0 \\ -2y_{21} & -y_{21}+y_{23} & 0 \\ 2x_{21} & x_{21}-x_{23} & 0 \\ 0 & -4 & 0 \\ 0 & -y_{31}+y_{32} & -2y_{31} \\ 0 & x_{31}-x_{32} & 2x_{31} \end{bmatrix},$$

$$\mathbf{B}_{\chi 2}^T = \begin{bmatrix} 0 & 0 & -4 \\ -2y_{12} & 0 & -y_{12}+y_{13} \\ 2x_{12} & 0 & x_{12}-x_{13} \\ -12 & -12 & -4 \\ 4y_{21} & 4y_{23} & y_{21}+y_{23} \\ -4x_{21} & -4x_{23} & -x_{21}-x_{23} \\ 0 & 0 & -4 \\ 0 & -2y_{32} & y_{31}-y_{32} \\ 0 & 2x_{32} & -x_{31}+x_{32} \end{bmatrix},$$

and

$$\mathbf{B}_{\chi 3}^T = \begin{bmatrix} -4 & 0 & 0 \\ y_{12}-y_{13} & 0 & -2y_{13} \\ -x_{12}+x_{13} & 0 & 2x_{13} \\ -4 & 0 & 0 \\ y_{21}-y_{23} & -2y_{23} & 0 \\ -x_{21}+x_{23} & 2x_{23} & 0 \\ -4 & -12 & -12 \\ y_{31}+y_{32} & 4y_{32} & 4y_{31} \\ -x_{31}-x_{32} & -4x_{32} & -4x_{31} \end{bmatrix}.$$

By using a natural curvature constitutive matrix $\mathbf{C}_\chi = \mathbf{T}^T\mathbf{C}\mathbf{T}$ the higher order stiffness matrix becomes

$$\mathbf{K}_h = \int_A \mathbf{B}_{\chi d}^T \mathbf{C}_\chi \mathbf{B}_{\chi d}\, dA,$$

where $\mathbf{B}_{\chi_d} = \mathbf{B}_\chi - \bar{\mathbf{B}}_\chi$ and $\bar{\mathbf{B}}_\chi = \mathbf{B}_{\chi 0} + \frac{1}{3}(\mathbf{B}_{\chi 1} + \mathbf{B}_{\chi 2} + \mathbf{B}_{\chi 3})$.

4.4.3 ANDES higher order stiffness by direct curvature readings.

The three node ANDES element is based on direct curvature interpolation of the natural curvatures. As reference lines Millitello [45] chose the three side edges, which function as Hermitian beams. The nodal strain gage readings expressed as function of the visible degrees of freedom can be written

$$\mathbf{g} = \mathbf{Q}\mathbf{v} = \mathbf{Q}_F * \mathbf{F}\mathbf{v} \ , \tag{4.4.2}$$

where

$$\begin{aligned} \mathbf{g}^T &= [\, \kappa_{31|1} \quad \kappa_{12|1} \quad \kappa_{12|2} \quad \kappa_{23|2} \quad \kappa_{23|3} \quad \kappa_{31|3} \,], \\ \mathbf{v}^T &= [\, v_{z1} \quad \theta_{x1} \quad \theta_{y_1} \quad v_{z2} \quad \theta_{x2} \quad \theta_{y_2} \quad v_{z3} \quad \theta_{x3} \quad \theta_{y_3} \,], \end{aligned} \tag{4.4.3}$$

$$\mathbf{Q}_F = \begin{bmatrix} -6 & 4 & 4 & 0 & 0 & 0 & 6 & 2 & 2 \\ -6 & -4 & -4 & 6 & -2 & -2 & 0 & 0 & 0 \\ & & & & & & & & \\ 6 & 2 & 2 & -6 & 4 & 4 & 0 & 0 & 0 \\ 0 & 0 & 0 & -6 & -4 & -4 & 6 & -2 & -2 \\ & & & & & & & & \\ 0 & 0 & 0 & 6 & 2 & 2 & -6 & 4 & 4 \\ 6 & -2 & -2 & 0 & 0 & 0 & -6 & -4 & -4 \end{bmatrix} \tag{4.4.4}$$

and

$$\mathbf{F} = \begin{bmatrix} \mathbf{F}_{31} & \mathbf{F}_{31} & \mathbf{F}_{31} \\ \mathbf{F}_{12} & \mathbf{F}_{12} & \mathbf{F}_{12} \\ & & \\ \mathbf{F}_{12} & \mathbf{F}_{12} & \mathbf{F}_{12} \\ \mathbf{F}_{23} & \mathbf{F}_{23} & \mathbf{F}_{23} \\ & & \\ \mathbf{F}_{23} & \mathbf{F}_{23} & \mathbf{F}_{23} \\ \mathbf{F}_{31} & \mathbf{F}_{31} & \mathbf{F}_{31} \end{bmatrix} \quad \text{where} \quad \begin{aligned} \mathbf{F}_{12} &= \begin{bmatrix} \frac{1}{l_{12}^2} & \frac{n_{12x}}{l_{12}} & \frac{n_{12y}}{l_{12}} \end{bmatrix} \\ \mathbf{F}_{23} &= \begin{bmatrix} \frac{1}{l_{23}^2} & \frac{n_{23x}}{l_{23}} & \frac{n_{23y}}{l_{23}} \end{bmatrix} . \\ \mathbf{F}_{31} &= \begin{bmatrix} \frac{1}{l_{31}^2} & \frac{n_{31x}}{l_{31}} & \frac{n_{31y}}{l_{31}} \end{bmatrix} \end{aligned} \tag{4.4.5}$$

The six curvature gage readings in $\mathbf{g}$ give two curvature gage readings at each node. But three natural coordinate curvature readings are necessary to transform to the Cartesian strains at each node. A third reading is obtained by invoking the following *projection rule* [45]: the natural curvature κ_{ij} is assumed to vary linearly along side ij and constant along lines normal to side ij. Node k is then assigned a κ_{ij} value according to the projection of the node on line ij. This assumption can be expressed as the matrix relationship

$$\boldsymbol{\kappa} = \mathbf{A}_\kappa \mathbf{g} \ , \tag{4.4.6}$$

where

$$\mathbf{A}_\kappa = \tag{4.4.7}$$

$$\begin{bmatrix} 0 & \zeta_1 + \lambda_{12}\zeta_3 & \zeta_1 + \lambda_{21}\zeta_3 & 0 & 0 & 0 \\ 0 & 0 & 0 & \zeta_2 + \lambda_{23}\zeta_1 & \zeta_2 + \lambda_{32}\zeta_1 & 0 \\ \zeta_1 + \lambda_{13}\zeta_2 & 0 & 0 & 0 & 0 & \zeta_3 + \lambda_{31}\zeta_2 \end{bmatrix}$$

and

$$\lambda_{ij} = \frac{-\mathbf{s}_{ki}^T \mathbf{s}_{ij} l_{ki}}{l_{ij}} \ .$$

The deviatoric parts of the strains are now obtained by subtracting the mean strain:

$$\mathbf{A}_{\kappa d} = \mathbf{A}_\kappa - \int_A \mathbf{A}_\kappa \, dA \ ,$$

which gives

$$\mathbf{A}_{\kappa d} = \tag{4.4.8}$$

$$\begin{bmatrix} 0 & \tilde{\zeta}_1 + \lambda_{12}\tilde{\zeta}_3 & \tilde{\zeta}_1 + \lambda_{21}\tilde{\zeta}_3 & 0 & 0 & 0 \\ 0 & 0 & 0 & \tilde{\zeta}_2 + \lambda_{23}\tilde{\zeta}_1 & \tilde{\zeta}_2 + \lambda_{32}\tilde{\zeta}_1 & 0 \\ \tilde{\zeta}_1 + \lambda_{13}\tilde{\zeta}_2 & 0 & 0 & 0 & 0 & \tilde{\zeta}_3 + \lambda_{31}\tilde{\zeta}_2 \end{bmatrix}$$

in which $\tilde{\zeta}_i = \zeta_i - \frac{1}{3}$.

The deviatoric cartesian curvatures.
The deviatoric cartesian strain distribution over the element can now be expressed as

$$\kappa_d = \mathbf{T}\boldsymbol{\kappa} = \mathbf{T}\mathbf{A}_{\kappa d}\mathbf{g} = \mathbf{T}\mathbf{A}_{\kappa d}\mathbf{Q}\mathbf{v} = \mathbf{B}_d\mathbf{v} \ ,$$

where $\mathbf{T}$ is defined in equation (4.3.15).

The higher order stiffness.
Finally, the higher order stiffness can be computed from the deviatoric strains as

$$\mathbf{K}_h = \int_A \mathbf{B}_d^T \mathbf{C}\mathbf{B}_d \ dA \ . \tag{4.4.9}$$

4.5 Nonlinear extensions for a triangular shell element.

The linear triangular shell element is now ready to be incorporated in the co-rotational formulation discussed in Chapter 2. The shadow element C_{0n} is best fit to the deformed element C_n by a rigid body motion of the undeformed initial element C_0. However this "best fit" is not unique. The rotation gradient matrix $\mathbf{G}$ defined in equation (2.4.12) can be split into contributions from each node as

$$\delta\tilde{\boldsymbol{\omega}}_r = \tilde{\mathbf{G}}\,\delta\tilde{\mathbf{v}} \quad \text{where} \quad \tilde{\mathbf{G}} = [\,\tilde{\mathbf{G}}_1 \quad \tilde{\mathbf{G}}_2 \quad \tilde{\mathbf{G}}_3\,] = \begin{bmatrix} \tilde{\mathbf{G}}_{\theta_x} \\ \tilde{\mathbf{G}}_{\theta_y} \\ \tilde{\mathbf{G}}_{\theta_z} \end{bmatrix}, \tag{4.5.1}$$

and $\delta\tilde{\mathbf{v}}$ is defined as

$$\delta\tilde{\mathbf{v}} = \begin{Bmatrix} \delta\tilde{\mathbf{v}}_1 \\ \delta\tilde{\mathbf{v}}_2 \\ \delta\tilde{\mathbf{v}}_3 \end{Bmatrix} \quad \text{where} \quad \delta\tilde{\mathbf{v}}_i = \begin{Bmatrix} \delta\tilde{\mathbf{u}}_i \\ \delta\tilde{\boldsymbol{\omega}}_i \end{Bmatrix}. \tag{4.5.2}$$

Three techniques for fitting the shadow element are discussed below. Each technique produces different $\tilde{\mathbf{G}}_i$ submatrices.

4.5.1 Aligning a triangle side.

This procedure is similar to Rankin's alignment of the C_{0n} and C_n elements [46] in that it uses a common side edge direction for those configurations. Whereas Rankin picks side 13 for the unit-vector $\mathbf{e}_2$ and node 1 as the origin of the coordinate system, the current approach aligns the directions of side 12 with the $\mathbf{e}_1$ axis and uses the element nodal average (triangle centroid) as the origin of the coordinate system. This choice of centroid as origin is necessary in order to satisfy the orthogonality of $\mathbf{P}_T$ and $\mathbf{P}$ in equation (2.4.43) .

Through consistent variation of the foregoing choice of local coordinate system, the nodal submatrices $\tilde{\mathbf{G}}_i$ of equation (4.5.1) is obtained as

$$\begin{aligned}
\tilde{\mathbf{G}}_1 &= \frac{1}{2A}\begin{bmatrix} 0 & 0 & x_{32} & 0 & 0 & 0 \\ 0 & 0 & y_{32} & 0 & 0 & 0 \\ 0 & -\frac{2A}{l_{12}} & 0 & 0 & 0 & 0 \end{bmatrix}, \\
\tilde{\mathbf{G}}_2 &= \frac{1}{2A}\begin{bmatrix} 0 & 0 & x_{13} & 0 & 0 & 0 \\ 0 & 0 & y_{13} & 0 & 0 & 0 \\ 0 & \frac{2A}{l_{12}} & 0 & 0 & 0 & 0 \end{bmatrix}, \\
\tilde{\mathbf{G}}_3 &= \frac{1}{2A}\begin{bmatrix} 0 & 0 & x_{32} & 0 & 0 & 0 \\ 0 & 0 & y_{32} & 0 & 0 & 0 \\ 0 & 0 & 0 & 0 & 0 & 0 \end{bmatrix},
\end{aligned} \tag{4.5.3}$$

where A is the area of the triangle and l_{12} is length of side 12. (This variation is carried out in more detail for the four node shell element i Section 5.5.)

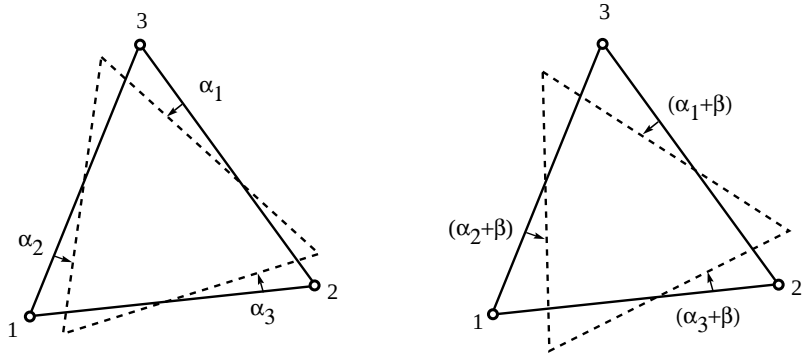

Figure 4.2. Definition of side edge angular errors.

The in-plane rotations can be recognized as $\omega_x = \frac{\partial w}{\partial y}$ and $\omega_y = -\frac{\partial w}{\partial x}$, using the geometric shape functions to interpolate w. This choice of shadow element fit satisfies the required splitting of the rotation gradient matrix as $\tilde{\mathbf{G}} = \tilde{\mathbf{X}}\mathbf{A}$ where only matrix $\mathbf{X}$ is coordinate dependent as required for the consistency condition in equation (2.5.8). On the other hand, this choice does not give an invariant deformational displacement vector for the element in the sense discussed in Section 2.10.1.

4.5.2 Least square fit of side edge angular errors.

Nygård [47] and Bjærum [17] place the C_{0n} element in the plane of the deformed element C_n with node 1 coinciding. The present study utilizes coinciding centroids. The in-plane orientation of the shadow element is then determined by a least square fit of the side edge angular errors. According to Figure 4.2 the squared-error sum is

$$e^2 = \alpha_1^2 + \alpha_2^2 + \alpha_3^2 \, . \tag{4.5.4}$$

By rotating the shadow element an angle β the square of the errors becomes

$$e^2(\beta) = (\alpha_1 + \beta)^2 + (\alpha_2 + \beta)^2 + (\alpha_3 + \beta)^2 \, . \tag{4.5.5}$$

Minimizing with respect to β:

$$\frac{\partial e^2(\beta)}{\partial \beta} = 0 \quad \Rightarrow \quad \beta = -\frac{1}{3}(\alpha_1 + \alpha_2 + \alpha 3) \, . \tag{4.5.6}$$

Consequently, the optimal in-plane position of the shadow element according to this algorithm is given by the mean of the side edge angular errors. This condition yields for the nodal submatrices

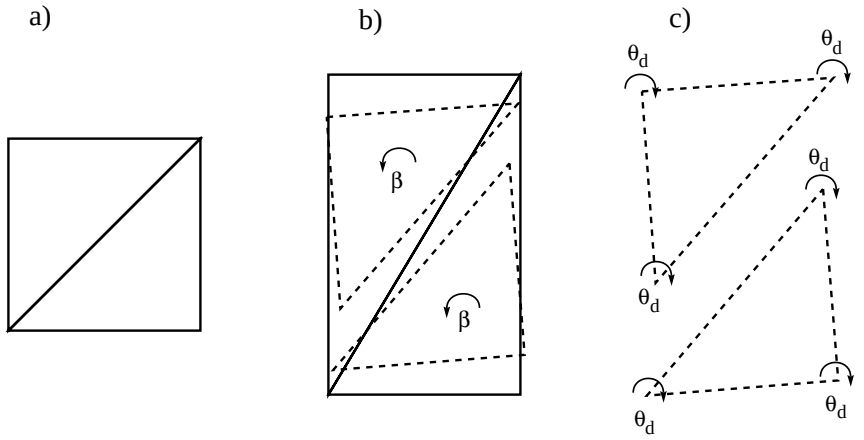

Figure 4.3. Patch of triangle elements subjected to pure stretching.

$$\tilde{\mathbf{G}}_i = \frac{1}{2A}\begin{bmatrix} 0 & 0 & x_{kj} & 0 & 0 & 0 \\ 0 & 0 & y_{kj} & 0 & 0 & 0 \\ \frac{2A}{3}(-\frac{s_{jy}}{l_j}+\frac{s_{ky}}{l_k}) & \frac{2A}{3}(\frac{s_{jx}}{l_j}-\frac{s_{kx}}{l_k}) & 0 & 0 & 0 & 0 \end{bmatrix}. \qquad (4.5.7)$$

The major advantage of this method is that it gives a unique fit independent of node numbering, which leads to a invariant deformational displacement vector as discussed in section 2.10.1. The rotational gradient matrix cannot be split into a coordinate dependent and independent part in order to be consistent with equation (2.5.8). However, again, this is of minor importance for triangular elements since the shadow element C_{0n} and the deformed element C_n will be close together for small membrane strains.

A more serious disadvantage of this fitting method is that it reintroduces the problem of fictitious normal rotations when an element is subjected to pure stretch.

This difficulty is illustrated in Figure 4.3, where the C_{0n} elements rotate due to the in-plane rotation of the diagonal. The deformational displacement vector is then computed as the difference between C_n and C_{0n}. A deformational normal rotation is thus picked up since the predictor step gives no rotation at the nodes and the deformational rotation is the total rotation minus the rigid body rotation

$$\theta_d = (\theta - \beta) = -\beta\ . \qquad (4.5.8)$$

This problem is similar to that pointed out by Irons and Ahmad [39] when defining drilling degrees of freedom as the mean of the side edge rotations at an

node. This was overcome by Bergan and Felippa [15] when they defined the normal rotation as $\theta_z = \frac{1}{2}(\frac{\partial v}{\partial x} - \frac{\partial u}{\partial y})$ for the linear FF membrane element. It is seen that the problem of fictitious normal rotations has been thus been re-introduced for the nonlinear case by the choice of shadow element positioning. This problem is even more pronounced with the side edge alignment procedure described in Section 4.5.1.

4.5.3 Fit according to CST-rotation.

As with the least square fit of side edge angular errors the shadow C_{0n} element is chosen to be co-planar with the deformed element C_n, and the centroids coincide.

By using the normal rotation of the CST element as the rigid body rotation β for the in-plane positioning of the shadow element, one avoids the problem of fictitious normal rotations when an element is subjected to pure stretching.

The definition $\theta_z = \frac{1}{2}(\frac{\partial v}{\partial x} - \frac{\partial u}{\partial y})$ gives an invariant definition of the normal rotation for the infinitesimal case. This also provides the variation of the rigid body rotation with respect to the visible degrees of freedom.

Extending the above definition to finite rotations seems to suggest

$$\theta_z = \frac{1}{2}(\tan^{-1}(\frac{\Delta v}{\Delta x}) - \tan^{-1}(\frac{\Delta u}{\Delta y})) \; . \tag{4.5.9}$$

However this choice gives slightly varying results with respect to the orientation of the (x, y)-coordinate system. In order to obtain a completely invariant positioning with respect to node numbering, the rigid body rotation can been computed as the average of the rotations obtained with the local x-axis along each of the three side edges. The continuum mechanics definition of the normal rotation is $\tilde{\theta}_z = \frac{1}{2}(\frac{\partial v}{\partial x} - \frac{\partial v}{\partial x})$. This definition is invariant with respect to the orientation of the x and y coordinate axis, and gives the rotation gradient matrix as

$$\tilde{\mathbf{G}}_i = \frac{1}{2A}\begin{bmatrix} 0 & 0 & x_{kj} & 0 & 0 & 0 \\ 0 & 0 & y_{kj} & 0 & 0 & 0 \\ -\frac{1}{2}x_{kj} & -\frac{1}{2}y_{kj} & 0 & 0 & 0 & 0 \end{bmatrix} \tag{4.5.10}$$

In the present investigation the three techniques just outlined for choosing the shadow element position were tested in the nonlinear problems reported in Chapters 7 and 8.

Chapter 5

Quadrilateral Shell Elements.

Flat quadrilateral shell elements have use limitations even in linear analysis, since a mesh that consists of strictly flat elements may be impossibly to construct over a doubly-curved shell surface. For large deflection nonlinear analysis this deficiency becomes more pronounced. Even if the initial mesh satisfies the flat element restriction, the deformations can become so large that warping of the elements can be significant. Finding ways of handling warped element geometries is thus of fundamental importance for quadrilateral shell elements.

The current research initially set out to develop a non-flat quadrilateral element that was able to satisfy self-equilibrium in a warped configuration. This proved to be difficult. Finding a basic stiffness $\mathbf{K}_b = \frac{1}{A}\mathbf{L}\mathbf{C}\mathbf{L}^T$ that maintained self equilibrium was especially troublesome. To achieve this goal one must have the lumped node forces from a constant stress state $\mathbf{f} = \mathbf{L}\boldsymbol{\sigma}$ to be in self equilibrium. Two questions arise at this point: What is a constant stress state for a warped shell element? Is a constant stress state for a warped surface an equilibrium state for arbitrary element shapes? These are key questions that remain to be answered in order to develop satisfactory FF and ANDES elements for such element geometries. It follows that those formulations have to be further extended for developing warped shell elements. The construction of the basic stiffness matrix needs special attention because the Individual Element Test is not clearly defined for curved or warped element geometries.

Restoring equilibrium in the warped element geometry can be done *a posteriori* for elements developed with reference to the flat projected "footprint" by using a projector matrix. This is the approach that has been chosen for the current quadrilateral element. It allows independent development of the membrane and bending components since these two stiffness contributions decouple, which greatly simplifies the development of the element. Both linear and nonlinear projectors have been developed for the quadrilateral element. Both versions give identical results for linear static problems, but the linear projector is recommended for linear finite element codes because its formulation is much simpler than that of the nonlinear projector.

5.1 Geometric definitions for a quadrilateral element.

This section describes geometric relationships for a quadrilateral element. The development covers both warped geometry and the flat "best fit" element obtained by setting the z coordinate for each node equal to zero. The flat projection relationships are later used for the development of the membrane and bending stiffness of the shell element. The non-flat relationships are needed for the development of the nonlinear projector for quadrilaterals.

A vector $\mathbf{r}$ to a point on a nonflat quadrilateral element can be parametrized with respect to the natural coordinates ξ and η as

$$\mathbf{r}(\xi,\eta) = \left\{ \begin{array}{c} x \\ y \\ z \end{array} \right\} = \left[\begin{array}{ccc} \mathbf{N} & \mathbf{0} & \mathbf{0} \\ \mathbf{0} & \mathbf{N} & \mathbf{0} \\ \mathbf{0} & \mathbf{0} & \mathbf{N} \end{array} \right] \left\{ \begin{array}{c} \mathbf{x} \\ \mathbf{y} \\ \mathbf{z} \end{array} \right\}, \tag{5.1.1}$$

where

$$\mathbf{x} = \left\{ \begin{array}{c} x_1 \\ x_2 \\ x_3 \\ x_4 \end{array} \right\}, \qquad \mathbf{y} = \left\{ \begin{array}{c} y_1 \\ y_2 \\ y_3 \\ y_4 \end{array} \right\}, \qquad \mathbf{z} = \left\{ \begin{array}{c} z_1 \\ z_2 \\ z_3 \\ z_4 \end{array} \right\}, \tag{5.1.2}$$

and x_i, y_i and z_i denote the global coordinates of node i. Row vector $\mathbf{N}$ contains the "usual" bi-linear isoparametric interpolation for a quadrilateral [68]. These functions and their partial derivatives with respect to ξ and η are

$$\begin{aligned} \mathbf{N} \quad &= \frac{1}{4}\left[(1-\xi)(1-\eta) \quad (1+\xi)(1-\eta) \quad (1+\xi)(1+\eta) \quad (1-\xi)(1+\eta) \right], \\ \mathbf{N}_{,\xi} &= \frac{1}{4}\left[-(1-\eta) \quad (1-\eta) \quad (1+\eta) \quad -(1+\eta) \right], \\ \mathbf{N}_{,\eta} &= \frac{1}{4}\left[-(1-\xi) \quad -(1+\xi) \quad (1+\xi) \quad (1-\xi) \right]. \end{aligned} \tag{5.1.3}$$

Using these geometric relations the variation of the position vector $\mathbf{r}$ can be written as

$$\left\{ \begin{array}{c} dx \\ dy \\ dz \end{array} \right\} = \left\{ \begin{array}{c} \frac{\partial x}{\partial \xi} d\xi + \frac{\partial x}{\partial \eta} d\eta \\ \frac{\partial y}{\partial \xi} d\xi + \frac{\partial y}{\partial \eta} d\eta \\ \frac{\partial z}{\partial \xi} d\xi + \frac{\partial z}{\partial \eta} d\eta \end{array} \right\} = \left[\begin{array}{cc} \frac{\partial x}{\partial \xi} & \frac{\partial x}{\partial \eta} \\ \frac{\partial y}{\partial \xi} & \frac{\partial y}{\partial \eta} \\ \frac{\partial z}{\partial \xi} & \frac{\partial z}{\partial \eta} \end{array} \right] \left\{ \begin{array}{c} d\xi \\ d\eta \end{array} \right\} \tag{5.1.4}$$

$$= \left[\begin{array}{cc} \mathbf{N}_{,\xi}\mathbf{x} & \mathbf{N}_{,\eta}\mathbf{x} \\ \mathbf{N}_{,\xi}\mathbf{y} & \mathbf{N}_{,\eta}\mathbf{y} \\ \mathbf{N}_{,\xi}\mathbf{z} & \mathbf{N}_{,\eta}\mathbf{z} \end{array} \right] \left\{ \begin{array}{c} d\xi \\ d\eta \end{array} \right\} = \left[\mathbf{g}_\xi \quad \mathbf{g}_\eta \right] \left\{ \begin{array}{c} d\xi \\ d\eta \end{array} \right\}$$

or

$$d\mathbf{r} = \mathbf{J} d\boldsymbol{\xi} \, .$$

The Jacobian $\mathbf{J}$ introduced above is also used for computing partial derivatives with respect to the natural coordinates ξ and η:

$$\begin{aligned}\left\{ \begin{array}{c} \frac{\partial(\cdot)}{\partial \xi} \\ \frac{\partial(\cdot)}{\partial \eta} \end{array} \right\} &= \left\{ \begin{array}{l} \frac{\partial(\cdot)}{\partial x}\frac{\partial x}{\partial \xi} + \frac{\partial(\cdot)}{\partial y}\frac{\partial y}{\partial \xi} \\ \frac{\partial(\cdot)}{\partial x}\frac{\partial x}{\partial \eta} + \frac{\partial(\cdot)}{\partial y}\frac{\partial y}{\partial \eta} \end{array} \right\} = \left[\begin{array}{cc} \frac{\partial x}{\partial \xi} & \frac{\partial y}{\partial \xi} \\ \frac{\partial x}{\partial \eta} & \frac{\partial y}{\partial \eta} \end{array} \right] \left\{ \begin{array}{c} \frac{\partial(\cdot)}{\partial x} \\ \frac{\partial(\cdot)}{\partial y} \end{array} \right\} \\ &= \left[\begin{array}{cc} \mathbf{N}_{,\xi}\mathbf{x} & \mathbf{N}_{,\xi}\mathbf{y} \\ \mathbf{N}_{,\eta}\mathbf{x} & \mathbf{N}_{,\eta}\mathbf{y} \end{array} \right] \left\{ \begin{array}{c} \frac{\partial(\cdot)}{\partial x} \\ \frac{\partial(\cdot)}{\partial y} \end{array} \right\} \end{aligned} \tag{5.1.5}$$

or

$$\frac{\partial(\cdot)}{\partial \boldsymbol{\xi}} = \mathbf{J}^T \frac{\partial(\cdot)}{\partial \mathbf{x}} \, . \tag{5.1.6}$$

It should be noted that only the x and y components are included in the above relationship for the partial derivatives. This is a consequence of assuming that the element represents a best fit of the warped quadrilateral in the (x, y)-plane.

If the z-coordinate is neglected the relationship between (x, y) and (ξ, η) is isoparametric and the inverse relation can be formed as

$$\left\{ \begin{array}{c} \frac{\partial(\cdot)}{\partial x} \\ \frac{\partial(\cdot)}{\partial y} \end{array} \right\} = \left[\begin{array}{cc} J^{-T}_{x\xi} & J^{-T}_{x\eta} \\ J^{-T}_{y\xi} & J^{-T}_{y\eta} \end{array} \right] \left\{ \begin{array}{c} \frac{\partial(\cdot)}{\partial \xi} \\ \frac{\partial(\cdot)}{\partial \eta} \end{array} \right\} . \tag{5.1.7}$$

5.1.1 Geometric quantities for a flat quadrilateral element.

By defining l_{ij} to be length of side edge ij one obtains

$$l_{ij} = \sqrt{x_{ji}^2 + y_{ji}^2} \, . \tag{5.1.8}$$

The unit vector $\mathbf{s}_{ij}$ along side ij and the outward normal vector $\mathbf{n}_{ij}$ of side ij can then be defined as

$$\mathbf{s}_{ij} = \left\{ \begin{array}{c} s_{ix} \\ s_{iy} \\ 0 \end{array} \right\} = \frac{1}{l_{ij}} \left\{ \begin{array}{c} x_{ji} \\ y_{ji} \\ 0 \end{array} \right\} \qquad \text{and} \qquad \mathbf{n}_{ij} = \left\{ \begin{array}{c} n_{ix} \\ n_{iy} \\ 0 \end{array} \right\} = \left\{ \begin{array}{c} -s_{iy} \\ s_{ix} \\ 0 \end{array} \right\} . \tag{5.1.9}$$

5.2 The quadrilateral membrane element.

Nygård [47] developed a 4-node membrane element with drilling degrees of freedom based on the Free Formulation, which is called the FFQ element. The element has given accurate results for plane membrane problems. Unfortunately, the element is computationally expensive because the formation of each element stiffness requires the numerical inversion of a 12×12 matrix. The goal of the present development is to construct a 4-node membrane element with the same freedom configuration and similar accuracy as the FFQ, but that avoids those expensive matrix inversion.

Recall that element stiffness of the ANDES element is the sum of the basic and higher order contributions:

$$\mathbf{K} = \mathbf{K}_b + \mathbf{K}_h = \frac{1}{A}\mathbf{L}\mathbf{C}\mathbf{L}^T + \int_A \mathbf{B}_h^T \mathbf{C}\mathbf{B}_h \, dA \, . \tag{5.2.1}$$

These matrices are now developed for the membrane component.

5.2.1 Basic stiffness.

The basic stiffness for the membrane element is developed by lumping the constant stress state over side edges to consistent nodal forces at the neighboring nodes according to a boundary displacement field. When the boundary displacement field is defined so that interelement compatibility is satisfied, pairwise cancelation of nodal forces for a constant stress state is assured, and thus satisfaction of the Individual Element Test [11]. In turn, satisfaction of the Individual Element Test ensures that the conventional multi-element Patch Test is passed.

A very successful lumping scheme for membrane stresses was first introduced by Bergan and Felippa [15] in the paper describing the triangular membrane FF element with drilling degrees of freedoms. This procedure has since been used by Nygård [47] and Militello [45].

The presentation here rewrites the lumping matrix, in terms of nodal submatrices. The expressions of the lumping matrix thus becomes valid for elements of arbitrary number of corner nodes.

It is convenient to order the visible degrees of freedom as translations along x, y and drilling rotation about z-axis for each node. This gives the lumping of the constant stress $\boldsymbol{\sigma}$ state to nodal forces $\mathbf{f}$ as

$$\mathbf{f} = \mathbf{L}\boldsymbol{\sigma} \qquad \text{where} \qquad \boldsymbol{\sigma} = \left\{ \begin{array}{c} \sigma_{xx} \\ \sigma_{yy} \\ \tau_{xy} \end{array} \right\}, \tag{5.2.2}$$

$$\mathbf{L} = \begin{bmatrix} \mathbf{L}_1 \\ \mathbf{L}_2 \\ \mathbf{L}_3 \\ \mathbf{L}_4 \end{bmatrix} \quad \text{and} \quad \mathbf{f} = \begin{Bmatrix} \mathbf{f}_1 \\ \mathbf{f}_2 \\ \mathbf{f}_3 \\ \mathbf{f}_4 \end{Bmatrix} \quad \text{where} \quad \mathbf{f}_i = \begin{Bmatrix} f_{xi} \\ f_{y_i} \\ m_{zi} \end{Bmatrix}. \tag{5.2.3}$$

By using the Hermitian beam shape function for a side edge one obtains a boundary displacement field that is compatible between adjacent elements because the displacements along an edge are only functions of the end nodes freedoms. This again gives a lumping matrix $\mathbf{L}$ where each nodal contribution $\mathbf{L}_j$ is only a function of its adjoining side edges ij and jk:

$$\mathbf{L}_j = \frac{1}{2} \begin{bmatrix} y_{ki} & 0 & -x_{ki} \\ 0 & -x_{ki} & y_{ki} \\ \frac{\alpha}{6}(y_{ij}^2 - y_{kj}^2) & \frac{\alpha}{6}(x_{ij}^2 - x_{kj}^2) & \frac{\alpha}{3}(x_{kj}y_{kj} - x_{ij}y_{ij}) \end{bmatrix}. \tag{5.2.4}$$

The nodal indices (i, j, k, l) for a four node element undergo cyclic permutations of $(1, 2, 3, 4)$ in the equation above. Factor α represents a scaling of the contributions of the drilling freedom to the normal boundary displacements; see [15] for details.

5.2.2 Higher order stiffness.

To construct $\mathbf{K}_h$ a set of higher order degrees of freedoms that vanish for rigid body and constant strain states is constructed.

Higher order degrees of freedom.
The 12 visible nodal degrees of freedom v_x, v_y and θ for each node are ordered in an element displacement vector $\mathbf{v}$ as

$$\mathbf{v} = \begin{Bmatrix} \mathbf{v}_x \\ \mathbf{v}_y \\ \boldsymbol{\theta} \end{Bmatrix}, \quad \text{where} \quad \begin{aligned} \mathbf{v}_x^T &= [\, v_{x1} \quad v_{x2} \quad v_{x3} \quad v_{x4} \,], \\ \mathbf{v}_y^T &= [\, v_{y1} \quad v_{y2} \quad v_{y3} \quad v_{y4} \,], \\ \boldsymbol{\theta}^T &= [\, \theta_1 \quad \theta_2 \quad \theta_3 \quad \theta_4 \,]. \end{aligned} \tag{5.2.5}$$

The correct rank of the element stiffness matrix for the quadrilateral membrane element is 9, coming from 12 degrees of freedom minus 3 rigid body modes. The basic stiffness gives is rank 3 from the 3 constant strain modes. The higher order stiffness must therefore be a rank 6 matrix. This can be conveniently achieved by introducing 6 higher order "intrinsic" degrees of freedom, which are collected in a vector $\tilde{\mathbf{v}}$ defined below.

Experience from the 3-node ANDES membrane element with drilling degrees of freedom [27] and the 4-node ANDES tetrahedron solid element with

rotational degrees of freedom [33], suggests using the hierarchical rotations $\tilde{\boldsymbol{\theta}}$ as higher order degrees of freedom:

$$\tilde{\boldsymbol{\theta}} = \boldsymbol{\theta} - \boldsymbol{\theta}_0 \ , \qquad \boldsymbol{\theta}_0^T = [\, \theta_0 \quad \theta_0 \quad \theta_0 \quad \theta_0 \,] \, , \tag{5.2.6}$$

where the subtracted θ_0 represents the overall or mean rotation of the element, associated with rigid body and constant strain rotation motions. Furthermore, splitting the hierarchical rotations into their mean and deviatoric parts as

$$\tilde{\boldsymbol{\theta}} = \bar{\boldsymbol{\theta}} + \boldsymbol{\theta}', \qquad \bar{\boldsymbol{\theta}}^T = [\, \bar{\theta} \quad \bar{\theta} \quad \bar{\theta} \quad \bar{\theta} \,] \, , \tag{5.2.7}$$

has the advantage of singling out the often troublesome "drilling mode", or "torsional mode", where all the drilling node rotations take the same value with all the other degrees of freedom being zero.

Unfortunately, the hierarchical rotations give only 4 higher order degrees of freedom and at most a rank 4 update of the stiffness matrix. Two more higher order degrees of freedom must be found. The element has 8 translational degrees of freedom represented by $\mathbf{v}_x$ and $\mathbf{v}_y$. The 3 rigid body and 3 constant strain modes can all be described by the translational degrees of freedom. There are still 2 higher order modes which can be described by the translational degrees of freedom. These two modes must be recognized so as to associate two higher order degrees of freedom with them. The amplitudes of the six higher order degrees of freedom are then represented as

$$\tilde{\mathbf{v}}^T = [\, \theta_1' \quad \theta_2' \quad \theta_3' \quad \theta_4' \quad \bar{\theta} \quad \alpha_1 \quad \alpha_2 \,] \, , \tag{5.2.8}$$

where α_1 and α_2 are associated with the two higher order translational modes. Although 7 degrees of freedom appear in this vector, the hierarchical rotation constraint

$$\sum_{i=1}^{4} \theta_i' = 0 \tag{5.2.9}$$

reduces (5.2.8) effectively to six independent components.

Higher order rotational degrees of freedom.
θ_0 is evaluated as the rotation of the bi-linear quadrilateral computed at the element center given by $(\xi = 0, \eta = 0)$, and is function of the translational degrees of freedom only:

$$\theta_0 = \frac{1}{2}(\frac{\partial v}{\partial x} - \frac{\partial u}{\partial y}) = \frac{1}{2}\left[-\mathbf{N}_{,y} \quad \mathbf{N}_{,x} \right] \left\{ \begin{array}{c} \mathbf{v}_x \\ \mathbf{v}_y \end{array} \right\}. \tag{5.2.10}$$

By using the partial derivative expressions in equation (5.1.7) one obtains the expressions for the rigid body and constant strain rotation as

$$\begin{aligned} -\mathbf{N}_{,y} &= -(J_{y\xi}^{-T}\mathbf{N}_{,\xi} + J_{y\eta}^{-T}\mathbf{N}_{,\eta}) = \frac{1}{16|\mathbf{J}|}\left[x_{24} \quad x_{31} \quad x_{42} \quad x_{13} \right], \\ \mathbf{N}_{,x} &= -(J_{x\xi}^{-T}\mathbf{N}_{,\xi} + J_{x\eta}^{-T}\mathbf{N}_{,\eta}) = \frac{1}{16|\mathbf{J}|}\left[y_{24} \quad y_{31} \quad y_{42} \quad y_{13} \right], \end{aligned} \tag{5.2.11}$$

where

$$|\mathbf{J}| = \frac{1}{8}((x_1y_2 - x_2y_1) + (x_2y_3 - x_3y_2) + (x_3y_4 - x_4y_3) + (x_4y_1 - x_1y_4)). \tag{5.2.12}$$

The higher order rotational degrees of freedom θ_h can be expressed in terms of the visible degrees of freedoms as

$$\boldsymbol{\theta}_h = \mathbf{H}_{\theta v}\mathbf{v}, \qquad \boldsymbol{\theta}_h^T = \left[\theta_1' \quad \theta_2' \quad \theta_3' \quad \theta_4' \quad \bar{\theta} \right], \tag{5.2.13}$$

$$\mathbf{H}_{\theta v} = \begin{bmatrix} 0 & 0 & 0 & 0 & 0 & 0 & 0 & 0 & \frac{3}{4} & -\frac{1}{4} & -\frac{1}{4} & -\frac{1}{4} \\ 0 & 0 & 0 & 0 & 0 & 0 & 0 & 0 & -\frac{1}{4} & \frac{3}{4} & -\frac{1}{4} & -\frac{1}{4} \\ 0 & 0 & 0 & 0 & 0 & 0 & 0 & 0 & -\frac{1}{4} & -\frac{1}{4} & \frac{3}{4} & -\frac{1}{4} \\ 0 & 0 & 0 & 0 & 0 & 0 & 0 & 0 & -\frac{1}{4} & -\frac{1}{4} & -\frac{1}{4} & \frac{3}{4} \\ \frac{x_{42}}{f} & \frac{x_{13}}{f} & \frac{x_{24}}{f} & \frac{x_{31}}{f} & \frac{y_{42}}{f} & \frac{y_{13}}{f} & \frac{y_{24}}{f} & \frac{y_{31}}{f} & \frac{1}{4} & \frac{1}{4} & \frac{1}{4} & \frac{1}{4} \end{bmatrix} \tag{5.2.14}$$

and $f = 16|\mathbf{J}|$.

Higher order translational degrees of freedom.
The translational degrees of freedom can be split into rigid body and constant strain displacements and higher order displacements:

$$\mathbf{v} = \mathbf{v}_{rc} + \mathbf{v}_h \quad \text{where} \quad \mathbf{v} = \left\{ \begin{array}{c} \mathbf{v}_x \\ \mathbf{v}_y \end{array} \right\}. \tag{5.2.15}$$

$\mathbf{v}_{rc}$ can be written as a linear combination of the rc-modes as

$$\mathbf{v}_{rc} = \mathbf{R}\mathbf{a} \quad \text{with} \quad \mathbf{R} = [\, \mathbf{r}_x \quad \mathbf{r}_y \quad \mathbf{r}_{\theta_z} \quad \mathbf{c}_{\epsilon_{xx}} \quad \mathbf{c}_{\epsilon_{yy}} \quad \mathbf{c}_{\epsilon_{xy}} \,], \tag{5.2.16}$$

where $\mathbf{r}_x$, $\mathbf{r}_y$ and $\mathbf{r}_{\theta_z}$ are the rigid translations in the x and y directions, and the rigid rotation about the z axis, respectively. $\mathbf{c}_{\epsilon_{xx}}$, $\mathbf{c}_{\epsilon_{xx}}$ and $\mathbf{c}_{\epsilon_{xx}}$ are the constant strain displacement modes. By combining equations (5.2.15) and (5.2.16), and requiring that the higher order displacement vector be orthogonal to the rc-modes, that is $\mathbf{R}^T\mathbf{v}_h = \mathbf{0}$, one obtains

$$\mathbf{R}^T\mathbf{v} = \mathbf{R}^T\mathbf{R}\mathbf{a} + \mathbf{R}^T\mathbf{v}_h \quad \Rightarrow \quad \mathbf{a} = (\mathbf{R}^T\mathbf{R})^{-1}\mathbf{R}^T\mathbf{v}\,. \tag{5.2.17}$$

On the basis of this relation two projector matrices $\mathbf{P}_{rc}$ and $\mathbf{P}_h$ that project the displacement vector $\mathbf{v}$ on the rc and h subspaces, respectively, can be constructed:

$$\begin{array}{l} \mathbf{v}_{rc} = \mathbf{P}_{rc}\mathbf{v}\,, \\ \mathbf{v}_h = \mathbf{P}_h\mathbf{v}\,, \end{array} \quad \text{where} \quad \begin{array}{l} \mathbf{P}_{rc} = \mathbf{R}(\mathbf{R}^T\mathbf{R})^{-1}\mathbf{R}^T\,, \\ \mathbf{P}_h = \mathbf{I} - \mathbf{R}(\mathbf{R}^T\mathbf{R})^{-1}\mathbf{R}^T\,. \end{array} \tag{5.2.18}$$

The higher order translational modes can now be found either as the null-space of $\mathbf{P}_{rc}$, or as eigenvectors of $\mathbf{P}_h$ with associated eigenvalues equal to one, that is $\mathbf{P}_h\mathbf{v}_h = \mathbf{v}_h$. The latter scheme is the simpler one because the projector matrices enjoy the property $\mathbf{P}\mathbf{P} = \mathbf{P}$. Every column in $\mathbf{P}_h$ is thus its own eigenvector with eigenvalue one, and a higher order mode.

To write down these higher order modes in compact form it is convenient to expresses the vector that goes from the element centroid to the nodes $\mathbf{r}_i$ with respect to the local coordinate system $(\mathbf{g}_\xi, \mathbf{g}_\eta)$. These base vectors are the ξ- and η- gradient vectors computed at the element center according to equation (5.1.4). The nodal vector $\mathbf{r}_i$ can thus be expressed as

$$\mathbf{r}_i = \left\{ \begin{array}{c} x_i \\ y_i \end{array} \right\} = [\, \mathbf{g}_\xi \quad \mathbf{g}_\eta \,] \left\{ \begin{array}{c} \xi_i \\ \eta_i \end{array} \right\}. \tag{5.2.19}$$

The nodal coordinates ξ_i and η_i in the $(\mathbf{g}_\xi, \mathbf{g}_\eta)$ coordinate system are then obtained from

$$\left\{ \begin{array}{c} \xi_i \\ \eta_i \end{array} \right\} = \mathbf{T}_\xi \left\{ \begin{array}{c} x_i \\ y_i \end{array} \right\}, \qquad \mathbf{T}_\xi = \mathbf{J}^{-1} = [\, \mathbf{g}_\xi \quad \mathbf{g}_\eta \,]^{-1} \,. \tag{5.2.20}$$

The higher order translational mode is then given by

$$\mathbf{v}_h = \left\{ \begin{array}{c} \varsigma_3 \\ \varsigma_4 \\ \varsigma_1 \\ \varsigma_2 \end{array} \right\} = \left\{ \begin{array}{c} \xi_3\eta_3 - a \\ \xi_4\eta_4 - a \\ \xi_1\eta_1 - a \\ \xi_2\eta_2 - a \end{array} \right\}, \qquad a = \frac{1}{4}\sum_{i=1}^{4} \xi_i\eta_i \,. \tag{5.2.21}$$

The higher order translational degrees of freedom are the components along this higher order mode for the x and y nodal displacements $\mathbf{v}_x$ and $\mathbf{v}_y$ respectively. Expressed in term of the visible degrees of freedom this becomes

$$\tilde{\mathbf{v}}_t = \mathbf{H}_{tv}\mathbf{v} \,, \tag{5.2.22}$$

$$\left\{ \begin{array}{c} \tilde{v}_x \\ \tilde{v}_y \end{array} \right\} = \left[\begin{array}{cccccccccccc} \varsigma_3 & \varsigma_4 & \varsigma_1 & \varsigma_2 & 0 & 0 & 0 & 0 & 0 & 0 & 0 & 0 \\ 0 & 0 & 0 & 0 & \varsigma_3 & \varsigma_4 & \varsigma_1 & \varsigma_2 & 0 & 0 & 0 & 0 \end{array} \right] \mathbf{v} \,. \tag{5.2.23}$$

If one defines the higher order translational degrees of freedom to be the higher order translational components along the ξ and η directions the relationship becomes

$$\left\{ \begin{array}{c} \tilde{v}_\xi \\ \tilde{v}_\eta \end{array} \right\} = \left[\begin{array}{cccccccc|c} \varsigma_3 s_{\xi x} & \varsigma_4 s_{\xi x} & \varsigma_1 s_{\xi x} & \varsigma_2 s_{\xi x} & \varsigma_3 s_{\xi y} & \varsigma_4 s_{\xi y} & \varsigma_1 s_{\xi y} & \varsigma_2 s_{\xi y} & \mathbf{0} \\ \varsigma_3 s_{\eta x} & \varsigma_4 s_{\eta x} & \varsigma_1 s_{\eta x} & \varsigma_2 s_{\eta x} & \varsigma_3 s_{\eta y} & \varsigma_4 s_{\eta y} & \varsigma_1 s_{\eta y} & \varsigma_2 s_{\eta y} & \mathbf{0} \end{array} \right] \mathbf{v} \tag{5.2.24}$$

where $\mathbf{0} = [\, 0 \quad 0 \quad 0 \quad 0 \,]$, and $s_{\xi i}$ and $s_{\eta i}$ denotes the unit vectors along the ξ- and η-directions, respectively:

$$\mathbf{s}_\xi = \left\{ \begin{array}{c} s_{\xi x} \\ s_{\xi y} \end{array} \right\}, \qquad \mathbf{s}_\eta = \left\{ \begin{array}{c} s_{\eta x} \\ s_{\eta y} \end{array} \right\}. \tag{5.2.25}$$

The total higher order degrees of freedom vector $\tilde{\mathbf{v}}$ can then be obtained from the visible degrees of freedom $\mathbf{v}$ as

$$\tilde{\mathbf{v}} = \mathbf{H}\mathbf{v} \quad \text{where} \quad \mathbf{H} = \left[\begin{array}{c} \mathbf{H}_{\theta v} \\ \mathbf{H}_{vt} \end{array} \right] \quad \text{and} \quad \begin{array}{l} \tilde{\mathbf{v}}^T = [\, \theta'_1 \quad \theta'_2 \quad \theta'_3 \quad \theta'_4 \quad \bar{\theta} \quad \tilde{v}_\xi \quad \tilde{v}_\eta \,] \\ \mathbf{v}^T = [\, \mathbf{v}_x^T \quad \mathbf{v}_y^T \quad \boldsymbol{\theta}^T \,] \,. \end{array} \tag{5.2.26}$$

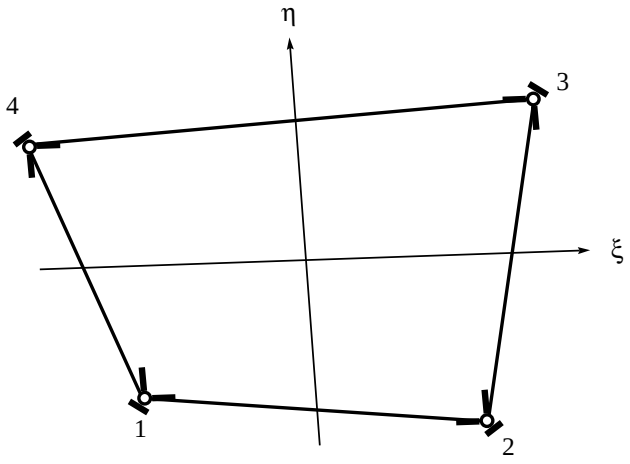

Figure 5.1. Nodal strain gages for membrane.

Higher order strains.
The distribution of higher order strains is expressed in terms of natural strain gage readings. The strain gage locations are placed at the 4 nodes (quadrilateral corners). Readings along three directions are required. These directions are: the ξ and η axis (quadrilateral medians) and the diagonal passing through the neighboring nodes. See Figure 5.1.

The nodal natural strain readings are thus defined as

$$\boldsymbol{\epsilon}_1 = \left\{ \begin{array}{c} \epsilon_\xi \\ \epsilon_\eta \\ \epsilon_{24} \end{array} \right\}, \quad \boldsymbol{\epsilon}_2 = \left\{ \begin{array}{c} \epsilon_\xi \\ \epsilon_\eta \\ \epsilon_{13} \end{array} \right\}, \quad \boldsymbol{\epsilon}_3 = \left\{ \begin{array}{c} \epsilon_\xi \\ \epsilon_\eta \\ \epsilon_{24} \end{array} \right\}, \quad \boldsymbol{\epsilon}_4 = \left\{ \begin{array}{c} \epsilon_\xi \\ \epsilon_\eta \\ \epsilon_{13} \end{array} \right\}. \tag{5.2.27}$$

The next step is to connect these readings to the higher order degrees of freedom. This can be done by defining a generic template

$$\boldsymbol{\epsilon}_i = \mathbf{Q}_i \tilde{\mathbf{v}} \,, \tag{5.2.28}$$

where $\mathbf{Q}_i$ are 3×7 matrices. These templates are worked out below.

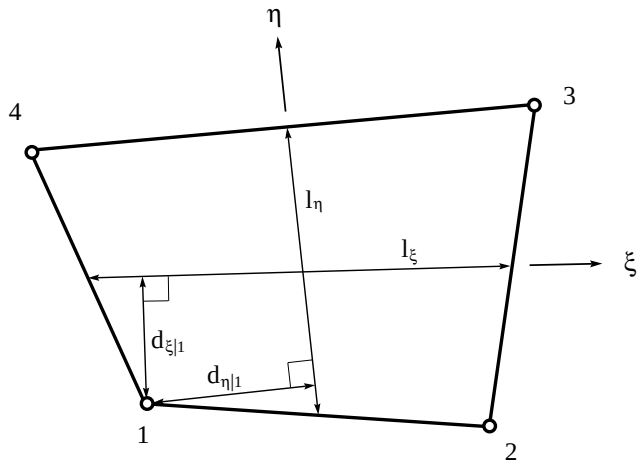

Figure 5.2. Geometric dimensions for a quadrilateral element.

Higher order bending strain field.
The main displacement and strain mode that the field is trying to match is the pure bending of the element along an arbitrary direction. The bending strain field is associated with the higher order degrees of freedom θ_i', $\tilde{v}_\xi$ and $\tilde{v}_\eta$. If one considers pure bending of the element along the ξ direction, it seems intuitive that the ξ strain should be proportional to the distance d_ξ from the ξ-axis. The ξ strain should also be proportional to the curvature along the ξ-axis. In terms of the rotational degrees of freedoms this curvature will have the form $\Delta\theta/l_\xi$ where l_ξ is the element length along the ξ-axis. The ξ strain thus gets coefficients of the form d_ξ/l_ξ associated with the rotational degrees of freedom. Following a similar reasoning for the η strains the strain distribution factors associated with the ξ and η strains are established to be

$$\chi_{\xi|i} = \frac{d_{\xi|i}}{l_\xi} \,, \qquad \chi_{\eta|i} = \frac{d_{\eta|i}}{l_\eta} \,, \tag{5.2.29}$$

where

$$d_{\xi|i} = \sqrt{(\mathbf{r}_i \times \mathbf{s}_\xi) \cdot (\mathbf{r}_i \times \mathbf{s}_\xi)} \,, \quad l_\xi = \sqrt{\mathbf{r}_\xi \cdot \mathbf{r}_\xi} \,, \quad \mathbf{r}_\xi = \frac{1}{2}(\mathbf{r}_2 + \mathbf{r}_3 - \mathbf{r}_1 - \mathbf{r}_4) \,,$$

$$d_{\eta|i} = \sqrt{(\mathbf{r}_i \times \mathbf{s}_\eta) \cdot (\mathbf{r}_i \times \mathbf{s}_\eta)} \,, \quad l_\eta = \sqrt{\mathbf{r}_\eta \cdot \mathbf{r}_\eta} \,, \quad \mathbf{r}_\eta = \frac{1}{2}(\mathbf{r}_3 + \mathbf{r}_4 - \mathbf{r}_1 - \mathbf{r}_2) \,.$$

The quantities $d_{\xi|i}$, $d_{\eta|i}$, l_ξ and l_η are illustrated in Figure 5.2.

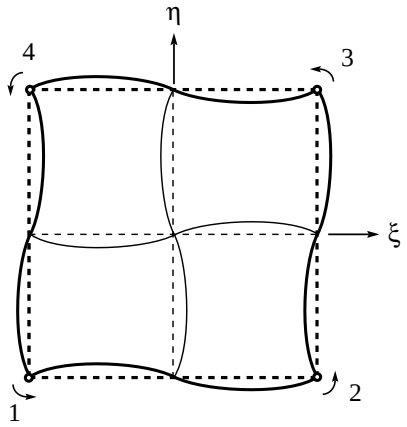

Figure 5.3. Torsional mode for four node membrane element.

The strain distribution sensed by the diagonal strain gages are similarly assumed to be proportional to the curvature along the diagonal, and proportional to the distance from the diagonal as

$$\chi_{24} = \frac{d_{24}}{2l_{24}} , \qquad \chi_{13} = \frac{d_{13}}{2l_{13}} , \tag{5.2.30}$$

where

$$d_{24} = \sqrt{(\mathbf{r}_{31} \times \mathbf{e}_{24}) \cdot (\mathbf{r}_{13} \times \mathbf{e}_{24})} , \quad l_{24} = \sqrt{\mathbf{r}_{24} \cdot \mathbf{r}_{24}} , \quad \mathbf{r}_{24} = (\mathbf{r}_2 - \mathbf{r}_4) ,$$

$$d_{13} = \sqrt{(\mathbf{r}_{31} \times \mathbf{e}_{24}) \cdot (\mathbf{r}_{13} \times \mathbf{e}_{24})} , \quad l_{13} = \sqrt{\mathbf{r}_{13} \cdot \mathbf{r}_{13}} , \quad \mathbf{r}_{13} = (\mathbf{r}_1 - \mathbf{r}_3) .$$

Torsional strain field.
The torsional strain field is associated to the $\bar{\theta}$ higher order degree of freedom. As a guide for the construction of this strain field one can use the torsional displacement mode illustrated in Figure 5.3. This figure indicates that this displacement mode should not induce shear strains, and that ϵ_ξ should be positive in 1st and 3rd quadrants and negative in 2nd and 4th. Similarly, ϵ_η should be positive in 2nd and 4th, and negative in 1st and 3rd quadrants. A simplified strain distribution function for the strains ϵ_ξ and ϵ_η can thus be $N_t = \xi\eta$.

With a unit rotation at all the nodes, the maximum displacement in the ξ direction, u_ξ, will be proportional to the length l_η. Since the strain ϵ_ξ is the gradient of the displacement u_ξ in the ξ direction this strain will be proportional to $1/l_\xi$. The torsional strain field is thus assumed to be

$$\epsilon_\xi = \alpha \frac{l_\eta}{l_\xi} \xi\eta = \alpha \chi_{\xi t}\, \xi\eta, \qquad \epsilon_\eta = -\alpha \frac{l_\xi}{l_\eta} \xi\eta = -\alpha \chi_{\eta t}\, \xi\eta. \tag{5.2.31}$$

Generic nodal strain templates.
With the strain assumptions just described, the nodal strain gage readings can be written down as

$$\mathbf{Q}_1 = \tag{5.2.32}$$
$$\begin{bmatrix} \rho_1\chi_{\xi|1} & \rho_2\chi_{\xi|1} & \rho_3\chi_{\xi|1} & \rho_4\chi_{\xi|1} & \alpha\chi_{\xi t} & -\beta_1\frac{\chi_{\xi|1}}{\bar{\chi}_\xi l_\xi} & 0 \\ -\rho_1\chi_{\eta|1} & -\rho_4\chi_{\eta|1} & -\rho_3\chi_{\eta|1} & -\rho_2\chi_{\eta|1} & -\alpha\chi_{\eta t} & 0 & -\beta_1\frac{\chi_{\eta|1}}{\bar{\chi}_\eta l_\eta} \\ \rho_5\chi_{24} & \rho_6\chi_{24} & \rho_7\chi_{24} & \rho_8\chi_{24} & 0 & \beta_2\frac{c_{24\xi}}{l_{24}} & -\beta_2\frac{c_{24\eta}}{l_{24}} \end{bmatrix},$$

$$\mathbf{Q}_2 = \tag{5.2.33}$$
$$\begin{bmatrix} -\rho_2\chi_{\xi|2} & -\rho_1\chi_{\xi|2} & -\rho_4\chi_{\xi|2} & -\rho_3\chi_{\xi|2} & -\alpha\chi_{\xi t} & -\beta_1\frac{\chi_{\xi|2}}{\bar{\chi}_\xi l_\xi} & 0 \\ \rho_4\chi_{\eta|2} & \rho_1\chi_{\eta|2} & \rho_2\chi_{\eta|2} & \rho_3\chi_{\eta|2} & \alpha\chi_{\eta t} & 0 & \beta_1\frac{\chi_{\eta|2}}{\bar{\chi}_\eta l_\eta} \\ \rho_8\chi_{13} & \rho_5\chi_{13} & \rho_6\chi_{13} & \rho_7\chi_{13} & 0 & -\beta_2\frac{c_{13\xi}}{l_{13}} & \beta_2\frac{c_{13\eta}}{l_{13}} \end{bmatrix},$$

$$\mathbf{Q}_3 = \tag{5.2.34}$$
$$\begin{bmatrix} \rho_3\chi_{\xi|3} & \rho_4\chi_{\xi|3} & \rho_1\chi_{\xi|3} & \rho_2\chi_{\xi|3} & \alpha\chi_{\xi t} & \beta_1\frac{\chi_{\xi|3}}{\bar{\chi}_\xi l_\xi} & 0 \\ -\rho_3\chi_{\eta|3} & -\rho_2\chi_{\eta|3} & -\rho_1\chi_{\eta|3} & -\rho_4\chi_{\eta|3} & -\alpha\chi_{\eta t} & 0 & \frac{\beta_1\chi_{\eta|3}}{\bar{\chi}_\eta l_\eta} \\ \rho_7\chi_{13} & \rho_8\chi_{13} & \rho_5\chi_{13} & \rho_6\chi_{13} & 0 & -\beta_2\frac{c_{13\xi}}{l_{13}} & \beta_2\frac{c_{13\eta}}{l_{13}} \end{bmatrix},$$

$$\mathbf{Q}_4 = \tag{5.2.35}$$
$$\begin{bmatrix} -\rho_4\chi_{\xi|4} & -\rho_3\chi_{\xi|4} & -\rho_2\chi_{\xi|4} & -\rho_1\chi_{\xi|4} & -\alpha\chi_{\xi t} & \beta_1\frac{\chi_{\xi|4}}{\bar{\chi}_\xi l_\xi} & 0 \\ \rho_2\chi_{\eta|4} & \rho_3\chi_{\eta|4} & \rho_4\chi_{\eta|4} & \rho_1\chi_{\eta|4} & \alpha\chi_{\eta t} & 0 & -\beta_1\frac{\chi_{\eta|4}}{\bar{\chi}_\eta l_\eta} \\ \rho_6\chi_{13} & \rho_7\chi_{13} & \rho_8\chi_{13} & \rho_5\chi_{13} & 0 & \beta_2\frac{c_{13\xi}}{l_{13}} & -\beta_2\frac{c_{13\eta}}{l_{13}} \end{bmatrix},$$

where $c_{13\xi} = \mathbf{s}_{13}^T\mathbf{s}_\xi$, $c_{13\eta} = \mathbf{s}_{13}^T\mathbf{s}_\eta$, $c_{24\xi} = \mathbf{s}_{24}^T\mathbf{s}_\xi$ and $c_{24\eta} = \mathbf{s}_{24}^T\mathbf{s}_\eta$.

The cartesian strain displacement matrices at the nodes are obtained by the transformations

$$\begin{aligned} \mathbf{B}_{h1} &= \mathbf{T}_{13}\mathbf{Q}_1 \ , \\ \mathbf{B}_{h3} &= \mathbf{T}_{13}\mathbf{Q}_3 \ , \end{aligned} \quad \text{where} \quad \mathbf{T}_{13}^{-1} = \begin{bmatrix} {s_\xi}_x^2 & {s_\xi}_y^2 & s_{\xi_x}s_{\xi_y} \\ {s_\eta}_x^2 & {s_\eta}_y^2 & s_{\eta_x}s_{\eta_y} \\ {s_{24}}_x^2 & {s_{24}}_y^2 & s_{24_x}s_{24_y} \end{bmatrix}, \tag{5.2.36}$$

$$\begin{aligned} \mathbf{B}_{h2} &= \mathbf{T}_{24}\mathbf{Q}_2 \ , \\ \mathbf{B}_{h4} &= \mathbf{T}_{24}\mathbf{Q}_4 \ , \end{aligned} \quad \text{where} \quad \mathbf{T}_{24}^{-1} = \begin{bmatrix} {s_\xi}_x^2 & {s_\xi}_y^2 & s_{\xi_x}s_{\xi_y} \\ {s_\eta}_x^2 & {s_\eta}_y^2 & s_{\eta_x}s_{\eta_y} \\ {s_{13}}_x^2 & {s_{13}}_y^2 & s_{13_x}s_{13_y} \end{bmatrix}. \tag{5.2.37}$$

A higher order strain field over the element can now be obtained by interpolating the nodal Cartesian strains by use of the bi-linear shape functions defined in (5.1.3).

$$\begin{aligned}\mathbf{B}_h(\xi,\eta) = \quad & (1-\xi)(1-\eta)\mathbf{B}_{h1} + (1+\xi)(1-\eta)\mathbf{B}_{h2} \\ & +(1+\xi)(1+\eta)\mathbf{B}_{h3} + (1-\xi)(1+\eta)\mathbf{B}_{h4} \ .\end{aligned} \tag{5.2.38}$$

Interpolation of these nodal strains does not automatically give a deviatoric higher order strain field. Such a condition can be achieved by subtracting the mean strain values:

$$\mathbf{B}_d(\xi,\eta) = \mathbf{B}_h(\xi,\eta) - \bar{\mathbf{B}}_h \quad \text{where} \quad \bar{\mathbf{B}}_h = \int_A \mathbf{B}(\xi,\eta)\, dA \ . \tag{5.2.39}$$

Optimal coefficients for the strain computation.
When computing the strain displacement expressions symbolically using Mathematica, the contributions of the different coefficients ρ_i and β_i were evaluated with respect to certain higher order strain modes. Based on pure bending of rectangular element shapes the following dependencies between the coefficients were obtained:

$$\begin{aligned} &\rho_2 = -\rho_1 \ , \qquad \rho_3 = \rho_2 \ , \qquad \rho_4 = \rho_1 \ , \\ &\rho_6 = \beta_1 - \rho_1 \ , \qquad \beta_1 = \frac{1}{2} + \rho_1 \ , \\ &\rho_8 = -\rho_6 \ , \qquad \rho_5 = \rho_7 = \beta_2 = 0 \ . \end{aligned} \tag{5.2.40}$$

As seen this makes all the coefficients a function of ρ_1. Optimizing ρ_1 with respect to irregular meshes for the cantilever described in the numerical section suggests $\rho_1 = 0.1$, and the following set of optimal coefficients:

$$\begin{array}{cccc} \rho_1 = 0.1 & \rho_2 = -0.1 & \rho_3 = -0.1 & \rho_4 = 0.1 \\ \rho_5 = 0.0 & \rho_6 = 0.5 & \rho_7 = 0.0 & \rho_8 = -0.5 \\ & \beta_1 = 0.6 & \beta_2 = 0.0 & \end{array} \tag{5.2.41}$$

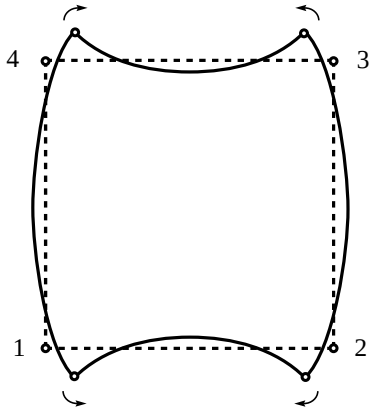

Figure 5.4. Spurious membrane mode for the four node ANDES element.

Stiffness computation for the membrane element.
According to the ANDES formulation the element stiffness is computed as

$$\mathbf{K} = \frac{1}{A}\mathbf{L}\mathbf{C}\mathbf{L}^T + \mathbf{H}^T\tilde{\mathbf{K}}_d\mathbf{H} \quad \text{where} \quad \tilde{\mathbf{K}}_d = \int_A \mathbf{B}_d^T\mathbf{C}\mathbf{B}_d \, dA \, . \tag{5.2.42}$$

Numerical experiments, however, indicate that the element performs better when the element stiffness is computed as

$$\mathbf{K} = \frac{1}{A}\mathbf{L}\mathbf{C}\mathbf{L}^T + \mathbf{H}^T\tilde{\mathbf{K}}_h\mathbf{H} \quad \text{where} \quad \tilde{\mathbf{K}}_h = \int_A \mathbf{B}_h^T\mathbf{C}\mathbf{B}_h \, dA \, , \tag{5.2.43}$$

that is when the non-deviatoric higher order strains are used. This is not strictly justified according to the standard ANDES formulation since the higher order strains displacement matrix $\mathbf{B}_h$ is not energy orthogonal with respect to the constant strain modes for arbitrary element geometries. However, both of the above element stiffness matrices satisfy the Individual Element Test and thus also the conventional Patch Test.

Rank of the stiffness matrix.
Performing an eigenvalue analysis of the element stiffness matrices given in equations (5.2.42) and (5.2.43) it was found that the element has one spurious zero energy mode in addition to the correct three rigid body modes. This spurious mode occurred using a 2×2 Gauss integration rule. It is expected that this spurious mode would disappear with a 3×3 integration rule. For a square element

as shown in Figure 5.4 this spurious mode is defined by the nodal displacement pattern

$$\begin{aligned}\mathbf{v}^T &= [\, v_{x1} \quad v_{x2} \quad v_{x3} \quad v_{x4} \quad v_{y1} \quad v_{y2} \quad v_{y3} \quad v_{y4} \quad \theta_{z1} \quad \theta_{z2} \quad \theta_{z3} \quad \theta_{z4} \,] \\ &= [\ \ 1 \quad -1 \quad -1 \quad\ \ 1 \quad -1 \quad -1 \quad\ \ 1 \quad\ \ 1 \quad\ \ 4 \quad -4 \quad\ \ 4 \quad -4 \,]\,. \end{aligned} \tag{5.2.44}$$

Analysis of a mesh of two elements shows that this the pattern (5.2.44) can not occur in a mesh of more than one element. The spurious mode is then not practically significant for the performance of the element.

5.3 The quadrilateral bending element.

The current approach to deriving the quadrilateral plate bending element utilizes reference lines. Hrennikoff [35] first used this concept for plate modeling where the goal was to come up with a beam framework useful as a model for bending of flat plates.

Park and Stanley [49,61] used the reference line concept in their development of several plate and shell elements based on the ANS formulation. The reference lines were used to find beam-like curvatures; these curvatures were then used to find the plate curvatures through various Assumed Natural Strain distributions. These plate and shell elements were of Mindlin-Reissner type, and the reference lines were treated as Timoshenko beams.

The present element is a Kirchhoff type plate and the reference lines are thus treated like Euler-Bernoulli (or Hermitian) beams.

5.3.1 Basic stiffness.

The basic stiffness for a flat quadrilateral bending element has been developed by extending the triangle element lumping matrices $\mathbf{L}_l$ and $\mathbf{L}_q$ of Militello to four node elements. $\mathbf{L}_l$ and $\mathbf{L}_q$ denotes lumping with respect to a linear and quadratic variation in the normal side rotation respectively.

By ordering the element degrees of freedom as rotation about x and y axis and translation in z direction for each node one obtains the lumped forces from bending as

$$\mathbf{f} = \mathbf{L}_l \boldsymbol{\sigma} \quad \text{or} \quad \mathbf{f} = \mathbf{L}_q \boldsymbol{\sigma} \quad \text{where} \quad \boldsymbol{\sigma} = \begin{Bmatrix} m_{xx} \\ m_{yy} \\ m_{xy} \end{Bmatrix}, \tag{5.3.1}$$

$$\mathbf{L}_l = \begin{bmatrix} \mathbf{L}_{l1} \\ \mathbf{L}_{l2} \\ \mathbf{L}_{l3} \\ \mathbf{L}_{l4} \end{bmatrix}, \qquad \mathbf{L}_q = \begin{bmatrix} \mathbf{L}_{q1} \\ \mathbf{L}_{q2} \\ \mathbf{L}_{q3} \\ \mathbf{L}_{q4} \end{bmatrix} \tag{5.3.2}$$

and

$$\mathbf{f} = \begin{Bmatrix} \mathbf{f}_1 \\ \mathbf{f}_1 \\ \mathbf{f}_1 \\ \mathbf{f}_1 \end{Bmatrix} \quad \text{where} \quad \mathbf{f}_i = \begin{Bmatrix} m_x \\ m_y \\ f_z \end{Bmatrix}. \tag{5.3.3}$$

The lumped node forces at a node j given by lumping matrix $\mathbf{L}_j$, receive contributions from the moments from adjoining sides ij and jk. The lumped force vector at a node j is thus a function of the coordinates of the sides ij and jk only. With linear interpolation of the normal and tangential rotations along a side the lumping matrix becomes

$$\mathbf{L}_{lj} = \frac{1}{2} \begin{bmatrix} 0 & 0 & 0 \\ 0 & -x_{ki} & y_{ki} \\ -y_{ki} & 0 & -x_{ki} \end{bmatrix}, \tag{5.3.4}$$

where superscript l denotes linear variation of normal rotation. If the normal rotation is assumed to vary quadratically in accordance to Hermitian interpolation whereas and the tangential rotation still varies linearly the lumping matrix becomes

$$\mathbf{L}_{qj} = \begin{bmatrix} -c_{jk}s_{jk} + c_{ij}s_{ij} & c_{jk}s_{jk} - c_{ij}s_{ij} & -(s_{jk}^2 - c_{jk}^2) + (s_{ij}^2 + s_{ij}^2) \\ \frac{1}{2}(s_{jk}^2 x_{jk} + s_{ij}^2 x_{ij}) & \frac{1}{2}(c_{jk}^2 x_{jk} + c_{ij}^2 x_{ij}) & -c_{jk}^2 y_{jk} - c_{ij}^2 y_{ij} \\ \frac{1}{2}(s_{jk}^2 y_{jk} + s_{ij}^2 y_{ij}) & \frac{1}{2}(c_{jk}^2 y_{jk} + c_{ij}^2 y_{ij}) & -s_{jk}^2 x_{jk} - s_{ij}^2 x_{ij} \end{bmatrix} \tag{5.3.5}$$

where superscript q is used to denote quadratic variation of normal rotations. The nodal indices (i, j, k, l) in the equations above undergo cyclic permutations of $(1, 2, 3, 4)$ as for the membrane lumping.

5.3.2 Higher order stiffness

The higher order stiffness is computed as the deviatoric part of an ANS type element using the Euler-Bernoulli beam as a reference line strain guide.

Nodal curvatures of a Euler-Bernoulli beam.
The transverse displacement of a Euler-Bernoulli beam, written as a function of the nodal displacements and rotations is

$$w = \mathbf{N}_w \mathbf{v}_{bij} \ , \tag{5.3.6}$$

where

$$\mathbf{N}^T = \frac{1}{8} \begin{Bmatrix} 2\,(\ \ 2+\xi)(-1+\xi)^2 \\ l\,(\ \ 1+\xi)(-1+\xi)^2 \\ 2\,(\ \ 2-\xi)(\ \ 1+\xi)^2 \\ l\,(-1+\xi)(\ \ 1+\xi)^2 \end{Bmatrix} \quad \text{and} \quad \mathbf{v}_{bij} = \begin{Bmatrix} w_i \\ \theta_{ni} \\ w_j \\ \theta_{nj} \end{Bmatrix}.$$

The beam curvatures are

$$\kappa = \frac{\partial^2 w}{\partial x^2} = \frac{1}{l^2} \begin{Bmatrix} 6\xi \\ l\,(-1+3\xi) \\ -6\xi \\ l\,(-1+3\xi) \end{Bmatrix} \mathbf{v}_{bij} \ , \tag{5.3.7}$$

The nodal curvatures are then

$$\begin{Bmatrix} \kappa_{ij|i} \\ \kappa_{ij|j} \end{Bmatrix} = \frac{1}{l^2} \begin{bmatrix} -6 & -4l & 6 & -2l \\ 6 & 2l & -6 & 4l \end{bmatrix} \mathbf{v}_{bij} \tag{5.3.8}$$

The nodal displacements of a reference-line from node i to j can be expressed in terms of the visible degrees of freedom at those nodes as

$$\mathbf{v}_{bij} = \mathbf{T}_{vij} \mathbf{v}_{ij} \tag{5.3.9}$$

$$\begin{Bmatrix} w_i \\ \theta_{ni} \\ w_j \\ \theta_{nj} \end{Bmatrix} = \begin{bmatrix} 1 & 0 & 0 & 0 & 0 & 0 \\ 0 & n_{ij_x} & n_{ij_y} & 0 & 0 & 0 \\ 0 & 0 & 0 & 1 & 0 & 0 \\ 0 & 0 & 0 & 0 & n_{ij_x} & n_{ij_y} \end{bmatrix} \begin{Bmatrix} w_i \\ \theta_{xi} \\ \theta_{y_i} \\ w_j \\ \theta_{y_j} \\ \theta_{y_j} \end{Bmatrix}. \tag{5.3.10}$$

The nodal curvatures expressed in terms of the visible dofs at node i and j then become

$$\begin{Bmatrix} \kappa_{ij|i} \\ \kappa_{ij|j} \end{Bmatrix} = \frac{1}{l^2} \begin{bmatrix} -6 & -4l\,n_{ij_x} & -4l\,n_{ij_y} & 6 & -2l\,n_{ij_x} & -2l\,n_{ij_y} \\ 6 & 2l\,n_{ij_x} & 2l\,n_{ij_y} & -6 & 4l\,n_{ij_x} & 4l\,n_{ij_y} \end{bmatrix} \mathbf{v} \ . \tag{5.3.11}$$

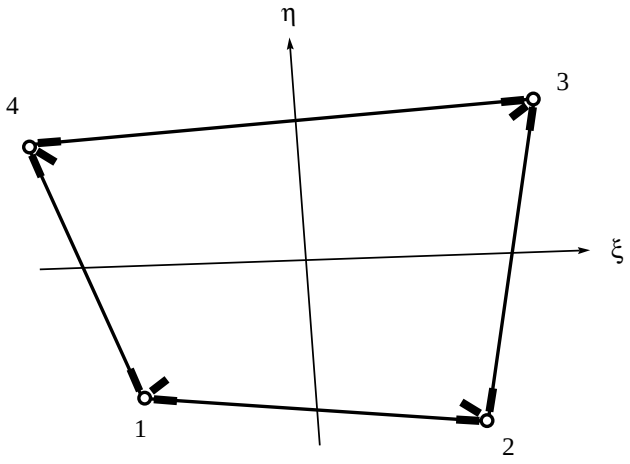

Figure 5.5. Nodal curvature gages for bending.

Nodal natural coordinate curvatures for a quadrilateral.
When one collects all the nodal straingages in a vector $\mathbf{g}$, the strain-gage displacement relationship becomes

$$\mathbf{g} = \mathbf{Q}\mathbf{v} = \mathbf{Q}_F * \mathbf{F}\mathbf{v} \ , \tag{5.3.12}$$

where $*$ denotes entry by entry matrix multiplication, and

$$\begin{aligned} \mathbf{g}^T = [\, &\kappa_{41|1} \quad \kappa_{12|1} \quad \kappa_{13|1} \quad \kappa_{12|2} \quad \kappa_{23|2} \quad \kappa_{24|2} \\ &\kappa_{23|3} \quad \kappa_{34|3} \quad \kappa_{13|3} \quad \kappa_{34|4} \quad \kappa_{41|4} \quad \kappa_{24|4} \,] , \end{aligned} \tag{5.3.13}$$

$$\mathbf{Q}_F = \begin{bmatrix} -6 & 4 & 4 & 0 & 0 & 0 & 0 & 0 & 0 & 6 & 2 & 2 \\ -6 & -4 & -4 & 6 & -2 & -2 & 0 & 0 & 0 & 0 & 0 & 0 \\ -6 & -4 & -4 & 0 & 0 & 0 & 6 & -2 & -2 & 0 & 0 & 0 \\ & & & & & & & & & & & \\ 6 & 2 & 2 & -6 & 4 & 4 & 0 & 0 & 0 & 0 & 0 & 0 \\ 0 & 0 & 0 & -6 & -4 & -4 & 6 & -2 & -2 & 0 & 0 & 0 \\ 0 & 0 & 0 & -6 & -4 & -4 & 0 & 0 & 0 & 6 & -2 & -2 \\ & & & & & & & & & & & \\ 0 & 0 & 0 & 6 & 2 & 2 & -6 & 4 & 4 & 0 & 0 & 0 \\ 0 & 0 & 0 & 0 & 0 & 0 & -6 & -4 & -4 & 6 & -2 & -2 \\ 6 & 2 & 2 & 0 & 0 & 0 & -6 & 4 & 4 & 0 & 0 & 0 \\ & & & & & & & & & & & \\ 0 & 0 & 0 & 0 & 0 & 0 & 6 & 2 & 2 & -6 & 4 & 4 \\ 6 & -2 & -2 & 0 & 0 & 0 & 0 & 0 & 0 & -6 & -4 & -4 \\ 0 & 0 & 0 & 6 & 2 & 2 & 0 & 0 & 0 & -6 & 4 & 4 \end{bmatrix} , \tag{5.3.14}$$

$$\mathbf{F} = \begin{bmatrix} \mathbf{F}_{41} & \mathbf{F}_{41} & \mathbf{F}_{41} & \mathbf{F}_{41} \\ \mathbf{F}_{12} & \mathbf{F}_{12} & \mathbf{F}_{12} & \mathbf{F}_{12} \\ \mathbf{F}_{13} & \mathbf{F}_{13} & \mathbf{F}_{13} & \mathbf{F}_{13} \\ & & & \\ \mathbf{F}_{12} & \mathbf{F}_{12} & \mathbf{F}_{12} & \mathbf{F}_{12} \\ \mathbf{F}_{23} & \mathbf{F}_{23} & \mathbf{F}_{23} & \mathbf{F}_{23} \\ \mathbf{F}_{24} & \mathbf{F}_{24} & \mathbf{F}_{24} & \mathbf{F}_{24} \\ & & & \\ \mathbf{F}_{23} & \mathbf{F}_{23} & \mathbf{F}_{23} & \mathbf{F}_{23} \\ \mathbf{F}_{34} & \mathbf{F}_{34} & \mathbf{F}_{34} & \mathbf{F}_{34} \\ \mathbf{F}_{13} & \mathbf{F}_{13} & \mathbf{F}_{13} & \mathbf{F}_{13} \\ & & & \\ \mathbf{F}_{34} & \mathbf{F}_{34} & \mathbf{F}_{34} & \mathbf{F}_{34} \\ \mathbf{F}_{41} & \mathbf{F}_{41} & \mathbf{F}_{41} & \mathbf{F}_{41} \\ \mathbf{F}_{24} & \mathbf{F}_{24} & \mathbf{F}_{24} & \mathbf{F}_{24} \end{bmatrix} \quad \text{where} \quad \begin{aligned} \mathbf{F}_{12} &= \begin{bmatrix} \frac{1}{l_{12}^2} & \frac{n_{12_x}}{l_{12}} & \frac{n_{12_y}}{l_{12}} \end{bmatrix} \\ \mathbf{F}_{23} &= \begin{bmatrix} \frac{1}{l_{23}^2} & \frac{n_{23_x}}{l_{23}} & \frac{n_{23_y}}{l_{23}} \end{bmatrix} \\ \mathbf{F}_{34} &= \begin{bmatrix} \frac{1}{l_{34}^2} & \frac{n_{34_x}}{l_{34}} & \frac{n_{34_y}}{l_{34}} \end{bmatrix} \\ \mathbf{F}_{41} &= \begin{bmatrix} \frac{1}{l_{41}^2} & \frac{n_{41_x}}{l_{41}} & \frac{n_{41_y}}{l_{41}} \end{bmatrix} \\ \mathbf{F}_{13} &= \begin{bmatrix} \frac{1}{l_{13}^2} & \frac{n_{13_x}}{l_{13}} & \frac{n_{13_y}}{l_{13}} \end{bmatrix} \\ \mathbf{F}_{24} &= \begin{bmatrix} \frac{1}{l_{24}^2} & \frac{n_{24_x}}{l_{24}} & \frac{n_{24_y}}{l_{24}} \end{bmatrix} \end{aligned} . \tag{5.3.15}$$

Cartesian curvatures for a quadrilateral.
The cartesian curvatures $\boldsymbol{\kappa}^T = [\, \kappa_{xx} \quad \kappa_{yy} \quad \kappa_{xy} \,]$ at the nodes can now be obtained as

$$\mathbf{g}_C = \mathbf{Q}_C \mathbf{v} \tag{5.3.16}$$

or

$$\begin{Bmatrix} \boldsymbol{\kappa}_{|1} \\ \boldsymbol{\kappa}_{|2} \\ \boldsymbol{\kappa}_{|3} \\ \boldsymbol{\kappa}_{|4} \end{Bmatrix} = \begin{bmatrix} \mathbf{B}_1 \\ \mathbf{B}_2 \\ \mathbf{B}_3 \\ \mathbf{B}_4 \end{bmatrix} \mathbf{v} = \begin{bmatrix} \mathbf{T}_{\kappa 1} \mathbf{Q}_1 \\ \mathbf{T}_{\kappa 2} \mathbf{Q}_2 \\ \mathbf{T}_{\kappa 3} \mathbf{Q}_3 \\ \mathbf{T}_{\kappa 4} \mathbf{Q}_4 \end{bmatrix} \mathbf{v} \,,$$

where

$$\begin{aligned} \mathbf{T}_{\kappa 1}^{-1} &= \begin{bmatrix} {s_{41}}_x^2 & {s_{41}}_y^2 & s_{41_x} s_{41_y} \\ {s_{12}}_x^2 & {s_{12}}_y^2 & s_{12_x} s_{12_y} \\ {s_{13}}_x^2 & {s_{13}}_y^2 & s_{13_x} s_{13_y} \end{bmatrix} , \\ \mathbf{T}_{\kappa 2}^{-1} &= \begin{bmatrix} {s_{12}}_x^2 & {s_{12}}_y^2 & s_{12_x} s_{12_y} \\ {s_{23}}_x^2 & {s_{23}}_y^2 & s_{23_x} s_{23_y} \\ {s_{24}}_x^2 & {s_{24}}_y^2 & s_{24_x} s_{24_y} \end{bmatrix} , \\ \mathbf{T}_{\kappa 3}^{-1} &= \begin{bmatrix} {s_{23}}_x^2 & {s_{23}}_y^2 & s_{23_x} s_{23_y} \\ {s_{34}}_x^2 & {s_{34}}_y^2 & s_{34_x} s_{34_y} \\ {s_{13}}_x^2 & {s_{13}}_y^2 & s_{13_x} s_{13_y} \end{bmatrix} , \\ \mathbf{T}_{\kappa 4}^{-1} &= \begin{bmatrix} {s_{34}}_x^2 & {s_{34}}_y^2 & s_{34_x} s_{34_y} \\ {s_{41}}_x^2 & {s_{41}}_y^2 & s_{41_x} s_{41_y} \\ {s_{24}}_x^2 & {s_{24}}_y^2 & s_{24_x} s_{24_y} \end{bmatrix} . \end{aligned}$$

The Cartesian curvatures over the element can then be obtained by interpolation of the nodal values as

$$\boldsymbol{\kappa} = \mathbf{B}(\xi, \eta) \mathbf{v} \,, \tag{5.3.17}$$

where

$$\begin{aligned}\mathbf{B}(\xi,\eta) = \quad & (1-\xi)(1-\eta)\mathbf{B}_1 + (1+\xi)(1-\eta)\mathbf{B}_2 \\ & +(1+\xi)(1+\eta)\mathbf{B}_3 + (1-\xi)(1+\eta)\mathbf{B}_4\end{aligned} \ . \tag{5.3.18}$$

Higher order stiffness for the element.
The ANDES higher order stiffness is computed as

$$\mathbf{K}_d = \int_A \mathbf{B}_d^T \mathbf{C}\mathbf{B}_d \, dA \quad \text{where} \quad \mathbf{B}_d = \mathbf{B} - \frac{1}{A}\int_A \mathbf{B} \, dA \ . \tag{5.3.19}$$

5.3.3 The ANS quadrilateral plate bending element.

Clearly one can form an ANS type element by

$$\mathbf{K} = \int_A \mathbf{B}^T \mathbf{C}\mathbf{B} \, dA \tag{5.3.20}$$

i.e. without extracting the mean part of the strain displacement matrix and not including the basic stiffness described in Section 5.3.1.

5.4 The linear non-flat quadrilateral shell element.

The objective of this section is to develop a technique that allows the use of the flat quadrilateral membrane and bending element as parts of a non-flat shell element for linear problems. This is obtained by formulating a linear projector matrix, which for the linear case restores equilibrium at the undeformed element geometry. This can also be obtained by using the nonlinear projector with respect to the initial geometry. In fact the linear and nonlinear projector gives identical results for linear problems. However the linear projector is recommended for linear finite element codes due to its greater simplicity.

The four node shell element is obtained by assembling the membrane element and bending element to the appropriate degrees of freedom. This is sufficient as long as the shell element is strictly flat since both the membrane and bending elements are developed as flat elements. Unfortunately, four node shell elements on a "real" structure quite often end up being warped. To restore or improve the behavior of the warped element one can use a projection technique similar to that developed by Rankin and coworkers [46,53].

The element stiffness matrix does not have the correct rigid body modes if the element geometry is warped since the element stiffness has been developed using the projected flat positions of the element nodes. This causes two deficiencies of the element stiffness:

1. The element picks up strains and thus forces from a rigid body displacement vector i.e. $\mathbf{f}_r = \mathbf{K}\mathbf{v}_r \neq \mathbf{0}$.

2. The element forces are not in self equilibrium and the force vector will thus pick up energy for a rigid body motion. $\mathbf{v}_r^T\mathbf{f} = \mathbf{v}_r^T\mathbf{K}\mathbf{v} \neq \mathbf{0}$.

These two statements are equivalent for a symmetric element stiffness matrix. If an element stiffness has columns that are in self equilibrium the element has the correct rigid body modes and vice versa.

The foregoing deficiencies lead to the investigation of the element internal energy

$$\begin{aligned}\Phi &= \frac{1}{2}\mathbf{v}^T\mathbf{K}\mathbf{v} = \frac{1}{2}(\mathbf{v}_r^T + \mathbf{v}_d^T)\mathbf{K}(\mathbf{v}_r + \mathbf{v}_d) \\ &= \frac{1}{2}(\mathbf{v}_d^T\mathbf{K}\mathbf{v}_d + \mathbf{v}_d^T\mathbf{K}\mathbf{v}_r + \mathbf{v}_r^T\mathbf{K}\mathbf{v}_d + \mathbf{v}_r^T\mathbf{K}\mathbf{v}_r).\end{aligned} \tag{5.4.1}$$

If the element fails the equilibrium and rigid-body conditions;

$$\mathbf{v}_r^T\mathbf{K}\mathbf{v}_r \neq 0\ , \quad \mathbf{v}_r^T\mathbf{K}\mathbf{v}_d \neq 0 \quad \text{and} \quad \mathbf{v}_d^T\mathbf{K}\mathbf{v}_r \neq 0\ . \tag{5.4.2}$$

To extract the deformational energy, the total displacements are split into deformational and rigid body motions, the latter being spanned by the matrix $\mathbf{R}$:

$$\mathbf{v} = \mathbf{v}_d + \mathbf{v}_r = \mathbf{v}_d + \mathbf{R}\mathbf{a}. \tag{5.4.3}$$

By requiring that the deformational displacement vector be orthogonal to the rigid body modes one must have $\mathbf{R}^T\mathbf{v}_d = \mathbf{0}$. On pre-multiplying the equation above with $\mathbf{R}^T$ the rigid body amplitudes can be solved for:

$$\mathbf{R}^T\mathbf{v} = \mathbf{R}^T\mathbf{R}\mathbf{a} \quad \Rightarrow \quad \mathbf{a} = (\,\mathbf{R}^T\mathbf{R}\,)^{-1}\mathbf{R}\mathbf{v}\ , \tag{5.4.4}$$

from which the deformational displacement vector can be extracted as

$$\mathbf{v}_d = \mathbf{v} - \mathbf{v}_r = (\,\mathbf{I} - \mathbf{R}\,(\,\mathbf{R}^T\mathbf{R}\,)^{-1}\mathbf{R}\,)\,\mathbf{v} = \mathbf{P}_d\mathbf{v}. \tag{5.4.5}$$

If $\mathbf{R}$ is orthonormal the foregoing expression simplifies to

$$\mathbf{P}_d = \mathbf{I} - \mathbf{R}\mathbf{R}^T. \tag{5.4.6}$$

Applying this projection to gain invariance of the internal energy with respect to rigid body motion $\Phi(\mathbf{v}) = \Phi(\mathbf{v}_d)$ yields

$$\Phi(\mathbf{v}_d) = \frac{1}{2}\mathbf{v}_d^T\mathbf{K}\mathbf{v}_d = \frac{1}{2}\mathbf{v}^T\mathbf{P}_d^T\mathbf{K}\mathbf{P}_d\mathbf{v} = \frac{1}{2}\mathbf{v}^T\mathbf{K}_d\mathbf{v}\ . \tag{5.4.7}$$

5.4.1 Linear projector matrix for a general quad.

In order to express the rigid body modes one defines the vector $\mathbf{r}_i$ from the element centroid to node i as

$$\tilde{\mathbf{r}}_i = \mathbf{r}_i - \bar{\mathbf{r}} \ , \quad \text{where} \quad \mathbf{r}_i = \left\{ \begin{array}{c} x_i \\ y_i \\ z_i \end{array} \right\} \quad \text{and} \quad \bar{\mathbf{r}} = \frac{1}{4} \sum_{i=1}^{4} \mathbf{r}_i \ . \tag{5.4.8}$$

By ordering the element degrees of freedom as

$$\mathbf{v} = \left\{ \begin{array}{c} \mathbf{v}_1 \\ \mathbf{v}_2 \\ \mathbf{v}_3 \\ \mathbf{v}_4 \end{array} \right\} \qquad \text{where} \qquad \mathbf{v}_i = \left\{ \begin{array}{c} v_{xi} \\ v_{yi} \\ v_{zi} \\ \theta_{xi} \\ \theta_{yi} \\ \theta_{zi} \end{array} \right\} \tag{5.4.9}$$

the rigid body modes can be expressed as

$$\mathbf{R} = \begin{bmatrix} \mathbf{R}_1 \\ \mathbf{R}_2 \\ \mathbf{R}_3 \\ \mathbf{R}_4 \end{bmatrix}, \qquad \mathbf{R}_i = \begin{bmatrix} \mathbf{I} & -\mathrm{Spin}(\tilde{\mathbf{r}}_i) \\ \mathbf{0} & \mathbf{I} \end{bmatrix} = \begin{bmatrix} 1 & 0 & 0 & 0 & \tilde{z}_i & -\tilde{y}_i \\ 0 & 1 & 0 & -\tilde{z}_i & 0 & \tilde{x}_i \\ 0 & 0 & 1 & \tilde{y}_i & -\tilde{x}_i & 0 \\ 0 & 0 & 0 & 1 & 0 & 0 \\ 0 & 0 & 0 & 0 & 1 & 0 \\ 0 & 0 & 0 & 0 & 0 & 1 \end{bmatrix} . \tag{5.4.10}$$

The projector matrix becomes

$$\mathbf{P}_d = \mathbf{I} - \mathbf{R}(\mathbf{R}^T\mathbf{R})^{-1}\mathbf{R}^T \ , \tag{5.4.11}$$

where

$$\mathbf{R}^T\mathbf{R} = \begin{bmatrix} 4\mathbf{I} & \mathbf{0} \\ \mathbf{0} & \mathbf{S} \end{bmatrix} \quad \text{with} \quad \mathbf{S} = 4\mathbf{I} - \sum_{i=1}^{4} \mathrm{Spin}(\tilde{\mathbf{r}}_i)\mathrm{Spin}(\tilde{\mathbf{r}}_i) \ .$$

This simplifies the computation of the projector matrix because only the lowest 3×3 submatrix of $\mathbf{R}^T\mathbf{R}$ is non-diagonal, and $(\mathbf{R}^T\mathbf{R})^{-1}$ can be efficiently formed.

5.5 Nonlinear extensions for quadrilateral shell element.

The nonlinear extensions for an element consists of defining a procedure that aligns the shadow element C_{0n} as close as possible to the deformed element C_n. This defines the element deformational displacement vector $\mathbf{v}_d$.

One also needs to form the rotational gradient of the shadow element with respect to the visible degrees of freedom of the deformed element, as stated in equation (2.4.12). In the local coordinate system this relation is

$$\delta\tilde{\boldsymbol{\omega}}_r = \frac{\partial\tilde{\boldsymbol{\omega}}_r}{\partial\tilde{v}_i}\delta v_i = \tilde{\mathbf{G}}\,\delta\tilde{\mathbf{v}}\ . \tag{5.5.1}$$

The local coordinate relationship is sought since this is is needed in forming the geometric stiffness of the element as expressed in equation (2.8.22) .

The rotation of the shadow element is most easily obtained from the rotation of the shared or common local frame for the C_{0n} and C_n configurations. This orthogonal element coordinate frame with unit axis vectors $\mathbf{e}_1$, $\mathbf{e}_2$ and $\mathbf{e}_3$ is rigidly attached to the shadow element C_{0n}, since this element only moves as a rigid body, and elastically attached to the deformed and elastic element C_n. This local coordinate system for a quadrilateral element can be defined in various ways. Most researchers select the element z-axis unit vector as the cross product of the diagonals vectors $\mathbf{d}_{13}$ and $\mathbf{d}_{24}$

$$\mathbf{e}_3 = \frac{\mathbf{d}_{13}\times\mathbf{d}_{24}}{A_p} \quad \text{where} \quad A_p = \sqrt{(\mathbf{d}_{13}\times\mathbf{d}_{24})^T(\mathbf{d}_{13}\times\mathbf{d}_{24})} \tag{5.5.2}$$

This defines A_p as the area of the element projection on the local $x-y$ plane.

The positioning of the x and y axis unit vectors $\mathbf{e}_1$ and $\mathbf{e}_2$ differs among researchers. Rankin and Brogan [52] chooses $\mathbf{e}_2$ to coincide with the projection of the side edge 24 on the plane normal to $\mathbf{e}_3$. This effectively lets only one of the side edges determine the rigid rotation of the element about the local z axis. The origin of the element coordinate system is chosen to coincide with node 1. When this procedure is performed for both the C_0 and C_n element configurations the net result is that the shadow element C_{0n} will be positioned relative to C_n so that nodes 1 coincide and the projections of side edge 24 on the (x, y) plane coincide. A consequence of this choice is that the element deformational displacement vector $\mathbf{v}_d$, which is the difference between the coordinate between the C_n and C_{0n} coordinates, is not invariant with respect to the element node numbering.

Bergan and Nygård [47] choose vector $\mathbf{e}_1$ and $\mathbf{e}_2$ to coincide with the directions of side edge 12 and 14 for a rectangle that is positioned relative to the quadrilateral element so that the sum of the angles between the side edges of the quadrilateral and rectangle is zero. The origin of the coordinate system

is chosen at node 1. By applying this to both the C_0 and C_n configurations the shadow element C_{0n} is positioned relative to the deformed element C_n so that the element centroids coincide and so that the sum of the square of the angles between the side edges of C_{0n} and C_n is minimized. This represents a least square fit with respect to the side edge angular errors. This procedure gives a element deformational displacement vector $\mathbf{v}_d$ which produces an internal force vector $\mathbf{f}_e = \mathbf{K}_e\mathbf{v}_d$ that is invariant with respect to the node numbering of the element, provided that the element stiffness matrix $\mathbf{K}_e$ satisfies the correct rigid body translations.

5.5.1 Aligning side 12 of C_{0n} and C_n.

The element frame is positioned at the element centroid. This change from Rankin's positioning at node 1 has been done in order to satisfy the orthogonality condition for $\mathbf{P}_T\mathbf{P}_R = \mathbf{0}$ as expressed in equation (2.4.43) . Rankin's formulation did not contain $\mathbf{P}_T$ so this requirement was ignored.

By expressing the nodal coordinates of the element in the local coordinate system equation (5.5.2) gives

$$\tilde{\mathbf{e}}_3 = \begin{Bmatrix} \tilde{e}_{3x} \\ \tilde{e}_{3y} \\ \tilde{e}_{3z} \end{Bmatrix} = \frac{1}{A_p} \begin{Bmatrix} \tilde{y}_{31}\tilde{z}_{42} - \tilde{y}_{42}\tilde{z}_{31} \\ -\tilde{x}_{31}\tilde{z}_{42} + \tilde{x}_{42}\tilde{z}_{31} \\ \tilde{x}_{31}\tilde{y}_{42} - \tilde{x}_{42}\tilde{y}_{31} \end{Bmatrix}, \tag{5.5.3}$$

where

$$A_p = \sqrt{(\tilde{y}_{31}\tilde{z}_{42} - \tilde{y}_{42}\tilde{z}_{31})^2 + (-\tilde{x}_{31}\tilde{z}_{42} + \tilde{x}_{42}\tilde{z}_{31})^2 + (\tilde{x}_{31}\tilde{y}_{42} - \tilde{x}_{42}\tilde{y}_{31})^2}\ . \tag{5.5.4}$$

These expressions simplify, but the full expressions has to be kept in order to obtain the correct variation with respect to the nodal coordinates. The $\tilde{\omega}_x$ and $\tilde{\omega}_y$ variation can now be obtained from the variation of e_{3y} and e_{3x} respectively

$$\begin{aligned} \delta\tilde{\omega}_x &= -(\frac{\partial\tilde{e}_{3y}}{\partial\tilde{x}_i}\delta\tilde{x}_i + \frac{\partial\tilde{e}_{3y}}{\partial\tilde{y}_i}\delta\tilde{y}_i + \frac{\partial\tilde{e}_{3y}}{\partial\tilde{z}_i}\delta\tilde{z}_i)\ , \\ \delta\tilde{\omega}_y &= \ \ (\frac{\partial\tilde{e}_{3x}}{\partial\tilde{x}_i}\delta\tilde{x}_i + \frac{\partial\tilde{e}_{3x}}{\partial\tilde{y}_i}\delta\tilde{y}_i + \frac{\partial\tilde{e}_{3x}}{\partial\tilde{z}_i}\delta\tilde{z}_i)\ . \end{aligned} \tag{5.5.5}$$

The variation of $\tilde{\omega}_x$ and $\tilde{\omega}_y$ with respect to the in-plane coordinate components of the nodes $\tilde{x}_i$ and $\tilde{y}_i$ is zero since

$$\frac{\partial\tilde{e}_{3x}}{\partial\tilde{x}_i} = \frac{\partial\tilde{e}_{3x}}{\partial\tilde{y}_i} = \frac{\partial\tilde{e}_{3y}}{\partial\tilde{x}_i} = \frac{\partial\tilde{e}_{3y}}{\partial\tilde{y}_i} = 0\ . \tag{5.5.6}$$

This gives the variation of the in-plane rotations $\tilde{\omega}_x$ and $\tilde{\omega}_y$ as function of the out of plane displacements only:

$$\begin{aligned} \delta\tilde{\omega}_x &= -\frac{\partial \tilde{e}_{3x}}{\partial \tilde{z}_i}\delta\tilde{z}_i = \sum_{i=1}^{4} \frac{\tilde{x}_{lj}}{A_p}\delta\tilde{z}_i \ , \\ \delta\tilde{\omega}_y &= \ \ \frac{\partial \tilde{e}_{3y}}{\partial \tilde{z}_i}\delta\tilde{z}_i = \sum_{i=1}^{4} \frac{\tilde{y}_{lj}}{A_p}\delta\tilde{z}_i \ , \end{aligned} \qquad \text{with} \quad A_p = \tilde{x}_{31}\tilde{y}_{42} - \tilde{x}_{42}\tilde{y}_{31} \ , \tag{5.5.7}$$

where the nodal indices (i, j, k, l) takes cyclic permutations of $(1, 2, 3, 4)$.

The $\mathbf{e}_1$ vector is chosen to lie along the projection of side 12 in the x-y plane. This gives the y axis unit vector as

$$\mathbf{e}_2 = \frac{\mathbf{e}_3 \times \mathbf{r}_{12}}{l_{12}} \ , \tag{5.5.8}$$

where l_{12} is the projected length of side 12 in the x-y plane. By expressing $\mathbf{e}_2$ in the local coordinate system the variation of $\tilde{\omega}_z$ can be obtained as

$$\delta\tilde{\omega}_z = -(\frac{\partial \tilde{e}_{2x}}{\partial \tilde{x}_i}\delta\tilde{x}_i + \frac{\partial \tilde{e}_{2x}}{\partial \tilde{y}_i}\delta\tilde{y}_i + \frac{\partial \tilde{e}_{2x}}{\partial \tilde{z}_i}\delta\tilde{z}_i) \ . \tag{5.5.9}$$

Carrying out the derivations gives

$$\delta\tilde{\omega}_z = \frac{1}{l_{12}}(\delta\tilde{y}_1 + \delta\tilde{y}_2) - \sum_{i=1}^{4} \frac{\tilde{x}_{lj}\, z_{21}}{A_p}\delta\tilde{z}_i \ , \tag{5.5.10}$$

where A_p is defined in equation (5.5.7).

The rotation gradient matrix in equation (5.5.1) can now be expressed as

$$\tilde{\mathbf{G}} = [\, \tilde{\mathbf{G}}_1 \quad \tilde{\mathbf{G}}_2 \quad \tilde{\mathbf{G}}_3 \,] = \begin{bmatrix} \tilde{\mathbf{G}}_{\omega_x} \\ \tilde{\mathbf{G}}_{\omega_y} \\ \tilde{\mathbf{G}}_{\omega_z} \end{bmatrix} \tag{5.5.11}$$

where

$$\begin{aligned} \tilde{\mathbf{G}}_1 &= \frac{1}{A_p}\begin{bmatrix} 0 & 0 & x_{42} & 0 & 0 & 0 \\ 0 & 0 & y_{42} & 0 & 0 & 0 \\ 0 & -\frac{A_p}{l_{12}} & x_{42}z_{21} & 0 & 0 & 0 \end{bmatrix}, \\ \tilde{\mathbf{G}}_2 &= \frac{1}{A_p}\begin{bmatrix} 0 & 0 & x_{13} & 0 & 0 & 0 \\ 0 & 0 & y_{13} & 0 & 0 & 0 \\ 0 & \frac{A_p}{l_{12}} & x_{13}z_{21} & 0 & 0 & 0 \end{bmatrix} \\ \tilde{\mathbf{G}}_3 &= \frac{1}{A_p}\begin{bmatrix} 0 & 0 & x_{24} & 0 & 0 & 0 \\ 0 & 0 & y_{24} & 0 & 0 & 0 \\ 0 & 0 & x_{24}z_{21} & 0 & 0 & 0 \end{bmatrix}, \\ \tilde{\mathbf{G}}_4 &= \frac{1}{A_p}\begin{bmatrix} 0 & 0 & x_{31} & 0 & 0 & 0 \\ 0 & 0 & y_{31} & 0 & 0 & 0 \\ 0 & 0 & x_{42}z_{31} & 0 & 0 & 0 \end{bmatrix}. \end{aligned} \tag{5.5.12}$$

The rotation gradient matrix as expressed here can be split as $\tilde{\mathbf{G}} = \tilde{\mathbf{X}}\mathbf{A}$ where $\tilde{\mathbf{X}}$ contains all the coordinate dependencies and $\mathbf{A}$ is constant matrix. This is possible since none of the vector components of $\delta\tilde{\boldsymbol{\omega}}$ is a function of more than three distinct coordinate expressions. This $\tilde{\mathbf{G}}$ thus satisfies the consistency requirement set forth in equation (2.5.8).

5.5.2 Least square fit of side edge angular errors.

The orientation of $\mathbf{e}_3$ is the same as with Rankin's procedure, which gives identical expressions for the rotations $\tilde{\omega}_x$ and $\tilde{\omega}_y$. The positioning procedure of Bergan and Nygårds [47] positioning procedure can be viewed as a least square fit of the side edge angular errors between the C_{0n} and C_n configurations. This gives different expressions for the variation of the angle $\tilde{\omega}_z$ with respect to the visible degrees of freedom. The nodal submatrices $\tilde{\mathbf{G}}_i$ of $\tilde{\mathbf{G}}$ can then be defined as

$$\mathbf{G}_i = \frac{1}{A_p}\begin{bmatrix} 0 & 0 & x_{lj} & \\ 0 & 0 & y_{lj} & \mathbf{0} \\ \frac{A_p}{4}(\frac{n_{ij\,x}}{l_{ij}} - \frac{n_{ki\,x}}{l_{ki}}) & \frac{A_p}{4}(\frac{n_{ij\,y}}{l_{ij}} - \frac{n_{ki\,y}}{l_{ki}}) & (x_{lj}f_x + y_{lj}f_y) & \end{bmatrix}, \quad (5.5.13)$$

where

$$\begin{aligned} f_x &= \frac{1}{4}(\frac{z_{21}x_{21}}{l_{21}} + \frac{z_{32}x_{32}}{l_{32}} + \frac{z_{43}x_{43}}{l_{43}} + \frac{z_{14}x_{14}}{l_{14}}) \,, \\ f_y &= \frac{1}{4}(\frac{z_{21}y_{21}}{l_{21}} + \frac{z_{32}y_{32}}{l_{32}} + \frac{z_{43}y_{43}}{l_{43}} + \frac{z_{14}y_{14}}{l_{14}}) \,, \end{aligned} \quad (5.5.14)$$

and $\tilde{\mathbf{n}}_{ij}$ and l_{ij} is the outward normal and length of side edge ij respectively:

$$\mathbf{n}_{ij} = \frac{1}{l_{ij}}\begin{Bmatrix} y_{ji} \\ -x_{ji} \\ 0 \end{Bmatrix} \quad \text{and} \quad l_{ij} = \sqrt{x_{ij}^2 + y_{ij}^2} \,. \quad (5.5.15)$$

The nodal indices (i, j, k, l) undergo cyclic permutations of $(1, 2, 3, 4)$.

The $\tilde{\mathbf{G}}$ derived above can not be expressed as $\tilde{\mathbf{G}} = \tilde{\mathbf{X}}\mathbf{A}$ where the 3×3 matrix $\tilde{\mathbf{X}}$ contains all the coordinate dependencies of $\tilde{\mathbf{G}}$, since the expressions for $\tilde{\omega}_z$ contains more than three distinct coordinate expressions. This will give a loss in convergence rate if the deformed configuration C_n and shadow configuration C_{0n} are far apart since the present tangent stiffness expressions have omitted terms containing the unbalanced element forces. See Section 2.5.2.

Chapter 6

Numerical examples for linear analysis.

This Chapter presents numerical examples of several linear test problems. These are used to validate the formulation of the linear ANDES elements that represents the "kernel" of the co-rotational formulation.

6.1 Patch tests.

The Patch Test has become a standard test for evaluation of new finite elements. Though neither a necessary or sufficient condition for convergence, it has a strong following who considers the test "necessary" for an element to be considered reliable. However, there is little disagreement about the tests value as a debugging tool when an element is implemented in an actual finite element code.

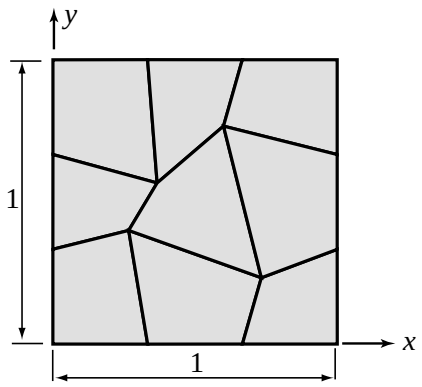

Figure 6.1. Patch test for quadrilateral elements.

The patch shown on Figure 6.1 has been used to perform the patch test for the new ANDES4 element by giving the boundary nodes displacements according to a constant strain pattern. The patch test requires that the internal nodes get displacements that satisfies this constant strain displacement mode exactly.

Membrane tests.

$$u = x \qquad \Rightarrow \epsilon_{xx} = \frac{\partial u}{\partial x} = 1 \qquad : \quad \text{Identically satisfied.}$$

$$v = y \qquad \Rightarrow \epsilon_{yy} = \frac{\partial v}{\partial y} = 1 \qquad : \quad \text{Identically satisfied.}$$

$$u = y, v = x \qquad \Rightarrow \gamma_{xy} = (\frac{\partial u}{\partial y} + \frac{\partial v}{\partial x}) = 2 \qquad : \quad \text{Identically satisfied.}$$

Bending tests.

$$w = x^2 \qquad \Rightarrow \kappa_{xx} = \frac{\partial^2 w}{\partial x^2} = 2 \qquad : \quad \text{Identically satisfied.}$$

$$w = y^2 \qquad \Rightarrow \kappa_{yy} = \frac{\partial^2 w}{\partial y^2} = 2 \qquad : \quad \text{Identically satisfied.}$$

$$w = xy \qquad \Rightarrow \kappa_{xy} = 2\frac{\partial^2 w}{\partial x \partial y} = 2 \qquad : \quad \text{Identically satisfied.}$$

The membrane patch test for the ANDES4 element are satisfied regardless of whether the higher order strain displacement matrix $\mathbf{B}_h$ or the deviatoric higher order strain displacement matrix $\mathbf{B}_d = \mathbf{B}_h - \bar{\mathbf{B}}_h$ is used for the higher order membrane stiffness according to equation (5.2.42) and (5.2.43).

6.2 Membrane problems.

6.2.1 Shear-loaded cantilever beam.

A shear loaded cantilever beam is defined according to Figure 8.1. This Figure also shows the 16×4 regular and irregular element meshes.

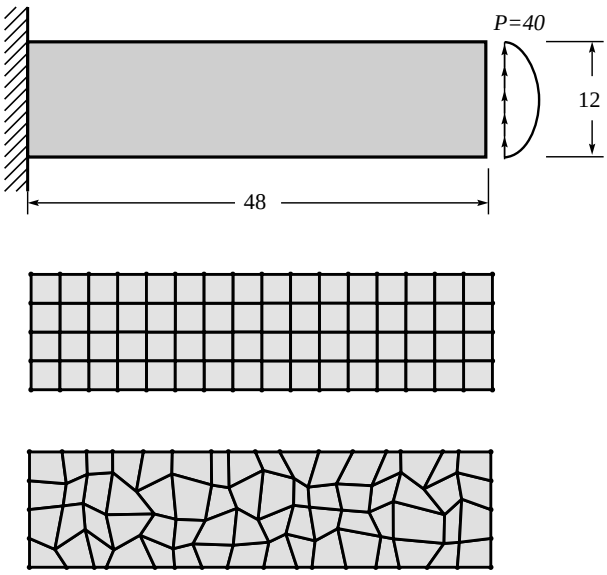

Figure 6.2. Cantilever under end shear. $E = 30000$ $\nu = 0.25$

The test has been run using a totally clamped boundary at the fixed end, and the applied nodal forces on the end cross-section are consistent lumping of a shear load with parabolic variation in the y-direction.

The comparison value is the tip deflection of 0.35583 at the end of the beam. This number is the exact solution of the two-dimensional plane stress as given in [28] . The numerical results have been scaled so that the analytical displacement of 0.35583 corresponds to 100 in Table 6.1. Table 6.1 also includes numerical results for the quatrilateral FFQ and the triangular FFT as described by Nygård in [47].

Table 6.1. Tip deflection of cantilever beam.

Element	$x \times y$ -subdivisions				
	4×1	8×2	16×4	32×8	64×16
Regular element mesh					
CST	25.48	55.24	82.66	94.96	98.71
QSHELL3	111.78	101.18	100.03	99.97	100.01
QSHELL4	97.72	98.86	99.54	99.87	100.00
Irregular element mesh					
CST	27.86	55.84	81.47	94.27	98.41
QSHELL3	98.16	100.12	99.66	99.87	99.97
QSHELL4	103.93	98.60	99.45	99.90	100.01

Table 6.1 shows very similar convergence rates for the QSHELL3 and QSHELL4 element compared to Nygårds FFT and FFQ element. However, the ANDES elements tend to be more flexible for very coarse meshes.

6.3 Bending problems.

6.3.1 Centrally loaded square plate.

A square plate subjected to a central load of $P = 40.0$. The test has been run with both simply supported and fully clamped boundary conditions.

Plate dimensions are 100.0×100.0 with thickness $t = 2.0$ and material properties $E = 1500.0$ and $\nu = 0.2$. Due to symmetry only a quarter of the plate have been modeled.

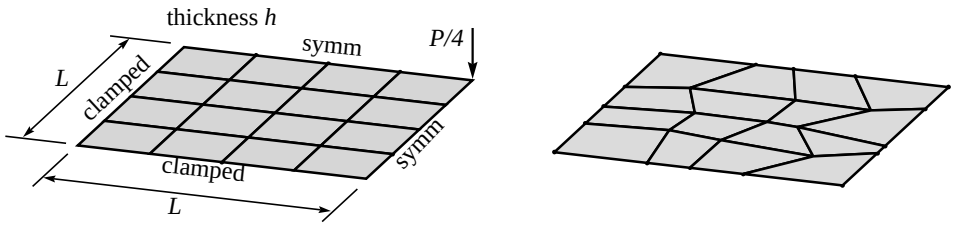

Figure 6.3. 4×4 quarter model of centrally loaded square plate.

Table 6.2. Central deflection of square plate with clamped boundary. Displacement 2.1552 is scaled to 100.00 .

Element type	Mesh over quarter plate 1×1	2×2	4×4	8×8	16×16	32×32
Regular mesh.						
BCIZ-SQ	88.223	102.71	101.18	100.37	100.10	100.02
ANDES3	92.798	103.75	101.57	100.50	100.15	100.04
ANDES4	88.944	100.07	100.18	100.07	100.02	100.00
Irregular mesh.						
BCIZ-SQ	88.223	99.805	101.27	99.781	99.983	99.938
ANDES3	92.798	102.48	102.38	100.40	100.23	100.02
ANDES4	88.944	99.793	101.71	100.19	100.14	100.02

6.4 Shell problems.

6.4.1 Pinched cylinder problem.

An open cylinder is subjected to two diametrically opposite point loads. Due to symmetry only 1/8 of the problem is modeled. The geometry of the 1/8 model is shown in Figure 6.4.

The mesh has been given an increasing distortion angle θ. As θ increases the four node elements are no longer flat elements. This induced warping gives different results for the projected and unprojected versions of the ANDES4 element. The ANDES3 element is invariant under projection because the element always possesses the correct rigid body modes.

The improvement with the projected stiffness matrix for the ANDES4 element is dramatic. This example displays the importance of correct rigid body modes, as well as showing the robustness of the stiffness projection procedure.

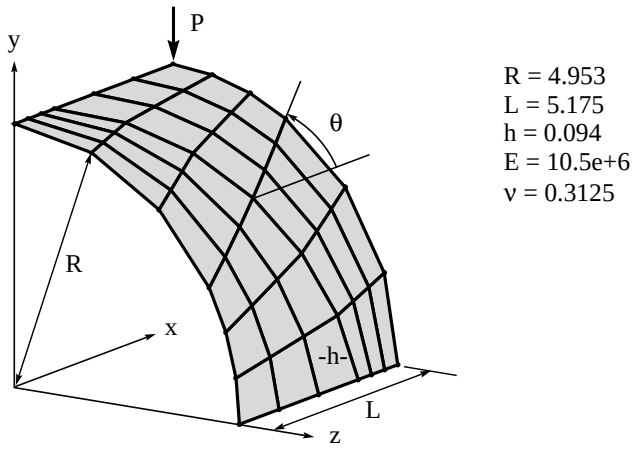

Figure 6.4. Pinched cylinder problem.

Table 6.3. Vertical displacement under load for pinched cylinder. Displacement 4.5301×10^{-3} is scaled to 100.00.

Element type	Distortion angle $\theta = 0°$	$\theta = 10°$	$\theta = 20°$	$\theta = 30°$	$\theta = 40°$
ANDES3 Unproj	99.578	99.136	98.737	98.296	97.608
ANDES3 Proj	99.578	99.136	98.737	98.296	97.608
ANDES4 Unproj	99.430	30.594	12.652	9.381	7.960
ANDES4 Proj	99.430	99.334	99.255	99.125	98.789

6.4.2 Pinched hemisphere problem.

A hemispherical shell is subjected to two pairs of diametrically opposite loads along the x and y axis respectively. Due to symmetry only a 1/4 model is used according to Figure 6.5.

This problem is often modelled with a hole at the top of the hemisphere. This allows using a mesh of strictly flat quadrilateral elements, which makes the test much less demanding for quadrilateral elements. One has chosen to model the hemisphere without a hole since this gives warped elements for the quadrilateral element meshes, and thus poses a much more severe test for those elements.

For the triangular ANDES3 two discretizations are used. Mesh 1 in Table 6.4 refers to a mesh where two triangular elements join at the loaded nodes, whereas Mesh 2 has one element attached to the loaded nodes.

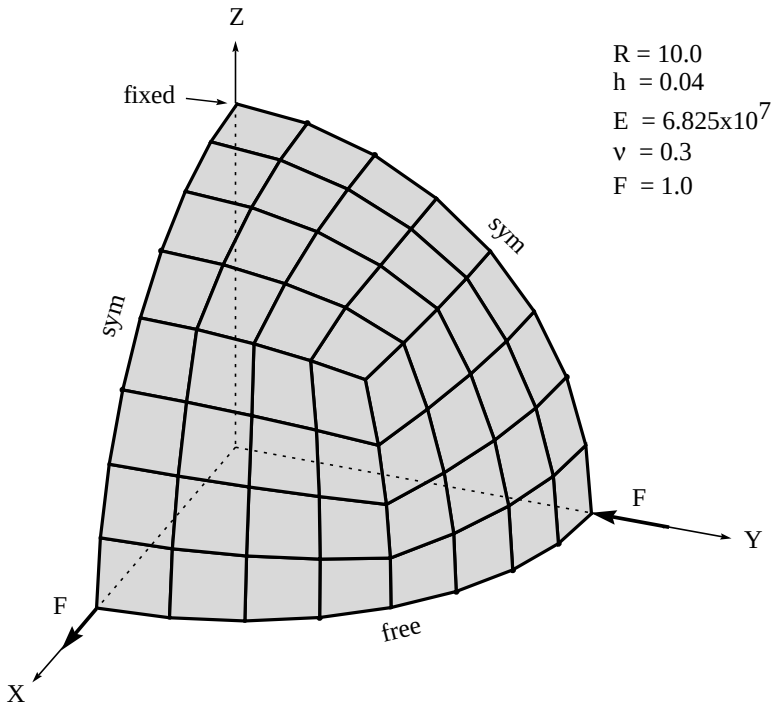

Figure 6.5. Pinched hemisphere problem.

Table 6.4. Displacements under loads for pinched hemisphere. Displacement 9.1898×10^{-2} is scaled to 100.00.

Element	Elements per side					
type	2	4	8	12	16	20
ANDES3 Mesh 1	0.18	2.59	25.30	61.44	83.23	92.52
ANDES3 Mesh 2	0.42	4.07	31.91	68.23	86.85	94.23
ANDES4 Unproj	13.57	6.13	12.85	19.49	25.17	30.18
ANDES4 Proj	67.55	23.73	85.53	97.24	99.39	100.00

This test again shows the dramatic improvement of the performance of the ANDES4 element when the stiffness projection is used.

Chapter 7

Numerical examples for linearized buckling analysis.

7.1 Buckling analysis of square plate compressed in one direction.

The buckling of a square plate subjected to in-plane uniaxial compression is considered. The geometry and material constants of the plate are given in Figure 7.1. The plate is simply supported along all edges with the in-plane deformations being unconstrained.

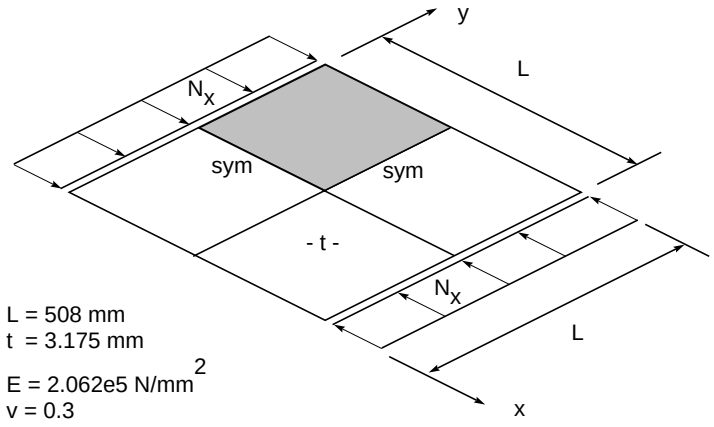

Figure 7.1. Square plate subjected to uniaxial compression.

The plate is compressed in its middle plane by a uniform load N_x along the edges $x = 0$ and $x = L$. Timoshenko [63] gives the analytical critical value of the compressive force per unit length as

$$(N_x)_{cr} = \frac{\pi^2 D}{L^2}(m + \frac{1}{m})^2 \qquad \text{where} \qquad D = \frac{Et^3}{12(1-\nu^2)}. \tag{7.1.1}$$

where L is plate side length, t is the plate thickness, ν is the Poisson's ratio and m is the number of half-waves in the compressive direction. The buckling modes are associated with odd values of m.

The geometric stiffness is based on the incremental solution at a load level of 1% of the critical load level. The results from the numerical analysis is tabulated in Table 7.2 and compared to results obtained by Bjærum [17] with

the QSEL and FFQC elements. The QSEL and FFQC elements performs better than ANDES3 and ANDES4 for the higher order buckling modes. This is due to the "tuned" higher order geometric stiffness matrix used for those elements. However the geometric stiffness matrices used for the QSEL and FFQC element do not give a consistent tangent stiffness for nonlinear continuation analysis.

Table 7.1. Numerical results of square plate subjected to compression, normalized by the analytical solution of the first mode ($m = 1$).

Element Type	Analytical Solution	Mesh used for quarter of plate 4×4	8×8	16×16	32×32
ANDES3	$m = 1$: 1.000	1.008	1.002	1.000	1.000
	$m = 3$: 2.778	3.070	2.854	2.797	2.783
	$m = 5$: 6.760	8.342	7.270	6.893	6.798
ANDES4	$m = 1$: 1.000	1.043	1.011	1.002	1.001
	$m = 3$: 2.778	3.278	2.898	2.808	2.786
	$m = 5$: 6.760	10.11	7.522	6.950	6.815
QSEL	$m = 1$: 1.000	1.010	1.002	1.001	1.000
	$m = 3$: 2.778	3.032	2.840	2.793	2.782
	$m = 5$: 6.760	8.751	7.265	6.884	6.791
FFQC	$m = 1$: 1.000	0.973	0.993	0.998	1.000
	$m = 3$: 2.778	2.673	2.745	2.769	2.778
	$m = 5$: 6.760	6.750	6.694	6.738	6.754

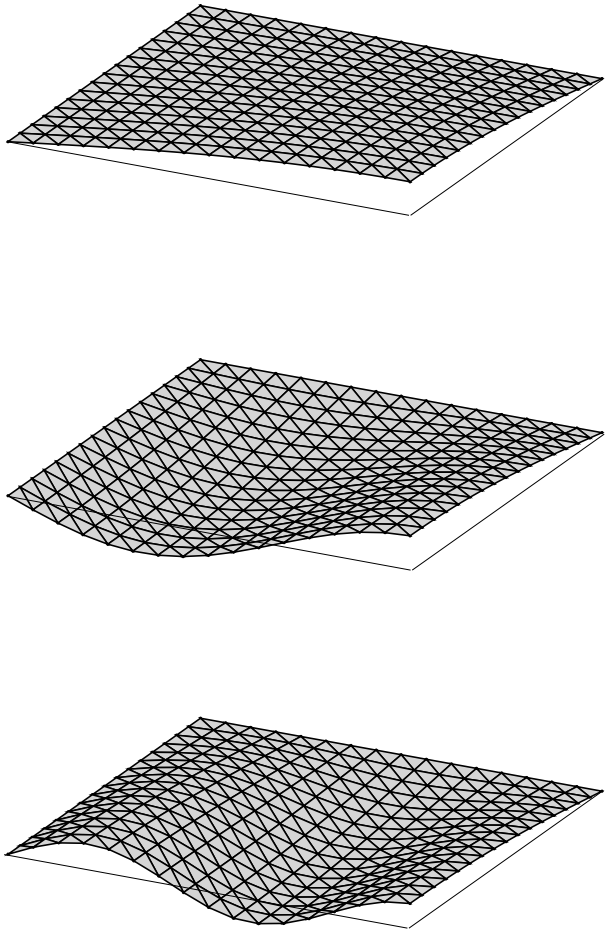

Figure 7.2. Buckling modes for $m = 1$, 3 and 5 according to equation (7.1.1) for square plate subjected to uniaxial compression.

7.2 Buckling analysis of shear loaded square plate.

A simply supported square plate with geometry and material constants given in Figure 7.3 is subjected to shear loads uniformly applied along the edges. The out-of-plane displacements and rotations are constrained whereas the in-plane rotations and translations along the boundaries are left free.

The critical shear force associated with the first buckling mode is give analytically by Timoshenko [63] as

$$(N_{xy})_{cr} = 9.34\frac{\pi^2 D}{L^2} \qquad \text{where} \qquad D = \frac{Et^3}{12(1-\nu^2)}. \tag{7.2.1}$$

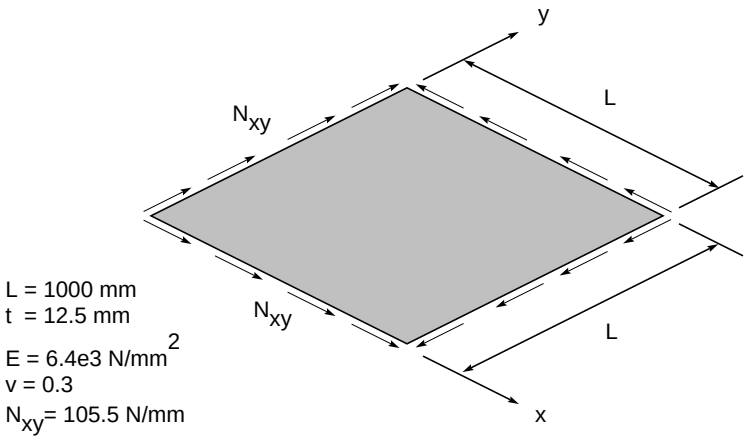

Figure 7.3. Square plate subjected to shear load.

Table 7.2. Numerical results of square plate subjected to shear, normalized by the analytical solution $(N_{xy})_{cr} = 105.5\frac{N}{mm}$.

Element Type		Mesh used for the plate 4×4	8×8	16×16	32×32	64×64
ANDES3	$m = 1$:	1.446	1.145	1.057	1.013	
	$m = 2$:	2.174	1.293	1.240	1.238	
	$m = 3$:	8.631	2.974	2.709	2.675	
ANDES4	$m = 1$:	2.175	1.297	1.088	1.022	
	$m = 2$:	3.079	1.528	1.298	1.250	
	$m = 3$:		4.300	3.013	2.739	
QSEL	$m = 1$:	1.387	1.065	1.008	0.997	0.993
	$m = 2$:	2.096	1.385	1.268	1.242	1.233
	$m = 3$:	207.3	3.582	2.840	2.691	2.642
FFQC	$m = 1$:	0.781	0.908	0.967	0.987	0.994
	$m = 2$:	1.060	1.144	1.206	1.227	1.233
	$m = 3$:	2.073	2.301	2.518	2.614	2.643

This problem again shows that the higher order geometric stiffness matrix for the QSEL and FFQC element outperforms the consistent geometric stiffness matrix of the ANDES elements for linearized buckling analysis. The ANDES3 element performs better than the ANDES4 element simply because

meshes of $N \times N$ elements contains twice as many ANDES3 elements as ANDES4 elements since two triangles are required to fill one quadrilateral. This gives a "finer" discretization with respect to the rigid body displacements and thus a better global geometric stiffness matrix.

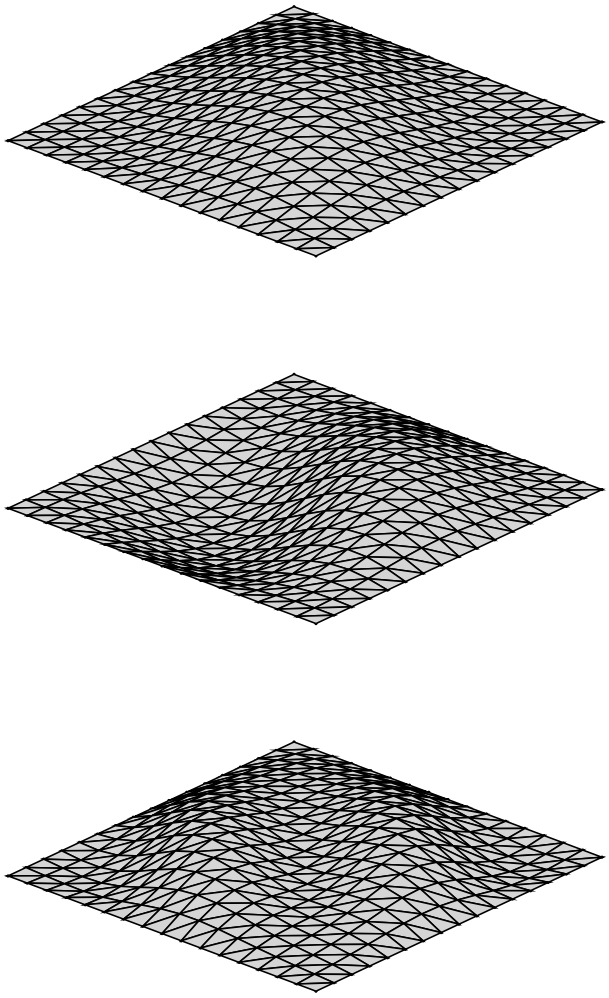

Figure 7.4. First three buckling modes for shear loaded square plate.

Chapter 8

Numerical examples for nonlinear analysis.

8.1 Smooth path following problems.

8.1.1 Cantilever beam subjected to end moment.

The cantilever in Figure 6.2 is used to demonstrate the large rotation and large displacement capabilities. The problem is usually formulated so that bending about one of the global axes takes place. The cantilever here is oriented arbitrarily in space so that the example becomes more demanding as regards the treatment of finite rotations as non-vectorial quantities. The position of the cantilever is defined by the auxiliary coordinate system

$$\begin{Bmatrix} \bar{x} \\ \bar{y} \\ \bar{z} \end{Bmatrix} = \frac{1}{7} \begin{bmatrix} 6 & -2 & -3 \\ 3 & 6 & 2 \\ 2 & -3 & 6 \end{bmatrix} \begin{Bmatrix} x \\ y \\ z \end{Bmatrix}, \tag{8.1.1}$$

and letting one side of the cantilever follow the $\bar{x}$-axis. This auxiliary system is used for modeling purposes only. The actual computations take place in the global (x, y, z)-system.

The exact solution is obtained from Bernoulli-Euler beam theory, and gives the deflected shape of the beam as a circle with radius

$$R = \frac{EI}{M_{\bar{y}}} \, . \tag{8.1.2}$$

This gives the tip deflections as

$$\frac{\bar{w}}{L} = \frac{EI}{M_{\bar{y}}L}(1 - \cos\frac{M - \bar{y}L}{EI}) \quad \text{and} \quad \frac{\bar{v}}{L} = -\frac{EI}{M_{\bar{y}}L}\sin\frac{M - \bar{y}L}{EI} \tag{8.1.3}$$

where $\bar{w}$ and $\bar{v}$ are the deflections in the $\bar{x}$- and $\bar{z}$- directions.

The problem was solved using load control with the incremental load steps $\Delta M_{\bar{y}} = \frac{2\pi}{40}\frac{ML}{EI}$, thus requiring 40 steps to bend the beam into a full circle. This small load step was required for the triangular element due to the large unbalanced membrane forces that are introduced during the iterations. The triangular element does not give symmetry about the center line of the cantilever, and thus converges more slowly than a comparable four node element, as described by Nygård [47] . For the ANDES4 element the beam was bent into a full circle using 10 load steps.

Table 8.1 gives convergence rates and number of iterations for the cantilever modeled with 20 ANDES3 elements. The label "Fit type" refers to the **G** matrix used for fitting the shadow element, with 1, 2 and 3 signifying side 12 alignment, least square fit of side edge angular errors and CST rotation, respectively. "1 diag" means that side 12 is directed along the diagonal of a rectangle assembly of two elements whereas "1 edge" means that side 12 is directed along

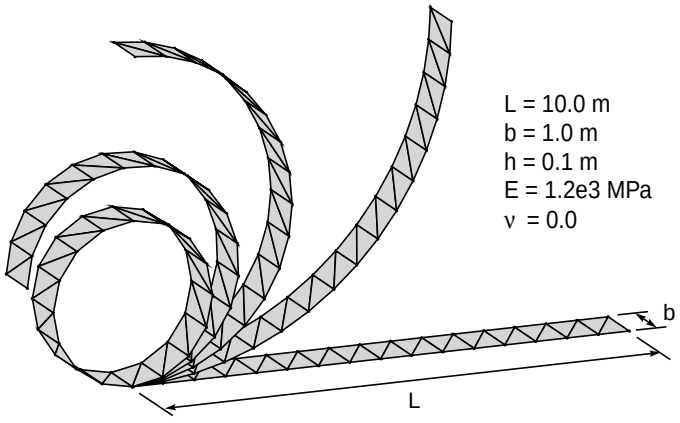

Figure 8.1. Cantilever oriented arbitrarily in space subjected to end moment.

the beam axis. Table 8.1 illustrates two points: Side 12 alignment is not orientation invariant since it doubles the number of iterations of the "1 diag" mesh compared to "1 edge". Also, the applied load is a moment load, which gives a geometric stiffness that does not go towards symmetry as equilibrium is approached. The symmetrized stiffness will thus give poor convergence compared to the nonsymmetric tangent stiffness.

8.1.2 Hinged cylindrical shell under concentrated load.

The hinged cylindrical shell subjected to concentrated load is a common test case for geometrical nonlinearities. Nygård [47] performs an extensive comparison with other elements. Bjærum [17] gives a thorough comparison of different path-following algorithms for this example. The thinner shell of thickness $h = 6.35mm$ has a dramatic snap-back behavior well suited for verifying path following capabilities of the solution algorithm.

One quarter of the shell has been modeled using 8×8 rectangular units of two three node elements. The actual equilibrium path shown in Figures 8.4 and 8.5 agrees well with results obtained by Nygård [47].

The arc-length algorithm did not evidence convergence difficulties. With the thin shell the path has been followed using 26 steps and convergence was obtained within 5 iterations even at the snap-back section of the equilibrium path.

Table 8.1. Iterations for the first 10 steps.

Symmetric stiffness											
Fit type	Num. of iterations										Conv.
1 edge.	4	4	5	5	6	7	8	8	8	9	L
1 diag.	9	9	9	9	9	10	11	9	10	10	L
2	5	5	5	6	6	7	8	8	8	8	L
3	4	4	5	5	6	7	8	8	8	9	L
Non-symmetric stiffness											
Fit type	Num. of iterations										Conv.
1 edge.	4	4	4	4	4	4	4	4	4	4	Q
1 diag.	8	8	8	9	8	8	9	9	9	9	Q
2	5	5	5	5	5	5	5	5	5	5	Q
3	4	4	4	4	4	4	4	4	4	4	Q

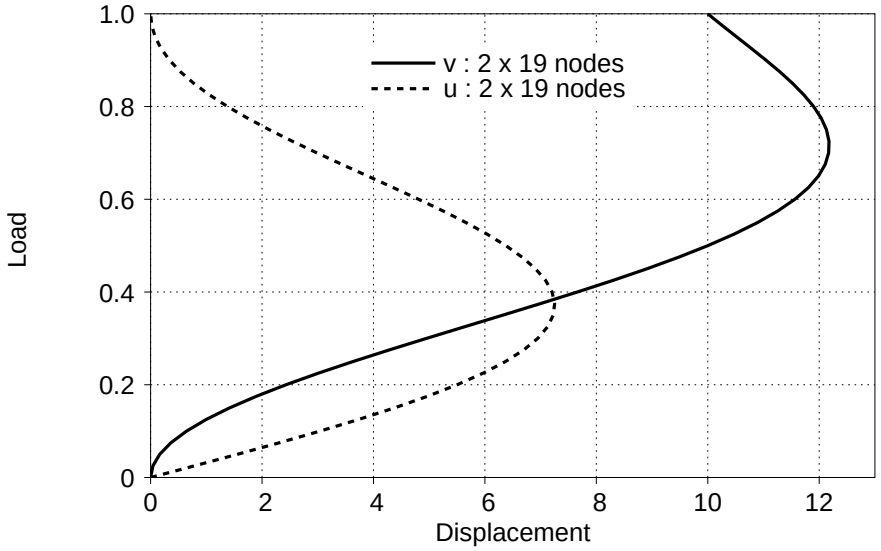

Figure 8.2. Tip displacements of the cantilever beam subjected to end moment.

8.1.3 Pinching of a clamped cylinder.

A cantilevered cylinder is subjected to two diametrically opposite forces of magnitude F at the open end. Due to symmetry only a quarter of the structure is

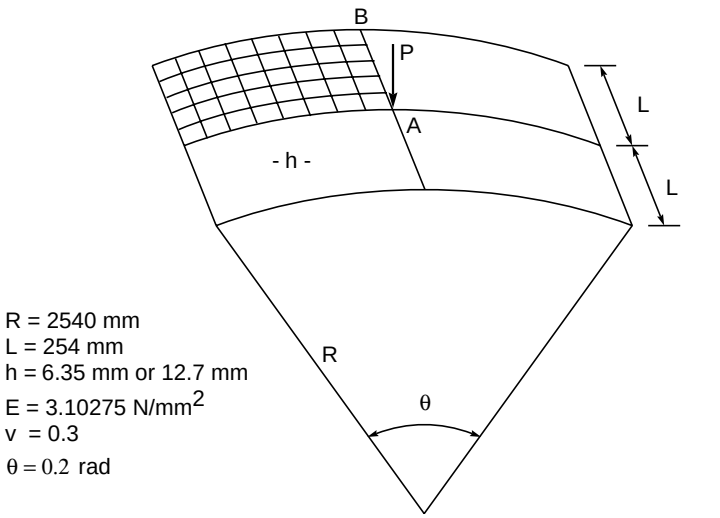

Figure 8.3. Geometry and material properties for hinged cylindrical shell.

modelled. The problem has been studied by Stander et al. [60] and Parisch [48] using uniform element meshes. Mathisen, Kvamsdal and Okstad [43] have studied this problem using adaptive mesh techniques. The present analysis was performed using displacement control of the loaded point with 16 equal step up to a total displacement of 1.6 times the radius of the cylinder.

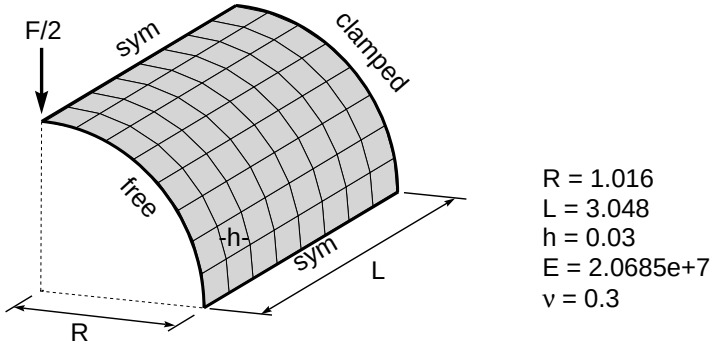

Figure 8.6. Geometry and material properties for the pinched cylinder problem.

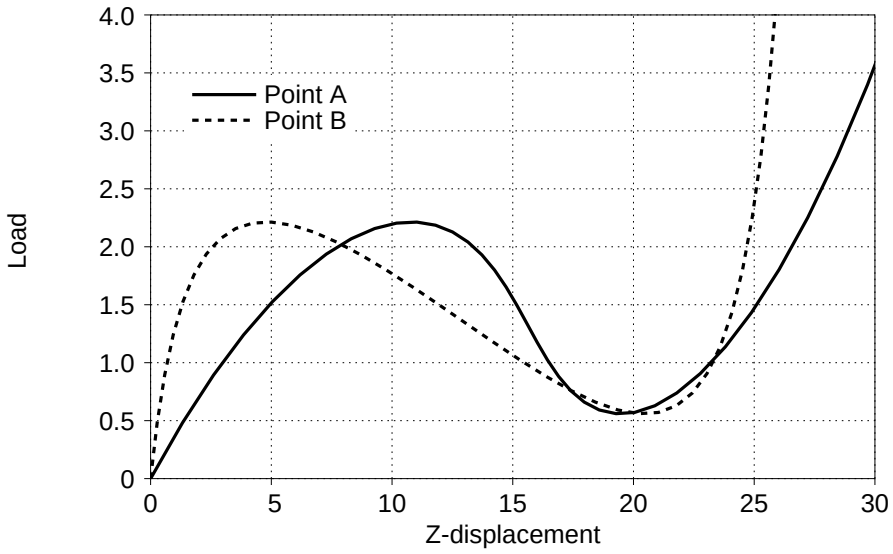

Figure 8.4. Vertical deflection at points A and B
for hinged cylindrical panel with $t = 12.7mm$.

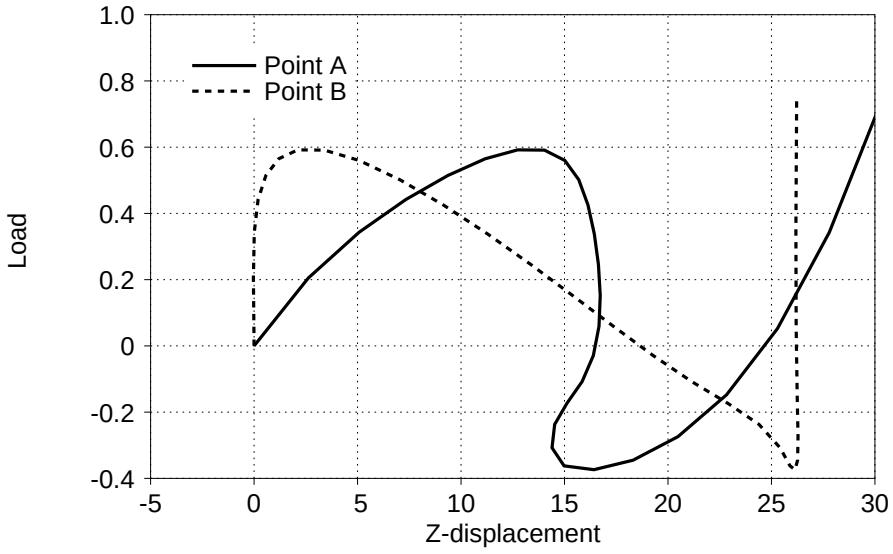

Figure 8.5. Vertical deflection at points A and B
for hinged cylindrical panel with $t = 6.35mm$.

This example shows that the ANDES4 element is better than the ANDES3 element with respect to membrane strain gradients. A mesh of 16×16

ANDES3 elements diverges before the analysis is completed, whereas a mesh of 16×16 ANDES4 elements is sufficient to complete the analysis as shown in Figure 8.7. The results in Figure 8.7 shows good agreement with the results obtained by Stander et al. [60] and Parish [48], both of whom used quadrilateral elements.

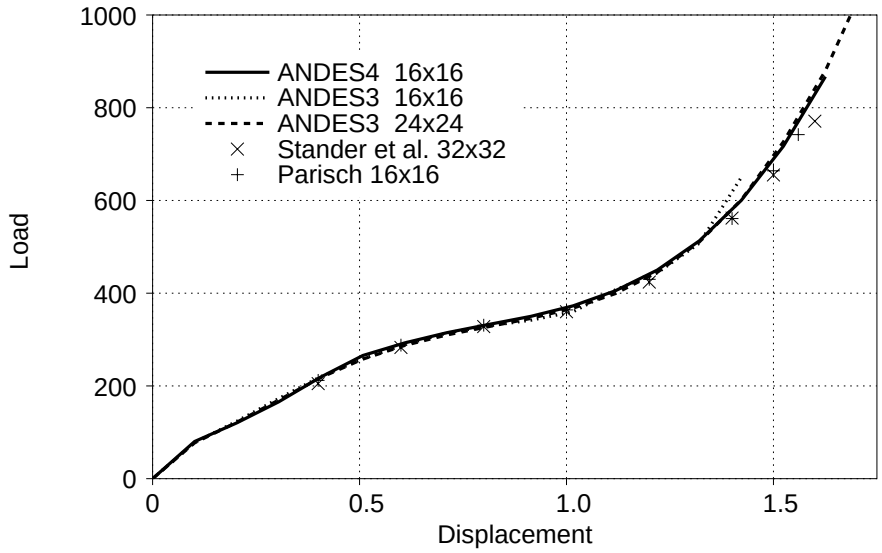

Figure 8.7. Vertical displacement at loading point for the pinched cylinder problem.

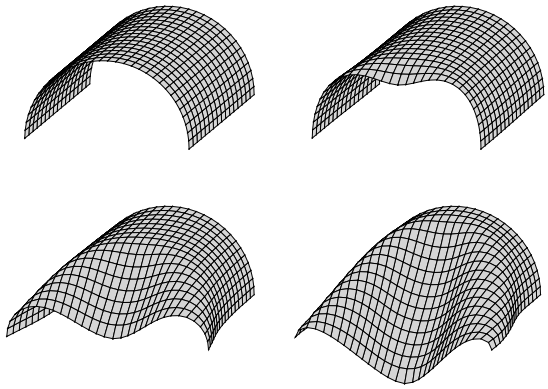

Figure 8.8. Deformed finite element mesh at various loads.

8.1.4 Stretched cylinder with free ends.

A open cylinder with free ends are subjected to two diametrically opposite forces at the halflength. Geometric data for the cylinder are given in Figure 8.9. This problem was first discussed by Gruttman et al. [32], and later by Perić and Owen [50]. Figure 8.10 shows the results of the present analysis with a mesh of 8×16 ANDES4 elements compared with Perić and Owens analysis using a mesh of 10×20 elements. The displacement of the loaded point agrees well with the results reported in [50] .

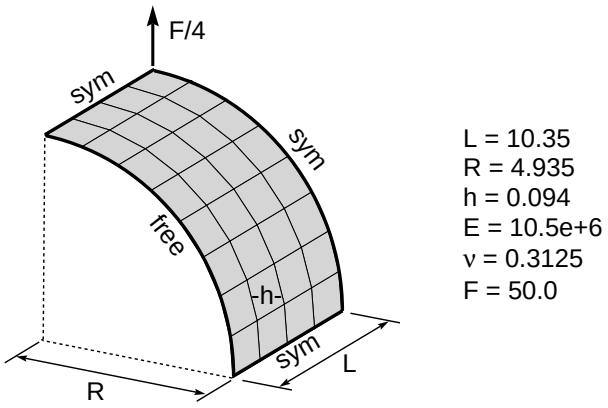

Figure 8.9. Geometry and material properties for the stretch cylinder problem.

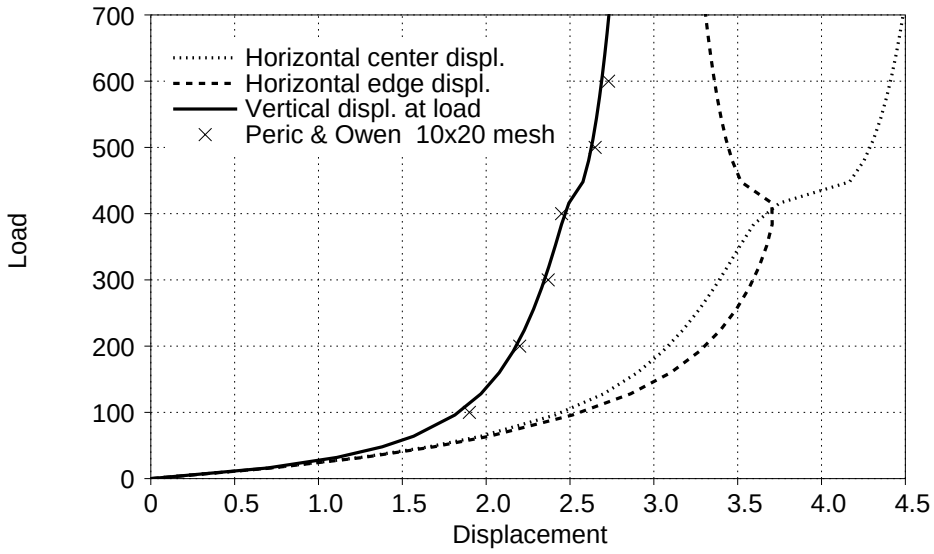

Figure 8.10. Load displacement curves for the stretched cylinder problem.

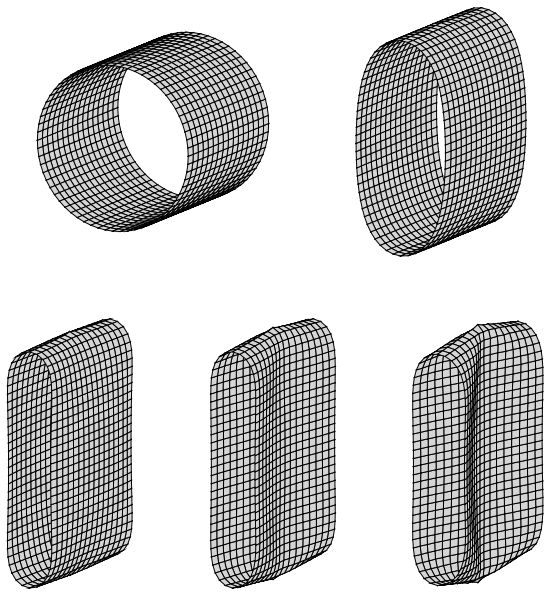

Figure 8.11. Deformed finite element mesh at various loads.

8.2 Path-following problems with bifurcation.

8.2.1 Post-buckling analysis of square plate compressed in one direction.

The geometry and material properties of the square plate are presented in Figure 7.1. The applied load is normalized with respect to the analytical buckling load for this problem given in equation (7.1.1) .

The post-buckling analysis is performed in order to evaluate the stiffness properties of the plate after bifurcation is encountered. One has used a 8×8 mesh of ANDES4 elements over the quarter model. This mesh gave about 1% error in determining the linearized buckling load.

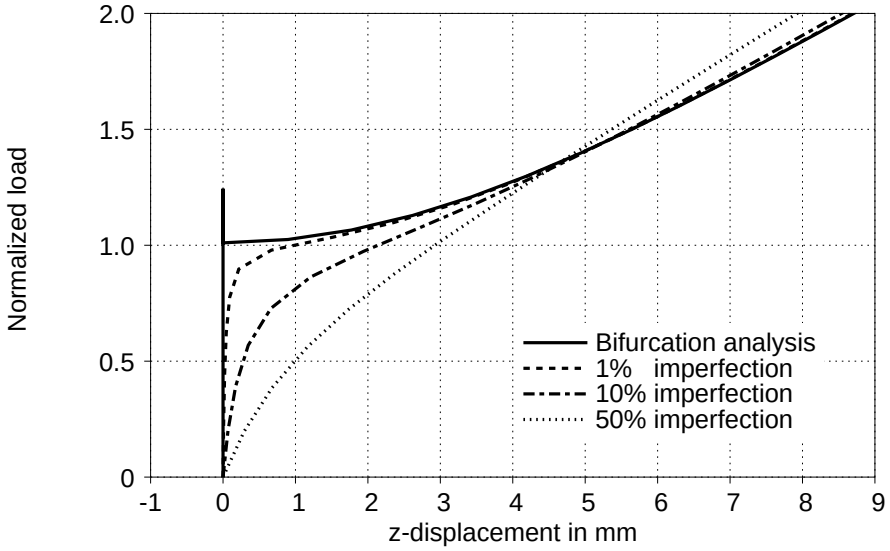

Figure 8.12. Out of plane displacement at plate center for square plate subjected to compression.

As seen in the load displacements curves in Figure 8.12 the structure shows a stable post-buckling response where it can withstand increased load after bifurcation. Figure 8.12 also shows the response of the plate with various geometric imperfection levels. The buckling mode of the structure has been scaled so that the largest out of plane imperfection is equal to 1%, 10% and 50% of the plate thickness.

8.2.2 Post-buckling analysis of shear loaded square plate.

The geometry and material properties of the square plate are described in Figure 7.3. The applied load is normalized with respect to the analytical buckling load $N_{xy_{cr}} = 105.5\frac{N}{mm}$.

A 16×16 mesh of ANDES3 elements over the quarter model is used. This mesh gave about 5% error in determining the linearized buckling load. It should be noted that the shear loaded plate has traditionally been a difficult problem for triangular elements.

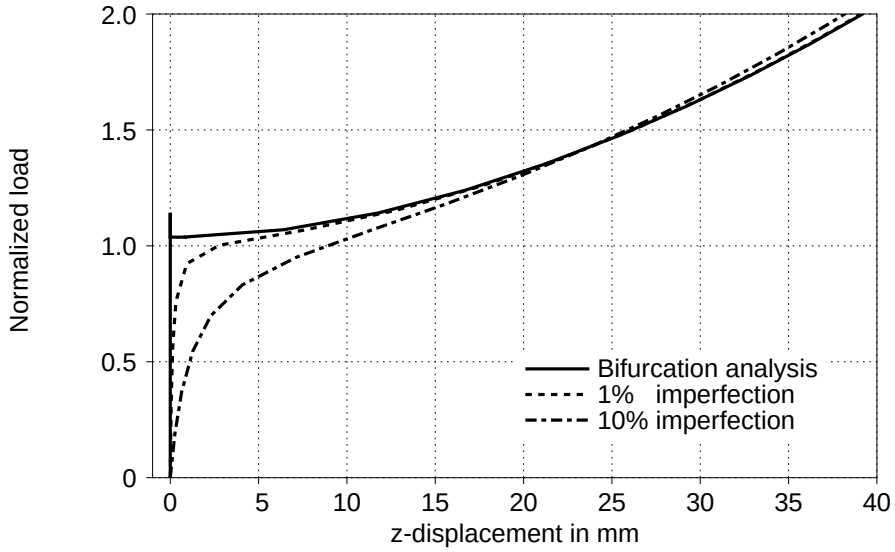

Figure 8.13. Out of plane displacement at plate center for square plate subjected to compression.

As seen in the load displacements curves in Figure 8.13 the structure shows a stable post-buckling response where it can withstand increased load after bifurcation. Figure 8.13 also shows the response of the plate with various geometric imperfection levels. The buckling mode of the structure has been scaled so that the largest out of plane imperfection is equal to 1% and 10% of the plate thickness.

8.2.3 Buckling of a deep circular arch.

This problem of snap-through of a deep circular arch has been investigated by Huddlestone [37] . The asymmetric displacement path has been studied by Simons et al. [59] and Feenstra and Schellekens [23] using a small geometric imperfection to induce the buckling mode. Bjærum [17] analyzed the problem using branch switching to follow the secondary path. The present analysis follows Bjærum's in that no imperfection is used, and the branch switching algorithm has been used to traverse the bifurcation and continuing along the secondary path.

The dimensions of the arch are given in Figure 8.14. The arch has hinged boundary conditions at both ends and is modelled using 20 quadrilateral shell elements with the z displacements constrained.

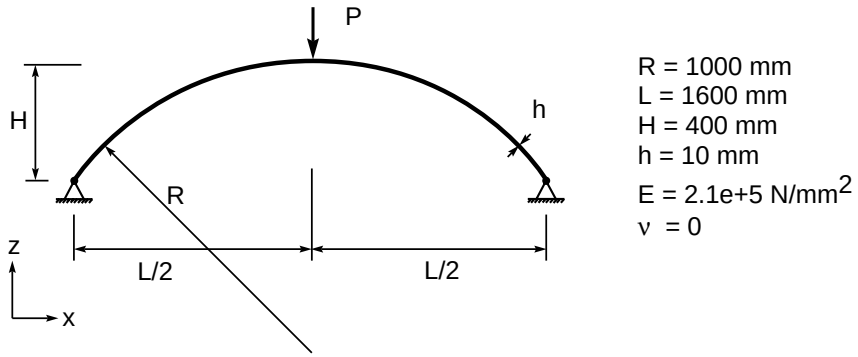

Figure 8.14. Geometry and material properties for the deep circular arch.

Figure 8.15 shows the response of the structure for the primary path, and the secondary path obtained by doing a branch switching at the first bifurcation point at $\frac{PR^2}{EI} = 13.2$. Bjærum reports a bifurcation point at $\frac{PR^2}{EI} = 12.0$, and from his plot of the secondary path one can see that the load then jumps to approximately 13.0. Such a gap between detected and converged bifurcation points as reported by Bjærum can indicate an inconsistent tangent stiffness matrix. The deflections of these paths are also illustrated in Figure 8.16

The problem displays some puzzling behaviour. For instance, the primary path appears not to intersect with the secondary path. The primary path keeps doing spiraling motions for the vertical displacement versus load as plotted in Figure 8.17. For each spiraling motion another wavelike deformation is

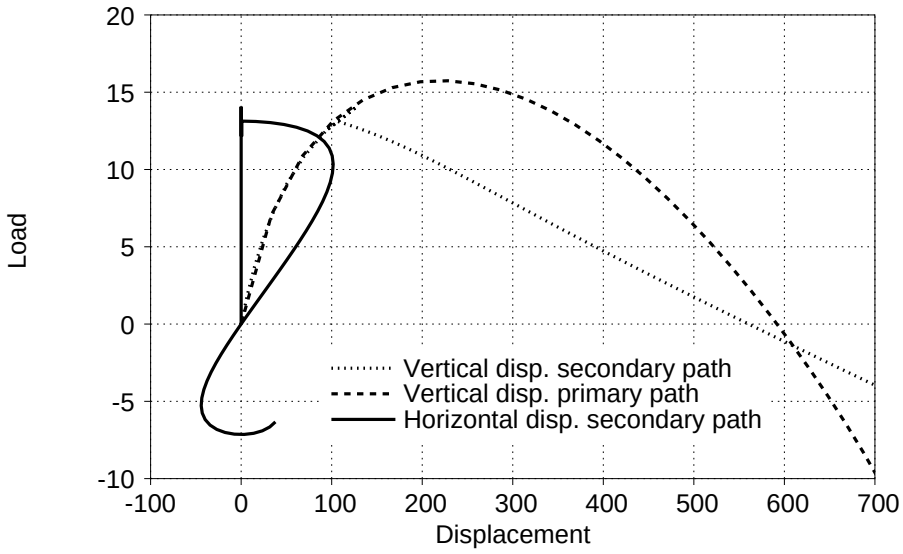

Figure 8.15. Displacements for the primary and secondary paths.

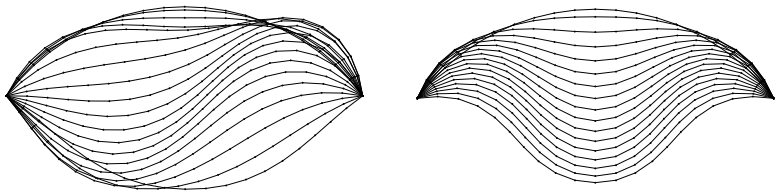

Figure 8.16. Deformations for the secondary and primary paths.

fed into the arch as shown in Figure 8.18. The fact that the primary and secondary path do not intersect can be discerned from the fact that the primary path never achieves the same vertical deflection for the midpoint of the arch as the secondary path.

The secondary path keeps doing figure-of-eight like motions for the midpoint of the arch. The branch switching algorithm does not pick up a new bifurcation point at the bottom point of the secondary path as would be expected.

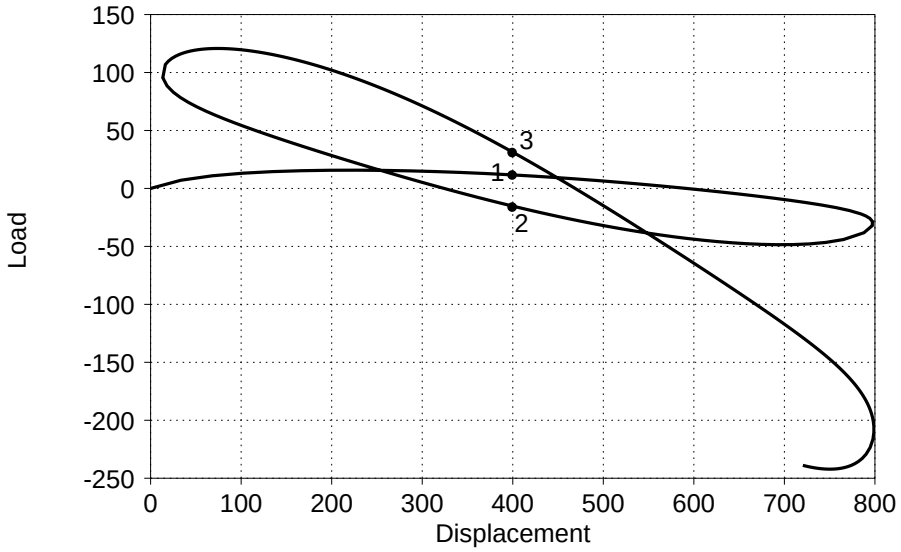

Figure 8.17. Vertical displacement for the primary path. Numbers 1 2 and 3 show the location of the deformed element geometries in Figure 8.18.

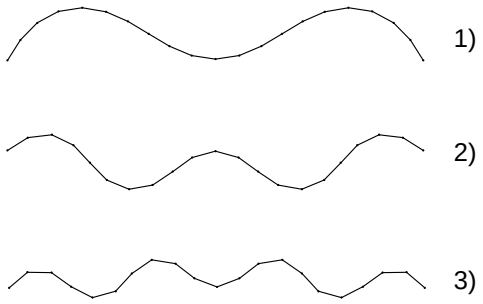

Figure 8.18. Displacements for the primary path. Numbers refer to the load-displacement curves in Figure 8.17.

This conclusion seems to agree with Bjærum, since no such bifurcation point is reported. The "mismatch" is a surprise since one expects the structure to be able to pick up additional load once it hits bottom. But detecting and switching to the new stable path seems to be computationally difficult.

8.2.4 Right angle frame subjected to in-plane load.

The right angle frame in Figure 8.19 is subjected to a in-plane load. The applied load acts on the lower corner of the tip. This problem has been studied by Nour-Omid and Rankin [46] in the post-critical domain.

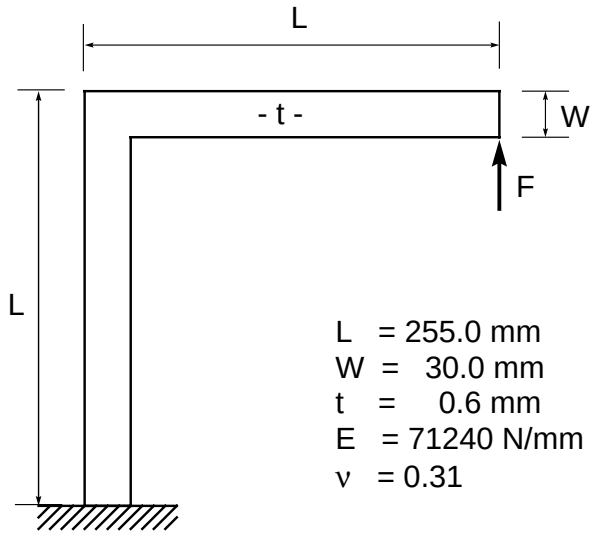

Figure 8.19. Geometry and material properties for the right angle frame.

Table 8.2 lists the critical loads given by different element types and mesh refinements. Results from Nour-Omid and Rankin are included in Table 8.2 for comparison. The postcritical response for the structure is shown in Figure 8.20 for different element meshes with ANDES3 and ANDES4 elements.

Table 8.3 gives the number of steps and iterations for this problem with the various consistent formulations. The convergence rates are measured at the stable "upswing" section of the equilibrium path. For large sections of the analysis this convergence rate is not obtained due to ill-conditioning at the "flat" section of the equilibrium path.

Table 8.2. Critical load for the right angle frame.

Element type	Num. of elements	F_{cr}
ANDES3	17×2	1.164
ANDES3	68×2	1.142
ANDES3	153×2	1.135
ANDES4	17	1.146
ANDES4	68	1.134
ANDES4	153	1.130
Nour-Omid & Rankin [46]	17	1.138
Nour-Omid & Rankin [46]	64	1.130

Table 8.3. Convergence of the 17×2 ANDES3 mesh.

	Symmetric stiff.			Non-symmetric stiff.		
Formulation	N.steps	N.iter.	C.rate.	N.steps	N.iter.	C.rate.
C	18	179	L.	18	152	Q.
CSE	18	174	Sl.	18	145	Q.
CSSE	18	145	Q.	18	145	Q.

Figure 8.20. Post buckling response for the right angle frame.

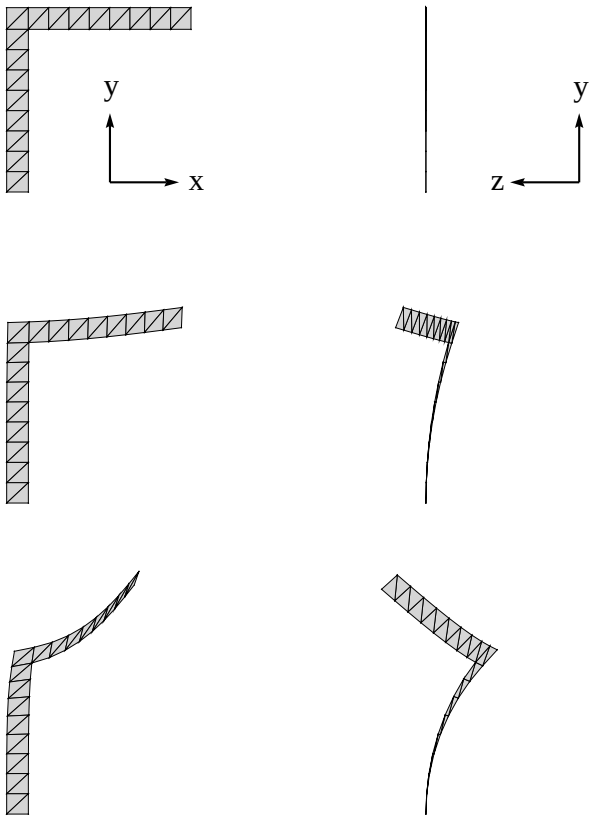

Figure 8.21. Deformations for $F = 1.164$, $F = 1.26$ and $F = 2.0$ with a mesh of 17×2 ANDES3 elements.

8.2.5 Right angle frame subjected to end moments.

The following two problems were modeled with the beam elements described in Appendix 1. The problems were included in the present work because of the numerical challenges they offer as regards branch switching and continuation algorithms.
The right-angle frame subjected to end moments was first introduced by Argyris [3] and later studied by Nour-Omid and Rankin [46] . The frame has been modeled using 10 Timoshenko beam elements for a half model. Beam elements have been chosen to model the frame since the moment loads are impossible to introduce for shell elements without using follower forces that are non-conservative and hence introduce follower-load stiffness matrix. Such a contribution has not been implemented for the shell elements developed in this work.

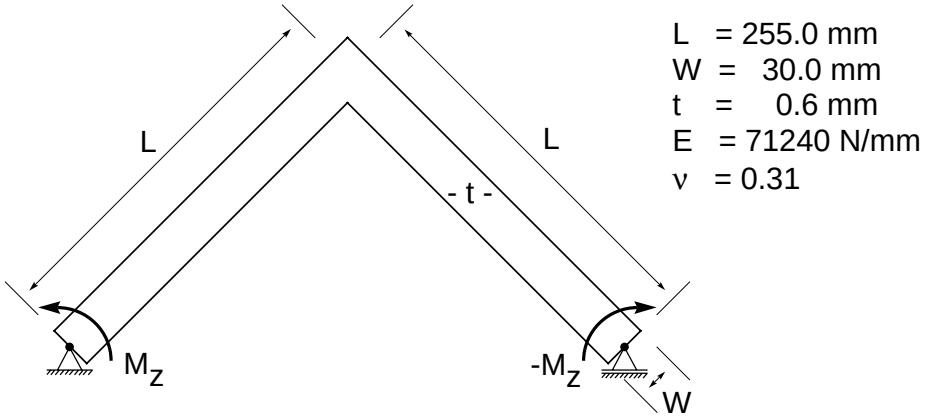

Figure 8.22. Geometry and material properties for the symmetric frame.

The response of the structure displays two distinct equilibrium paths. The primary path has only displacements in the x-y plane, whereas the secondary path switches to out of plane displacements after bifurcation. The response shows that the frame rotates a full 360° as the frame ends rotate through a full circle about the z axis. Finally the frame rotates back to the x-y plane with the load reversed. The out of plane bifurcation happens at $M_z = \pm M_{cr} = 6.464 Nmm$. The analysis can be run repeated indefinitely. If the bifurcation starts at $M_z = +M_{cr}$ a full out of plane revolution will be obtained at $M_z = -M_{cr}$. A second revolution will then take place after which the structure finally returns to the same configuration of the first bifurcation with load $M_z = +M_{cr}$.

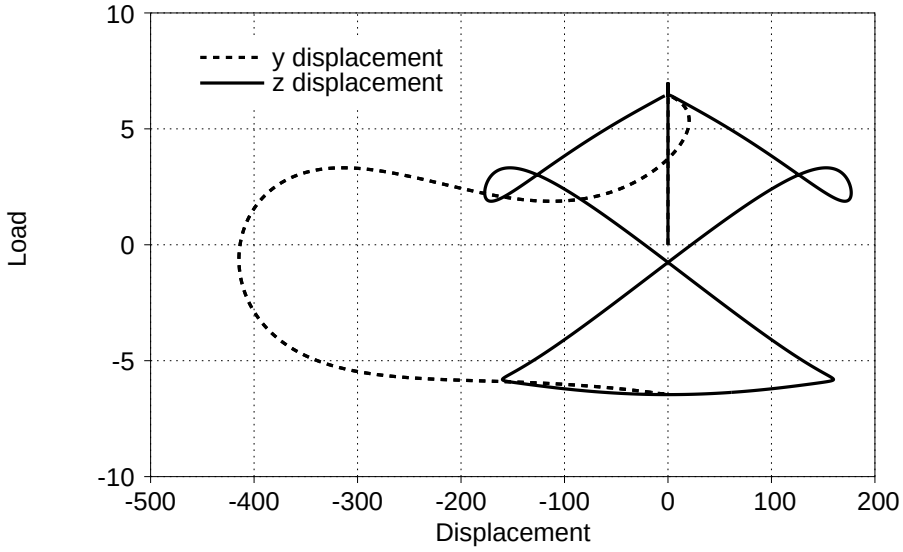

Figure 8.23. y and z displacements for the apex of the right angle frame.

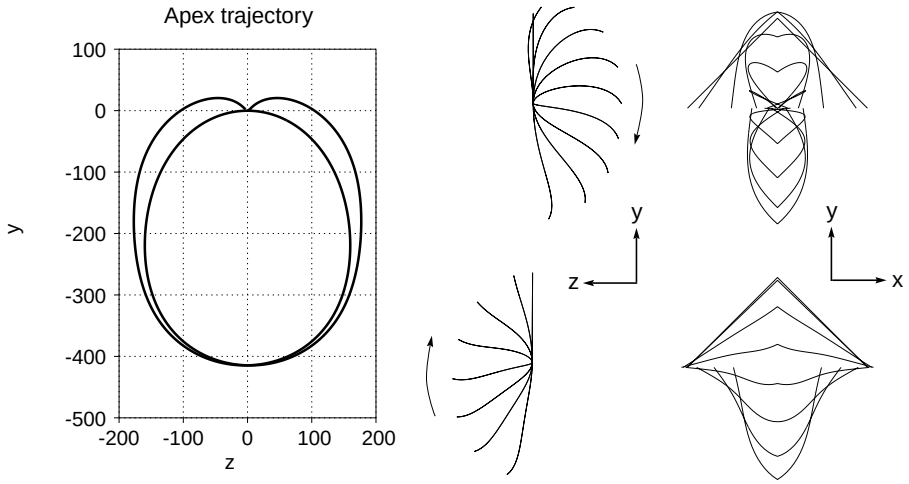

Figure 8.24. Deformations for the for the frame subjected to end moments. Arrows indicate direction of motion.

8.2.6 Cable Hockling.

An initially straight cable is subjected to a tip torsional moment. One end of the cable is fully clamped, whereas the loaded tip is free to rotate about the

longitudinal x axis, and moves along it. No rotation is allowed about the y and z axes at the loaded end. The material and geometrical properties of the cable are defined in Figure 8.25. The Euler-Bernoulli beam element described in Appendix 1 is used to discretize the cable.

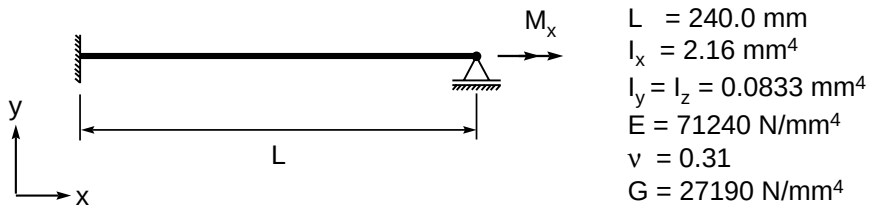

Figure 8.25. Cable geometry and material properties.

This problem was first studied in the postbuckling regime by Nour-Omid and Rankin [46]. The cable exhibits linear response with twisting and no lateral displacement up to the bifurcation point. After bifurcation the cable forms a loop with the loaded end moving towards the clamped end. Finally a full circular loop is formed after the path has traversed a second bifurcation point and the applied load returns back to zero.

The analysis is made more stable by restricting the midpoint of the cable from moving out of the x-y plane. The position of the loop is otherwise undetermined in the y-z plane. The equilibrium path has been followed without this restriction, but the convergence rate is impaired. This additional boundary condition is consistent with that used by Nour-Omid and Rankin.

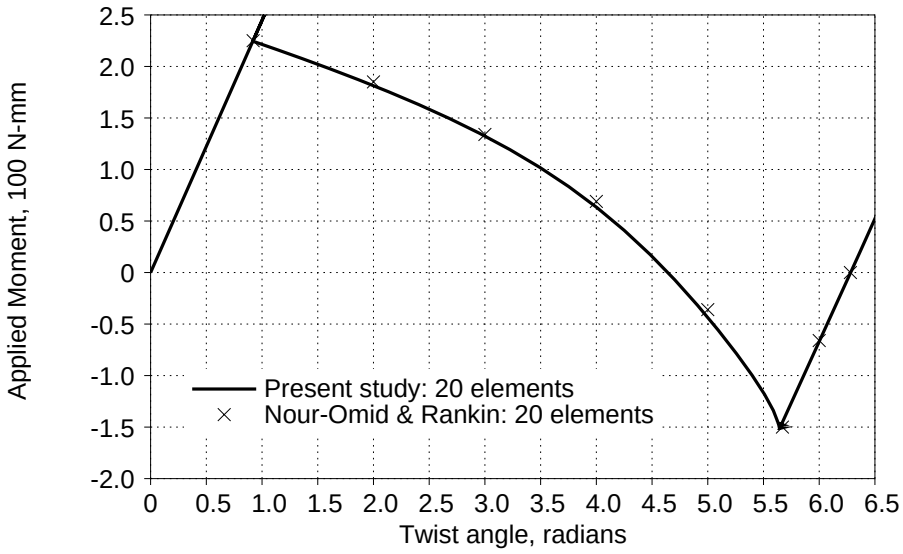

Figure 8.26. Cable hockling. Moment versus tip rotation.

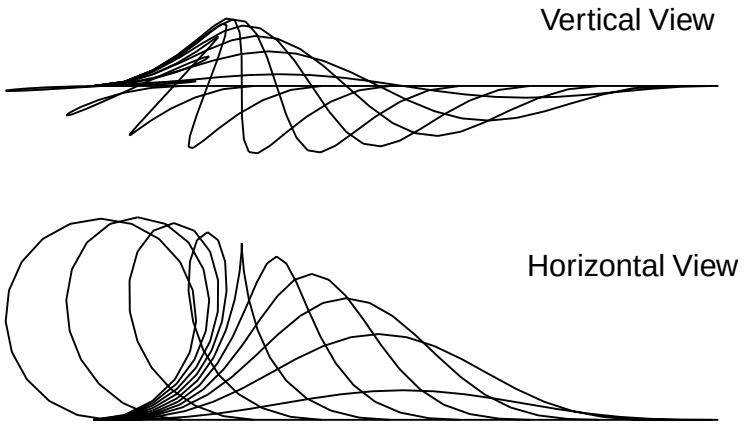

Figure 8.27. Deformations for the for the cable subjected to end moment.

Chapter 9

Conclusions.

9.1 Summary of work.

The main objective to the present research has been the development, application and evaluation of low-order, high-performance shell finite elements to the analysis of the geometrically nonlinear static response and stability of shell structures. The technology for constructing such elements within the framework of the FF and ANDES formulations, however, has been well developed to date only for linear elasticity and flat element geometries. This motivated the use of the co-rotational kinematic description to facilitate reuse of such technology in the intended applications. Although such a choice carries with it some modeling limitations, such as restriction to small deformational strains, it was felt that the advantages of starting from a sound theoretical foundation outweighed those limitations.

The co-rotational kinematic description of geometrically nonlinear structural finite element is still an evolving subject actively pursued by several research groups. The departure point of for the formulation developed here has been the work of two such groups: Bergan and co-workers at Trondheim-NTH and Rankin and co-workers at Lockheed Palo Alto Research Laboratory. The formulations produced by these groups share the ability of handling arbitrarily large rigid body motions (translations and rotations) without causing element self-straining. Taken separately, however, the formulations lack certain desirable attributes investigated during the course of this research.

The main contribution of the present work towards co-rotational theory has been the development of a unified formulation that satisfies those attributes identified as most desirable: self-equilibrium, consistency, invariance, symmetrizability and element-independence. The unified formulation includes those of the aforementioned groups in a hierarchical framework, in the sense that they can be recovered by making certain simplifying kinematic and static assumptions. This unification offers additional flexibility to finite element developers in that tradeoffs between simplicity, robustness and generality can be more clearly understood.

The nonlinear response of the co-rotational finite element models is obtained by incremental/iterative continuation methods. The equilibrium-path-following algorithm combines a standard arc length predictor phase with two alternative versions of a true-Newton corrector phase. One version implements

the normal-plane corrector of Riks-Wempner whereas the other version implements the orthogonal trajectory accession corrector proposed by Fried. Both predictor and corrector algorithms as well as the equilibrium-convergence acceptance criterion are treated with scaling techniques that aim to make the solution algorithm performance insensitive to mesh adaptation or refinement processes as well as independent of the physical units chosen for the model. The numerical experiments reported in Chapter 8 indicate that the orthogonal trajectory corrector in general outperformed the normal plane corrector in terms of robustness and allowance of larger stepsizes when tracing smooth response paths. The normal plane corrector, however, is still preferable when dealing with traversal of the bifurcation points.

A modification of the predictor-corrector continuation algorithm to handle traversal of bifurcation points has been developed. The modified algorithm is enabled when a critical point detected along the equilibrium path is classified as being of bifurcation type. The identification relies on linearized buckling analysis carried out at two "bracketing" configurations in the neighborhood of the point. The estimated buckling mode is used to initiate branch switching into the outgoing (secondary) path. The corrector constraint is modified to avoid the "switch-back" to the incoming (primary) path. This modification has proven to be robust in handling symmetric bifurcation points in the test problems reported here.

The development of high-performance triangular and quadrilateral shell finite elements as "linear kernels" to be used in the co-rotational description is based on the ANDES formulation. Both element geometries include the corner drilling rotation as membrane degrees of freedom. The main contribution of the present work to element technology is the construction of a new four-noded quadrilateral shell element using assumed strain distributions for the higher-order stiffness component. This element is derived with reference to a flat geometry defined by the median plane of the generally-warped quadrilateral. Projector matrices are used to fulfill self-equilibrium conditions in the warped geometry. The numerical results indicate that the new quadrilateral element delivers modeling accuracy similar to that of the Free Formulation Quadrilateral (FFQ) of Nygård, but without the burden of numerical inversion of 12×12 matrices required in the formation of the FFQ higher order stiffness.

The numerical results reported in Chapters 6, 7 and 8 indicate that the three-pronged combination of hierarchical co-rotational formulation, discretization-independent nonlinear solution algorithm and ANDES based shell elements generally handled the test problems in a robust and computationally efficient manner. The performance of co-rotated 3-D beam elements in several difficult prob-

lems involving very large rotations reinforces that conclusion as regards the co-rotational formulation as well as the path-following and branch-switching algorithms developed in this research. Performance expectations had to be tempered, however, in the case of linearized prebuckling problems discussed in Chapter 7. For such problems, elements with specially tuned plate-bending geometric stiffness are observed to deliver better buckling load prediction for coarse discretizations.

9.2 Directions for future research.

The present co-rotational formulation of geometrically nonlinear analysis has shown to be robust and computationally effective in conjunction with *low order* elements. These include two-node beam elements, three-node triangular shell element, and "moderately" warped four-node quadrilateral shell elements. For the latter it is shown that reasonable physical behavior can be obtained with the use of best-fit and projection techniques to pass, back and forth, from the actual warped configuration to the flat projection on the quadrilateral-median plane.

On the other hand, *higher order* elements such as three noded beams and nine-noded shell quadrilaterals would not be adequately handled by the present co-rotational description because the geometry of the shadow element and the deformed element can drift far apart even in the absence of significant membrane strains. This "element-level snap-through" is illustrated in Figure 2.4. A co-rotational description that works properly for higher order elements would be desirable to handle certain troublesome, but nevertheless practical, modeling situations. (One such example would be a mesh that contains both low-order and higher-order elements, with the former being treated by co-rotational formulation.) Extending the shadow element concept to curved geometries appears to clash with the element independence attribute. Furthermore, a naive implementation may bring up metric-update complications typically associated with the Updated Lagrangian and convected-coordinate description, losing the key benefit of "reuse" of linear elements.

Another research area that merits attention is the extension to nonflat shell elements of high-performance elements development methods that rely on the Free Formulation, ANDES formulation and their variants. Such methodology has given excellent results for flat, low-order elements. The key ingredient is the basic-plus-higher-order decomposition of the stiffness equations, with the basic component taking care *a priori* of the satisfaction of the Individual Element Test (IET). The methodology is extended here to cover warped four-node quadrilaterals through projector techniques. However, as discussed in Section

2.11, projectors can significantly change the stiffness properties of highly warped elements. Such changes would be unacceptable for higher order, high precision elements.

The key difficulty in extending the FF and ANDES formulations to higher order, initially curved beam and shell elements centers on the construction of the basic stiffness matrix. This requirement poses in turn two question sets that offer opportunity for further research work:

(a) How can a *converged equilibrium stress state* be precisely characterized over an initially curved element? Can this state be defined in a continuous form without going through an "element dimension shrinking" limiting process? Or, can the state be characterized discretely through Barlow points without undergoing a limiting process?

(b) How does the solution of (a) impact the definition of the IET? And, can the IET be made to hold for shell elements (or shell and beam elements) intersecting at finite angles?

It seems unlikely that the two preceding questions can be fully answered in the near future. Most likely they may have to be addressed by first looking at restricted kinds of curved geometries, such as cylinders and spheres. One such "incremental research path" might be to consider an infinite, circular-cylinder thin shell under pure extension, pure torsion and uniform pressure solicitations, and study the perturbation of the exact solution states induced by laying out an arbitrary mesh on the surface. Such studies may have to rely heavily on computer algebra systems.

As regards nonlinear solution algorithms for tracing equilibrium paths, the present state of the art in arc length methods and their variants appears to satisfactory handle many routine problems, including traversal of smooth limit points. Certain refinements and extensions to cover difficult cases may, however, be worth pursuing. Among these the following study areas may be cited:

(1) More comprehensive evaluation of the relative effectiveness of the standard arc length correctors based on pre-defined algebraic constraints (e.g. the normal-plane and hyperspherical correctors) versus the orthogonal trajectory corrector, and in particular, sensitivity of the latter to the type of critical point (limit vs. bifurcation) to be traversed.

(2) Robust and effective techniques for automatic traversal of unsymmetric bifurcation points in the absence of a governing energy functional, and smart procedures for "branch switching" from a secondary to the primary path without recourse to special techniques such as artificial imperfections or dynamics.

A final general recommendation concerns the beneficial "symbiotic" effect of motivated research. It would be desirable to pursue one or more of the aforementioned research topics not in a thematic isolation, but as component of an application-driven, integrated research program.

References

[1] K. Alvin, H. M. de la Fuente, B. Haugen and C. A. Felippa, Membrane triangles with corner drilling freedoms: I. The EFF element. *Finite Elements in Analysis & Design*, **12**, 167-188, 1992.

[2] J. H. Argyris, Continua and Discontinua, *Proceedings 1st Conference on Matrix Methods in Structural Mechanics*, AFFDL-TR-66-80, Air Force Institute of Technology, Dayton, Ohio, 1965.

[3] J. H. Argyris, H. Balmer, J. St. Doltsinis, P. C. Dunne, M. Haase, M. Klieber, G. A. Malejannakis, J. P. Mlejenek, M. Muller, and D. W. Scharpf, Finite element method – the natural approach, *Comput. Methods Appl. Mech. Engrg.*, **17/18**, 1-106, 1979.

[4] J. H. Argyris, An Excursion into Large Rotations, *Comput. Methods Appl. Mech. Engrg.*, **32**, 85-155, 1985.

[5] K. J. Bathe and A. P. Cimento, Some practical procedures for the solution of nonlinear finite element equations, *Comp. Methods Appl. Mech. Engrg.*, **22**, 59-85, 1980.

[6] K. J. Bathe and E. N. Dvorkin, On the automatic solution of nonlinear finite element equations, *Computer and Structures*, **17**, 871-879, 1983.

[7] K. J. Bathe and E. N. Dvorkin, A four-node plate bending element based on Mindlin-Reissner plate theory and a mixed interpolation, *Int. J. Numer. Methods Engrg.*, **21**, 367-383, 1985.

[8] J. L. Batoz and G. Dhatt, Incremental displacement algorithms for nonlinear problems, *Int. J. Numer. Methods Engrg.*, **14**, 1262-1266, 1979.

[9] G. B. Bazeley, Y. K. Cheung, B. M. Irons and O. C. Zienkiewicz, Triangular elements in plate bending – conforming and nonconforming solutions, *Proceedings 1st Conference on Matrix Methods in Structural Mechanics*, AFFDL-TR-66-80, Air Force Institute of Tecnology, Dayton, Ohio, 547-584, 1966.

[10] T. Belytschko and B. J. Hsieh, Non-linear transient finite element analysis with convected co-ordinates, *Int. J. Numer. Methods Engrg.*, **7**, 255-271, 1973.

[11] P. G. Bergan and L. Hanssen, A new approach for deriving "good" finite elements, MAFELAP II Conference, Brunel University, 1975, in *The Mathematics of Finite Elements and Applications – Volume II,* ed. by J. R. Whiteman, Academic Press, London, 483-497, 1976.

[12] P. G. Bergan and G. Horrigmoe, Incremental variational principles and finite element models for nonlinear problems, *Comput. Methods Appl. Mech. Engrg.*, **7**, 201-217, 1976.

[13] P. G. Bergan, I. Holand and T. H. Søreide, Use of the current stiffness parameter in solutions of nonlinear problems, In: R. Glowinski, E. Y. Rodin and O. C. Zienkiewicz (Eds.), *Energy Methods in Finite Element Analysis*, John Wiley & Sons, London, 1979.

[14] P. G. Bergan and M. K. Nygård, Finite elements with increased freedom in choosing shape functions, *Int. J. Numer. Methods Engrg.*, **20**, 643-664, 1984.

[15] P. G. Bergan and C. A. Felippa, A triangular membrane element with rotational degrees of freedom, *Comput. Methods Appl. Mech. Engrg.*, 1985.

[16] P. G. Bergan and M. K. Nygård, Nonlinear shell analysis using Free Formulation finite elements, in *Finite Element Methods for Nonlinear Problems*, Springer Verlag, Berlin, 317-338, 1989.

[17] R. O. Bjærum, Finite element formulations and solution algorithms for buckling and collapse analysis of thin shells. *Dr. Ing. Thesis,* Div. of Structural Mechanics, Norwegian Institute of Technology, Trondheim, Norway, 1992.

[18] R. L. Burden and J. D. Faires, *Numerical Analysis*, 4th ed., PWS-KENT Publishing Company, 1988.

[19] A. Cardona, An integrated approach to mechanism analysis, *Ph.D thesis*, University of Liege, Belgium, 1989.

[20] M. A. Crisfield, A fast incremental/iterative solution procedure that handles "snap-through", *Computers and Structures* , **13**, 55-62, 1981.

[21] M. A. Crisfield, Accelerating and damping the modified Newton-Raphson method, *Computers and Structures*, **18**, 395-407, 1984.

[22] M. A. Crisfield, A consistent co-rotational formulation for nonlinear three-dimensional beam element, *Comput. Methods Appl. Mech. Engrg.*, **81**, 131-150, 1990.

[23] P. H. Feenstra and J. C. J. Schellekens, Self-adaptive solution algorithm for a constrained newton-raphson method, TNO Building and Construction Research, Report nr. BI-91-124, TNO-Bouw, Delft, The Netherlands, 1991.

[24] C. A. Felippa, Refined finite element analysis of linear and nonlinear two-dimensional structures, *Ph.D Dissertation*, Department of Civil Engineering, University of California, Berkeley, CA, 1966.

[25] C. A. Felippa, Parametrized multifield variational principles in elasticity: I. Mixed functionals, *Comm. Appl. Numer. Methods*, **5**, 79-88, 1989.

[26] C. A. Felippa, Parametrized multifield variational principles in elasticity: II. Hybrid functionals and the free formulation, *Comm. Appl. Numer. Methods*, **22**, pp 79-88, 1989.

[27] C. A. Felippa and C. Militello, Membrane triangles with corner drilling freedoms: II. The ANDES element, *Finite Elements in Analysis & Design*, **12**, 189-201, 1992.

[28] C. A. Felippa and S. Alexander, Membrane triangles with corner drilling freedoms: III. Implementation and performance evaluation. *Finite Elements in Analysis & Design*, **12**, 203-239, 1992.

[29] C. A. Felippa, B. Haugen and C. Militello, From the individual element test to finite element templates: Evolution of the patch test, accepted for publication in *Int. J. Numer. Meth. Engrg.*

[30] B. M. Fraeijs de Veubeke, The dynamics of flexible bodies, *Int. J. Engrg. Sci.*, Pergamon Press, 895-913, 1976.

[31] I. Fried, Orthogonal trajectory accession on the non linear equilibrium curve, *Comput. Methods Appl. Mech. Engrg.*, **47**, 283-297, 1984.

[32] F. Gruttmann, E. Stein and P. Wriggers, Theory and numerics of thin elastic shells with finite rotation, *Ing. Arch.*, **59**, 54-67, 1989.

[33] B. Haugen and C. A. Felippa, A tetrahedron element with rotational degrees of freedom based on the ANDES-formulation, *Internal report*, 1992.

[34] G. Horrigmoe and P. G. Bergan, Instability analysis of free-form shells by flat finite elements, *Comput. Methods Appl. Mech. Engrg.*, **16**, 11-35, 1978.

[35] A. Hrennikoff, Solution of problems of elasticity by a framework method, *J. Appl. Mech.*, **8**, 169-175, 1941.

[36] H. C. Huang and E. Hilton, A new nine node degenerated shell element with enhanced membrane and shear interpolation, *Int. J. Numer. Methods Engrg.*, **22**, 73-92, 1986.

[37] J. V. Huddlestone, Finite deflections and snap-through of high circular arches, *J. Appl. Mech.*, ASME, **35**, 763-769, 1968.

[38] T. J. R. Hughes, *The Finite Element Method: Linear Static and Dynamic Finite Element Analysis*, Prentiss-Hall, Englewood Cliffs, N.J., 1987.

[39] B. M. Irons and S. Ahmad, *Techniques of Finite Elements*, Ellis Horwood Limited, Chichester, 1980.

[40] E. Levold, Solid mechanics and material models including large deformations, *Dr. Ing. Thesis,* Div. of Structural Mechanics, Norwegian Institute of Technology, Trondheim, Norway, 1990.

[41] R. H. MacNeal, Derivation of element stiffness matrices by assumed strain distribution, *Nuclear Engrg. Design*, **70**, 3-12, 1978.

[42] K. M. Mathisen, Large displacement analysis of flexible and rigid systems considering displacement-dependent loads and nonlinear constraints. *Dr. Ing. Thesis,* Div. of Structural Mechanics, Norwegian Institute of Technology, Trondheim, Norway, 1990.

[43] K. M. Mathisen, T. Kvamsdal and K. M. Okstad, Adaptive strategies for nonlinear finite element analysis of shell structures, In: *Numerical Methods in Engineering '92,* C. Hirchs et al. (Eds.), Elsevier Science Publishers B. V., 1992.

[44] C. Militello and C. A. Felippa, Variational formulation of high performance finte elements: Parametrized variational principles, *Computers and Structures,* **36**, 1990, 1990.

[45] C. Militello, Application of parametrized variational principles to the finite element method. *Ph.D Dissertation*, Department of Aerospace Engineering Sciences, University of Colorado, Boulder CO, 1991.

[46] B. Nour-Omid and C. C. Rankin, Finite rotation analysis and consistent linearization using projectors, *Comput. Methods App. Mech.*, **93**, 353-384, 1991.

[47] M. K. Nygård, The free formulation for nonlinear finite elements with application to shells, *Dr. Ing. Thesis,* Div. of Structural Mechanics, Norwegian Institute of Technology, Trondheim, Norway, 1986.

[48] H. Parisch, An investigation of a finite rotation four node assumed strain shell element, *Int. J. Numer. Methods Engrg.*, **31**, 127-150, 1991.

[49] K. C. Park and G. M. Stanley, A curved C^0 shell element based on assumed natural-coordinate strains, *J. Appl. Mech.*, **53**, 278-290, 1986.

[50] D. Perić and D. R. J. Owen, The Morley thin shell finite element for large deformations problems: Simplicity versus sophistication. *Proc. 4th Int. Conf. on Nonlin. Engrg. Comput. (NEC-91)*, 121-142, 1991.

[51] E. Ramm, Strategies for tracing the nonlinear response near limit points. In: W. Wunderlich, E. Stein and K. J. Bathe (Eds.), *Nonlinear Finite Element Analysis in Structural Mechanics*, Springer-Verlag, Berlin and Heidelberg, 63-89, 1981.

[52] C. C. Rankin and F. A. Brogan, An element-independent corotational procedure for the treatment of large rotations, *ASME J. Pressure Vessel Technology*, **108**, 165-174, 1986.

[53] C. C. Rankin and B. Nour-Omid, The use of projectors to improve finite element performance, *Computers and Structures*, **30**, 257-267, 1988.

[54] E. Riks, The application of Newton's method to the problem of elastic stability, *J. Appl. Mech.*, **39**, 1060-1066, 1972.

[55] E. Riks, Bifurcation and stability, a numerical approach. In: W. K. Liu, T. Belytschko and K. C. Park (Eds.), *Innovative Methods for Nonlinear Problems*, Pineridge Press Ltd., Swansea, 313-344, 1984.

[56] P. Sharifi and E. P. Popov, Nonlinear buckling analysis of sandwich arches, *Proc. ASCE, J. Engrg. Div.*, **97**, 1397-1412, 1971.

[57] J. C. Simo, A finite strain beam formulation. The tree dimensinonal dynamic problem. Part I., *Comput. Methods Appl. Mech. Engrg.*, **49**, 55-70, 1985.

[58] J. C. Simo and T. J. R. Hughes, On the variational foundations of assumed strain methods, *J. Appl. Mech.*, **53**, 51-54, 1986.

[59] J. Simons, P. G. Bergan and M. K. Nygård, Hyperplane displacement control methods in nonlinear analysis. In: W.K. Liu, T. Belytschko and K.C. Park (Eds.), *Innovative Methods for Nonlinear Problems*, 345-364, Pineridge Press Ltd., Swansea, 1984.

[60] N. Stander, A. Matzenmiller and E. Ramm, An assessment of assumed strain methods in finite rotation shell analysis, *Engrg. Comput.*, **6**, 58-66, 1989.

[61] G. M. Stanley, Continuum-based shell elements, *Ph.D Dissertation*, Department of Applied Mechanics, Stanford University, Stanford, CA, 1985.

[62] M. L. Szwabowicz, Variational formulation in the geometrically non-linear thin elastic shell theory, *Int. J. Solids Structures*, **22**, 1161-1175, 1986.

[63] S. P. Timoshenko and J. M. Gere, *Theory of Elastic Stability*, 2nd ed., McGraw-Hill, New York., 1963.

[64] G. A. Wempner, Finite elements, finite rotations and small strains of flexible shells, *Int. J. Solids Structures*, **5**, 117-153, 1969.

[65] G. A. Wempner, Discrete approximations related to non-linear theories of solids, *Int. J. Solids Structures*, **7**, 1581-1599, 1971.

[66] P. Wriggers and J. C. Simo, A general procedure for the direct computation of turning and bifurcation points, *Int. J. for Numer. Methods in Engrg.*, **30**, 155-176, 1990.

[67] E. W. Wright and E. H. Gaylord, Analysis of unbraced multistory steel rigid frames. *Proc. ASCE, J. Struct. Div.*, **94**, 1143-1163, 1968.

[68] O. C. Zienkiewicz, *The Finite Element Method*, 3rd ed., McGraw-Hill, London, 1976.

Appendix 1

Beam elements.

A1.1 Linear beam elements.

The linear tangent stiffness matrix for the Euler-Bernoulli beam can be found in several sources such as Hughes [38]. Expressed in local coordinate system with the local x axis along the beam element as shown in Figure A1.1, the element stiffness matrix is

$$\tilde{\mathbf{K}}_e = \begin{bmatrix} \frac{EA}{l} & 0 & 0 & 0 & 0 & 0 \\ 0 & 12\frac{EI_z}{l^3} & 0 & 0 & 0 & 6\frac{EI_z}{l^2} \\ 0 & 0 & 12\frac{EI_y}{l^3} & 0 & -6\frac{EI_y}{l^2} & 0 \\ 0 & 0 & 0 & \frac{GI_x}{l} & 0 & 0 \\ 0 & 0 & -6\frac{EI_y}{l^2} & 0 & 4\frac{EI_y}{l} & 0 \\ 0 & 6\frac{EI_z}{l^2} & 0 & 0 & 0 & 4\frac{EI_z}{l} \\ -\frac{EA}{l} & 0 & 0 & 0 & 0 & 0 \\ 0 & -12\frac{EI_z}{l^3} & 0 & 0 & 0 & -6\frac{EI_z}{l^2} \\ 0 & 0 & -12\frac{EI_y}{l^3} & 0 & 6\frac{EI_y}{l^2} & 0 \\ 0 & 0 & 0 & -\frac{GI_x}{l} & 0 & 0 \\ 0 & 0 & -6\frac{EI_y}{l^2} & 0 & -2\frac{EI_y}{l} & 0 \\ 0 & 6\frac{EI_z}{l^2} & 0 & 0 & 0 & -2\frac{EI_z}{l} \end{bmatrix} \begin{bmatrix} -\frac{EA}{l} & 0 & 0 & 0 & 0 & 0 \\ 0 & -12\frac{EI_z}{l^3} & 0 & 0 & 0 & 6\frac{EI_z}{l^2} \\ 0 & 0 & -12\frac{EI_y}{l^3} & 0 & -6\frac{EI_y}{l^2} & 0 \\ 0 & 0 & 0 & -\frac{GI_x}{l} & 0 & 0 \\ 0 & 0 & 6\frac{EI_y}{l^2} & 0 & -2\frac{EI_y}{l} & 0 \\ 0 & -6\frac{EI_z}{l^2} & 0 & 0 & 0 & -2\frac{EI_z}{l} \\ \frac{EA}{l} & 0 & 0 & 0 & 0 & 0 \\ 0 & 12\frac{EI_z}{l^3} & 0 & 0 & 0 & -6\frac{EI_z}{l^2} \\ 0 & 0 & 12\frac{EI_y}{l^3} & 0 & 6\frac{EI_y}{l^2} & 0 \\ 0 & 0 & 0 & \frac{GI_x}{l} & 0 & 0 \\ 0 & 0 & 6\frac{EI_y}{l^2} & 0 & 4\frac{EI_y}{l} & 0 \\ 0 & -6\frac{EI_z}{l^2} & 0 & 0 & 0 & 4\frac{EI_z}{l} \end{bmatrix} \tag{A1.1}$$

where I_x, I_y and I_z are moments of inertia associated with bending about x, y and z axis respectivly. E is Young's modulus and the shear modulus G is expressed with respect to Young's modulus and Poisson ratio ν as $G = \frac{E}{2(1+\nu)}$.

Using the same local coordinate system and material and cross-section definitions one can express the Timoshenko beam [38] with reduced integration on the shear energy as

$$\tilde{\mathbf{K}}_e = \begin{bmatrix}
\frac{EA}{l} & 0 & 0 & 0 & 0 & 0 \\
0 & \frac{GA}{l} & 0 & 0 & 0 & \frac{GA}{2} \\
0 & 0 & \frac{GA}{l} & 0 & -\frac{GA}{2} & 0 \\
0 & 0 & 0 & \frac{GI_x}{l} & 0 & 0 \\
0 & 0 & -\frac{GA}{2} & 0 & (\frac{EI_y}{l} + \frac{GAl}{4}) & 0 \\
0 & \frac{GA}{2} & 0 & 0 & 0 & (\frac{EI_z}{l} + \frac{GAl}{4}) \\
-\frac{EA}{l} & 0 & 0 & 0 & 0 & 0 \\
0 & -\frac{GA}{l} & 0 & 0 & 0 & -\frac{GA}{2} \\
0 & 0 & -\frac{GA}{l} & 0 & \frac{GA}{2} & 0 \\
0 & 0 & 0 & -\frac{GI_x}{l} & 0 & 0 \\
0 & 0 & -\frac{GA}{2} & 0 & (-\frac{EI_y}{l} + \frac{GAl}{4}) & 0 \\
0 & \frac{GA}{2} & 0 & 0 & 0 & (-\frac{EI_z}{l} + \frac{GAl}{4})
\end{bmatrix}$$

$$\begin{bmatrix}
-\frac{EA}{l} & 0 & 0 & 0 & 0 & 0 \\
0 & -\frac{GA}{l} & 0 & 0 & 0 & \frac{GA}{2} \\
0 & 0 & -\frac{GA}{l} & 0 & -\frac{GA}{2} & 0 \\
0 & 0 & 0 & -\frac{GI_x}{l} & 0 & 0 \\
0 & 0 & \frac{GA}{2} & 0 & (-\frac{EI_y}{l} + \frac{GAl}{4}) & 0 \\
0 & -\frac{GA}{2} & 0 & 0 & 0 & (-\frac{EI_z}{l} + \frac{GAl}{4}) \\
\frac{EA}{l} & 0 & 0 & 0 & 0 & 0 \\
0 & \frac{GA}{l} & 0 & 0 & 0 & -\frac{GA}{2} \\
0 & 0 & \frac{GA}{l} & 0 & \frac{GA}{2} & 0 \\
0 & 0 & 0 & \frac{GI_x}{l} & 0 & 0 \\
0 & 0 & \frac{GA}{2} & 0 & (\frac{EI_y}{l} + \frac{GAl}{4}) & 0 \\
0 & -\frac{GA}{2} & 0 & 0 & 0 & (\frac{EI_z}{l} + \frac{GAl}{4})
\end{bmatrix}. \quad (A1.2)$$

A1.2 Nonlinear extensions.

The local co-rotated chosen for two node beam elements has the local x axis on the line through node 1 and 2 as illustrated in Figure A1.1.

$$\mathbf{i}_1^n = \frac{1}{l}(\mathbf{x}_2 - \mathbf{x}_1) \quad \text{where} \quad l = \|(\mathbf{x}_2 - \mathbf{x}_1)\| \, . \qquad (A1.3)$$

The initial local z axis is given by the vector $\mathbf{i}_3^0$, which will usually be defined by input data. Based on the rotation of each node $\mathbf{R}_1$ and $\mathbf{R}_2$ one compute a rotated nodal z-axis for each node and the mean z axis $\mathbf{z}_m$ as

$$\mathbf{z}_1 = \mathbf{R}_1\mathbf{i}_3^0, \quad \mathbf{z}_2 = \mathbf{R}_2\mathbf{i}_3^0 \quad \text{and} \quad \mathbf{z}_m = \mathbf{z}_1 + \mathbf{z}_2 \, . \qquad (A1.4)$$

In general $\mathbf{z}_m$ will not be perpendicular to the beam element, or the local x axis. The $\mathbf{z}_m$ vector is chosen to be in the local (x, y) plane by computing the local y axis as the cross-product of the local z and x axis

$$\mathbf{i}_2^n = \frac{\mathbf{z}_m \times \mathbf{i}_1^n}{f} \quad \text{where} \quad f = \|\mathbf{z}_m \times \mathbf{i}_1^n\| \,. \tag{A1.5}$$

Finally, the perpendicular z axis is computed as

$$\mathbf{i}_3^n = \mathbf{i}_1^n \times \mathbf{i}_2^n \,. \tag{A1.6}$$

This defines the element transformation matrix

$$\mathbf{T}_n = \begin{bmatrix} \mathbf{i}_1^{nT} \\ \mathbf{i}_2^{nT} \\ \mathbf{i}_3^{nT} \end{bmatrix} . \tag{A1.7}$$

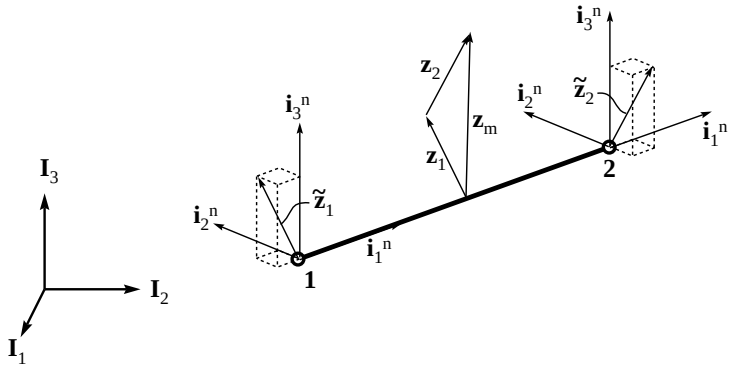

Figure A1.1. Local coordinate system a beam element.

Variation of this coordinate definition, measured in local coordinate system, gives the rigid body rotation of the element with respect to the visible degrees of freedom as

$$\delta\tilde{\boldsymbol{\omega}}_r = \tilde{\mathbf{G}}\delta\tilde{\mathbf{v}} \tag{A1.8}$$

where

$$\tilde{\mathbf{G}} = \begin{bmatrix} 0 & -\frac{1}{l}\frac{\tilde{z_{m\,x}}}{\tilde{z_{m\,z}}} & 0 & \frac{\tilde{z_{1\,z}}}{\tilde{z_{m\,z}}} & 0 & -\frac{\tilde{z_{1\,x}}}{\tilde{z_{m\,z}}} & 0 & \frac{1}{l}\frac{\tilde{z_{m\,x}}}{\tilde{z_{m\,z}}} & 0 & \frac{\tilde{z_{2\,z}}}{\tilde{z_{m\,z}}} & 0 & -\frac{\tilde{z_{2\,x}}}{\tilde{z_{m\,z}}} \\ 0 & 0 & \frac{1}{l} & 0 & 0 & 0 & 0 & 0 & -\frac{1}{l} & 0 & 0 & 0 \\ 0 & -\frac{1}{l} & 0 & 0 & 0 & 0 & 0 & \frac{1}{l} & 0 & 0 & 0 & 0 \end{bmatrix} . \tag{A1.9}$$

In the equation above l is the element length and the local coordinate z vectors are defined as

$$\left\{ \begin{array}{c} \tilde{z}_{1x} \\ \tilde{z}_{1y} \\ \tilde{z}_{1z} \end{array} \right\} = \mathbf{T}_n \mathbf{z}_1, \quad \left\{ \begin{array}{c} \tilde{z}_{2x} \\ \tilde{z}_{2y} \\ \tilde{z}_{2z} \end{array} \right\} = \mathbf{T}_n \mathbf{z}_z \quad \text{and} \quad \left\{ \begin{array}{c} \tilde{z_{mx}} \\ \tilde{z_{my}} \\ \tilde{z_{mz}} \end{array} \right\} = \mathbf{T}_n \mathbf{z}_m \qquad (A1.10)$$

where $\mathbf{z}_1$, $\mathbf{z}_2$ and $\mathbf{z}_m$ are defined in equation (A1.4) .